

NORTHWESTERN UNIVERSITY

A Chemical Approach to Understanding
Oxide Surface Structure and Reactivity

A DISSERTATION

SUBMITTED TO THE GRADUATE SCHOOL
IN PARTIAL FULFILLMENT OF THE REQUIREMENTS

For the degree

DOCTOR OF PHILOSOPHY

Field of Chemistry

By

James Andrew Enterkin

EVANSTON, ILLINOIS

September 2010

© Copyright by James A. Enterkin 2010

All Rights Reserved

ABSTRACT

A Chemical Approach to Understanding Oxide Surface Structure and Reactivity

James A. Enterkin

Transmission electron microscopy and diffraction are powerful tools for solving complex structural problems. They complement other analytical techniques, such as x-ray diffraction, elucidating problems which cannot be solved by other techniques. One area where they are of particularly great value is in the determination of surface structures. The research presented herein uses electron microscopy and diffraction as the primary experimental techniques in the development of a chemistry of surface structures.

High-resolution electron microscopy revealed that the $\text{La}_4\text{Cu}_3\text{MoO}_{12}$ structure has turbostratic disorder and a lower symmetry space group (Pm) than was previously found. The refinement of the x-ray data was significantly improved by using a disordered model and the Pm space group. A bond valence analysis confirmed that the disordered structure is the superior model.

Strontium titanate, SrTiO_3 , single crystal surfaces were examined principally via transmission electron diffraction. A homologous series with intergrowths was discovered on the (110) surface of strontium titanate, marking the first time that these important concepts of solid state chemistry have been found at the surface. Atmospheric adsorbates, such as H_2O and CO_2 , were found to help to stabilize undercoordinated surface structures on the (100) surface. It was

shown that chemical bonding, bond valence, atomic coordination, and stoichiometry greatly influence the development of surface structures. Additionally, such chemistry based analysis was demonstrated to be able to predict surface structure stability and reactivity.

Application of a modified Wulff construction to the observed shape of strontium titanate nanocuboids revealed that the surface structure and particle stoichiometry are interlinked, with control over one allowing equally precise control over the other. Platinum nanoparticles on the strontium titanate nanocuboids were shown via high resolution electron microscopy to have cube-on-cube epitaxy, with the shape of the platinum nanoparticles governed by the Winterbottom construction. Precise modification of the support surface will therefore allow engineering of supported metal particles with precise control over which facets are exposed. These results suggest that control over the support surface chemistry can be used to engineer thermodynamically stable, face selective catalysts.

Professor Kenneth R. Poeppelmeier

Professor Laurence D. Marks

Acknowledgements

I would like to begin by thanking my advisors, Professors Ken Poeppelmeier and Laurie Marks for their support, guidance, and advice over the past five years. Without their input, not only would the research detailed in the rest of this work never have turned out the way it did, but I would never even have started work on it. Through the research I performed with both, I have learned much about science, and discovered many things about myself as well. I would like to thank my committee members, Professors Randy Snurr and Don Ellis, for their time and energy, now and for the support and feedback which they have provided along the way and each time that the committee has sat for my presentations.

I am also indebted to many collaborators who helped out along the way. Some people have contributed significantly to particular sections of this work, and without them those sections might not exist, certainly not in their current form. Special thanks go out to: Chapter 2: Paul Maggard, Chris Own, Julien Lesage, Job Rijssenbeek, Charlotte Stern Shintaro Ishiwata, Masaki Azuma, and Mikio Takano; Chapter 3: Arun, Courtney, Bruce Russell, and Martin Castell; Chapter 4: Andres and Danielle; Chapter 5: Toshitaka Kuob; Chapter 6: Federico, Peter Stair, Jeff Elam, and Emilie. Thanks to Jim C., Courtney, and Yingmin for teaching me how to navigate SPEAR. Thank you to those students who will be taking the results outlined herein and moving them into the future: Robert, Yuyuan, and Chundao. A special mention also goes to Alicia for her work on the SrTiO₃ (110) (1xn) structures. Thank you as well to the rest of the Poeppelmeier and Marks groups, past and present, who have contributed insights at meetings and through informal discussions. I also owe thanks to all the people behind the scenes, who made

things run: Pat and Jasmine in the Catalysis center, Beth and Jonathan in the Chemistry department, Shoyou and Jinsong in EPIC, and Ken Eberly from Hitachi.

Thank you to all my friends who have helped me through this: Martin, Patrick, Katie, Dan, Chris, Teddy, Roman, Roger, Joey, Dana, Chris, Mike, Nicole, Tony, Cabby, Amy/Jen, Jeremy, Bekki, and everyone else (I'm sure I've left several people out). Special thanks to Brandon. With you guys, the good times are better, and the bad times become bearable.

Thank you to all of my relatives and in-laws for all the support you've offered along the way in good times and bad. To the Docster family, for accepting me into your family and treating me as one of your own. To all my aunts, uncles, and cousins. To my grandparents, Nana and Granpa, Grandmother and Grandpa Jack, for always being there and supporting me and believing in me and for all the other things you've done, which is more than I could ever properly thank you for. You are the best grandparents anyone could ever ask for. To Beth, I'm glad you moved out to Chicago; I never thought something like that would happen, but it's good to have family around. Also, did you ever think you'd finish school before me? Thank you especially to Mom and Dad: for always believing in me, for supporting me and helping me through all my difficulties, for teaching me how to think for myself and figure things out, for proofreading this thesis, and for other things without number. I love you all.

Thanks to Dougal and Crilly, for keeping me sane when you weren't driving me insane.

Finally, thank you to Elise. Meeting you was the absolute best thing that has come out of going to Northwestern. You are everything I could ever want or hope for. Thank you for love, friendship, understanding, joy, and, of course, for dinner.

Table of Contents

ABSTRACT.....	3
Acknowledgements	5
List of Figures.....	10
List of Tables	15
Chapter 1: Introduction	17
1.1: The Chemical Approach	18
1.2: Motivation.....	20
1.3: Organization.....	21
Chapter 2: Inorganic Chemistry of a Bulk Oxide: The Disordered Structure of La₄Cu₃MoO₁₂.....	24
2.1: Introduction.....	25
2.2: Experimental	28
2.2.1: <i>Synthesis</i>	28
2.2.2: <i>Crystallographic Structure Determination</i>	30
2.2.3: <i>Electron Microscopy</i>	35
2.2.4: <i>Bond Valence Analysis</i>	35
2.3: Results and Discussion	37
2.3.1: <i>Structural Disorder and Electron Microscopy</i>	37
2.3.2: <i>Bond Valence Analysis</i>	48
2.4: Conclusions.....	52
Chapter 3: Inorganic Chemistry of an Oxide Surface: A Homologous Series of Structures on the Surface of SrTiO₃ (110).....	53
3.1: Introduction.....	54
3.2: Experimental Methods	56
3.2.1: <i>Diffraction analysis</i>	56
3.2.2: <i>Bond Valence Sums</i>	57
3.2.3: <i>DFT calculations</i>	57
3.2.4: <i>STM Simulations</i>	60
3.3: Results.....	61

3.4:	Discussion.....	71
3.5:	Comparison to Other SrTiO ₃ (110) Surface Models.....	77
3.6:	Conclusions.....	80
Chapter 4: Reactivity of an Oxide Surface: Adsorbates on SrTiO₃ (1 0 0).....		82
4.1:	Introduction.....	83
4.2:	Experimental Methods.....	84
4.2.1:	<i>Sample Preparation</i>	85
4.2.2:	<i>X-ray Photoelectron Spectroscopy</i>	87
4.2.3:	<i>Transmission Electron Microscopy and Transmission Electron Diffraction</i>	88
4.2.4:	<i>Annealing</i>	89
4.2.5:	<i>Density Functional Theory Calculations</i>	91
4.2.6:	<i>Bond valence sum calculations</i>	92
4.3:	Results.....	92
4.3.1:	<i>Reconstructions after annealing in air</i>	92
4.3.2:	<i>H₂O on the c(4x2) reconstruction</i>	93
4.3.3:	<i>H₂O on the (√13x√13)-R33.7° reconstruction</i>	99
4.3.4:	<i>H₂O on the (2x1) reconstruction</i>	104
4.3.5:	<i>Calculations of H₂O and CO₂ on unreconstructed Sr- and Ti-terminations</i>	111
4.3.6:	<i>Desorption calculations for H₂O on the (2x1) structure</i>	117
4.3.7:	<i>Bond valence sums for structural models</i>	118
4.4:	Discussion.....	122
4.5:	Conclusions.....	133
Chapter 5: A Chemical Approach to Surface Science: Bond Valence Analysis of SrTiO₃ Surfaces.....		134
5.1:	Introduction.....	135
5.2:	Methods.....	140
5.3:	Bond valence sums and DFT structural relaxations.....	142
5.4:	BVS of model oxide surfaces.....	145
5.4.1:	<i>SrTiO₃ (110)</i>	145
5.4.2:	<i>SrTiO₃ (111)</i>	147
5.4.3:	<i>SrTiO₃ (100)</i>	158

5.5:	Adsorbates on surface structures	169
5.6:	Conclusions.....	171
Chapter 6: Towards Catalytic Applications: SrTiO₃ Nanocuboids.....		172
6.1:	Introduction.....	173
6.2:	Experimental Methods	176
6.2.1:	<i>Sample Preparation</i>	176
6.2.2:	<i>Transmission Electron Microscopy and Transmission Electron Diffraction</i>	177
6.2.3:	<i>Wulff and Winterbottom Calculations</i>	178
6.3:	Results.....	184
6.3.1:	<i>General nanocuboid morphology and bulk structure</i>	184
6.3.2:	<i>Nanocuboid annealing and TEM surface characterization</i>	185
6.3.3:	<i>Acid etching of SrTiO₃ nanocuboids</i>	191
6.3.4:	<i>Annealing of acid etched nanocuboids</i>	193
6.3.5:	<i>Wulff Construction for SrTiO₃ Nanocuboids</i>	193
6.3.6:	<i>Platinum Nanoparticles on SrTiO₃ Nanocuboids</i>	198
6.4:	Discussion.....	201
6.4.1:	<i>Voids in SrTiO₃ nanocuboids</i>	201
6.4.2:	<i>SrTiO₃ nanocuboid surfaces</i>	203
6.4.3:	<i>Platinum nanoparticles on SrTiO₃ nanocuboids</i>	208
6.5:	Conclusions.....	210
Chapter 7: Conclusions		212
References.....		215
Appendices.....		230
A.1:	XPS Peak Fits for All XPS Spectra in Chapter 4.....	230
A.2:	CIFs for All Structures, Including Bond Valence Sums.....	234
A.2.1:	<i>CIFs for La₄Cu₃MoO₁₂</i>	234
A.2.2:	<i>CIFs for SrTiO₃ (1 1 0) surface structures</i>	239
A.2.3:	<i>CIFs for SrTiO₃ (1 0 0) surface structures</i>	254
A.2.4:	<i>CIFs for SrTiO₃ (1 1 1) surface structures</i>	293

List of Figures

- Figure 2.1:** Perspective view of the fully ordered structure of $\text{La}_4\text{Cu}_3\text{MoO}_{12}$. Lanthanum atoms are grey and oxide ions are red. The blue and yellow bipyramidal polyhedra represent the CuO_5 and MoO_5 units, respectively. 26
- Figure 2.2:** Scanning electron micrograph of a $\text{La}_4\text{Cu}_3\text{MoO}_{12}$ crystal illustrating the external hexagonal morphology that reflects the internal hexagonal symmetry of the YAlO_3 sublattice.. 29
- Figure 2.3:** Structural view of a single layer of the triangular lattice of $\text{La}_4\text{Cu}_3\text{MoO}_{12}$ perpendicular to the b -axis. The copper ions are blue, oxide ions are red and molybdenum yellow. The CuO_5 trigonal pyramids are blue, MoO_5 trigonal bipyramids are yellow, and the Cu_3O trimers are outlined in green. The thick black line denotes the ab -face of the unit cell. ... 38
- Figure 2.4:** Direct methods solutions from precession electron diffraction on $\text{La}_4\text{Cu}_3\text{MoO}_{12}$ using amplitudes (a) and intensities (b). The cation positions show mixed Cu/Mo tetrahedral within each column. Figure courtesy of Chris Own.¹² 39
- Figure 2.5:** Left to right: precession electron diffraction pattern (courtesy of Chris Own¹²), TED pattern along $[0\ 0\ 1]$ zone axis, and TED pattern along $[2\ 0\ 1]$ zone axis. 40
- Figure 2.6:** Electron diffraction pattern along the $[010]$ zone axis. Monoclinic unit cell in red, pseudo-hexagonal sub-cell in blue. 41
- Figure 2.7:** Top: TEM image of a $\text{La}_4\text{Cu}_3\text{MoO}_{12}$ crystal with a 60° twin around the $[0\ 1\ 0]$ zone axis. Bottom, left to right: TED patterns taken along the zone axis from region A, from entire crystallite, and from region B. 42
- Figure 2.8:** Left: HREM image taken on the $[010]$ zone axis with Fourier transform insert. Right: post-processed images of a smaller region taken at three different foci (32 nm focus step). The processing involved performing a Fourier transform, masking spots besides the (101) , (-101) , $(-10-1)$, and $(10-1)$ spots of interest, and performing an inverse Fourier transform. This leaves an image dominated by the (101) and (-101) lattice fringes. 44
- Figure 2.9:** View down the a -axis of $\text{La}_4\text{Cu}_3\text{MoO}_{12}$ with the proposed twin boundary, shown by the green line. The twinning model is equivalent to disorder in the stacking between the layers, but preserving perfect intra-layer ordering. Copper atoms occupy blue polyhedra, molybdenum atoms occupy yellow polyhedra, and the lanthanum atoms are gray. 46
- Figure 2.10:** Left: Electron diffraction pattern along the $[100]$ zone axis with shorter exposure times overlaid over center of longer exposure times. Right: Close up of diffuse lines, marked with arrows. Unit cell in red. 47
- Figure 3.1:** TED pattern for the (3×1) reconstruction taken slightly off zone axis to improve the surface to bulk ratio of the signal and to make the surface diffraction more kinematical. Three different exposure times are overlaid to make more of the diffractions pattern visible. The bulk unit cell is outlined in yellow, the surface (1×1) in green, the (3×1) reconstruction in red, and the minor concurring (1×4) reconstruction in blue. 62

- Figure 3.2:** Scattering potential for the (3x1) surface structure with the surface atoms overlaid on the left half. The light features on the scattering potential map indicate areas of stronger scattering potential (i.e., strong scattering species). Titanium in blue and oxygen in red. 64
- Figure 3.3:** STM image of a (3x1) surface with an intergrowth of (4x1) with simulations overlaid (Sample bias = 0.9 V, tunneling current = 0.4 nA). 65
- Figure 3.4:** Surface structure of (3x1) reconstruction and the top bulk layer. Surface TiO_4 tetrahedra shown in blue, bulk TiO_6 octahedra in yellow, oxygen in red, and strontium in orange. Views perpendicular (top) and parallel (bottom) to the surface with unit cell outlined in black. 66
- Figure 3.5:** Surface structures of the homologous series of (nx1) surface structures viewed perpendicular to the surface. For clarity, the bulk is omitted. TiO_4 tetrahedra are shown in blue, with oxide anions in red. Unit cells are outlined in black, from left to right $n=2,3,4,5,6,\infty$ 68
- Figure 3.6:** Plot of surface energies for (nx1) surfaces and several previously proposed surfaces. The convex hull construction (blue line) shows the stable surface for a given composition. 68
- Figure 3.7:** STM (experimental with simulation overlaid) of intergrowths of (4x1) and (5x1) reconstructions (Sample bias = 0.9 V, tunneling current = 0.4 nA). 69
- Figure 3.8:** STM (experimental with simulation overlaid) of intergrowths of (5x1) and (6x1) reconstructions (Sample bias = 0.9 V, tunneling current = 0.4 nA). 70
- Figure 3.9:** Plot of energy per formula unit as a function of unit cell volume for TiO_2 in the coesite and rutile structure types. Volume is normalized to the DFT optimized volume of the rutile unit cell. An increase in unit cell volume is equivalent to a decrease in pressure. At normal pressures (volume close to 1) the rutile structure is favored, while at negative pressures (volume greater than 1) the coesite structure is preferred. 73
- Figure 4.1:** c(4x2) surface structure with top bulk layer. Surface TiO_5 trigonal bipyramids in green, bulk TiO_6 octahedra in yellow, strontium cations in orange, and oxygen anions in red. .. 94
- Figure 4.2:** c(4x2) diffraction pattern after annealing in air at 950°C for 5 hours. 95
- Figure 4.3:** O1s peak region of the XPS spectra from a sample with the c(4x2) reconstruction showing reduction of high binding energy should upon annealing. Counts per second for each spectra offset by a constant value for ease of viewing. 96
- Figure 4.4:** TED after annealing sample with c(4x2) reconstruction at 800°C for 20 minutes. Only a few spots at the locations of the brightest c(4x2) spots are still visible. 98
- Figure 4.5:** O1s peak region of the XPS spectra from a sample which began with the $(\sqrt{13}\times\sqrt{13})$ -R33.6 reconstruction (bottom) which disappeared (top) upon annealing. Counts per second for each spectra offset by a constant value for ease of viewing. The low binding energy shoulder is an artifact from the sample holder and should be ignored. 100
- Figure 4.6:** $(\sqrt{13}\times\sqrt{13})$ -R33.7° diffraction pattern after annealing in air at 850°C for 5 hours. 101

- Figure 4.7:** O1s peak region of the XPS spectra from a sample which began with the $(\sqrt{13}\times\sqrt{13})$ -R33.6 reconstruction (bottom) and transformed into a streaked (2x1) reconstruction (top) upon annealing. Counts per second for each spectra offset by a constant value for ease of viewing..... 102
- Figure 4.8:** Streaked diffraction pattern with higher intensity where (2x1) spots would exist as found after annealing a sample exhibiting the $(\sqrt{13}\times\sqrt{13})$ -R33.7° reconstruction in UHV..... 103
- Figure 4.9:** (2x1) surface structure with top bulk layer. Top: Clean surface. Bottom: H₂O saturated surface. TiO₅ trigonal bipyramids in blue, TiO₆ octahedra in yellow, strontium cations in orange, oxygen anions in red, and hydrogen cations in black. 105
- Figure 4.10:** (2x1) diffraction pattern with streaks in the (100) directions nearly resolving into a (5x1) reconstruction from a sample annealed in air at 950°C for 5h..... 106
- Figure 4.11:** O1s peak region of the XPS spectra from a sample which began with the (2x1) reconstruction showing changes in high binding energy shoulder upon annealing and exposure to air. Counts per second for each spectra offset by a constant value for ease of viewing..... 107
- Figure 4.12:** (2x1) diffraction pattern with decreased streaking and no indications of a (5x1) reconstruction following annealing at 750°C in 2×10^{-2} torr O₂. High pass filter applied to left half of image to enhance visibility of (2x1) diffraction spots..... 108
- Figure 4.13:** Dark-field TEM image showing TiO₂ particles growing on the surface of SrTiO₃. 109
- Figure 4.14:** TED pattern from an area of the SrTiO₃ sample with TiO₂ particles on the surface. 110
- Figure 4.15:** SrO (1x1) termination with H₂O (top) and CO₂ (bottom) adsorbed. Titanium octahedral in blue, strontium in orange, oxygen in red, carbon and hydrogen in black. 112
- Figure 4.16:** TiO₂ (1x1) termination with H₂O (top) and CO₂ (bottom) adsorbed. Titanium octahedral in blue, strontium in orange, oxygen in red, carbon and hydrogen in black. 114
- Figure 4.17:** SrTiO₃ (2x2) structure with top bulk layer. TiO₅ trigonal bipyramids in blue, TiO₆ octahedra in yellow, strontium cations in orange, oxygen anions in red. 123
- Figure 4.18:** Proposed pathway for transformation of (2x1) (left) to c(4x2) (right) with (2x2) (middle) as intermediate. To change from the (2x1) to (2x2) structures, sufficiently few hydroxyl groups must be present to allow the titanium cations to arrange into a structure which is less favorable for hydroxyl groups. TiO₅ trigonal bipyramids in green, TiO₆ octahedra in yellow, strontium cations in orange, oxygen anions in red. Black arrows show titanium cation movements necessary to transform to the next structure. 131
- Figure 5.1:** Global, surface, and bulk instability indices and energy plotted as a function of geometry optimization step. Energy is relative to the final energy. 143

- Figure 5.2:** SrTiO₃ (111) models 5 (left) and 6 (right). Top: plan view. Bottom: profile view. TiO₆ octahedra as yellow polyhedra, 3-coordinate Ti as blue spheres, Sr as orange spheres, and O as red spheres. Unit cell outlined in black. 149
- Figure 5.3:** SrTiO₃ (111) models 7 (left) and 8 (right), Top: plan view. Bottom: profile view. TiO₆ octahedra as yellow polyhedra, 3-coordinate Ti as blue spheres, Sr as orange spheres, and O as red spheres. Unit cell outlined in black. 150
- Figure 5.4:** SrTiO₃ (111) models 3 (left) and 4 (right), Top: plan view. Bottom: profile view. TiO₆ octahedra as yellow polyhedra, TiO₅ square-pyramids as green polyhedra, TiO₄ tetrahedra as blue polyhedra, Sr as orange spheres, and O as red spheres. Unit cell outlined in black..... 152
- Figure 5.5:** SrTiO₃ (111) models 1 (left) and 2 (right), Top: plan view. Bottom: profile view. TiO₆ octahedra as yellow polyhedra, 3-coordinate Ti as blue spheres, Sr as orange spheres, and O as red spheres. Unit cell outlined in black. 155
- Figure 5.6:** SrTiO₃ (111) models 9 (left) and 10 (right), Top: plan view. Bottom: profile view. TiO₆ octahedra as yellow polyhedra, TiO₇ irregular decahedra as silver polyhedra, Sr as orange spheres, and O as red spheres. Unit cell outlined in black..... 157
- Figure 5.7:** ($\sqrt{2}\times\sqrt{2}$)-R45° (bottom) surface structures. TiO₆ octahedra as yellow polyhedra, TiO₅ trigonal bipyramids as green polyhedra, Sr as orange spheres, and O as red spheres. 161
- Figure 5.8:** SrTiO₃ (100) Sr-atom (left) and O-vacancy (right) models for the ($\sqrt{5}\times\sqrt{5}$)-R26.6° reconstruction. Top: plan view. Bottom: profile view. TiO₆ octahedra as yellow polyhedra, TiO₅ square-pyramids as green polyhedra, TiO₄ tetrahedra as blue polyhedra, Sr as orange spheres, and O as red spheres. Unit cell outlined in black..... 163
- Figure 6.1:** Wulff construction¹⁵⁷ for platinum using $\gamma_{(111)}:\gamma_{(001)}$ ratio of 0.84 from Vitos et. al.¹⁷⁰ 179
- Figure 6.2:** Surface free energies and compositions for structures calculated by Professor Marks⁷³ and surface energies extrapolated to match calculation parameters for other structures of interest. Structures which are discussed in this work are labeled. Error bars shown only for calculated structures..... 182
- Figure 6.3:** Winterbottom construction¹⁵⁸ for platinum on a surface, showing relative energies for different possible degrees of truncation. Wulff shape in black, substrate surface in grey, with arrow indicating magnitude of $\gamma_{\text{Int}} - \gamma_{\text{Sub}}$ 183
- Figure 6.4:** Low resolution TEM images of as-prepared SrTiO₃ nanocuboids. 184
- Figure 6.5:** Left: HREM image of an as-prepared nanocuboid corner showing (100) and (110) step edges. Right: Near zone axis TED of a single as-prepared nanocuboid. 185
- Figure 6.6:** Samples annealed prior to dispersion on TEM grid. Left: 700°C for 5 hours in air. Right: 850°C for 1 hour in air. 186
- Figure 6.7:** Low resolution TEM (left) and HREM (right) images of nanocuboids annealed at 950°C for 20 hours showing smoother (100) faces and distinct (110) faceting at the corners... 187

- Figure 6.8:** TEM of nanocuboids annealed in flowing O₂ for 5 hours at 1100°C showing roughening of surface. 189
- Figure 6.9:** TEM of samples etched in 0.3N 3:1 (v/v) HCl:HNO₃ solution for 20 minutes. 190
- Figure 6.10:** TEM image of sample etched in 3:1 (v/v) HCl:HNO₃ solution. Left: 0.3N for 12 hours. Right: 3.0N for 15 minutes, showing a void which has become an exterior surface. 191
- Figure 6.11:** TEM of sample etched in 0.3N 3:1 (v/v) HCl:HNO₃ solution for 12 hours then annealed at 950°C for 5 hours in flowing O₂ showing irregular shape but well defined (100) and (110) facets. 192
- Figure 6.12:** TEM image of platinum nanoparticles on strontium titanate nanocuboids. 199
- Figure 6.13:** HREM image of platinum nanoparticles on the (100) face of a strontium titanate nanocuboid. Near perfect alignment of Pt (100) and SrTiO₃ (100) lattice fringes indicates a strong epitaxy. Wulff construction shapes for platinum are overlaid upon the platinum nanoparticles in red, showing that slightly more than half of the Wulff construction shape exists above the substrate surface. 200

List of Tables

Table 2.1: Single-crystal X-ray data refinement parameters for $\text{La}_4\text{Cu}_3\text{MoO}_{12}$	30
Table 2.2: Selected interatomic distances and bond angles for $\text{La}_4\text{Cu}_3\text{MoO}_{12}$	33
Table 2.3: Crystallographic data for $\text{La}_4\text{Cu}_3\text{MoO}_{12}$ based on the single crystal refinement in space group Pm with Mo disordered over 2 possible positions in every other layer and $a = 6.8560(6)$ Å, $b = 10.9802(10)$ Å, $c = 7.9147(7)$ Å, and $\beta = 90.0160(10)^\circ$. Numbers listed in the B_{eq} column are the isotropic equivalent thermal displacement parameters. All disordered sites were constrained to yield a full occupancy of the site.	33
Table 2.4: BVSs for the disordered and twinned model. Values for disordered fraction B only listed if they differ from values for fraction A by > 0.01	36
Table 3.1: Atomic coordinates for the (3x1) surface structure.	64
Table 3.2: Ti-O bond lengths for the (3x1) surface structure.	67
Table 3.3: Bond valence sums and Bader charges for the (3x1) surface structure.	67
Table 3.4: Comparison of coordination metrics across (nx1) series.....	72
Table 3.5: Bond valence sums and multiplicity (per (1x1) unit cell) of atoms at the surface and in the tow two bulk layers of SrTiO_3 (110) surface structures in the (nx1) homologous series... ..	75
Table 3.6: Bond valence sums and multiplicity (per (1x1) unit cell) of atoms at the surface and in the tow two bulk layers of other SrTiO_3 (110) surface structures.	78
Table 4.1: Bond valence sums and multiplicity (per (1x1) unit cell) for SrO terminated unreconstructed SrTiO_3 (100) surface, both clean and with H_2O and CO_2 adsorbed, showing surface and top two bulk layers.	119
Table 4.2: Bond valence sums and multiplicity (per (1x1) unit cell) for TiO_2 terminated unreconstructed SrTiO_3 (100) surface, both clean and with H_2O and CO_2 adsorbed, showing surface and top two bulk layers.	120
Table 4.3: Bond valence sums and multiplicity (per (1x1) unit cell) for (2x1) (both clean and hydroxylated) and c(4x2) structures, showing surface and top two bulk layers.....	121
Table 5.1: Bond valence sums for models of the DFT optimized SrTiO_3 (110) TiO (1x1) surface structure using a model with different numbers of slabs. *The SII includes only the surface and linking layers, not the 1 st bulk layer: the 1 SrTiO layer model was so thin that including the top (and only) SrTiO^{4+} layer would make the SII the same as the GII, and thus not a useful metric for comparison in this case.	144
Table 5.2: Bond valence sums and multiplicity (per 1x1 unit cell) of atoms at the surface and in the tow two bulk layers of SrTiO_3 (111) surface structure models 3, 4, 5, 6, 7, and 8.....	153

Table 5.3: Bond valence sums and multiplicity (per 1x1 unit cell) of atoms at the surface and in the top two bulk layers of SrTiO ₃ (111) surface models 1, 9, and 10 (oxidized) and model 2 (reduced).	154
Table 5.4: Bond valence sums and multiplicity (per 1x1 unit cell) of atoms at the surface and in the top two bulk layers of SrTiO ₃ (100) surface for SrO bulk termination, TiO ₂ bulk termination, (2x1), (2x2), ($\sqrt{2}\times\sqrt{2}$)-R45°, and c(4x2) reconstructions.	160
Table 5.5: Bond valence sums and multiplicity (per 1x1 unit cell) of atoms at the surface and in the top two bulk layers of SrTiO ₃ (100) surface for Sr-adatom models with $\theta \leq 0.25$ Sr-adatoms per 1x1 surface unit cell.	164
Table 5.6: Bond valence sums and multiplicity (per 1x1 unit cell) of atoms at the surface and in the top two bulk layers of SrTiO ₃ (100) surface for Sr-adatom models with $\theta > 0.25$ Sr-adatoms per 1x1 surface unit cell.	166
Table 5.7: Comparison of bond valence sums for Sr-adatom and O-vacancy models for SrTiO ₃ (100) ($(\sqrt{5}\times\sqrt{5})$)-R26.6° reconstruction.	168
Table 6.1: $d_{(110)}:d_{(100)}$ ratio for nanocuboids following various annealing conditions.	180
Table 6.2: $\gamma_{(110)}:\gamma_{(100)}$ ratios from calculations by Professor Marks ⁷³ and extrapolated energies. Values within one standard deviation of experiment are highlighted.	194
Table 6.3: Total contribution (in keV) to the free energy from surface free energies (eV) and bulk starvation for a stoichiometric 60nm diameter SrTiO ₃ nanocuboids with the observed $d_{(110)}:d_{(100)}$ ratio. Values within 10 keV of the lowest energy value are highlighted.	195
Table 6.4: Total contribution (in keV) to the free energy from surface free energies (eV) and bulk starvation for a 60nm diameter SrTiO ₃ nanocuboids with the observed $d_{(110)}:d_{(100)}$ ratio synthesized with a titanium rich surface. Values within 10 keV of the lowest energy value are highlighted.	196
Table A.1.1: Peak fitting for O1s peak region, including main O1s peak, the high binding energy shoulder (hydroxyl shoulder) and, when applicable, the holder artifact.	231
Table A.1.2: Peak fitting for Ti2p peak region, including Ti2p ^{3/2} and Ti2p ^{1/2} peaks and, when applicable, reduced titanium peaks.	232
Table A.1.3: Peak fitting for Sr3d and C1s peak regions, including Sr3d ^{5/2} and Sr3d ^{3/2} peaks, C1s peak and, when applicable, the non-charging C1s peak from the sample holder.	233

Chapter 1:
Introduction

1.1: The Chemical Approach

In 1661, Robert Boyle, in his book *The Sceptical Chymist*, described chemistry as “the subject of the material principles of mixt bodies.”¹ A more modern definition, reflecting the advances made in chemistry and encompassing the broad range of what chemistry has become, is given by Raymond Chang as “the study of matter and the changes it undergoes.”² Chemistry relies much on concepts such as bonding and symmetry to describe materials and reactions.

Physics also may deal with matter, but with a different approach, traditionally being more concerned with energy, force, and motion. Physics often uses more rigorous formulae and mathematics to describe interactions in the physical world. While the rigor is important and often necessary, it is easy to miss critical intuitive insights that are readily apparent when using simpler models. Chemistry and physics should not be viewed as rival disciplines, however. When working towards a better understanding of matter and its transformations, there is great benefit to using both approaches. This is especially true when attempting to solve difficult problems.

Understanding of inorganic structure and bonding took a large step forward in the early twentieth century. The first single crystal X-ray structures were published in 1913, among which was the NaCl structure by W. H. Bragg and W. L. Bragg.³ To describe the rock-salt structure, the ionic bonding model was devised by Born, Landé, and Madelung.⁴ According to the ionic bonding model, each sodium ion carries a single positive charge, while each chloride ion carries a single negative charge, with the crystal held together by the attractive forces between oppositely charged ions. Although the model is not perfect, it is most useful due to its simplicity

and ability to accurately describe the structure and chemistry of ionic crystals. Indeed, the ionic bonding model is still taught to chemistry students today. According to classical physics as it was conceived in the early twentieth century, however, such an array of charges would collapse into a singularity. A repulsive potential between atoms was therefore postulated and developed. It was the success of the ionic bonding model that led to this advancement of physics. In such manner, the twin approaches of chemistry and physics have often advanced each other and have led to the modern understanding of structures and materials.

The understanding of surfaces has, in general, lagged behind the understanding of the bulk. One reason is that the study of surfaces is inherently more difficult. A classic quotation, usually attributed to Wolfgang Pauli, states that while “God made the solid state, he left the surface to the devil.” One major reason for this difficulty is that there is far less available to study. In anything but the tiniest nanoparticles, the majority of the atoms in a material are not at the surface. This makes many bulk techniques difficult, and in some cases impossible, to apply to the study of surfaces. Similarly, the two dimensional nature of surfaces can create troubles for methods designed to be applied in three dimensions.

Perhaps another reason why the current understanding of the surface lags behind the understanding of the bulk is that the study of surface structures has not been subject to the same two pronged attack of chemistry and physics. Most models for understanding the surface are physics based. While analyses of the energies are often considered foremost, the chemical bonding and atomic coordination of solid surfaces are seldom discussed. One of the major goals of this work, therefore, is to advance the understanding of solid surfaces from a chemical

perspective. It is hoped that, by doing so, the understanding of surfaces can be elevated and brought in line with the understanding of bulk structures.

1.2: Motivation

Surfaces are, of course, of interest for many reasons. They play a significant role in the world all around us. It is through the surface that a material interacts with the environment around it. For example, every film that has been ever been grown on a substrate was formed upon the substrate's surface, with the surface structure of the substrate having a direct effect on the film, as compared to the bulk structure's indirect effect.

One area of particular interest in this work, and in which surface structure and chemistry play a great role, is heterogeneous catalysis. In heterogeneous catalysis, all reactions occur on the surface of the catalyst. Understanding the surface structure at the atomic level will allow for a better understanding of the active sites and how reactions occur. A predictive model of surface structures, when combined with this enhanced atomic level understanding of catalysis, may allow for the design of optimized catalysts. As almost all industrial chemical processes involve catalysis, the ability to manufacture a catalyst to meet specific needs would be invaluable. The second major goal of this work, therefore, is to apply this chemical understanding to heterogeneous catalysis.

1.3: Organization

This work begins with an examination of the inorganic chemistry of a bulk oxide structure, $\text{La}_4\text{Cu}_3\text{MoO}_{12}$. This complex structure exhibits a turbostratic disorder which was elucidated through a combination of several techniques. In Chapter 2, this structure is discussed. The $\text{La}_4\text{Cu}_3\text{MoO}_{12}$ structure serves as an introduction to solid state chemistry as it applies to bulk oxide materials. Additionally, several of the techniques which will be used later in this work to analyze surface structures, such as transmission electron microscopy (TEM), transmission electron diffraction (TED), and bond valence sums (BVS), are described in Chapter 2.

For the remainder of this work, attention turns to the surface, dealing mainly with the surface of strontium titanate, SrTiO_3 . Strontium titanate is a mixed metal oxide with the perovskite structure. It consists of a simple cubic strontium lattice with oxygen at the face centers and titanium at the body center. Alternatively, it can be viewed as a series of corner sharing TiO_6 octahedra with strontium cations in the interstitial spaces. Its greatest value to the current study is as a model, both for the perovskite structural class and for oxides in general.

In Chapter 3, the (1 1 0) surface of strontium titanate is examined. Solving the (3x1) structure from TED data allowed for the discovery of a homologous series with intergrowths, as was confirmed through density functional theory (DFT) calculations and comparison with collaborators' scanning tunneling microscopy (STM) images. While homologous series are common in the bulk, this is the first example of one seen at the surface. As revealed through trends in the BVS, it is found to follow the same rules as bulk structures. This homologous

series provides a strong indication that the principles governing bulk chemistry govern the chemistry of the surface as well.

In Chapter 4, attention begins to focus on the reactivity of surfaces through an investigation of adsorbates on the strontium titanate (1 0 0) surface. The manner in which water and carbon dioxide interact with the surface and the role that they play in the formation of surface structures are examined. It is found that the same rules of chemical bonding which govern bulk structures and surface structures also control how molecules interact with the surface.

Chapter 5 then examines the chemical bonding of surface structures in general. All the solved and proposed strontium titanate surface structures for which there are atomic scale models are reexamined from a bond valence perspective. It is shown that this simple chemical model not only explains the observed structures, but can predict both which models are likely to be correct and where foreign species are likely to adsorb on surfaces.

After having established how certain chemical principles can be used to explain surfaces, this work moves away from large single crystals in an attempt to apply this knowledge to heterogeneous catalysis. The most straightforward path to applying this knowledge to high surface area powders is through the use of nanocrystals, which have both high surface area and oriented surfaces. Chapter 6, therefore, deals with strontium titanate nanocubes, which are single crystals of strontium titanate of near cubic shape and diameters of approximately 60 nm. The surface of these nanocubes is analyzed, as are platinum nanoparticles deposited on the nanocubes. The surface of the nanocubes and the interface between the nanocubes and the

platinum nanoparticles is shown to determine the shape and surface exposure of the platinum. It is demonstrated, moreover, how control over the surface of the support can be used to create stable catalytic particles with certain facets preferentially exposed. Finally, the implications for face selective catalysis are discussed.

In summary, this work takes the rules governing bulk chemical bonding and demonstrates that those rules govern the surface as well and that those same rules can be used to predict surface structure and reactivity. It then shows how understanding and controlling the surface may be put to practical use in the field of heterogeneous catalysis.

Chapter 2:

Inorganic Chemistry of a Bulk Oxide:

The Disordered Structure of $\text{La}_4\text{Cu}_3\text{MoO}_{12}$

2.1: Introduction

Transition metals with unpaired d-electrons, such as Cu^{2+} (d^9 ; $S = 1/2$), can display a variety of magnetic behaviors beyond the familiar ferromagnetic or antiferromagnetic properties. Systems in which competing magnetic interactions make a single ordered ground state impossible are known as "frustrated". Investigations of frustrated spin systems are of interest not only for their unusual magnetic behavior, but also because of their far-reaching implications with respect to spin glasses and even how water freezes into ice.⁵

A simple example of a frustrated system is a two-dimensional triangular lattice of antiferromagnetically interacting spins. When magnetic spins are placed on the vertices of the triangles it becomes impossible to satisfy all of the anti-ferromagnetic interactions – only two of the three spins can be aligned anti-parallel simultaneously. The layered lattice of $\text{La}_4\text{Cu}_3\text{MoO}_{12}$ resembles such a frustrated system with slightly distorted Cu_3O triangular clusters isolated by MoO_5 trigonal bipyramids, shown in Figure 2.1. The overall structure is derived from the hexagonal YAlO_3 structure type with a 3:1 ordering of Cu^{2+} and Mo^{6+} cations superimposed on the B metal site. This structure was recently determined based on combined powder X-ray, electron and neutron diffraction data by Vander Griend *et al.*⁶

Magnetic susceptibility, high-field magnetization and specific heat measurements on polycrystalline samples of $\text{La}_4\text{Cu}_3\text{MoO}_{12}$ have shown that its magnetism is best described by three distinct temperature regimes.^{6,7} At high temperatures, individual Cu^{2+} spins act independently to produce a paramagnetic state. Below 250 K, strong intra-triangle antiferromagnetic interactions align two of the three spins to yield trimers with $S_{\text{total}} = 1/2$. The

localized moments on the trimers, which now form a square net, then align antiferromagnetically below 2.6 K as a result of weak inter-trimer interaction. Inelastic and elastic magnetic neutron scattering experiments have gauged the intra-trimer coupling constants and revealed that the inter-trimer ordering doubles the unit cell along the a direction. Recent theoretical studies have attempted to determine how the intra-triangle coupling affects the long-range ordering wave vector of the low-temperature phase.⁸⁻¹⁰ To relate theoretical predictions to the true magnetic

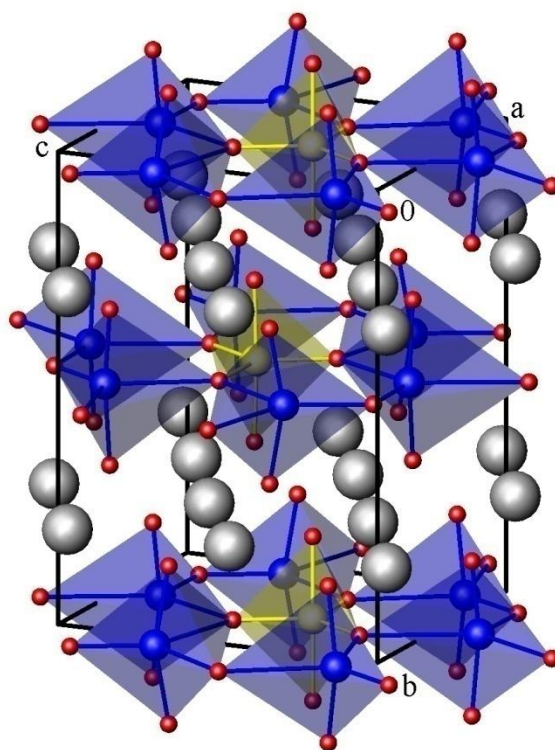


Figure 2.1: Perspective view of the fully ordered structure of $\text{La}_4\text{Cu}_3\text{MoO}_{12}$. Lanthanum atoms are grey and oxide ions are red. The blue and yellow bipyramidal polyhedra represent the CuO_5 and MoO_5 units, respectively.

ground state, single crystals are often necessary because anisotropic properties, such as the magnetization or electron spin resonance absorption, can then be measured along each axis. Unfortunately, single crystals of complex metal oxides are notoriously difficult to obtain.

The flux-growth technique has been used successfully for many years to grow single crystals of complex materials such as high- T_c cuprate superconductors.¹¹ However, the process is by no means trivial, and several factors must be considered when investigating a new system. The selection of the appropriate flux composition, growth temperature, cooling rate and starting materials, among many other factors, is critical for obtaining crystals of useful size and quality. For the current study, the choice of a CuO/KCl flux was a key to the successful growth of single crystals.

Attempts to grow $\text{La}_4\text{Cu}_3\text{MoO}_{12}$ from a melt of the same composition (*i.e.*, a self flux) were unsuccessful. The high temperatures required to melt the system led to significant volatilization of CuO and produced only small clear colorless crystals of La_2MoO_6 . To overcome these problems, copper oxide was chosen as a flux for two reasons: 1) to suppress the formation of La_2MoO_6 and 2) to lower the melting temperature. To further minimize the vaporization of CuO, the sample was sealed in a platinum capsule. Addition of KCl allowed the facile isolation of the $\text{La}_4\text{Cu}_3\text{MoO}_{12}$ crystals from the CuO flux and the residual starting material.

In polycrystalline samples of $\text{La}_4\text{Cu}_3\text{MoO}_{12}$, three distinct cation ordering patterns were observed depending on the thermal history of the sample.⁶ Quenched samples showed no ordering, with the Cu^{2+} and Mo^{6+} randomly distributed over the five-coordinate metal sites. This is reflected in the unit cell and space group ($a_h \approx 4 \text{ \AA}$, $c_h \approx 11 \text{ \AA}$, $P6_3/mmc$), which are closely

related to those of YAlO_3 . An intermediate cooling rate yielded partial ordering of the cations and consequently a larger unit cell ($a_o \approx a_h \approx 4 \text{ \AA}$, $b_o \approx \sqrt{3}a_h \approx 6.9 \text{ \AA}$, $c_o \approx c_h \approx 11 \text{ \AA}$, $Pmnm$). Finally, slower cooling at a rate of $36^\circ/\text{hr}$ allowed the cations to fully order within each Cu_3MoO_4 layer and produced the monoclinic unit cell ($a_m \approx 2a_h \approx 8 \text{ \AA}$, $b_m \approx \sqrt{3}a_h \approx 6.9 \text{ \AA}$, $c_m \approx c_h \approx 11 \text{ \AA}$, $\gamma \approx 90^\circ$, $P112_1/m$) with a triangular arrangement of coppers. The existence of these three possible phases dictated the use of the slow cooling rate.

Even after the crystals were grown, the structure was not easily solved. To improve the refinement, twinning was introduced into the structural model. While this significantly improved the R value from $\sim 10\%$ to $\sim 4\%$, several problems remained with the refinement, such as the presence of non-positive definite thermal parameters for many atoms. Additionally, the twin was not readily visible in TEM imaging or diffraction. Further, direct method analysis of precession electron diffraction data indicated that instead of a twin occurring in the $\text{La}_4\text{Cu}_3\text{MoO}_{12}$ structure, the copper and molybdenum might be disordered.¹²⁻¹⁴ Additional TEM and TED studies, coupled with further analysis of the X-ray diffraction data were therefore undertaken to conclusively determine the structure of the $\text{La}_4\text{Cu}_3\text{MoO}_{12}$ crystals.

2.2: Experimental

2.2.1: Synthesis.

Single crystals of $\text{La}_4\text{Cu}_3\text{MoO}_{12}$ were grown by Shintaro Ishiwata by means of a molten-salt flux of CuO/KCl . A polycrystalline sample was prepared by annealing a stoichiometric mixture of La_2O_3 , CuO and MoO_3 (all 99.99% pure) at 1025°C for 4 days with intermediate

regrindings. For the single-crystal growth, the resulting powder was mixed with CuO and KCl in a weight ratio of 1:0.5:0.3, respectively, placed in a platinum capsule (10 ϕ x 20 mm) and sealed by folding and pressing the ends. The capsule was heated to 1120 $^{\circ}$ C and allowed to soak for one hour. The sample was then slowly cooled to 900 $^{\circ}$ C at rate of 1 $^{\circ}$ C/h, and then cooled to room temperature over 40 hours. Deep red crystals of La₄Cu₃MoO₁₂ were recovered from the KCl/CuO flux by washing with water and could be distinguished from the remaining CuO by their plate-like morphology. It was necessary to cut the crystals, which were often intergrown, to obtain single crystals suitable for diffraction experiments. Scanning electron microscopy (JEOL JSM-6301F) and energy dispersive X-ray spectroscopy analyses (JEOL JED-2140) were performed on multiple crystals to examine the morphology and the composition. As shown in Figure 2.2, the hexagonal symmetry of the YAlO₃ sublattice is reflected in the external morphology of the crystal.

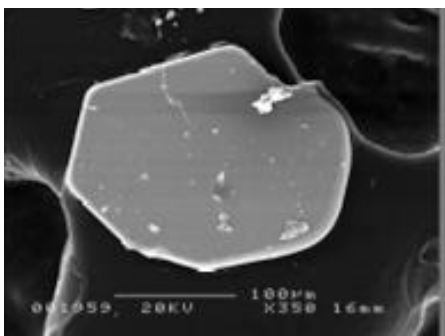


Figure 2.2: Scanning electron micrograph of a La₄Cu₃MoO₁₂ crystal illustrating the external hexagonal morphology that reflects the internal hexagonal symmetry of the YAlO₃ sublattice.

Table 2.1: Single-crystal X-ray data refinement parameters for $\text{La}_4\text{Cu}_3\text{MoO}_{12}$

Crystal Data		Data Collection and Refinement	
Formula	$\text{La}_4\text{Cu}_3\text{MoO}_{12}$	Radiation (λ)	Mo $K\alpha$ (0.71073 Å)
Space Group	P m (#6)	Unique reflections	2865
a (Å)	6.8560(6)	with $I > 2\sigma(I)$	2465
b (Å)	10.9802(10)	Number of parameters	152
c (Å)	7.9147(7)	h	-9 \rightarrow 9
α (°)	90	k	-14 \rightarrow 14
β (°)	90.0160(10)	l	-10 \rightarrow 10
γ (°)	90		
Z	2	$R[F^2 > 2\sigma(F^2)]$	0.0448
V (Å ³)	595.82(9)	$R(F^2)$	0.0514
d_{calc} (g cm ⁻³)	5.765	$sR2[F^2 > 2\sigma(F^2)]$	0.1424
μ (mm ⁻¹)	20.318	$wR2(F^2)$	0.1583
T (K)	153(2)	S (G.O.F.)	1.107
Crystal shape	Dark red plate		
Crystal dimensions (mm ³)	0.034 x 0.118 x 0.116		

2.2.2: Crystallographic Structure Determination.

Collection of the X-ray diffraction data and initial structural solution in space group $P2_1/m$ were carried out by Paul Maggard. X-ray diffraction data were collected on a Bruker CCD diffractometer operating at 153 K and indicated a monoclinic unit cell with $a = 6.8560(6)$ Å, $b = 10.9802(10)$ Å, $c = 7.9147(7)$ Å and $\beta = 90.0160(10)^\circ$. Relevant details regarding the data collection and refinement are given in Table 2.1. The structure was refined with SHELXTL¹⁵ using the published structure (derived from powder diffraction data) as the starting model. Refinement of the structure in space group $P2_1/m$ (No. 11), although yielding a better R -value than other space groups, initially did not produce a satisfactory solution. The observation that the $|E^2 - 1|$ statistic used for predicting whether or not a structure is centrosymmetric was much larger (1.330) than expected for a centrosymmetric space group (0.968), and that the

monoclinic β angle was very close to 90° suggested the possibility of a pseudo-merohedrally twinned structure¹⁶. In this situation, where the reflections from each twin component overlap, the structure emulates orthorhombic symmetry and is described by the twin law of the form $[1\ 0\ 0 / 0\ -1\ 0 / 0\ 0\ -1]$. The twin law describes, in matrix form, the relationship of the hkl indices of one monoclinic twin to those of the other. Introduction of twinning in the refinement reduced the $R1$ value from $\sim 10\%$ to $\sim 4\%$. The final anisotropic structure refinement in $P2_1/m$ converged at $R1 = 0.0396$ and $wR2 = 0.1094$, with a data to variable ratio of over 14:1. The relative amount of each twin component was refined and converged to 0.637(3), indicating the crystal was twinned with an approximate 64:36 ratio of one twin to the other. Three other twin laws were also found to have a nearly identical effect: $[-1\ 0\ 0 / 0\ -1\ 0 / 0\ 0\ 1]$, $[-1\ 0\ 0 / 0\ 1\ 0 / 0\ 0\ 1]$, and $[1\ 0\ 0 / 0\ 1\ 0 / 0\ 0\ -1]$. It should be noted that in the current study the standard setting of $P12_1/m1$ ($b = \text{unique}$) was used, whereas in the previous report the authors selected the non-standard $P112_1/m$ ($c = \text{unique}$) to facilitate comparisons between the various possible cation ordering patterns.

The absence of any evidence for twin domains of this type in the electron microscopy data (see below), even though the twin law significantly improved the refinement, suggested that some disorder existed which, when averaged over the area from which diffraction information was taken, had the same effect on the diffraction pattern as a pseudo-merohedral twin law. Because the major change to the structure upon application of the twin law is to change the stacking of Cu_3MoO_4 layers relative to each other, the structure was refined with disordered stacking of the Cu_3MoO_4 layers. Since such disordering of the stacking broke the crystal

symmetry, it was necessary to refine the structure in space group Pm , the only maximal subgroup of $P2_1/m$ whose symmetry did not constrain the relationship between the two Cu_3MoO_4 layers within the unit cell. Initial refinement in space group Pm converged at $R1 = 0.0598$ and $wR2 = 0.1966$, already an improvement upon the initial refinement in $P2_1/m$ for which $R1 \sim 0.10$. A partially disordered model was tested, where one of the two Cu_3MoO_4 planes could be in the original position or shifted by half the unit cell in the c direction, thus allowing the ions in that layer to be disordered over two of the four possible positions while maintaining all in-plane spacings. The refinement for this partially disordered model was superior to the twin model in Pm , converging at $R1 = 0.0456$ and $wR2 = 0.1583$. Attempts to refine a fully disordered model, with each atom disordered over all four possible positions, were unsuccessful, likely due to the high number of parameters being refined simultaneously. For completeness, the same twin law as used in space group $P2_1/m$ was also tested, but did not converge quite as well as the partially disordered model, with $R1 = 0.0503$ and $wR2 = 0.1654$. Atomic coordinates, isotropic-equivalent displacement parameters and selected inter-atomic distances and bond angles for the partially disordered structural model in space group Pm are listed in Table 2.2 and Table 2.3.

While the partially disordered model refined the best, it was still not perfect, likely because it modeled only a portion of the disorder, and not the disorder in totality. Only the lanthanum and molybdenum atoms could be refined anisotropically: refining lighter atoms anisotropically resulted in non positive definite thermal parameters. For the twinned model in Pm , even some lanthanum and molybdenum atoms were non positive definite when refined anisotropically, another indication that the disordered model is a better fit. Further, there were

large variations in the isotropic thermal parameters for atoms in the Cu_3MoO_4 plane. This, however, is consistent with the fully disordered model, as those positions would be occupied by

Table 2.2: Selected interatomic distances and bond angles for $\text{La}_4\text{Cu}_3\text{MoO}_{12}$.

Bond	Distance (Å)	Bonds	Angle (°)
Mo1 - O10	1.793(13)	O10 - Mo1 - O11	119.6(6)
Mo1 - O11	1.803(13)	O10 - Mo1 - O12	119.2(6)
Mo1 - O12	1.807(12)	O11 - Mo1 - O12	121.1(6)
Cu1 - O9	1.999(16)	Cu3 - O9 - Cu2	124.2(8)
Cu2 - O9	1.966(15)	Cu3 - O9 - Cu1	119.0(7)
Cu3 - O9	1.909(15)	Cu2 - O9 - Cu1	116.8(7)
Mo2A - O16A	1.78(3)	O16A - Mo2A - O15A	120.8(14)
Mo2A - O15A	1.88(3)	O16A - Mo2A - O14A	119.1(15)
Mo2A - O14A	1.98(4)	O15A - Mo2A - O14A	120.1(15)
Cu4A - O13A	2.03(5)	Cu5A - O13A - Cu4A	122(3)
Cu5A - O13A	1.99(5)	Cu5A - O13A - Cu6A	123(2)
Cu6A - O13A	2.07(5)	Cu4A - O13A - Cu6A	115(2)
Mo2B - O16B	1.81(2)	O16B - Mo2B - O15B	119.7(10)
Mo2B - O15B	1.82(2)	O16B - Mo2B - O14B	119.1(13)
Mo2B - O14B	1.95(3)	O15B - Mo2B - O14B	121.2(12)
Cu4B - O13B	2.05(4)	Cu6B - O13B - Cu5B	123.9(18)
Cu5B - O13B	2.02(4)	Cu6B - O13B - Cu4B	120.9(18)
Cu6B - O13B	1.95(3)	Cu5B - O13B - Cu4B	115.2(16)

Table 2.3: Crystallographic data for $\text{La}_4\text{Cu}_3\text{MoO}_{12}$ based on the single crystal refinement in space group Pm with Mo disordered over 2 possible positions in every other layer and $a = 6.8560(6)$ Å, $b = 10.9802(10)$ Å, $c = 7.9147(7)$ Å, and $\beta = 90.0160(10)^\circ$. Numbers listed in the B_{eq} column are the isotropic equivalent thermal displacement parameters. All disordered sites were constrained to yield a full occupancy of the site.

Atom	x	y	z	$B_{\text{eq}} (\text{\AA}^2)^*$	Occupancy
La1	0.25064(17)	0.74998(6)	0.11452(13)	0.0065(4)	1
La2	0.24841(16)	0.75036(6)	0.62688(13)	0.0066(4)	1
La3	0.76687(13)	0.74836(6)	0.36988(16)	0.0067(4)	1
La4	0.75349(15)	0.75127(6)	0.87158(18)	0.0061(3)	1
O1	0.4183(18)	0.8263(7)	0.3709(19)	0.0096(18)	1
O2	0.4109(18)	0.8363(7)	0.8690(18)	0.0081(17)	1
O3	0.9157(18)	0.8342(8)	0.1192(18)	0.009(2)	1
O4	0.9157(19)	0.8328(9)	0.6195(19)	0.012(2)	1
O5	0.0796(16)	0.6647(7)	0.8703(17)	0.0070(19)	1
O6	0.5831(17)	0.6708(7)	0.6203(16)	0.0059(18)	1
O7	0.5820(17)	0.6698(7)	0.1233(16)	0.0076(18)	1
O8	0.0836(16)	0.6642(7)	0.3708(16)	0.0044(18)	1
Mo1	0.4196(9)	1	0.3710(9)	0.0040(3)	1
Cu1	0.4712(9)	1	0.8708(9)	0.0142(6)	1
Cu2	0.8957(9)	1	0.0870(9)	0.0029(5)	1
Cu3	0.8940(9)	1	0.6543(9)	0.0028(5)	1
O9	0.763(2)	1	0.867(2)	0.009(3)	1
O10	0.681(2)	1	0.3688(19)	0.007(3)	1
O11	0.292(2)	1	0.5700(18)	0.010(3)	1
O12	0.289(2)	1	0.1727(17)	0.007(2)	1
Mo2A	0.5913(17)	0.5	0.1251(16)	0.025(2)	0.427(12)
Cu4A	0.5512(17)	0.5	0.6253(18)	0.000(2)	0.427(12)
Cu5A	0.1069(15)	0.5	0.8440(16)	0.025(2)	0.427(12)
Cu6A	0.1220(15)	0.5	0.3943(15)	0.022(2)	0.427(12)
O13A	0.256(7)	0.5	0.629(6)	0.014(11)	0.427(12)
O14A	0.303(5)	0.5	0.122(4)	0.000(7)	0.427(12)
O15A	0.732(4)	0.5	0.921(4)	0.001(5)	0.427(12)
O16A	0.715(5)	0.5	0.323(4)	0.010(6)	0.427(12)
Mo2B	0.5897(14)	0.5	0.6168(13)	0.0148(14)	0.573(12)
Cu4B	0.5480(13)	0.5	0.1211(14)	0.0000(14)	0.573(12)
Cu5B	0.1164(12)	0.5	0.3409(13)	0.0204(15)	0.573(12)
Cu6B	0.1110(12)	0.5	0.8983(12)	0.0148(14)	0.573(12)
O13B	0.250(5)	0.5	0.113(4)	0.013(8)	0.573(12)
O14B	0.306(5)	0.5	0.619(4)	0.006(6)	0.573(12)
O15B	0.725(3)	0.5	0.419(3)	0.001(4)	0.573(12)
O16B	0.720(3)	0.5	0.815(3)	0.006(5)	0.573(12)

atoms of different types in the fully disordered structure. Further supporting the fully disordered model was the fact that all large residual electron density on the difference map of the partially disordered structure was located where atoms would be located in the fully disordered structure.

2.2.3: Electron Microscopy.

High Resolution Transmission Electron Microscopy (HREM) and Transmission Electron Diffraction (TED) were performed using a JEOL JEM-2100 FAST TEM and a Hitachi HF-2000 TEM, both operated at 200kV. TED patterns were taken along the [0 1 0] and [1 0 0] zone axes using varying electron probe sizes, with smallest illuminated regions as small as 10 nanometers in radius. HREM images were also taken on the [0 1 0] zone axis. For high angle tilting experiments, a Hitachi H-8100 TEM was used, also operated at 200kV. TED patterns of a single crystallite were obtained from the [0 0 1] and [2 0 1].

2.2.4: Bond Valence Analysis

Bond valence sums (BVS)¹⁷ were also calculated for all three models in space group *Pm*. The KDist program within the Kalvados program suite was used to calculate the BVSs.¹⁸ Bonding interactions up to 3.5 Å were included in the calculation. A b value of 0.37 was used in all cases, with R_0 values of 1.679, 1.907 and 2.172 for $\text{Cu}^{2+}\text{-O}^{2-}$, $\text{Mo}^{6+}\text{-O}^{2-}$ and $\text{La}^{3+}\text{-O}^{2-}$ bonds.^{17,19} Global instability indices were calculated by hand. Full results are presented in Table 2.4. As a cautionary note, BVSs for disordered structures can be problematic,²⁰ and it is therefore important not to over-interpret the bond valence analysis. BVSs and the bond valence method are discussed in greater detail in Chapter 5.

Table 2.4: BVSs for the disordered and twinned model. Values for disordered fraction B only listed if they differ from values for fraction A by > 0.01 .

GII	Disordered Model				Twinned model	
	0.21				0.23	
	in or bonded to:					
	part A		part B			
Atom	Mult.	BVS	Mult.	BVS	Mult.	BVS
La1	2	3.13			2	3.12
La2	2	3.18			2	3.22
La3	2	3.22			2	3.16
La4	2	3.14			2	3.13
Mo1	1	6.00			1	5.56
Mo2	0.427	5.54	0.573	5.66	1	5.78
Cu1	1	1.83			1	2.09
Cu2	1	1.86			1	1.77
Cu3	1	1.87			1	2.06
Cu4	0.427	1.68	0.573	1.67	1	1.86
Cu5	0.427	1.93	0.573	1.86	1	1.77
Cu6	0.427	1.83	0.573	1.94	1	1.80
O1	2	-2.24			2	-2.21
O2	2	-2.05			2	-2.03
O3	2	-2.09			2	-2.11
O4	2	-2.07			2	-2.08
O5	2	-2.13			2	-2.12
O6	0.854	-1.89	1.146	-2.41	2	-2.36
O7	0.854	-2.47	1.146	-1.94	2	-2.02
O8	2	-2.07			2	-2.05
O9	1	-1.86			1	-1.80
O10	1	-1.84			1	-1.80
O11	1	-1.82			1	-1.29
O12	1	-1.80			1	-2.28
O13	0.427	-1.60	0.573	-1.68	1	-1.71
O14	0.427	-1.43	0.573	-1.47	1	-1.83
O15	0.427	-1.59	0.573	-1.79	1	-1.67
O16	0.427	-1.91	0.573	-1.80	1	-1.59

2.3: Results and Discussion

2.3.1: *Structural Disorder and Electron Microscopy.*

The lattice parameters determined from the single crystal data agree very well (all within 0.3%) with those reported previously based on neutron diffraction data for the slowly cooled polycrystalline samples. The three Cu^{2+} cations and the single Mo^{6+} cation occupy four distinct five-coordinate ($\text{MO}_{3/3+2}$) sites that share vertices to form Cu_3MoO_4 layers separated by O/La/O layers, as shown in Figure 2.1. The Cu_3MoO_4 planes can be envisioned as isolated Cu_3O triangles separated by MoO_3 units, as illustrated for a single layer in Figure 2.3. The three copper atoms that make up the triangles are significantly shifted towards the central oxygen, O(9), as reflected by the average in-plane Cu-O bond length, which is 1.988 Å in the triangles while it is 2.687 Å outside of them. These compare well to the values determined previously of 1.983 Å and 2.690 Å, respectively. In the present structural determination the triangles are slightly more regular than previously reported: the Cu-O-Cu angles for the layer without disorder are 116.8(7)°, 119.0(7)°, and 124.2(8)° as opposed to 121.1°, 115.3° and 123.6°. Unlike previous refinements, the apical bond lengths are completely isometric due to the mirror plane; although the average lengths are similar, 1.850 Å versus 1.841 Å. The smaller MoO_5 unit has an average Mo-O bond length of 1.836 Å in plane and 1.889 Å apical, and is also more regular than previously reported, with in-plane angles ranging from 119.1° to 121.2° versus 116.0° to 124.0°. Although unusually low for such a large cation, the coordination of the lanthanum cations is 6+2 and the bond lengths are comparable to those reported by Vander Griend *et al.*⁶ While powder

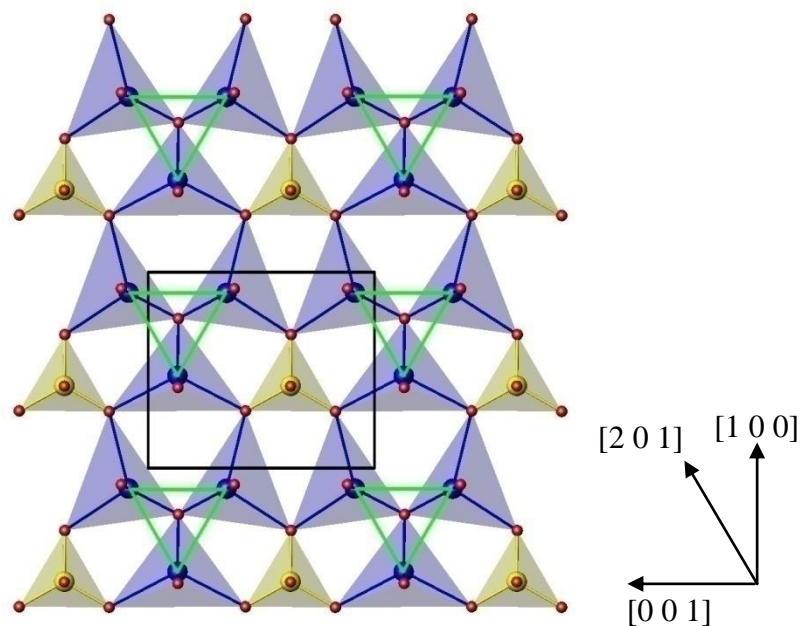


Figure 2.3: Structural view of a single layer of the triangular lattice of $\text{La}_4\text{Cu}_3\text{MoO}_{12}$ perpendicular to the b -axis. The copper ions are blue, oxide ions are red and molybdenum yellow. The CuO_5 trigonal pyramids are blue, MoO_5 trigonal bipyramids are yellow, and the Cu_3O trimers are outlined in green. The thick black line denotes the ab -face of the unit cell.

diffraction techniques were able to yield many features of the structure and show many similarities to the results from single crystal diffraction and TEM, there were several key structural elements that the powder diffraction was unable to determine.

Although the single-crystal growth experiments yielded a structure fully ordered in two dimensions, it was necessary to investigate whether disorder was present in the stacking of the Cu_3MoO_4 planes or if the twinned structural model was correct. Previous work by Chris Own had indicated that the structure was disordered rather than twinned.¹²⁻¹⁴ In that work, precession

electron diffraction had been obtained along the $[0\ 0\ 1]$ zone axis, and the structure solved using electron direct methods. Viewed along the $[0\ 0\ 1]$ zone axis, it would be expected that columns of only CuO_5 trigonal bipyramids would alternate with columns of half CuO_5 and half MoO_5 trigonal bipyramids. Instead, the precession electron diffraction revealed no difference between the columns, which indicated that every column was composed of a mix of CuO_5 and MoO_5 trigonal bipyramids and strongly supported a disordered model (Figure 2.4). However, if the crystal were rotated by 60° around the $[0\ 1\ 0]$ axis to arrive at the $[2\ 0\ 1]$ zone axis, although the sub-lattice would be identical each column would be composed of a 3:1 mix of CuO_5 and MoO_5 trigonal bipyramids (Figure 2.3). At such an orientation, the strong reflections

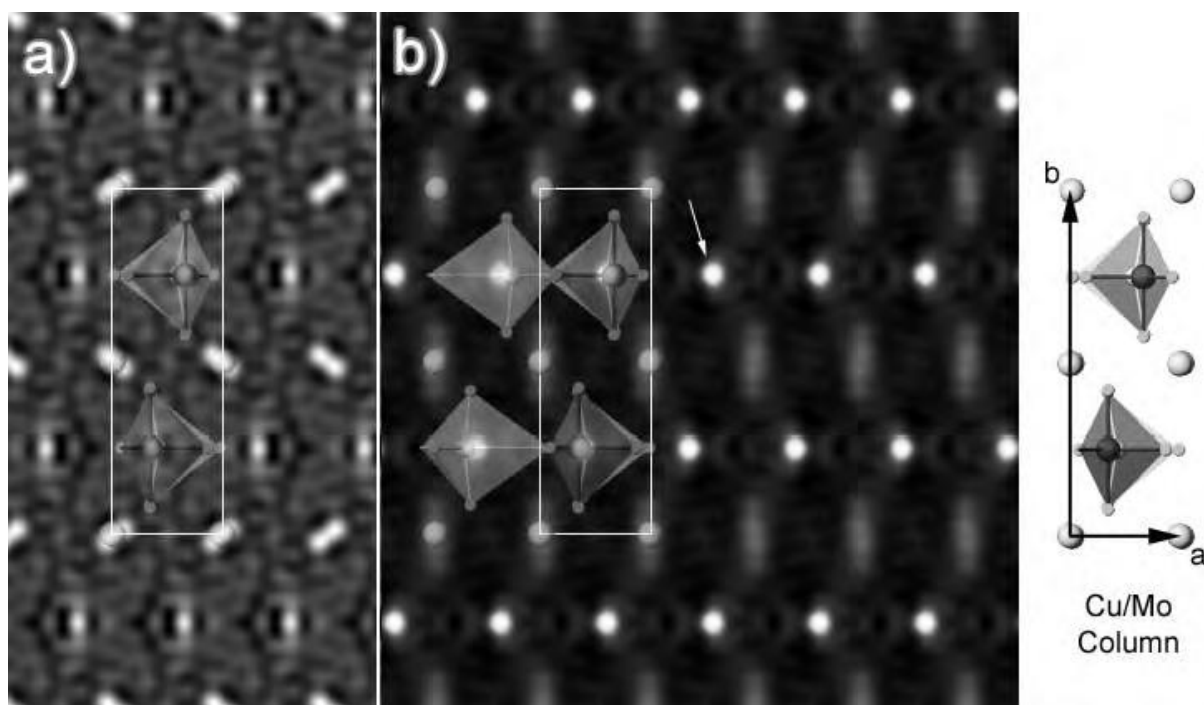


Figure 2.4: Direct methods solutions from precession electron diffraction on $\text{La}_4\text{Cu}_3\text{MoO}_{12}$ using amplitudes (a) and intensities (b). The cation positions show mixed Cu/Mo tetrahedral within each column. Figure courtesy of Chris Own.¹²

in the diffraction pattern would be identical to the $[0\ 0\ 1]$ diffraction pattern, with the only key difference being that some relatively weak spots would be completely absent at the $[2\ 0\ 1]$ zone axis. These weak spots were missing from the precession electron diffraction pattern (Figure 2.5), indicating that the data may have been obtained along the $[2\ 0\ 1]$ zone axis. However, it was also possible that such spots were simply too weak to be observed.

To determine conclusively whether the precession electron diffraction had been taken along the $[0\ 0\ 1]$ or $[2\ 0\ 1]$ zone axis, a single crystallite was tilted to both zone axes. The diffraction patterns were noticeably different, with the weak spots clearly visible along the $[0\ 0\ 1]$ zone axis (Figure 2.5). Thus the precession electron diffraction ought to have also shown the weak diffraction spots if it were indeed taken along the $[0\ 0\ 1]$ zone axis. As they were not present, it was concluded that the precession electron diffraction patterns must have been

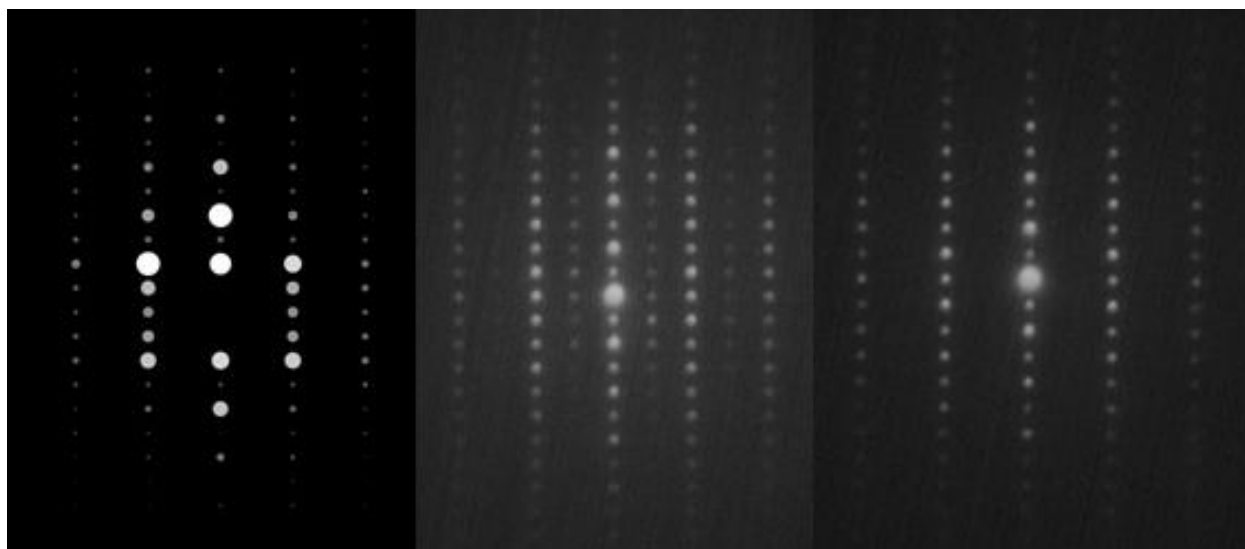


Figure 2.5: Left to right: precession electron diffraction pattern (courtesy of Chris Own¹²), TED pattern along $[0\ 0\ 1]$ zone axis, and TED pattern along $[2\ 0\ 1]$ zone axis.

obtained along the $[2\ 0\ 1]$ zone axis instead, and therefore these diffraction patterns would not indicate whether the structure was disordered or not.

A new approach was then taken, viewing the material along the $[0\ 1\ 0]$ zone axis. The TED pattern along the $[0\ 1\ 0]$ zone axis is shown in Figure 2.6, with the horizontal axis along $(0\ 0\ 1)$ (in reciprocal space) and the vertical axis along $(1\ 0\ 0)$ direction. When looking at a single crystallite, the diffraction patterns from different parts of the same crystallite were often rotated by 60° (Figure 2.7). This indicated that there was a twin present. The observed 60° rotation around the $[0\ 0\ 1]$ axis, however, was different from the twin law used in structural

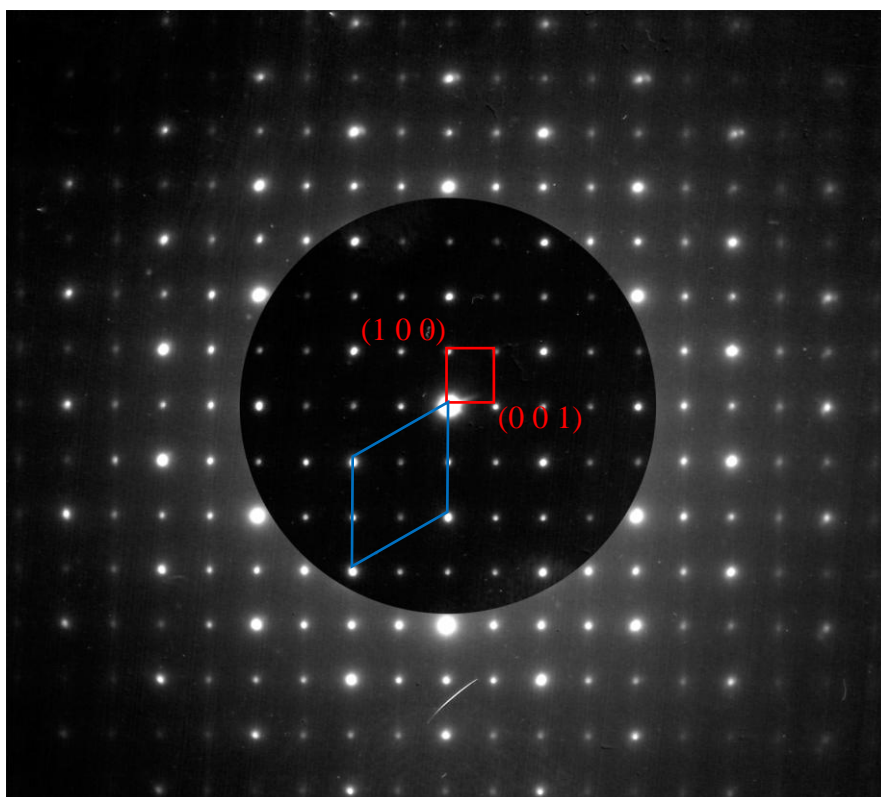


Figure 2.6: Electron diffraction pattern along the $[010]$ zone axis. Monoclinic unit cell in red, pseudo-hexagonal sub-cell in blue.

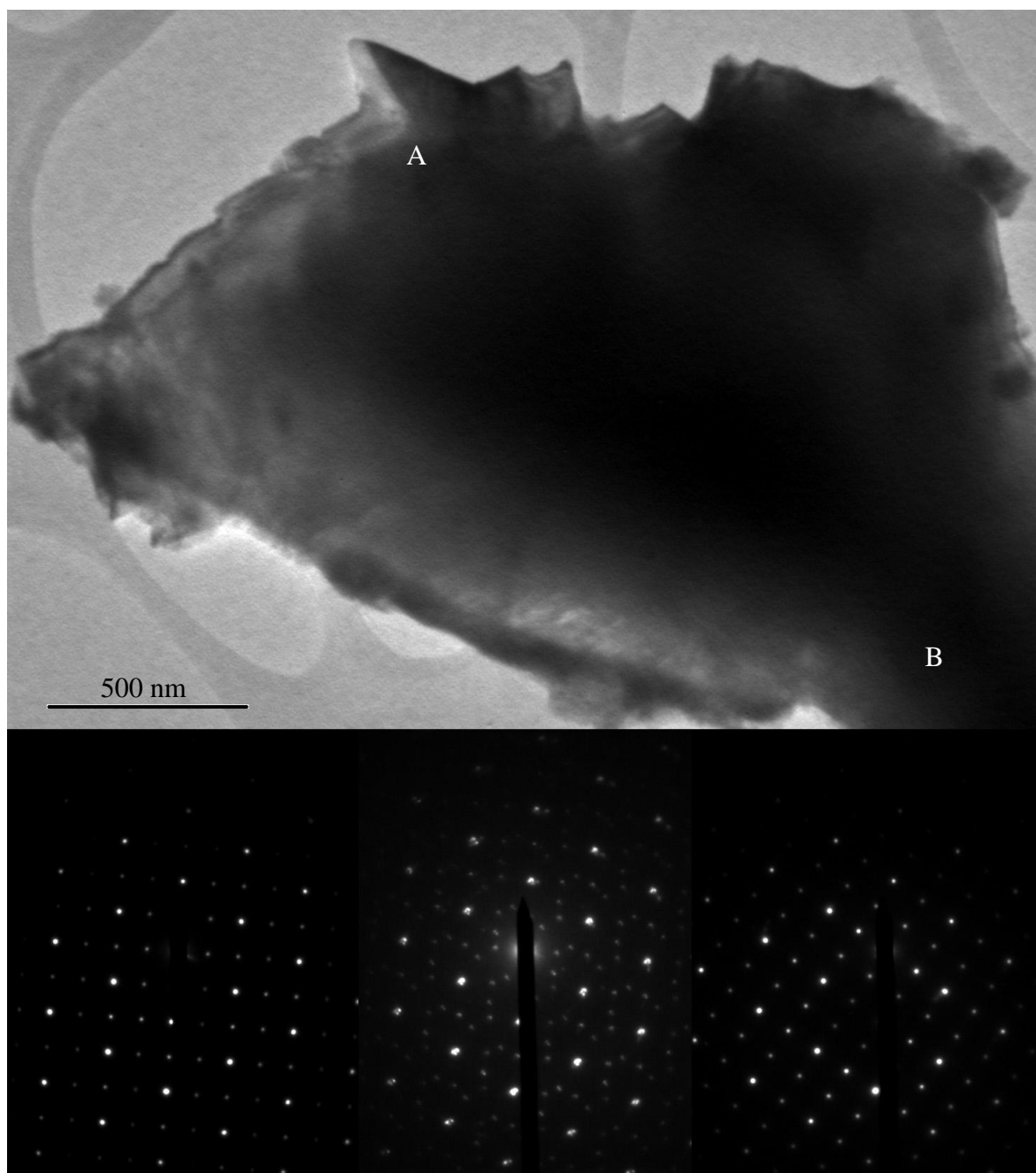


Figure 2.7: Top: TEM image of a $\text{La}_4\text{Cu}_3\text{MoO}_{12}$ crystallite with a 60° twin around the $[0\ 1\ 0]$ zone axis. Bottom, left to right: TED patterns taken along the zone axis from region A, from entire crystallite, and from region B.

refinement. This twin would keep the hexagonal sub-cell constant, with the only major difference across twin domains being the ordering of the copper and molybdenum. Essentially, the $[0\ 0\ 1]$ and $[2\ 0\ 1]$ would be interchanged on opposite sides of the twin domain. The presence of such a twin is consistent with the observation of intergrowths in the crystals.

Applying the observed twin to the X-ray diffraction data, however, did not improve the refinement. The observed twin domains were large ($> 1\ \mu\text{m}$) and care had been taken to avoid intergrowths in selecting and cutting the crystal from which X-ray diffraction data had been collected, making it plausible that such a twin was avoided. Further, the occupancy of the original domain was refined to over 90% occupancy, while the occupancy of the other two was at less than 10% combined. It was thus concluded that this twin was not present in any significant portion of the crystal from which X-ray diffraction was obtained.

In a diffraction pattern along the $[0\ 1\ 0]$ zone axis from a non-twinned, non-disordered crystal, there should be a noticeable difference in intensity between the $(1\ 0\ 1)/(-1\ 0\ -1)$ spot pair and the $(-1\ 0\ 1)/(1\ 0\ -1)$ spot pair. Which pair, $(1\ 0\ 1)/(-1\ 0\ -1)$ or $(-1\ 0\ 1)/(1\ 0\ -1)$, is more intense should be inverted at each twin boundary. While this might disappear due to dynamical effects if diffraction is taken from a large volume, they should be noticeable in local diffraction from small volumes and thin regions, where dynamical diffraction is much less of an issue. The absence of any such differences indicates that either there are no twin domains, or they are so small that even the very small electron probes ($\sim 10\ \text{nm}$ radius) diffracted from multiple domains simultaneously. In addition, HREM images were taken along the $[001]$ zone axis, shown in Figure 2.8, and processed by applying a Fourier transform, masking the spots beside the $(1\ 0\ 1)$,

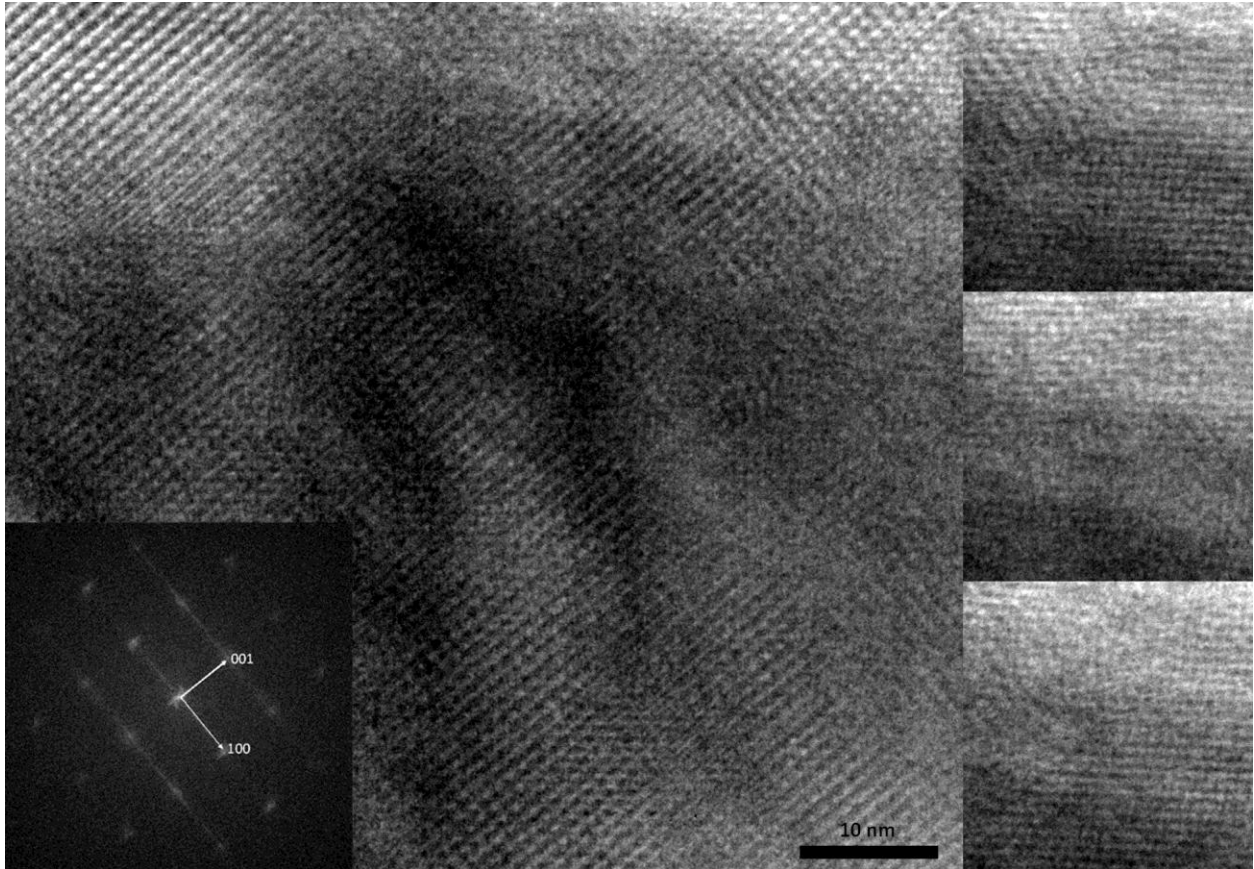


Figure 2.8: Left: HREM image taken on the $[010]$ zone axis with Fourier transform insert.

Right: post-processed images of a smaller region taken at three different foci (32 nm focus step).

The processing involved performing a Fourier transform, masking spots besides the (101) , (-101) , $(-10-1)$, and $(10-1)$ spots of interest, and performing an inverse Fourier transform. This leaves an image dominated by the (101) and (-101) lattice fringes.

$(-1\ 0\ 1)$, $(-1\ 0\ -1)$, and $(1\ 0\ -1)$ reflections of interest, and applying an inverse Fourier transform.

This procedure leaves an image dominated by the $(1\ 0\ 1)$ and $(-1\ 0\ 1)$ lattice fringes. Each twin domain would be dominated by one or the other set of lattice fringes, with twin boundaries

visible by the change in which set of lattice fringes dominates. Such differences, however, are minimal and also change with focus, thus indicating that no twin domains are present.

While a pseudo-merohedral twin law was originally used in the structural refinement to account for this disorder, the HREM and TED data revealed that no twin boundaries or twin domains could be found. The initially proposed twin law, i.e., $[1\ 0\ 0 / 0\ -1\ 0 / 0\ 0\ -1]$, is equivalent to a 180° rotation around the a -axis. The other three which had equivalent effect are a 180° rotation around the c -axis, a mirror on the bc -plane, and a mirror on the ab -plane. Any of these operations, when applied to the structure in real space and combined with an appropriate translation yields a structure that keeps the hexagonal sub-cell unchanged. Any such twinning would leave the lanthanum layer virtually unchanged, and would leave all in-plane relationships unchanged for the Cu_3MoO_4 layers. The only significant change would be in the stacking of one Cu_3MoO_4 layer relative to the next: in different Cu_3MoO_4 layers the Cu^{2+} cations could occupy different positions. A structural view down the a -axis of $\text{La}_4\text{Cu}_3\text{MoO}_{12}$ is shown in Figure 2.9, with the proposed twin boundary given by the green line. The two different twin domains match up nearly perfectly, the only difference being which MO_5 polyhedra contain the Mo atom and which contain the Cu atoms. This is equivalent to disorder in the stacking between the layers, while preserving perfect intra-layer ordering. However, as no distinct twin domains could be found, the structure is more accurately described as disordered.

Further evidence for disorder comes from electron diffraction patterns collected along the $[1\ 0\ 0]$ zone axis (Figure 2.10). The diffuse scattering, primarily manifested as lines along $(0\ 0\ 1)$, indicates real space frustration in the ordering in the perpendicular $[0\ 1\ 0]$ direction.

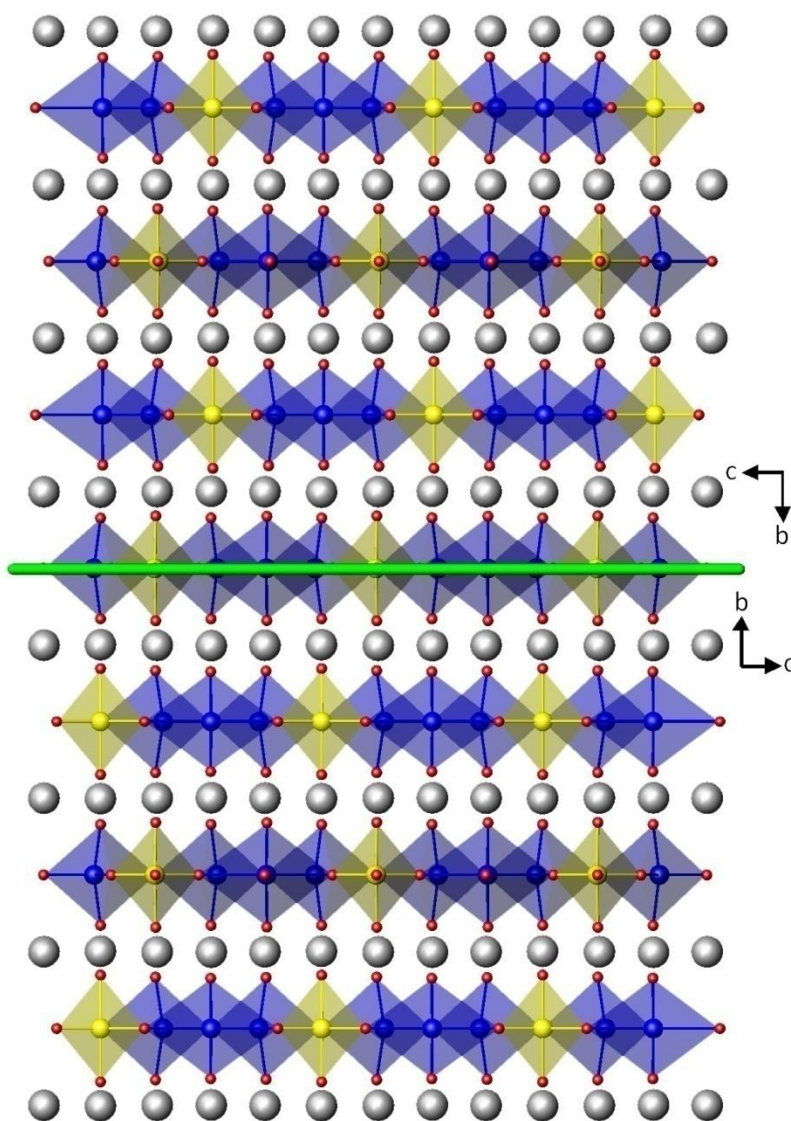


Figure 2.9: View down the a -axis of $\text{La}_4\text{Cu}_3\text{MoO}_{12}$ with the proposed twin boundary, shown by the green line. The twinning model is equivalent to disorder in the stacking between the layers, but preserving perfect intra-layer ordering. Copper atoms occupy blue polyhedra, molybdenum atoms occupy yellow polyhedra, and the lanthanum atoms are gray.

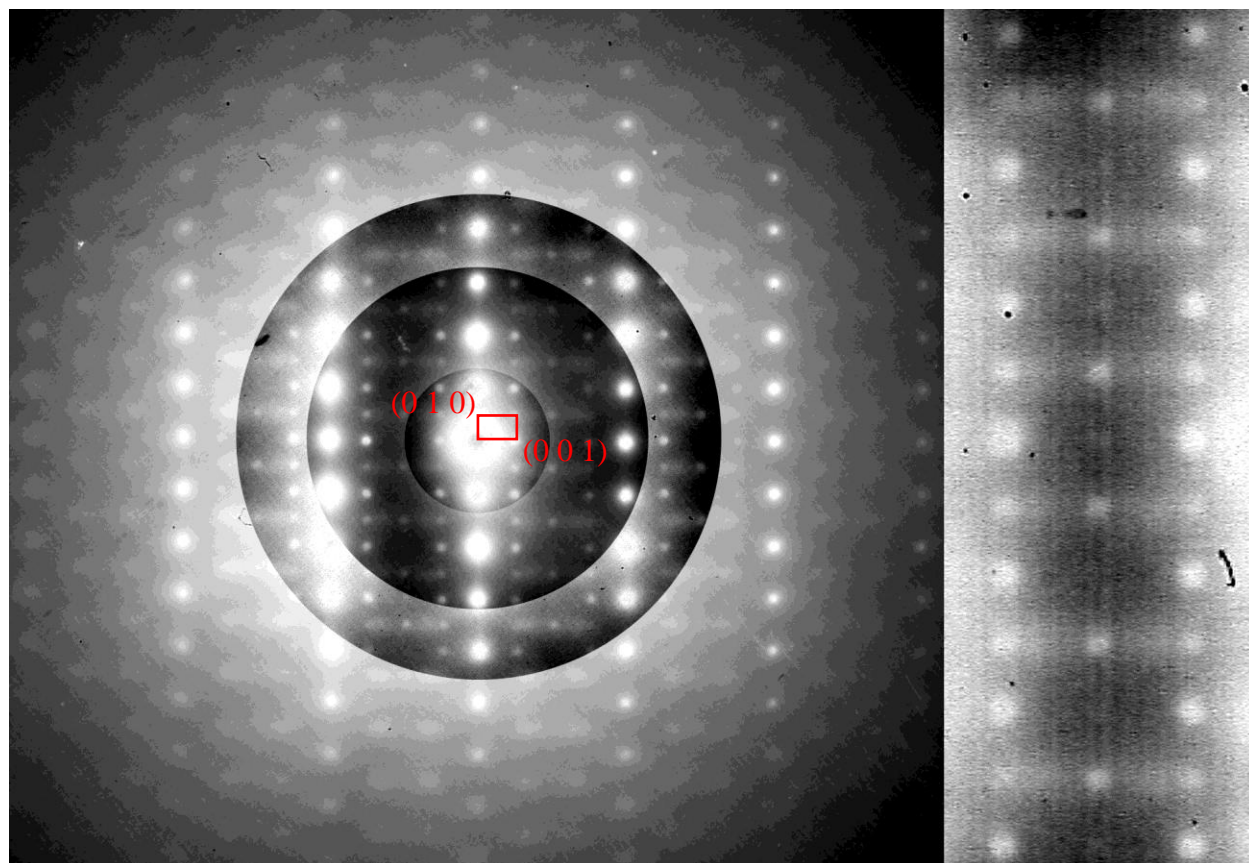


Figure 2.10: Left: Electron diffraction pattern along the $[100]$ zone axis with shorter exposure times overlaid over center of longer exposure times. Right: Close up of diffuse lines, marked with arrows. Unit cell in red.

While twin domains were not in fact observed, at least not with a twin domain size greater than the distance between Cu_3MoO_4 layers, the twin law successfully modeled a disorder in the stacking of the Cu_3MoO_4 layers. As changing the order of the Cu_3MoO_4 layer stacking broke symmetry, it was necessary to refine the structure in space group Pm to confirm the disorder model. In space group $P2_1/m$ and in all other maximal subgroups thereof, the positions

of the atoms in the second Cu_3MoO_4 layer were dependent on the positions of those in the first Cu_3MoO_4 layer. In space group Pm , however, the Cu_3MoO_4 layer lies in the mirror plane, and thus all atoms in both Cu_3MoO_4 layers are independent. A significant improvement in refinement was found when removing the dependence of one Cu_3MoO_4 layer on another even before disorder was introduced, indicating that the Cu_3MoO_4 layers are independent. This was confirmed by the further improvement in refinement when the disorder was introduced to the model. The inclusion of disorder in Cu_3MoO_4 layer stacking had a very similar effect to the inclusion of a twin law, i.e., the atomic positions in the model with disorder and the model with the pseudo-merohedral twin were very similar. The disordered structural model is further supported by the observation of diffuse scattering in TED patterns taken along the $[1\ 0\ 0]$ zone axis. Including more than two different stacking possibilities in the disorder model resulted in too many independent variables, and an unstable refinement. While the partially disordered model is a very good approximation, I believe that the actual structure is fully disordered with respect to the stacking of the Cu_3MoO_4 layers.

2.3.2: Bond Valence Analysis

Lanthanum and oxygen are almost certainly present as in the subject material La^{3+} and O^{2-} , respectively. For Molybdenum and copper, on the other hand, multiple oxidation states are possible. Molybdenum is usually 4+ or 6+, although 1+, 2+, 3+ and 5+ oxidation states are also known. Copper is usually 1+ or 2+, but occasionally is 3+ and rarely 4+. The four lanthanum would have a total valence of $(4 \times 3+ =) 12+$, while the 12 oxygen would have a total valence of $(12 \times 2- =) 24-$. To maintain valence neutrality, the 3 copper and 1 molybdenum must have a

combined valence of 12+, which could only be obtained from 1 Mo⁶⁺ plus 3 Cu²⁺ if each species is in one of their more common stable oxidation states. It is also possible, however unlikely, that some other combination of oxidation states is present in the material. As a change in the valence state of any atom in the Cu₃MoO₁₂ layer could change the unpaired electrons and have an effect on the magnetism, a bond valence analysis was carried out to determine conclusively the oxidation state of each atom present (Table 2.4). Additionally, a bond valence analysis may indicate whether the disordered or twinned model is a better fit.

All the lanthanum atoms had BVSs close to 3, as expected. However, the copper and molybdenum BVSs were both somewhat under-coordinated. The BVSs for the copper cations range from 1.67 to 1.92 when using the R₀ value for Cu²⁺-O²⁻ (1.679 Å).¹⁷ As they were somewhat under-coordinated, they were also calculated using the R₀ value for Cu¹⁺-O²⁻ (1.610 Å), but this produced a fit which was worse for every copper cation (the most under-coordinated copper ion had a BVS of 1.39). It was thus confirmed that all the copper was present as Cu²⁺, and would therefore have a spin of ½.

The molybdenum in the non-disordered Cu₃MoO₄ layer had a BVS of exactly 6.00 when using the Mo⁶⁺-O²⁻ R₀ value of 1.907 Å.¹⁷ The molybdenum in the disordered layer was significantly under-coordinated, with a BVS of 5.54 (5.56) for disordered fraction A (B), but did fit far better as Mo⁶⁺ than as Mo⁴⁺ (the other common oxidation state). The molybdenum in the disordered layer actually fit best as Mo⁵⁺, with a BVS of 5.12 (5.23) using a Mo⁵⁺-O²⁻ R₀ value of 1.878 Å.²¹ With all the lanthanum being La³⁺ and all the copper Cu²⁺, any Mo⁵⁺ would require the presence of an equal amount of O¹⁻ in order for valence neutrality to be maintained.

An O^{1-} would be extremely rare and unexpected; rare enough that R_0 values for cations bonded to O^{1-} are lacking in the literature, due to the lack of known structures with O^{1-} from which to determine a R_0 value. The lone exception is for $U^{2+}-O^{1-}$.¹⁹ Nevertheless, one of the oxygen atoms bonded to this molybdenum was indeed found to have a BVS closer to 1- than to 2-: oxygen 14A (B), has a BVS of -1.36 (-1.40) when using the $Mo^{5+}-O^{2-}$ R_0 value and a BVS of -1.43 (-1.47) when using the $Mo^{6+}-O^{2-}$ R_0 value.

The most likely explanation for these low BVSs is not that Mo^{5+} and O^{1-} are actually present, but that our model is inadequate to describe completely the true structure of the material. The Mo2A(B)–O14A(B) bond length in the disordered model is unusually long at 1.98 Å (1.95 Å), which causes the BVS for both molybdenum and oxygen to be lower in absolute value. In each atom site within the layer, there are four possible positions, depending on which site within that layer is occupied by the molybdenum. As only two of these were in the model, it is expected that to account for the residual scattering potential from the other two possibilities, the atoms would move slightly towards the average of these four possible positions. As the Cu–O bonds are in general longer than the Mo–O bonds, this would lead the Mo–O bond length to become longer in the model than in the actual crystal. Because of the two parts that were used in the model, the Mo–O bond that would be lengthened the most in the model by this process would be the Mo2–O14 bond. As such, we expect the actual bond length for the Mo2–O14 bond to be shorter and the BVS for Mo2 and O14 to be higher than those calculated with our disordered model. Thus it was concluded that the molybdenum and oxygen are, as expected, Mo^{6+} and O^{2-} .

This inadequacy of the model leads to some under-coordination in the Cu_3MoO_4 layers in general. The moving of the atoms to slightly more average positions would lead to less variation in bond lengths in the model than exist in the actual crystal. Due to the exponential nature of the bond valence equation, these more isotropic bond lengths would lead to lower BVSs. Thus the under-coordination that is observed in these layers could be explained, at least in part, as a product of our inability to correctly model the fully disordered structure.

The most drastic difference between the two disordered fractions was found in O6 and O7. Each had a high BVS (-2.41 and -2.47, respectively) when bonded to a molybdenum atom, and a slightly low BVS when bonded to a copper atom (-1.89 and -1.94, respectively). These oxygen atoms were not in the Cu_3MoO_4 layer, and were thus not allowed to assume different positions in the two different fractions. It is likely that in the actual material, these atoms will move slightly depending on whether they are bonded to a copper or molybdenum atom, thus keeping a good coordination at all times. The fact that they vary so greatly is therefore attributed to the constraints imposed by our model, particularly the use of only two disordered fractions.

In the Cu_3MoO_4 layers the BVSs showed less variation and were slightly closer to the expected values for the disordered model than for the twinned. The oxygen atoms in the Cu_3MoO_4 layers, for example, had BVSs ranging from -1.43 – -1.91 for the disordered model, and from -1.29 – -2.28 for the twinned model. This results in a superior global instability index for the disordered model ($\text{GII} = 0.21$ for disordered model, $\text{GII} = 0.23$ for twinned model). We would expect this improvement to be even more dramatic if we were able to model the full disorder believed to be present in the structure. This is a further indication that the disordered

model is superior to the twinned model. Additionally, the bond valence analysis confirmed that all atoms were at their expected oxidation states, and that the Cu^{2+} spin $\frac{1}{2}$ trimers should form as expected.

2.4: Conclusions

The $\text{La}_4\text{Cu}_3\text{MoO}_{12}$ crystals are perfectly ordered within any (0 1 0) plane, but exhibit turbostratic disorder between such planes. This may play a role in the ordering of the magnetic properties, and would likely have a large anisotropic effect. The ability to grow sizable single crystals of the complex cuprate $\text{La}_4\text{Cu}_3\text{MoO}_{12}$ makes possible detailed (anisotropic) electron spin resonance, magnetic and electronic studies of this interesting material. Furthermore, the synthetic strategies laid out herein may be beneficial for the crystal growth of other copper-containing complex oxides. For example, the related compound $\text{La}_3\text{Cu}_2\text{VO}_9$ displays a stunningly complicated ordering scheme^{22,23} which would benefit from single crystal diffraction data to confirm the structure as determined from polycrystalline powders. Finally, while modern powder diffraction techniques were able to yield a great deal of structural information, more sophisticated techniques are required to solve complex problems, such as the structure of $\text{La}_4\text{Cu}_3\text{MoO}_{12}$. Single crystal X-ray diffraction combined with TEM and TED provides a more powerful and complete toolbox for understanding complex oxides.

Chapter 3:

Inorganic Chemistry of an Oxide Surface:

A Homologous Series of Structures

on the Surface of SrTiO₃ (110)

3.1: Introduction

Strontium titanate, SrTiO_3 , is seeing increasing interest in fields ranging from thin film growth through water-splitting catalysis and electronic devices. While the surface structure and chemistry are of vital importance to many of these applications, theories about the driving forces vary widely.^{24,25} The structure of SrTiO_3 is a cubic close-packed lattice of strontium and oxygen with strontium in the corners and oxygen at the face centers, and titanium at the body centers occupying those octahedral holes which are surrounded only by oxygen. Along the (110) direction, SrTiO_3 is polar, composed of alternating layers of SrTiO^{4+} and O_2^{4-} , i.e. alternating layers with uncompensated nominal valence charges of $4+/4-$. In a fully ionic model, this leads to an unbalanced macroscopic dipole and infinite surface energy. Therefore one expects a (110) surface to have a nominal excess surface valence of either $2+$ or $2-$ per surface unit cell as, otherwise energetically unfavorable holes in the valence band or electrons in the conduction band would be formed.

There has been extensive discussion of the mechanisms of this “charge compensation” for polar oxide surfaces in the literature (see for instance²⁶⁻²⁸ and references therein). Various theories such as a reduction of Coulomb forces,²⁴ or a minimization of “dangling bonds,”²⁵ have been described as the driving force behind surface structure formation. An alternative model for oxide surfaces, first proposed for the SrTiO_3 (001) (2x1) surface²⁹, is that the rules of inorganic co-ordination chemistry dominate, although since the (001) surface is not polar, one might question the generality of this model.

For the SrTiO₃ (110) surface under oxidizing conditions, several surface reconstructions have been observed, including a (3x1), (4x1), (5x1) and (6x1) reconstructions,³⁰ which appear to be related. A reconstruction on the (110) surface is termed nxm, indicating that it has dimensions of n times the bulk unit cell length in the [001] direction and m times the bulk unit cell length in the [1-10] direction. These (nx1) (n=3-6) reconstructions show similar features in STM, and can evolve one from the next, often with two being present at the same time. Other reconstructions, including a (2x5), (3x4), (4x4), (4x7), (6x4),³¹ and c(2x6),³² have been found following UHV annealing and seem to be unrelated. A number of theoretical studies have been performed (see ³³⁻³⁶ and references therein), but with structures derived from bulk terminations that do not match the observed unit cells.

This chapter describes the solution to the (3x1) SrTiO₃ (110) surface structure obtained through transmission electron diffraction and direct methods, and confirmed via DFT calculations and STM images and simulations, consisting of rings of 6 or 8 corner sharing TiO₄ tetrahedra. Further, by changing the number of tetrahedra per ring, a homologous series of nx1 (n≥2) surface reconstructions can be formed. Calculations show that the lower members of the series (n≤6) are thermodynamically stable and the structures agree with STM images. While the surface energy of a crystal is usually thought to determine the structure and stoichiometry, the opposite is shown to occur. The nx1 reconstructions are sufficiently close in energy for the stoichiometry in the near surface region to determine which reconstruction is formed. The results indicate that the rules of inorganic co-ordination chemistry apply to oxide surfaces, and

that concepts such as homologous series and intergrowths are as valid at the surface as they are in the bulk.

3.2: Experimental Methods

3.2.1: Diffraction analysis

Samples were prepared and annealed, and electron diffraction was obtained by Arun Subramanian. Starting with a (110) oriented SrTiO₃ single-crystal wafer, samples were prepared by standard solid-state TEM sample preparation techniques: 3-mm disks were cut with a rotary cutter, mechanically polished to a thickness of about 120 μm, dimpled, then ion milled with Ar⁺ ions in a Gatan precision ion polishing system to produce electron-transparent samples. Samples were annealed in a tube furnace with flowing high purity oxygen. Electron diffraction patterns were obtained using a Hitachi UHV-9000 electron microscope at Northwestern University. A series of exposures was taken covering the entire dynamic range,³⁷ then digitized to eight bits with a 25-μm pixel size using an Optronics P-1000 microdensitometer, and intensities extracted using a cross-correlation technique.³⁸

The intensities of the diffraction patterns were averaged using a p2mm Patterson plane group symmetry, yielding 36 independent reflections. Under the exposure conditions used, the intensity readout from the microdensitometer was proportional to the true intensities of the diffraction spots. Beam damage was checked by comparing early exposures with exposures under identical conditions taken later on, and, as expected for strontium titanate, found to be negligible. As a glide plane was incommensurate with the bulk termination, only p11m, p1m1,

or p2mm plane group symmetries were possible for p2mm symmetry. Direct methods (see ^{39,40} and references therein) were employed for all possible plane groups to obtain plausible solutions. Final structure refinement was performed based on both R^2 and χ^2 , with the best results found in plane group p1m1 with $R = 0.07066$ and $\chi^2 = 2.64$.

3.2.2: Bond Valence Sums

Bond valence sums were calculated using the KDist program in the Kalvados program suite.¹⁸ Bonding interactions up to 3.5 Å were included in the calculation. A b value of 0.37 was used in all cases. Standard R_0 values of 2.118 Å and 1.815 Å were used for $\text{Sr}^{2+}-\text{O}^{2-}$ and $\text{Ti}^{4+}-\text{O}^{2-}$, respectively.^{17,19} Global, bulk, and surface instability indices were calculated by hand. More information about bond valence sums and the bond valence model is available in chapter 5.

3.2.3: DFT calculations

Density Functional Theory (DFT) is a method for approximating a solution to the Schrodinger equation for a many-particle quantum mechanical system. It is based upon calculating the ground state electron density, which in turn depends upon electron interactions, meaning that the electron density must first be known. To solve this paradox, the series of calculations are repeated iteratively until the change in ground state electron density between cycles is minimized.

The Hamiltonian for the many-particle problem was broken down by Kohn and Sham⁴¹ into four terms: the kinetic energy of the electrons, the potential of the atomic nuclei, the Hartree potential of an electron gas, and the exchange-correlation potential between electron pairs. The

latter term cannot be solved, so approximations are needed. Two common approximations are the local density approximation (LDA)⁴² and generalized gradient approximation (GGA), the latter of which is most commonly used as formulated by Perdew, Burke, and Ernzerhof (PBE).⁴³ LDA approximates the exchange-correlation potential from the known potential in a free electron gas, or jellium, assuming that the exchange correlation at every location is identical to that of a jellium of the same density. GGA is more complex, approximating the exchange-correlation potential from the local electron density and the gradient of the electron density. Which functional is used depends upon the system being examined. For example, while the GGA functional is considered more accurate than the LDA functional for bulk oxide structures, the LDA functional gives more accurate values for surface free energies (although this is attributed to a fortuitous cancelation).⁴⁴⁻⁴⁷ It is therefore important to choose a method of calculation which gives accurate results for systems similar to the one being calculated.

DFT calculations were performed using the all-electron augmented plane wave plus local orbitals (APW+lo) Wien2k code.⁴⁸ The APW+lo basis breaks space down into atomic spheres with a “muffin-tin” radius (RMT) around the atomic centers, and interstitial regions outside of the “muffin-tins.” Inside the RMT spherical harmonics and local atomic orbitals are used, and outside plane waves are used. The wavefunction is constrained to be continuous at the RMT boundary. Calculations were performed using five bulk SrTiO^{4+} layers separated by four bulk O_2^{4-} layers, with $\text{Ti}_{(n+2)/n}\text{O}_{(3n+4)/n}^{2-}$ surface on either side. This was found to be thick enough, as the innermost SrTiO^{4+} layer was only minimally distorted. The structural optimization was carried out by calculating the residual forces on the atomic nuclei following a self-consistent

calculation, moving the atomic positions so reduce these forces, and repeating until the forces on the atoms were minimized.⁴⁹ The current version of the structural relaxation was implemented in the Wien2k code by L. D. Marks. An RKmax of 6.12 was used with RMT's of 2.36, 1.72, and 1.54 for strontium, titanium, and oxygen, respectively. Such small values for RMT's were used to allow atomic positions to relax without the "muffin-tins" touching. The small values lead to a systematic error, with the calculated surface free energies lower than the true surface free energies. However, as the error is systematic, all surfaces calculated using the same parameters can be accurately compared with each other.

As mentioned above, the GGA functional gives poor results for surface energy calculations. Modifications have been made to improve upon the accuracy of the GGA method. A recently developed method for improving the PBE (GGA) method is the PBE0 method,^{50,51} which applies Hartree-Fock exact exchange to highly correlated orbitals. In this work, the PBE0 functional was used to optimize atomic positions, with the amount of exact exchange specified as 0.25 for titanium atoms and no exact exchange for other atoms. A TPSS functional⁵² was used for calculating the final energies, as the exchange-correlation energy used therein is the best currently available method for correctly accounting for long range jellium contributions. The TPSS functional is not yet implemented in a fully self-consistent manner, and thus it uses the electron density calculated via a PBE functional and applies an exchange-correlation correction. When applied to a PBE0 calculation, the method is known as TPSSh.⁵³

The use of improved functionals allows for more accurate calculations, while the comparison to less accurate functionals can allow for an estimation of the error in the calculation.

If the surface energies were known from experiment, it would be straightforward to compare the calculated energies to the experimental energies and find a calculation error. Since surface energies have in general not been found by experiment, small molecules may be substituted, as the same long-range decay of electrons into a vacuum which makes surface energies difficult for DFT calculations exists for small molecules. Previously, the atomization energies of several small titanium containing molecules were calculated and compared to experimental values.⁵⁴ This confirmed that the TPSSh functional was in the closest agreement with experiment, while the PBE functional had the greatest error, with the PBE0 and TPSS functional in between. The differences between the various functionals were found to correlate with the error of the functionals. It was therefore suggested that a reasonable estimate of the calculated error for the TPSSh was equal to $|E_{\text{TPSSh}} - E_{\text{PBE}}| / 3$.⁵⁴ The energies presented in this chapter were therefore calculated using both functionals. One third of the average difference between the TPSSh and PBE calculated energies for these structures was used as the approximate error for all calculations in this chapter.

3.2.4: STM Simulations

STM images were simulated using a modified Tersoff-Hamann approximation.⁵⁵ Extra electrons were added to the structure to partially fill the conduction band. The lapw5 protocol within the Wien2k program calculates the electron density as a function of location within a 2D plane. The lapw5 protocol was used to calculate the electron density for electrons from E_f to 1.0 eV above the conduction band edge on several planes, beginning at the surface and moving out

into the vacuum. The 2D electron density maps were merged in Matlab to create a 3D electron density map. A surface of constant density was then plotted, with brighter colors indicating higher elevations for the surface. Several different densities were attempted, and the match with the experimental STM images was good over a large range of densities. A density of 0.05 electrons / bohr³ (0.34 electrons / Å³) was used in the final figures presented below. To better compare to the resolution of experimental images, a Gaussian blur of 1Å radius was added using the Semper-7.0b image processing program.

3.3: Results

Annealing of single crystal (110) oriented TEM samples at 950°C yielded a diffraction pattern with streaking in the [110] direction. Increasing the temperature to 1000°C yielded a three-fold ordering along the [001] direction, while the streaking along the [110] direction remained. Further increasing the temperature to 1100°C allowed the surface to fully order, with a combination of (3x1) and (1x4) (Figure 3.1). Initially this was indexed as a (3x4) reconstruction. Later it was determined that it was in fact concurrent (3x1) and (1x4) reconstructions. Similar concurrent reconstructions had been previously observed via STM,³⁰ in which the (3x1) was the main phase with the (1x4) present only near the step edges.

Transmission electron diffraction (TED) is a powerful tool for solving surface structures and refining atomic positions. As only amplitudes are recorded and the phase information is lost, direct methods are used (see ^{39,40} and references therein) to obtain plausible solutions. Direct methods analysis was performed in space group p2mm, p11m, and p1m1. Direct methods

analysis did not provide any satisfactory solutions for a (3x4) reconstruction. However, all three space groups yielded some similar features. Specifically, all yielded a row of three bright (strong scattering) features in the a direction. Upon closer examination, it was observed that diffraction spots only existed where either $h = 3n$ or $k = 4n$ ($n = \text{integer}$). Consequently the diffraction pattern was re-indexed as concurrent (3x1) and (1x4) reconstructions.

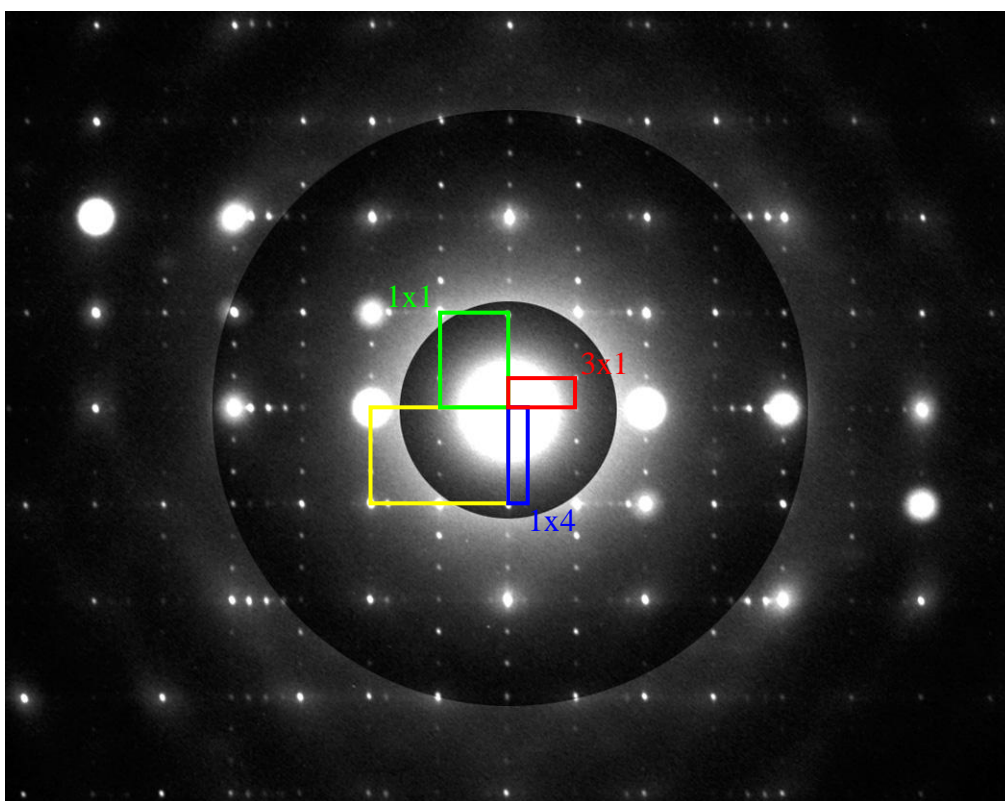


Figure 3.1: TED pattern for the (3x1) reconstruction taken slightly off zone axis to improve the surface to bulk ratio of the signal and to make the surface diffraction more kinematical. Three different exposure times are overlaid to make more of the diffractions pattern visible. The bulk unit cell is outlined in yellow, the surface (1x1) in green, the (3x1) reconstruction in red, and the minor concurring (1x4) reconstruction in blue.

Direct methods analysis of the (3x1) reconstruction was attempted in all three possible plane groups with p2mm Patterson symmetry (p2mm, p11m, and p1m1) as well as the lower symmetry plane groups (p1 and p2). Initially, the most distinctly atom-like features were found in plane group p1. Refinement in space group p1 worked only moderately well, with $R = 0.19$. The reason for the poor refinement was that a fragment of the true structure had been found. This fragment was then expanded to fit the three possible symmetries (p2mm, p11m, and p1m1). This was done either by moving the found atoms to match the desired symmetry, or by adding extra atoms to create the desired symmetry. This created multiple structural models. DFT structural relaxation was carried out for each case. The structure which had the lowest energy upon optimization was the structure in plane group p1m1 with atoms added to create the mirror plane.

Direct methods were then attempted again in plane group p1m1. Fewer beams were varied to yield a more complete search of phase space. In such a manner more possible solutions were covered, although with less resolution. The best solution in p1m1 had five features with high scattering potential, all of which were in the positions where titanium atoms were found in the DFT calculation. In the prior p1 solution, there had been only four such strong scattering features. The initial p1 solution and the final p1m1 solution were very similar, except that one of the strong scattering features was missing from the p1 solution. This indicated that the initial p1 solution had yielded only a fragment of the true structure.

The structure solved and refined in p1m1 plane group symmetry shows the strong scattering features arranged in rings of six or eight such features (Figure 3.2). These were found

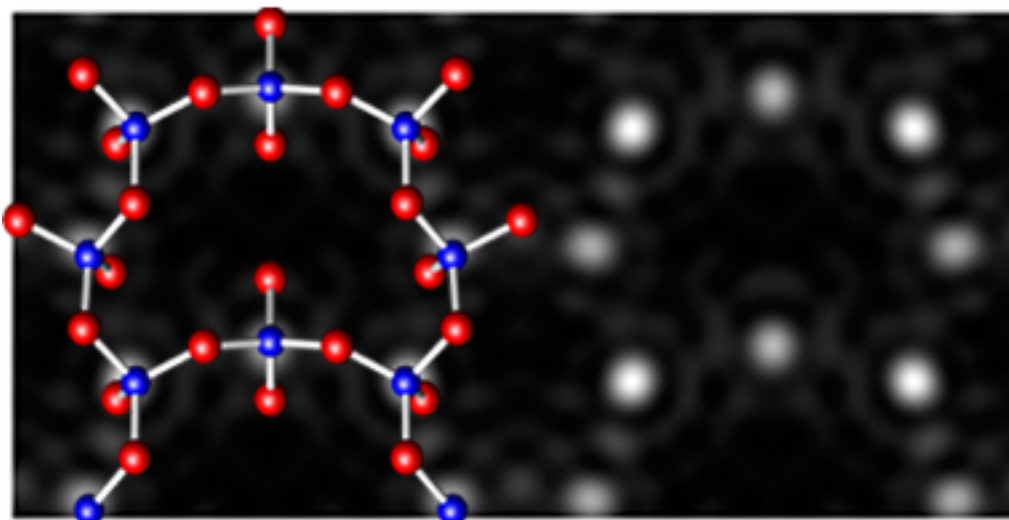


Figure 3.2: Scattering potential for the (3x1) surface structure with the surface atoms overlaid on the left half. The light features on the scattering potential map indicate areas of stronger scattering potential (i.e., strong scattering species). Titanium in blue and oxygen in red.

Table 3.1: Atomic coordinates for the (3x1) surface structure.

Surface Atoms		DFT	Refined	Difference	Linking Atoms		DFT	Refined	Difference
Ti1	x	0.6606	0.6773	0.0398 Å	O5	x	0.7266	0.6807	0.1095 Å
	y	0.8608	0.8623			y	0.8168	0.8121	
Ti2	x	0.1573	0.1362	0.0497 Å	O6	x	0.2250	0.2386	0.0342 Å
	y	0.7694	0.7694			y	0.1951	0.1917	
Ti3	x	0.9975	0.0111	0.0320 Å	O7	x	0.2254	0.3075	0.1940 Å
	y	0.5	0.5			y	0.5	0.5	
O1	x	0.9471	0.9212	0.1067 Å	O8	x	0.7491	0.7450	0.0097 Å
	y	0.1272	0.1526			y	0.5	0.5	
O2	x	0.4536	0.4311	0.0949 Å					
	y	0.7690	0.7919						
O3	x	0.5188	0.5657	0.1109 Å					
	y	0.0	0.0						
O4	x	0.0122	0.0670	0.1351 Å					
	y	0.3672	0.3559						

to be Ti atom sites, and using a combination of difference maps and least squares refinement, the oxygen sites were located. The structure refined very well in plane group $p1m1$ ($R = 0.07066$ and $\chi^2 = 2.64$). Further, refinement of the atomic positions against diffraction data and DFT calculated positions were very similar (Figure 3.3). These results confirmed that the structure was stable and of low energy as will be discussed further below. STM images for this structure were simulated, and were found to be comparable with experimental results (Figure 3.3). All

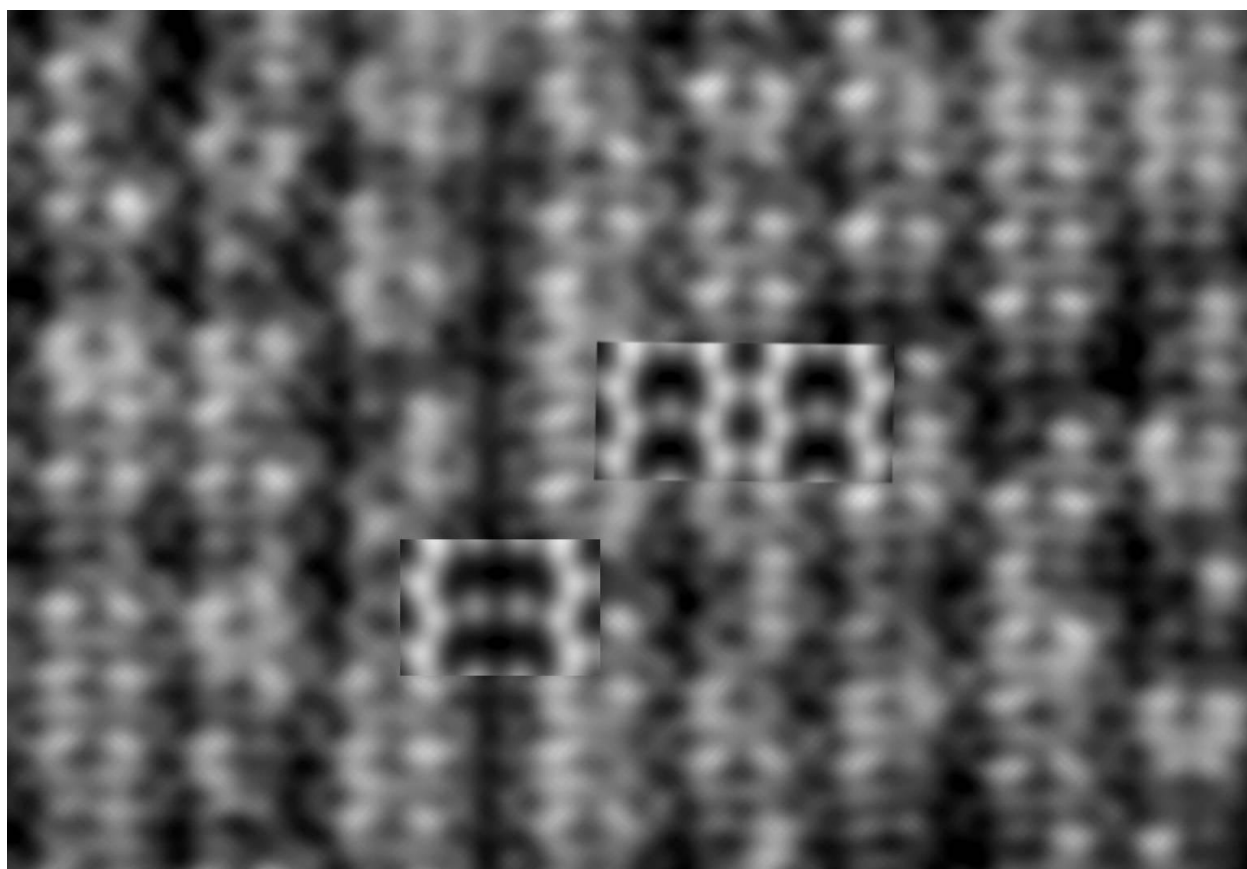


Figure 3.3: STM image of a (3x1) surface with an intergrowth of (4x1) with simulations overlaid (Sample bias = 0.9 V, tunneling current = 0.4 nA).

other structural possibilities examined had significantly inferior refinement, did not match the STM images, and were much higher in energy.

The (3x1) surface structure (Figure 3.4) is composed of corner-sharing TiO_4 tetrahedra, arranged into six- and eight-member rings. The tetrahedra in the six-member rings all corner share with three other surface tetrahedra and one sub-surface TiO_6 octahedron. The titanium tetrahedra in the middle of the eight member ring, the only one which is not also part of a six member ring, corner shares with two other surface tetrahedra, and edge shares with one sub-

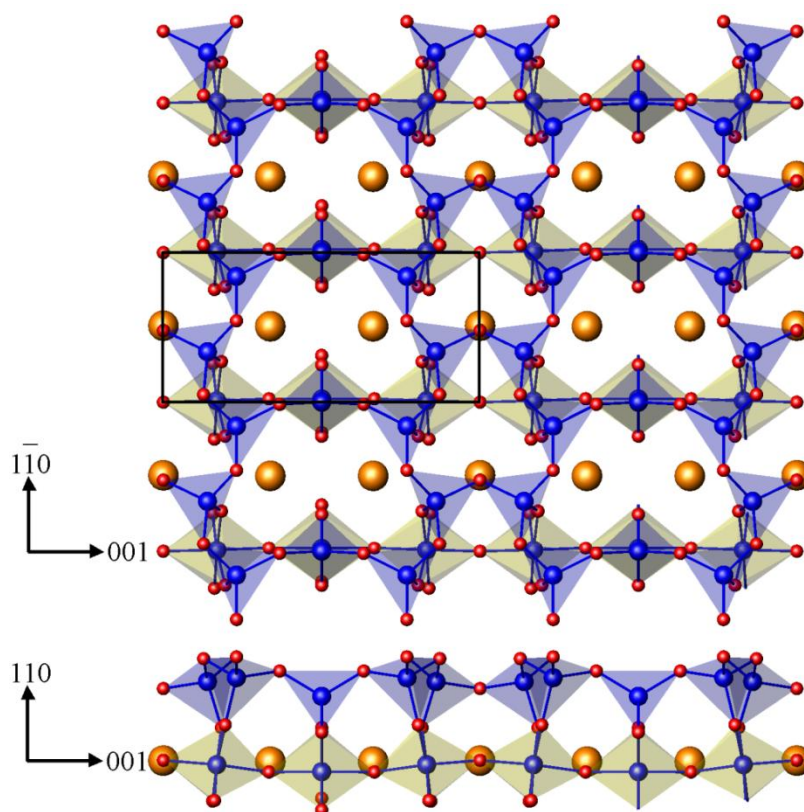


Figure 3.4: Surface structure of (3x1) reconstruction and the top bulk layer. Surface TiO_4 tetrahedra shown in blue, bulk TiO_6 octahedra in yellow, oxygen in red, and strontium in orange. Views perpendicular (top) and parallel (bottom) to the surface with unit cell outlined in black.

surface TiO_6 octahedron. The composition of the surface is $\text{Ti}_{5/3}\text{O}_{13/3}^{2-}$ per 1x1 unit cell, valence compensating the surface. Bond lengths are presented in Table 3.2 while bond valence sums and Bader charges are set forth in Table 3.3.

Table 3.2: Ti-O bond lengths for the (3x1) surface structure.

Bond	Type	Length (Å)	Bond	Type	Length (Å)
Ti1 – O1	Surface – Surface	1.800	Ti4 – O5	Linking – Bulk	1.998
Ti1 – O2	Surface – Surface	1.816	Ti4 – O6	Linking – Bulk	1.987
Ti1 – O3	Surface – Surface	1.827	Ti5 – O7	Linking – Bulk	2.002
Ti1 – O5	Surface – Linking	1.812	Ti5 – O8	Linking – Bulk	2.051
Ti2 – O1	Surface – Surface	1.819	Average	Surface – Surface	1.813
Ti2 – O2	Surface – Surface	1.808	Average	Surface – Linking	1.817
Ti2 – O4	Surface – Surface	1.807	Average	Linking – Bulk	2.004
Ti2 – O6	Surface – Linking	1.828	Average	Bulk – Bulk	1.953
Ti3 – O4	Surface – Surface	1.817			
Ti3 – O7	Surface – Linking	1.827			
Ti3 – O8	Surface – Linking	1.794			

Table 3.3: Bond valence sums and Bader charges for the (3x1) surface structure.

Atom	Type	Bond Valence Sum	Bader Charge	Atom	Type	Bond Valence Sum	Bader Charge
Ti1	Surface	4.04	2.32	O5	Linking	-2.11	-1.27
Ti2	Surface	4.04	2.33	O6	Linking	-1.99	-1.27
Ti3	Surface	4.08	2.33	O7	Linking	-2.06	-1.26
O1	Surface	-2.03	-1.15	O8	Linking	-2.01	-1.23
O2	Surface	-2.02	-1.17	Average	Surface Ti	4.06	2.33
O3	Surface	-2.19	-1.24	Average	Surface O	-2.05	-1.18
O4	Surface	-2.04	-1.21	Average	Linking O	-2.04	-1.26
				Average	Bulk Ti	4.14	2.30
				Average	Bulk O	2.08	-1.28

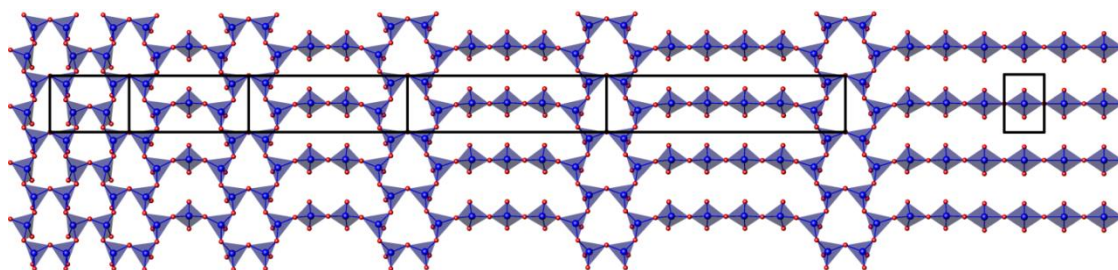


Figure 3.5: Surface structures of the homologous series of $(nx1)$ surface structures viewed perpendicular to the surface. For clarity, the bulk is omitted. TiO_4 tetrahedra are shown in blue, with oxide anions in red. Unit cells are outlined in black, from left to right $n=2,3,4,5,6,\infty$.

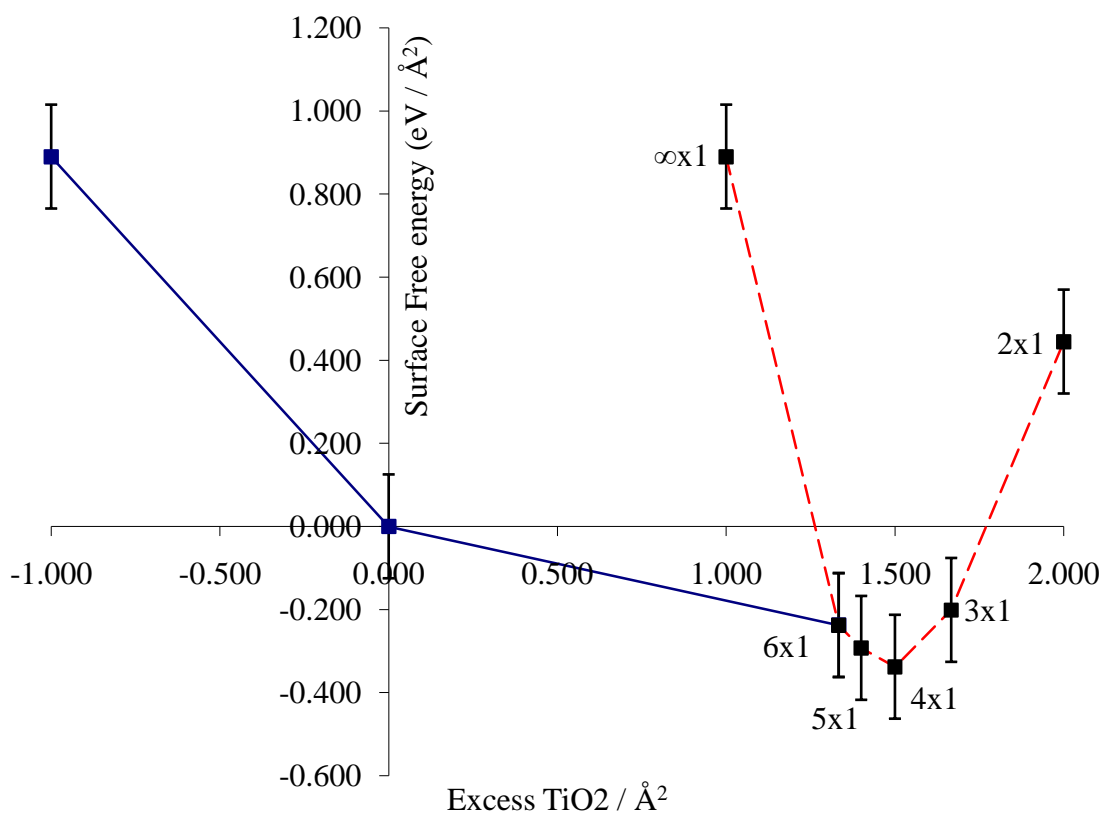


Figure 3.6: Plot of surface energies for $(nx1)$ surfaces and several previously proposed surfaces. The convex hull construction (blue line) shows the stable surface for a given composition.

As already mentioned, the (3x1) reconstruction is only one member of a series of (nx1) reconstructions. The (3x1) structure was extended to a homologous series by varying the size of the larger ring, as illustrated in Figure 3.5; reducing it to six TiO_4 tetrahedra gives a (2x1) reconstruction, increasing to ten a (4x1) reconstruction is formed. Varying the number of

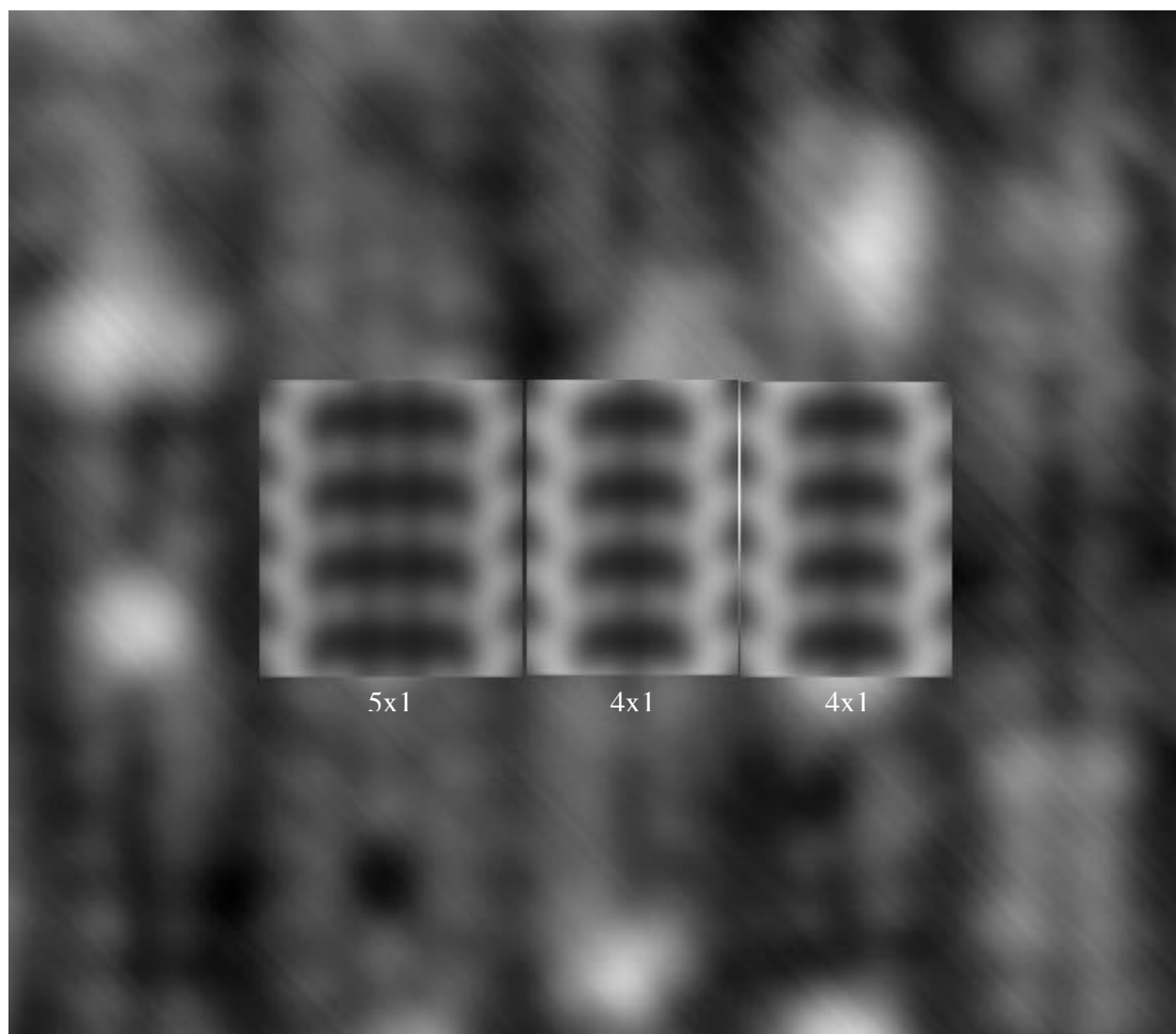


Figure 3.7: STM (experimental with simulation overlaid) of intergrowths of (4x1) and (5x1) reconstructions (Sample bias = 0.9 V, tunneling current = 0.4 nA).

tetrahedra in the smaller ring was also attempted, but resulted in significantly higher calculated energies. All the reconstructions in the series are fully valence compensated. They differ in the surface excess of TiO_2 , with nominal surface compositions of $\text{Ti}_{(n+2)/n}\text{O}_{(3n+4)/n}^{2-}$ per (1×1) unit cell. These structures were optimized via DFT for $2 \leq n \leq 6$ and $n = \infty$, and the energetics are summarized in Figure 3.6. A convex-hull construction implies that (within theoretical error) the structures lying on the hull should appear for different surface compositions, agreeing with the

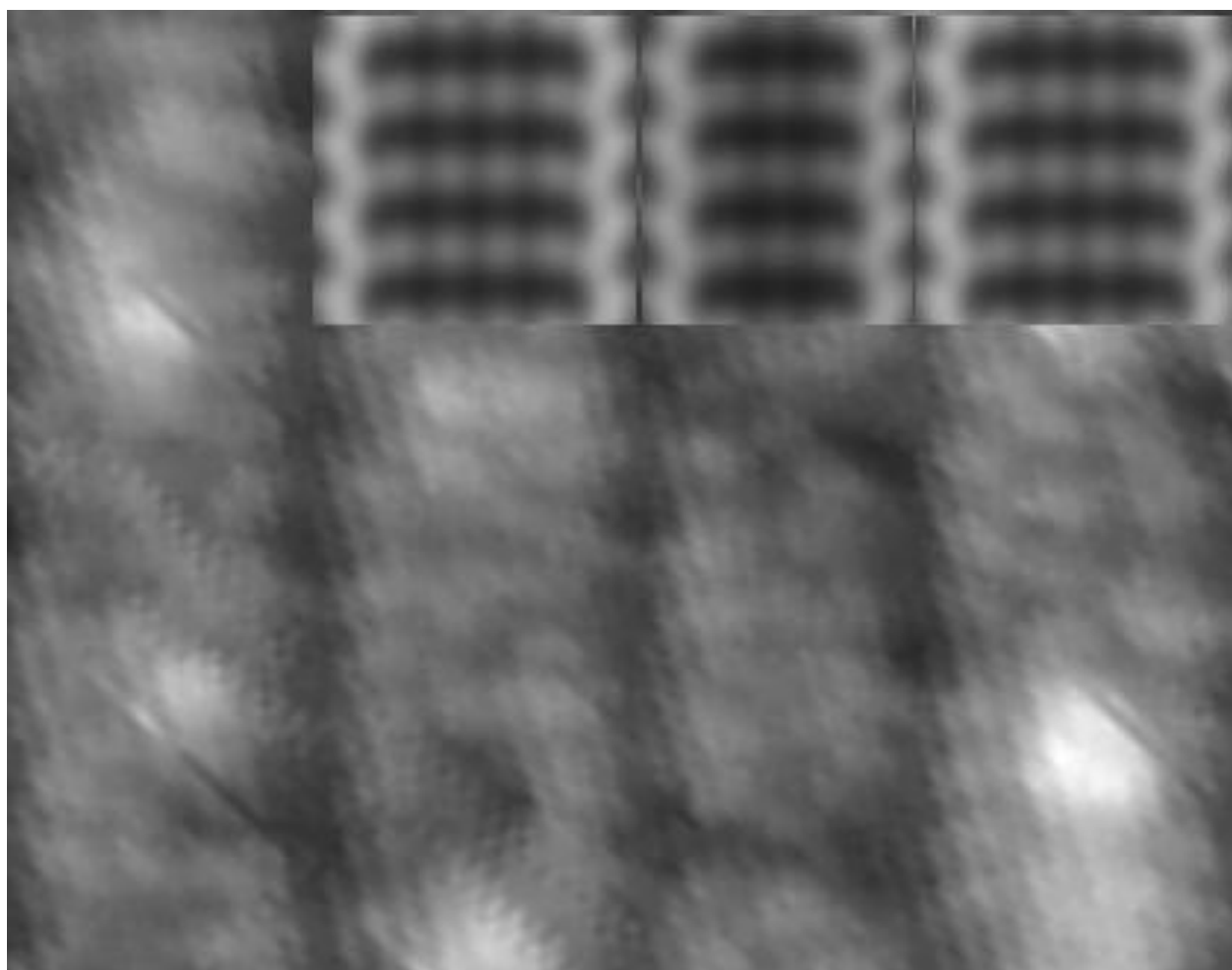


Figure 3.8: STM (experimental with simulation overlaid) of intergrowths of (5×1) and (6×1) reconstructions (Sample bias = 0.9 V, tunneling current = 0.4 nA).

experimental observations. As an independent check, simulated STM images were compared with experimental images of (3x1), (4x1), (5x1), and (6x1) reconstructions (see Figure 3.3, Figure 3.7, and Figure 3.8). These images and simulations correlate with each other in all major aspects. Note that the STM images indicate that layers of, for instance, (4x1) can occur as intergrowths in a matrix of (3x1), a point which will be returned to later.

3.4: Discussion

To form a specific structure, the structure must be both thermodynamically stable and kinetically accessible. While kinetics is beyond the scope of the present work, some conclusions can be drawn with respect to the thermodynamic stability. The most important factors contributing to the stability of the surfaces in this homologous series are maintenance of acceptable coordination environments combined with valence compensation and increased covalence at the surface.

As previously mentioned, the surface titanium atoms in the (3x1) structure are all tetrahedrally coordinated. For comparison, the bulk titanium atoms are octahedrally coordinated. With the reduced coordination, the non-bonded repulsions between the oxygen atoms are decreased, allowing shorter and more covalent bonds are formed. The decreased ionicity can be readily seen through the bond distances (Table 3.2), Bader charges (Table 3.3), and bond valence sums (Table 3.3). The bond lengths at the surface are, on a whole, slightly shorter and more covalent than in the bulk structure: the average Ti-O bond length for the surface structure is 1.814 Å, as compared to the 1.953 bulk Ti-O bond distance. The Bader charges indicate that the

surface species are less charged than the bulk, with the average Bader charge for an oxygen atom increasing from -1.18 at the surface, to -1.26 at the linking O₂ layer (oxygen bonded to both surface and sub-surface titanium), to -1.29 in the first sub-surface SrTiO layer, to ~-1.31 in deeper layers. Similarly, the Bader charge for a titanium atom increases from 2.33 at the surface to 2.36 at the first sub-surface SrTiO layer, and ~2.37 in deeper layers.

The Bader charges are similar for the n=3,4,5 and 6 structures (Table 3.4). For the n=∞ structure, the charge on the surface titanium is significantly less, while that on the first subsurface titanium is significantly higher than those deeper in the structure. While the linking oxygen is less charged, the surface oxygen is more charged than in the other members of the homologous series, and is nearly as strongly charged as bulk oxygen. The n=2 structure has Bader charges for the surface titanium that are similar to those of the other members of the homologous series. The oxygen Bader charges, however, are somewhat different. The surface oxygen are less charged while the linking oxygen are more charged. The average Bader charges

Table 3.4: Comparison of coordination metrics across (nx1) series.

		2x1	3x1	4x1	5x1	6x1	∞x1	Bulk
Bond length	Surface	1.838	1.814	1.819	1.864	1.870	1.891	1.953
Instability Index	Global	0.13	0.12	0.14	0.15	0.17	0.31	0.10
	Surface	0.13	0.09	0.10	0.12	0.15	0.43	
Ti BVS	Surface	4.10	4.06	3.99	3.93	3.87	3.19	4.14
O BVS	Surface	-2.11	-2.05	-1.99	-1.95	-1.88	-1.21	-2.08
	Linking	-1.98	-2.05	-2.05	-2.04	-2.04	-2.06	
Ti Bader Charge	Surface	2.32	2.33	2.33	2.33	2.33	2.28	2.37
O Bader Charge	Surface	-1.13	-1.18	-1.19	-1.20	-1.21	-1.28	-1.31
	Linking	-1.31	-1.26	-1.25	-1.25	-1.24	-1.21	

on the linking oxygen in the $n=2$ structure are identical to the bulk oxygen. This indicates that the $n=3-6$ structures, and to a lesser extent the $n=2$ structure, successfully minimize the charge at the surface. The unstable $n=\infty$ does not.

The tetrahedral coordination of the surface titanium is maintained throughout the homologous series. Just as SiO_2 can form an octahedral phase isostructural with rutile under pressure, DFT calculations show that tetrahedrally coordinated TiO_2 is not significantly higher in energy than rutile and would be more stable under negative pressure (Figure 3.9). In fact, tetrahedral coordination has been observed on the (001) surface of TiO_2 .⁵⁶

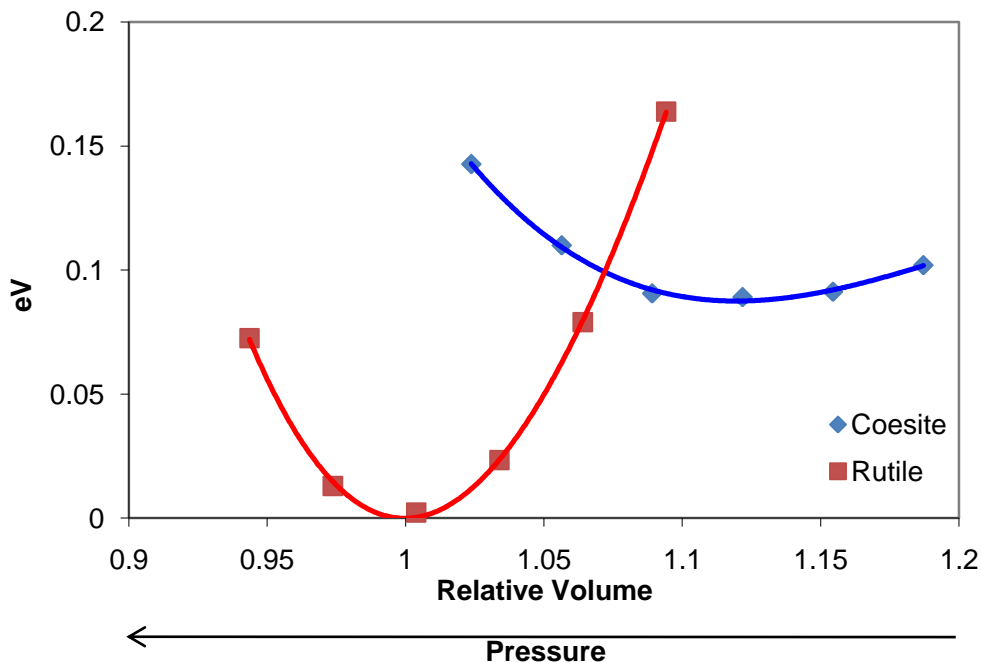


Figure 3.9: Plot of energy per formula unit as a function of unit cell volume for TiO_2 in the coesite and rutile structure types. Volume is normalized to the DFT optimized volume of the rutile unit cell. An increase in unit cell volume is equivalent to a decrease in pressure. At normal pressures (volume close to 1) the rutile structure is favored, while at negative pressures (volume greater than 1) the coesite structure is preferred.

In the $n=3$ structure, titanium bond valence sums range from 4.04 – 4.08, surface oxygen from -2.02 – -2.19, and linking O from -1.99 – -2.11 (Table 3.3). The oxygen at the middle of the 6-ring has a bond valence sum of -2.19 which is the furthest of any surface atom from either the bulk SrTiO_3 values or from the expected whole-number value. Every other atom in the surface structure has bond valence sums within 0.10 of both the bulk value for SrTiO_3 and the expected whole-number value. Complementary to the over-coordinated oxygen in the middle of the 6-ring is an under-coordinated (BVS = -1.75) oxygen in the top bulk SrTiO layer directly below center of the 6-ring. Besides this one oxygen atom, all the bond valence sums in the top bulk SrTiO layer are reasonably close to the expected values. These two phenomena, the over-coordination of the O in the middle of the 6-ring and the under-coordination of the O in the top bulk SrTiO layer directly below the 6-ring, hold throughout the homologous series.

The bond valence sums (Table 3.4 and Table 3.5) show that the more stable structures have coordination similar to that of the bulk. The $n=3$ structure has the best bond valence sums, while the bond valence sums gradually get worse the greater n changes from 3. An important trend running throughout this series is that the absolute values of the bond valence sums decrease as n increases. This is not surprising, as the excess TiO_2 at the surface also varies inversely with n : the lower the value of n , the more titanium and oxygen atoms are packed into the same area. The bond valence sum of the O in the middle of the 6-ring drops close to expected levels as n increases above 3, and the bond valence sums of other atoms which are part of the 6-ring remain close to expected values. At the same time the bond valence sums of those atoms which are not part of the 6-ring drops below the expected values. In the end limit of the series ($n=\infty$) the bond

Table 3.5: Bond valence sums and multiplicity (per (1x1) unit cell) of atoms at the surface and in the tow two bulk layers of SrTiO₃ (110) surface structures in the (nx1) homologous series.

	2x1			3x1			4x1			5x1			6x1			∞ x1		
SII	0.13			0.09			0.10			0.12			0.15			0.43		
	Atom	Mult.	BVS	Atom	Mult.	BVS												
Surface	Ti1	1	4.08	Ti1	2/3	4.08	Ti1	1/2	4.07	Ti1	2/5	4.04	Ti1	1/3	4.03	Ti1	1	3.19
	Ti2	1	4.12	Ti2	2/3	4.04	Ti2	1/2	3.97	Ti2	2/5	3.97	Ti2	1/3	3.96	O1	1	-1.21
	O1	1	-1.99	Ti3	1/3	4.04	Ti3	1/2	3.94	Ti3	2/5	3.85	Ti3	1/3	3.80			
	O2	1	-2.05	O1	2/3	-2.03	O1	1/2	-2.03	Ti4	1/5	3.82	Ti4	1/3	3.68			
	O3	1/2	-2.21	O2	2/3	-2.02	O2	1/2	-2.02	O1	1/5	-2.10	O1	1/6	-2.09			
	O4	1/2	-2.39	O3	1/3	-2.19	O3	1/2	-1.94	O2	2/5	-2.02	O2	1/3	-2.02			
				O4	2/3	-2.04	O4	1/4	-2.13	O3	2/5	-2.03	O3	1/3	-2.03			
							O5	1/4	-1.84	O4	2/5	-1.93	O4	1/3	-1.90			
										O5	2/5	-1.75	O5	1/3	-1.63			
													O6	1/6	-1.57			
Linking O ₂ Layer	O5	1	-1.95	O5	2/3	-2.11	O6	1/2	-2.10	O6	2/5	-2.10	O7	1/3	-1.95	O2	2	-2.06
	O6	1	-2.01	O6	2/3	-1.99	O7	1/2	-1.95	O7	2/5	-1.96	O8	1/3	-2.09			
				O7	1/3	-2.06	O8	1/2	-2.04	O8	2/5	-1.97	O9	1/3	-1.95			
				O8	1/3	-2.01	O9	1/2	-2.11	O9	2/5	-2.08	O10	1/3	-2.07			
										O10	1/5	-2.02	O11	1/3	-2.02			
										O11	1/5	-2.12	O12	1/3	-2.13			
1 st Bulk Layer	Sr1	1/2	2.12	Sr1	1/3	1.93	Sr1	1/4	1.91	Sr1	1/5	1.90	Sr1	1/6	1.91	Sr1	1	2.16
	Sr2	1/2	2.20	Sr2	2/3	2.12	Sr2	1/2	2.06	Sr2	2/5	2.05	Sr2	1/3	2.04	Ti2	1	4.06
	Ti3	1	4.03	Ti4	2/3	4.01	Sr3	1/4	2.14	Sr3	2/5	2.10	Sr3	1/3	2.04	O3	1	-1.96
	O7	1/2	-2.06	Ti5	1/3	4.18	Ti4	1/2	3.94	Ti5	2/5	3.90	Sr4	1/6	2.05			
	O8	1/2	-1.86	O9	1/3	-1.75	Ti5	1/2	4.21	Ti6	2/5	4.14	Ti5	1/3	3.87			
				O10	2/3	-2.04	O10	1/4	-1.74	Ti7	1/5	4.22	Ti6	1/3	4.10			
							O11	1/2	-2.00	O12	1/5	-1.66	Ti7	1/3	4.20			
							O12	1/4	-2.07	O13	2/5	-1.99	O13	1/6	-1.66			
										O14	2/5	-2.10	O14	1/3	-1.99			
													O15	1/3	-2.05			
												O16	1/6	-2.08				

valence sum of the Ti drops to 3.19 and that of O to -1.21, closer to Ti^{3+} and O^{1-} than to Ti^{4+} and O^{2-} . Additionally, the O directly below the 6-ring becomes increasingly under-coordinated as n increases. At the other end of the series, n=2, the structure becomes over-coordinated. Most notably, the O in the middle of the 6-ring has become very over-coordinated (BVS = -2.39), and the O in the middle of the other ring (which for n=2 has shrunk to a 6-ring as well) is also significantly over-coordinated (BVS = -2.21). Overall, this leads to a surface instability index of 0.13 for the n=2 structure, higher than that of the n=3,4 or 5 structures.

The foregoing implies that a structure composed only of 6-rings is too over-coordinated, and might be difficult to form. This conclusion fits with the DFT energy calculations where, even though it is on the convex hull by default, since it is the most TiO_2 rich structure calculated, the (2x1) structure is significantly higher in energy than the other members of the homologous series. Conversely, rings that are too large (i.e. structures with mostly straight TiO chains) will lead to under-coordination, and therefore to unstable structures. The optimum bond valence sums are reached when the TiO chains are broken up by rings at regular intervals. This again agrees with the DFT energy calculations, where the (3x1) and (4x1) structures, which have the overall best coordination and surface instability indices, lie on the convex hull, but higher n structures are above the convex hull. The (5x1) and (6x1) structures are only slightly above the convex hull (within calculation error), but the energy and surface instability indices are on steep upward trends. The (∞ x1) structure is above the convex hull by more than 1 eV and has the highest surface instability index.

3.5: Comparison to Other SrTiO₃ (110) Surface Models

The homologous series was compared to other proposed SrTiO₃ (110) surface structures, both in terms of DFT calculated energies, and coordination chemistry. The $n=\infty$ structure is identical to the previously proposed TiO (1x1) structure.³³⁻³⁶ Additionally, stoichiometric structures and strontium terminated structures have been proposed in the literature based on bulk-like terminations with some of the atoms removed. The stoichiometric structures are based on a half filled O₂⁴⁻ termination. The first type of half-O₂ (type A) is terminated in a bulk-like O₂ layer, but with half of the oxygen removed, either in straight lines³³⁻³⁶ or in zig-zags forming a (2 x 1) unit.³³ Another half-O₂ (type B) termination was considered with the oxygen bridging between two Sr atoms instead of in a bulk-like position.^{33,34} The Sr facet is simply a Sr-adatom in a bulk-like position (alternatively, it can be thought of as a SrTiO₄⁺ termination with TiO²⁺ removed).³³⁻³⁶ Bottin et. al.,³⁵ proposed more deeply faceted models similar to the first Sr model forming (1xn) supercells, the first two members of which are considered here. Initial calculations confirmed literature reports of the relative energies for surfaces with identical compositions. Only those structures with the best energy for each composition (Sr-faceted (1x2) and half-O₂ (type A) (2x1)) were carried out to the highest level of accuracy and are plotted in Figure 3.6. Bond valence sums were calculated for all models are presented in Table 3.6.

For the stoichiometric structural models, type A is superior to type B in terms of both DFT energies and bond valence sums. For type A, the two possible arrangements of missing oxygen lead to very similar bond valence sums (SII = 0.21 for both) and surface free energies. The bond valence sum of the surface O is nearly at the expected value (BVS = -1.94 or -1.96,

Table 3.6: Bond valence sums and multiplicity (per (1x1) unit cell) of atoms at the surface and in the two bulk layers of other SrTiO₃ (110) surface structures.

	halfO2			halfO2-2x1			halfO2B			Sr			Sr_faceted		
SII	0.21			0.21			0.41			0.26			0.29		
	Atom	Mult	BVS	Atom	Mult	BVS	Atom	Mult	BVS	Atom	Mult	BVS	Atom	Mult	BVS
Surface	O	1	-1.96	O	1	-1.94	O	1	-1.64	Sr	1	2.00	Sr	0.5	1.88
													O	1	-1.49
													Sr	1	1.93
													Ti	0.5	4.18
													O	0.5	-2.61
Linking	Sr	1	2.15	Sr	1	2.12	Sr	1	2.52	O	2	-1.73	O	1	-2.26
	Ti	1	3.81	Ti	1	3.83	Ti	1	3.30				O	1	-1.77
	O	1	-1.75	O	1	-1.82	O	1	-1.76						
1 st Bulk Layer	O	1	-2.05	O	1	-1.94	O	2	-2.19	Sr	1	1.87	Sr	0.5	2.19
	O	1	-2.36	O	1	-2.42				Ti	1	4.15	Sr	0.5	1.83
										O	1	-2.46	Ti	1	4.23
													O	1	-2.21

depending on exact arrangement). The bond valence sums of sub-surface SrTiO layer are close to the expected values, although the Ti and O in this layer are slightly under-coordinated. In the next layer down, the Sr and O are slightly over-coordinated. Taken together, the fit is rather close to the expected values. This implies that a structure terminated by a half-filled O₂ layer might be reasonable, and further that it is not highly dependent on the ordering of the missing oxygen. The missing oxygen could potentially be randomly spread out along the surface, which might be expected for a cleaved sample that has not had the opportunity to reconstruct to a more favorable structure. Half-O₂ type B, on the other hand, has bond valence sums that are very far from the expected values (SII = 0.41). The surface O has a bond valence sum of -2.95, close to O³⁻, with the sub-surface Sr, Ti, and O having bond valence sums of 3.34, 2.73, and -1.47,

respectively. These are so far from the expected values that the existence of any structure similar to this must be considered highly doubtful, a conclusion which is in agreement our calculations and those by Heifets et. al.³⁴ that find this termination significantly higher in energy than the half-O₂ type A termination.

For the strontium faceted models, the topmost Sr has a bond valence sum close to the expected value, but the O from the top O₂ layer bonded to the surface Sr are under-coordinated, while the O on the top SrTiO bulk layer (directly below the surface Sr) are over-coordinated. The surface Sr must relax towards the bulk to achieve sufficient coordination, while the top bulk O from the O₂ layer must relax upward towards the surface Sr and away from the bulk leaving it under-coordinated. The degree of this under-coordination is greater for the (1x2) faceted model than for the (1x1) model. However, for the (1x2) model, these atoms with poor coordination represent only half the number of atoms. Other models maintain bond valence sums close to the expected values. Therefore the less frequent an apex of the facet occurs, the more stable the structure will be. This, however, is not sufficient to explain why the (1x2) model was calculated to be more stable,³⁵ as the surface instability index remains greater for the (1x2) model (SII = 0.29) than the (1x1) model (SII = 0.26). One possible explanation for this is that the simple bond valence sum calculation does not fully reveal the instability of the strontium at the apex.

There are two additional chemical reasons why strontium at the apex would be unstable which are not picked up by bond valence sums. First, more than half of the apical strontium's coordination sphere is empty. A simple bond valence sum does not consider such geometrical concerns. Second, the apical strontium has become unusually close to the titanium in the layer

below it (3.00 Å Ti–Sr distance in the (1x1) model and 3.05 Å in the (1x2) model, compared to 3.38 Å in bulk SrTiO₃). There is no easy way to include this factor using bond valence sums, as cation-cation or anion-anion interactions are neglected.

The favorable bond valence sums for the half-O₂ type A structures fits with DFT calculations. The DFT calculations have found that the surface energy of the half-O₂ type A structures lies along the convex hull. The more favorable energies and surface instability indices for the $n \leq 6$ structures and the half-O₂ type A structures both indicate that the $n = \infty$ structure is unstable and unlikely to form. If a surface with such a composition existed, a more favorable form would be in some combination of (nx1) and half-O₂ type A structures. While the strontium faceted structures cannot be directly compared in terms of energy due to their composition, they have high surface instability indices, and are therefore considered unlikely to form. In terms of chemical bonding, the half-O₂ type A structures are also less satisfactory than the homologous series. The good coordination of the homologous series indicates that it will be more stable than any other surface structure for SrTiO₃ (110) so far proposed. The formation of the other structures in the proper environment cannot be ruled out (e.g. Sr-faceted structures in a Sr-rich environment). However, the bond valence sums indicate that the experimentally observed structures are the most stable.

3.6: Conclusions

Can oxide surface structures be predicted? I believe the answer is yes. First, the thermodynamic structures will in almost all cases (particularly under oxidizing conditions) be

valence compensated. Second, they will have polyhedral coordination chemistry similar to the bulk. Third, metrics such as bond-valence sums are useful and can be used effectively. Homologous series are well known in bulk oxides and if the STM images were HREM images of a bulk oxide the fact that they show intergrowths would be relatively unremarkable. The fact that homologous series and intergrowths occur in a single monolayer, however, is noteworthy. It is both significant and novel, being the first example of these important concepts for bulk oxides occurring at a surface. This demonstrates that the way to understand oxide surfaces is not to look out into the vacuum, but to look into the bulk. By doing so and applying what is known about the bulk, a century of inorganic chemistry can guide us to predict oxide surface structures.

Chapter 4:

Reactivity of an Oxide Surface:

Adsorbates on SrTiO₃ (1 0 0)

4.1: Introduction

An atomic level understanding of surface structures is a necessary first step to an atomic level understanding of heterogeneous catalysis. A full understanding also requires knowing how the reactants and products interact with the surfaces. A logical next step in this direction is to study the interaction of adsorbates with known surface structures.

Recent studies on the MgO⁵⁷ and NiO⁵⁸ (111) surfaces have examined the role of H₂O on surface structure formation. Both MgO and NiO have the relatively simple rock-salt structure, which in the (111) direction are composed of alternating planes of M²⁺ and O²⁻ (M = Mg, Ni). This leads to a polar surface, similar to the SrTiO₃ (110) surface described in Chapter 3. A (2x2) reconstruction, commonly referred to as an octapole, has been proposed by Wolf to compensate for the polar surface.^{24,59} While calculations show that the Wolf octapole is low in energy, it has never been experimentally observed. Ciston and coworkers^{57,58} analyzed multiple experimentally observed structures on the MgO and NiO (111) structures, and found that all were hydroxylated. They concluded that dissociated water and the dehydration and rehydration of the surface play a role in the formation of rock-salt surface structures and the transition between the various observed structures.

It is possible, perhaps even likely, that water or other adsorbates account for the differences between these observed and predicted surface structures. For example, on the SrTiO₃ (100) surface, the never observed $\sqrt{2}\times\sqrt{2}$ -R45° surface structure is calculated to be lower in energy than the experimentally solved (2x1) structure.⁶⁰

Hydrogen, however, is incredibly difficult to determine by diffractive techniques in bulk structures, and even more so on surface structures. It is also easy to miss the presence of hydrogen with surface sensitive chemical analysis such as x-ray photoelectron spectroscopy (XPS). However, a careful analysis of an XPS spectrum can reveal the presence of hydroxide as a high binding energy shoulder on the O1s peak.^{57,58,61-63}

This chapter presents a multi-tiered approach to examining the presence of adsorbates, particularly water and its derivatives, on the SrTiO₃ (100) surface. Transmission electron diffraction (TED) patterns and XPS spectra were obtained so that the presence of a surface reconstruction could be correlated with the presence of water. Without exposure to air, the samples were annealed, then further TED and XPS were obtained. Thus the conditions necessary to remove the adsorbates were determined. Simultaneously, density functional theory (DFT) calculations were used to determine the strength with which H₂O and CO₂ bind to unreconstructed SrTiO₃ (100) surfaces. Through these methods it is demonstrated how adsorbates are involved in the formation of SrTiO₃ (100) surface structures.

4.2: Experimental Methods

To determine under what conditions adsorbates were removed from various surface structures, it was necessary to anneal samples in a controlled environment and obtain XPS and TED data without exposure of the sample to atmosphere. The principle tool for this was the Specimen Preparation, Evaluation, Analysis and Reaction System (SPEAR). SPEAR is a large UHV system which contains, among other instruments, an XPS, a UHV-TEM, an electron gun

(for annealing samples) and a heating stage. Five major chambers of SPEAR were used in this work: a load-lock, a transfer chamber, a gas cell, an analytical chamber, and a Hitachi UHV-9000 TEM. Samples were introduced through the load-lock, the only chamber which was exposed to air. After the load-lock reached UHV conditions, samples were moved to the transfer chamber. From the transfer chamber, the samples were moved into each of the final three chambers as needed for annealing, XPS and TEM analysis. Each is discussed in greater detail below.

4.2.1: Sample Preparation

Samples were prepared by standard solid-state TEM sample preparation methods. Single crystals wafers of (100) oriented SrTiO₃ measuring 1cm x 1cm x 0.5mm and epi-polished on one side were obtained from MTI crystals. Three millimeter discs were cut from these wafers using a rotary cutter and an abrasive slurry. The discs were mechanically polished to a thickness of approximately 100 μm , and the center then thinned to a thickness of less than 25 μm using a Gatan Dimple Grinder. Samples were then ion milled using Ar⁺ ions in a Gatan Precision Ion Polishing System (PIPS) to electron transparency. An initial energy of 6 kV was used for the Ar⁺ ions, which was gradually decreased to the minimum possible value as the samples became thinner in order to minimize the damage from ion-milling. Below a minimum energy, which varied somewhat depending on the state of the PIPS, the ion guns would not fire. Thus the minimum energy used was not constant among samples, but was generally in the range of 2.5 – 3.0 kV.

If the PIPS system is not perfectly aligned or if it is contaminated, it can sputter other materials onto the sample, most commonly molybdenum. Additionally, the ion-milling itself damages the sample. In particular, the lighter oxygen is preferentially sputtered away, leaving a non-stoichiometric surface. To remove any sputtered impurities, samples were briefly washed (several seconds) in a 1:1 (volume/volume) solution of concentrated HCl:HNO₃. It is expected that this, like washing with NH₄F:HF,⁶⁴ should remove any strontium on the surface, leading to a titanium oxide rich surface. Samples were then rinsed several times in deionized water. After drying, samples were annealed to eliminate any damage from ion-milling and to obtain a flat and reconstructed surface. Samples were placed in an alumina sample boat within a fused silica tube inside a Carbolite STF 15/51/180 tube furnace, and heated to 850°C or 950°C in air. These temperatures were chosen as they had previously been observed to lead to the formation of the c(4x2) and (2x1) reconstructions, respectively,⁶⁵ desired targets for these studies. Exposure to water occurred only during this processing in air prior to entry into SPEAR, except where specifically stated to the contrary.

After they had cooled, samples were placed in an alumina ring and secured with a tungsten spring clip. Samples were then introduced into SPEAR. Initially, the load lock was baked to ~200°C as it was pumped down. Due to the fear that this would drive off adsorbates from the sample surface, the bake was eliminated and a cold trap was used to help the load lock chamber reach UHV conditions. This was done by wrapping the load lock in a thermal blanket and filling it with dry ice. After the load lock reached UHV conditions, samples were not exposed to atmosphere again except as specifically mentioned below.

4.2.2: X-ray Photoelectron Spectroscopy

XPS is an inherently surface sensitive method for examining chemical species and their bonding states. XPS data was collected in the analytical chamber using monochromated Al K- α X-ray source and a PHI model 05-458 hemispherical analyzer. The X-ray source irradiates the sample with 1486 eV incident X-rays. Electrons ejected from the sample were collected and their kinetic energy (KE) measured by the hemispherical analyzer. The electron orbital binding energy (BE) is then determined from the photoelectric effect:

$$BE = hv - KE - \varphi$$

The work function (φ) was accounted for by normalizing each scan to the known SrTiO₃ Ti-2p^{3/2} peak energy of 458.8 eV. The surface sensitivity is due to the small mean free path of photoelectrons, which are reabsorbed by the sample if they originate more than a few nanometers below the surface. Surface sensitivity can be enhanced by using a smaller angle θ between the sample surface and the detector, as the penetration depth is relative to $\sin(\theta)$. For this work an angle of $\theta = 45^\circ$ is preferred. It was found that at smaller angles the sample could not be aligned to eliminate a signal from the sample holder. When a signal from the holder was detected, it was often found to be shifted somewhat relative to the sample due to differential charging, in some cases making deconvolution of the data difficult.

To check for impurities, a survey scan from 1400 – 0 eV was conducted (0.5 – 0.4 eV step size, 0.5 – 0.655 s dwell time). Each region of interest (O1s, Ti2p, Sr3d and C1s) was scanned in more detail, as was the Al2p region to ensure that signal from the alumina holder was not being detected (0.1 eV step size, 0.5 – 0.655 s dwell time, averaging over 5 – 25 repeat

scans). The XPS analyzer output was shifted by a constant amount to align the highest point in the SrTiO₃ Ti-2p^{3/2} peak with a binding energy of 458.8 eV. XPS data was then fit using the free XPSPEAK 95 version 2.0 software.⁶⁶ A linear background averaged over 9 data points at the flat edges on each side of an area was subtracted and each peak was fit to a Gaussian curve. Initially, full-width at half-max (FWHM) was constrained to be equal for all peaks of a given type. The peak position, area, and FWHM were optimized. A final optimization was done in which each FWHM, as well as the peak position and area, were allowed to vary independently for each peak.

The main feature of interest was a high binding energy shoulder on the O1s peak, which can indicate the presence of hydroxyl groups on the surface.^{57,58,61-63} Hydroxyl groups, however, are not the only possible source of such a high binding energy shoulder. In TiO₂ rutile, the presence of Ti³⁺ also leads to a high binding energy shoulder on the O1s peak.^{62,63} It is therefore important to make sure that the sample is not reduced before attributing the O1s high binding energy shoulder to the presence of hydroxide. The oxidation state of titanium can easily be seen in XPS by looking at the Ti2p region at ~460 eV. The Ti⁴⁺ Ti2p^{3/2} peak in SrTiO₃ normally is present at 458.8 eV. If any Ti³⁺ is present, it would cause a low binding energy shoulder.^{62,63,67,68} The Ti2p^{3/2} peak was therefore checked for such a shoulder.

4.2.3: Transmission Electron Microscopy and Transmission Electron Diffraction

Transmission electron microscopy (TEM) has the advantage of providing near atomic scale information in both real and reciprocal space nearly simultaneously. TEM was performed in a Hitachi UHV-9000 TEM with a LaB₆ filament operated at 300 kV accelerating voltage and a

base pressure of $\sim 1 \times 10^{-1}$ torr. Transmission high energy electron diffraction (THEED, or simply TED), is very useful for obtaining high resolution structural data, as it avoids many of the lens aberration issues which hinder TEM imaging. For TED, a thin, flat, defect free area was first found in imaging mode. This area was tilted to align it slightly off zone axis ($\sim 2\text{-}3^\circ$) to minimize the amount of dynamic scattering visible in the diffraction pattern. This leads to a reduced contribution of bulk diffraction, while the effect on the surface is minimal due to the long rods of the two dimensional surface structure.⁶⁹ Additionally, this leads to more kinematical diffraction from the surface. A small (~ 50 nm) parallel probe was formed by using a small condenser aperture allowing diffraction information to be collected from a specific area without cutting off higher angle beams, which occurs when using a selected area aperture. Bright field imaging was accomplished by inserting an objective aperture to select only the transmitted beam from which the image was formed. Dark field imaging was accomplished by tilting the beam so that the desired diffracted beam was aligned down the microscope's optic axis, then inserting the objective aperture around that beam. Images and diffraction patterns were collected on photographic film. A range of exposure times from 0.5 – 60 seconds were collected for diffraction patterns to increase the dynamic range.

4.2.4: Annealing

After being introduced into SPEAR, samples were annealed using either the electron gun in the analytical chamber or in the heating stage in the gas cell. Annealing was carried out in either UHV or a controlled oxygen atmosphere. Oxygen, if used, was introduced into the chamber from a gas cylinder. The chamber was continuously pumped as the oxygen flowed in,

with the pressure being measured by a mass spectrometer. When a steady state was achieved at the desired oxygen pressure, the annealing procedure was begun. In the analytical chamber, oxygen (BOC Gases, grad 4.7) was flowed in through the ion gun and the chamber pumped via an ion pump. In the gas cell, oxygen (Physical Electronics Inc., 99.99% purity) was flowed in through a leak valve and the chamber pumped via a turbomolecular pump.

For electron gun heating, the sample was directly heated by bombardment with low energy electrons from a Kimball Physics Inc. EMG-14 electron gun with a LaB₆ filament operated at a 4.28 kV accelerating voltage. The temperature was raised by increasing the current to the electron source and focusing the source onto the central area of the sample. The temperature was measured by an optical pyrometer (Mikron M190 OS Infrared Thermometer, 1.0 – 1.6 μm spectral band, 90:1 F.O.V. ratio, 250 – 2000°C range) using an emissivity of $e = 0.100$. Very high temperatures could be achieved by this method; however, the heating was not uniform, as the electrons had to be focused onto an area far smaller than the sample diameter to achieve high temperatures. This also led to some inaccuracies in the temperature measurement, as the area which was being heated was smaller than the area focused on by the pyrometer. Finally, bombardment with low energy electrons is known to reduce titanium in rutile TiO₂ (for examples, see ⁶⁸ and references therein) It was found that titanium was being reduced by the electron beam even when annealing was carried out in an oxygen atmosphere.

In the gas cell, samples were heated on a heating platform. The temperature of the platform was measured by a thermocouple ~1 mm away. Using this temperature reading and a previously determined calibration curve, the temperature of the sample was calculated. This

method had the advantage of applying uniform heating, and the sample was not reduced. However, the maximum temperature was lower than annealing with the electron gun. For earlier experiments, temperatures of $\sim 825^\circ\text{C}$ could be reached. However, the maximum temperature slowly decreased with use, and by the final experiments the maximum that could be achieved was $\sim 750^\circ\text{C}$.

4.2.5: Density Functional Theory Calculations

Several possible models were created for both H_2O and CO_2 adsorbed on the unreconstructed Sr- and Ti-terminated (1x1) surfaces of SrTiO_3 . DFT structural relaxations were performed using the all-electron Wien2k⁴⁸ code with an augmented plane wave basis set with the general gradient approximation (GGA) defined by the PBE functional,⁴³ with an onsite exchange-correlation energy correction from the meta-GGA TPSS functional.⁵² Muffin-tin radii (RMTs) of 2.36 and 1.7 were used for strontium and titanium, respectively. For calculations involving H_2O , RMTs of 1.2 and 0.55 were used for oxygen and hydrogen, respectively. Due to the short C–O distance, smaller RMTs of 1.0 and 1.15 for O, and C, respectively, were used for calculations involving CO_2 . An RKMax of 2.5 was used for calculations involving H_2O and an RKMax of 4.75 was used for calculations involving CO_2 . The binding energy for the adsorbate was calculated by subtracting the energy of the adsorbate as a free molecule and the energy of an equivalent relaxed slab without an adsorbate from the energy of the slab relaxed with the adsorbate molecule.

The energies for all reconstructed SrTiO_3 (001) surfaces were provided by Andres Becerra-Toledo⁷⁰ and Danielle Kienzle.⁷¹

4.2.6: Bond valence sum calculations

Bond valence sums were calculated using the KDist program in the Kalvados program suite.¹⁸ For structures from DFT calculations the volume was changed isotropically to obtain the correct lattice parameter. Bonding interactions up to 3.5 Å were included in the calculation. A value of $b = 0.37$ was used in all cases. Standard R_0 values of 2.118 Å and 1.815 Å were used for $\text{Sr}^{2+}\text{-O}^{2-}$ and $\text{Ti}^{4+}\text{-O}^{2-}$, respectively.¹⁹ A R_0 of 0.957 Å, the O–H bond distance in gaseous H_2O , was used for $\text{H}^+\text{-O}^{2-}$. The global instability index (GII) and surface instability index (SII) were calculated by hand from the bond valence sums and the atomic multiplicities, as described in Chapter 5. The surface instability index is calculated in the same manner as the global instability index, except that only the atoms in the outermost surface and first bulk layer are included. A bulk instability index (BII) was similarly calculated from the central most stoichiometric unit in the model. For more details on bond valence sums, see Chapter 5.

4.3: Results

4.3.1: Reconstructions after annealing in air

Multiple samples were prepared, annealed in air, and introduced into SPEAR. TED was collected from multiple samples annealed at the same temperature for the same amount of time. Not all showed the same reconstruction. Three different reconstructions were observed in the course of this work: a (2x1), c(4x2) or a $(\sqrt{13}\times\sqrt{13})\text{-R}33.7^\circ$ was observed. At 850°C the $(\sqrt{13}\times\sqrt{13})\text{-R}33.7^\circ$ and (2x1) reconstructions were observed, with the $(\sqrt{13}\times\sqrt{13})\text{-R}33.7^\circ$ being

more common. At 950°C all three reconstructions were observed, with the (2x1) the most common. In one case, two samples annealed in the same sample boat exhibited different reconstructions: one a (2x1) reconstruction and the other a ($\sqrt{13}\times\sqrt{13}$)-R33.7° reconstruction. This indicates that other factors besides temperature and atmosphere during annealing influence which reconstruction forms. Among the most likely possibilities for such determining factors are the damage imparted during sample preparation, the degree of titanium enrichment at the surface, and the presence of adsorbates on the surface.

XPS was collected at various angles for each sample, and it was found that the Ti2p: Sr3d peak ratio was greater at lower collection angles. This indicates that the surface is rich in titanium, in agreement with the crystallographically solved structures for the (2x1),²⁹ and $c(4\times 2)$ ⁷² reconstructions and preliminary analysis of the ($\sqrt{13}\times\sqrt{13}$)-R33.7°^{71,73} reconstruction. However, the relative amounts of titanium enrichment for each sample could not be readily calculated, as the only collection angle for which data was available for all samples was 45°. Because 45° is the only angle at which data is uniformly available and because it is the lowest angle at which spectra were acquired without signal from the sample holder, data from 45° will be presented moving forward, except where specifically stated. Full data for all scans is available in the appendices.

4.3.2: H₂O on the c(4x2) reconstruction

A sample annealed at 950°C for five hours in air exhibited a strong $c(4\times 2)$ reconstruction (Figure 4.1 and Figure 4.2). XPS from that sample revealed a shoulder on the high binding energy side of the O1s peak with an area of 0.36 relative to the main O1s peak (Figure 4.3). The

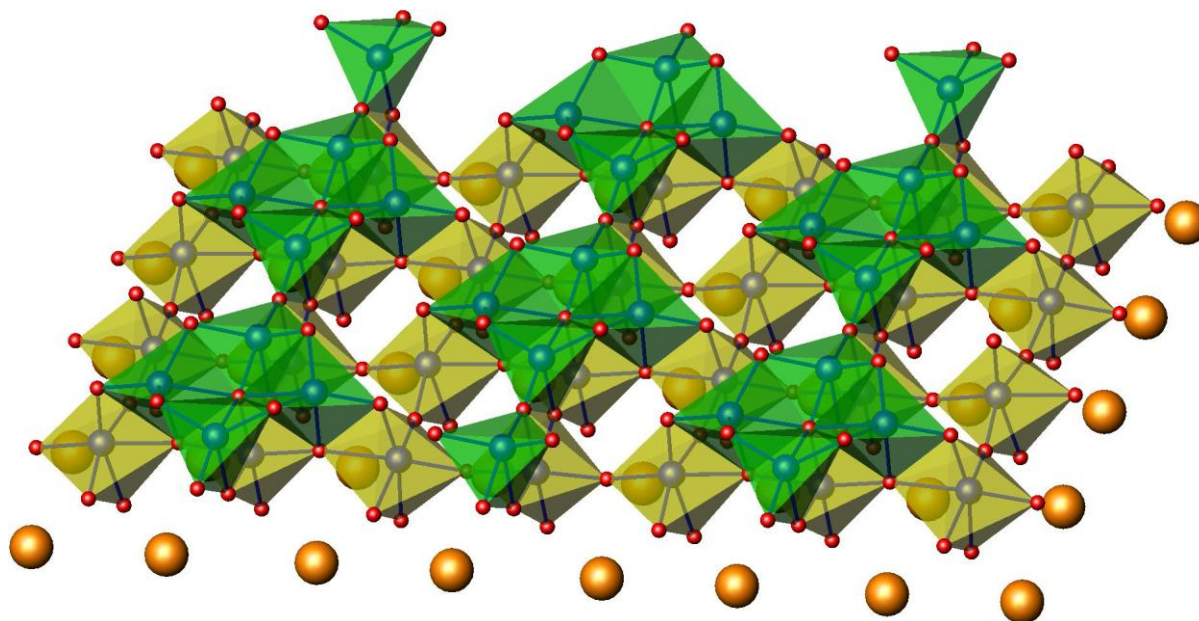


Figure 4.1: $c(4 \times 2)$ surface structure with top bulk layer. Surface TiO_5 trigonal bipyramids in green, bulk TiO_6 octahedra in yellow, strontium cations in orange, and oxygen anions in red.

sample had been prepared by annealing at 950°C for five hours in air. An additional feature at a slightly lower binding energy was attributed to differential charging of the sample and the holder and should be ignored whenever it is present. Additionally, XPS showed a sizable $\text{C}1s$ peak present in the spectra, with an area of 0.34 relative to the main $\text{O}1s$ peak. Annealing in 8×10^{-7} torr O_2 for 20 minutes at 400°C using the electron gun as a heating source produced minimal change in the reconstruction observed via TED. The $c(4 \times 2)$ reconstruction was still present, although slightly weaker. The fact that the reconstruction is weaker could be due to the thickness of the area examined or the precise sample tilt condition, and does not necessarily imply a difference in the surface structure. The high binding energy shoulder on the $\text{O}1s$ peak

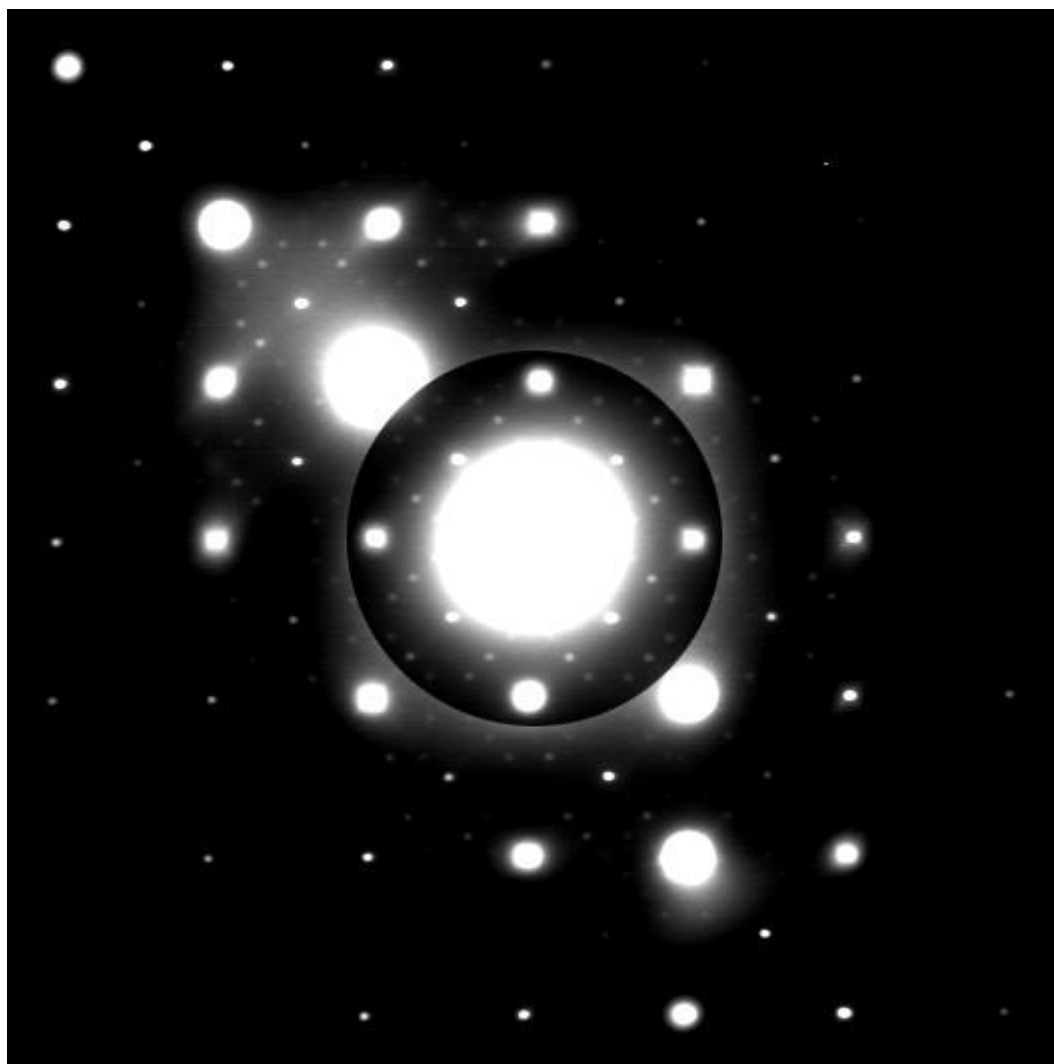


Figure 4.2: $c(4 \times 2)$ diffraction pattern after annealing in air at 950°C for 5 hours.

was larger than prior to the anneal, with an area of 0.55 relative to the main O1s peak (Figure 4.3). The C1s peak was slightly smaller than before the anneal, with an area of 0.30 relative to the main O1s peak.

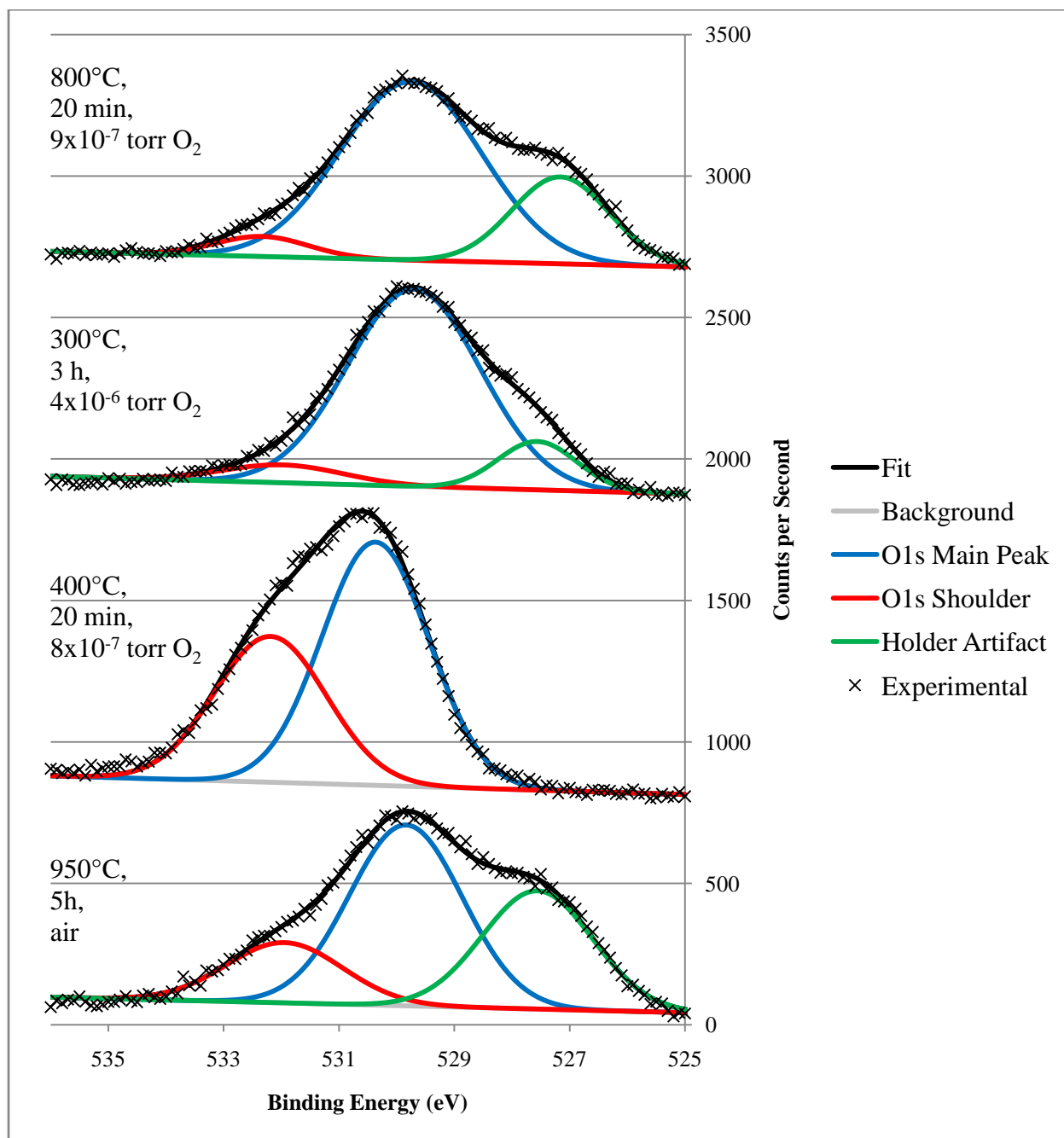


Figure 4.3: O1s peak region of the XPS spectra from a sample with the c(4x2) reconstruction showing reduction of high binding energy should upon annealing. Counts per second for each spectra offset by a constant value for ease of viewing.

After annealing in 4×10^{-6} torr O_2 at 300°C for 3 hours, again using the electron gun, the high binding energy shoulder on the O1s peak nearly disappeared, with an area relative to the main O1s peak of 0.08 (Figure 4.3). The C1s peak area decreased as well, to 0.15 relative to the main O1s peak. The c(4x2) reconstruction remained, with intensities similar to the intensities prior to the anneal. A second set of Ti2p peaks were present at a slightly lower binding energy, indicating the presence of reduced titanium (Ti^{3+}). This reduced titanium also contributed to the high binding energy shoulder on the O1s peak. The area of the high binding energy shoulder due to hydroxyl groups is therefore even less than 0.08 relative to the main O1s peak. Thus most, if not all, of the hydroxyl groups had been removed. The Ti^{3+} 2p peak area to Ti^{4+} 2p peak area ratio was 0.67 in the 45° scan, and only 0.60 in the 75° scan, implying that the reduced titanium was concentrated near the surface.

After annealing via electron gun in 9×10^{-7} torr O_2 at 800°C for 20 minutes the c(4x2) reconstruction nearly disappeared (Figure 4.4). The high binding energy shoulder on the O1s peak remained small, 0.07 relative to the main O1s peak, indicating that few to no hydroxyl groups were present (Figure 4.3). The C1s peak also remained small, 0.18 relative to the main O1s peak. The Ti^{3+} 2p peak area to Ti^{4+} 2p peak area ratio shrank to 0.26. However, the ratio was greater at 75° (0.46) than at 45° , indicating that the reduced titanium may have been deeper within the bulk of the material.

It is worth noting that the electron gun does not heat the sample evenly. For lower temperature annealing, the electron beam is not as focused, and therefore heats a larger area of the sample. To achieve higher temperatures, the electron beam must be focused into a small

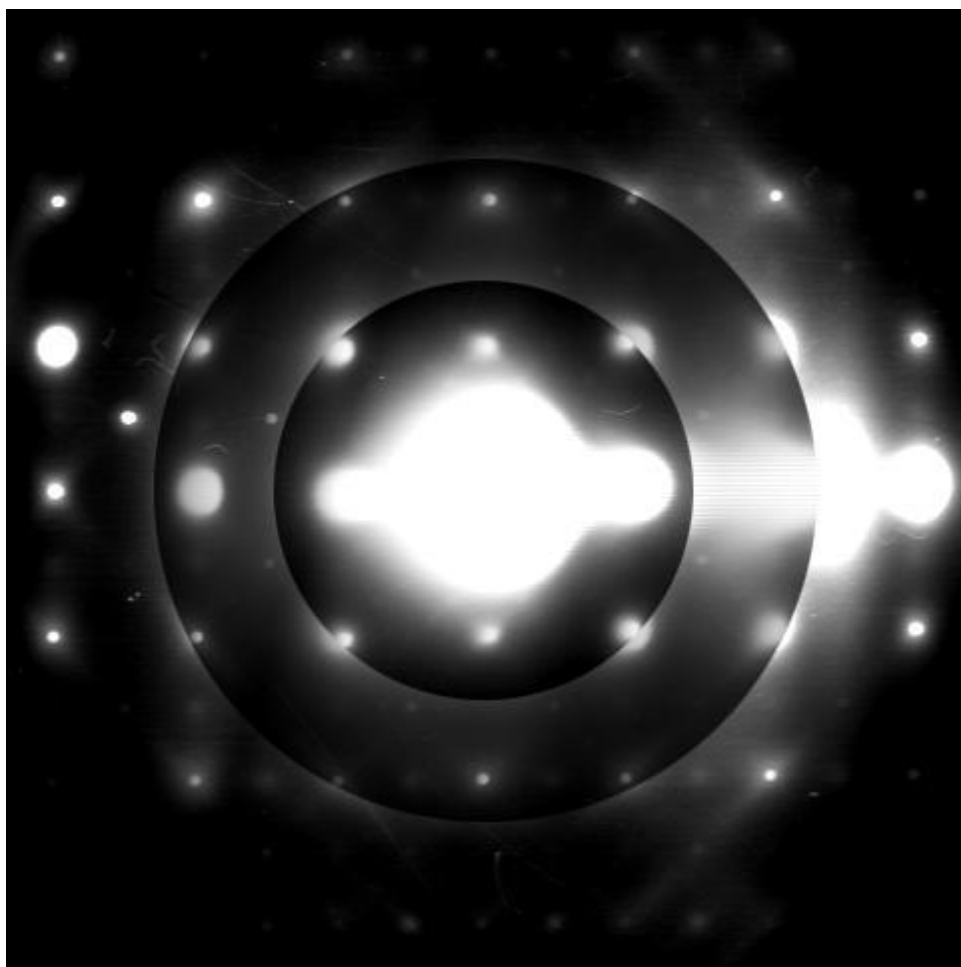


Figure 4.4: TED after annealing sample with c(4x2) reconstruction at 800°C for 20 minutes. Only a few spots at the locations of the brightest c(4x2) spots are still visible.

area, and therefore only the center of the sample is heated. It is likely that after the 800°C anneal the sample was no longer homogeneous. If the sample were not aligned exactly the same, the XPS signal would have come from different parts of the sample. This could explain the discrepancies observed between the 45° and 75° spectra after the 800°C anneal, and it is important not to over interpret such results. It is also likely that the signal from carbon and

hydroxide after annealing was due mostly to adsorbates near the edges of the sample. The center of the sample, which reached the hottest temperatures, probably has fewer adsorbates present than is indicated from the XPS spectra.

4.3.3: H_2O on the $(\sqrt{13}\times\sqrt{13})$ -R33.7° reconstruction

The $(\sqrt{13}\times\sqrt{13})$ -R33.7° reconstruction (Figure 4.6) was seen on multiple occasions and always H_2O was present as indicated by the high binding energy shoulder on the O1s peak. Often when the $(\sqrt{13}\times\sqrt{13})$ -R33.7° reconstruction was present light streaking was observed in the (100) directions, with stronger diffuse scattering in locations where the (2x1) type spots were present. Two samples which exhibited the $(\sqrt{13}\times\sqrt{13})$ -R33.7° reconstruction were annealed in SPEAR and XPS data is available from before and after the anneals for comparison.

The first sample with the $(\sqrt{13}\times\sqrt{13})$ -R33.7° reconstruction also exhibited streaking in the (100) directions with diffuse (2x1) spots. XPS showed a large high binding energy shoulder on the O1s peak, with an area of 0.61 relative to the main O1s peak (Figure 4.5). A large C1s peak was present, with an area of 0.49 relative to the main O1s peak. Additionally, there was a slight low binding energy shoulder on the Ti3p peak, indicative of reduced titanium (Ti^{3+}). Electron gun annealing in 3×10^{-9} torr O_2 for 20 minutes at $\sim 520^\circ C$ caused the O1s high binding energy shoulder to decrease to approximately half its former size (area of 0.30 relative to the main O1s peak, Figure 4.5). The C1s peak also decreased to an area of 0.31 relative to the main O1s peak. The TED showed no reconstruction, while TEM imaging indicated that the surface had roughened and was no longer terraced. The loss of the reconstruction was attributed to the reduction. The Ti^{3+} peak had increased, from an area of 0.15 to 0.42 relative to the Ti^{4+} 2p peak.

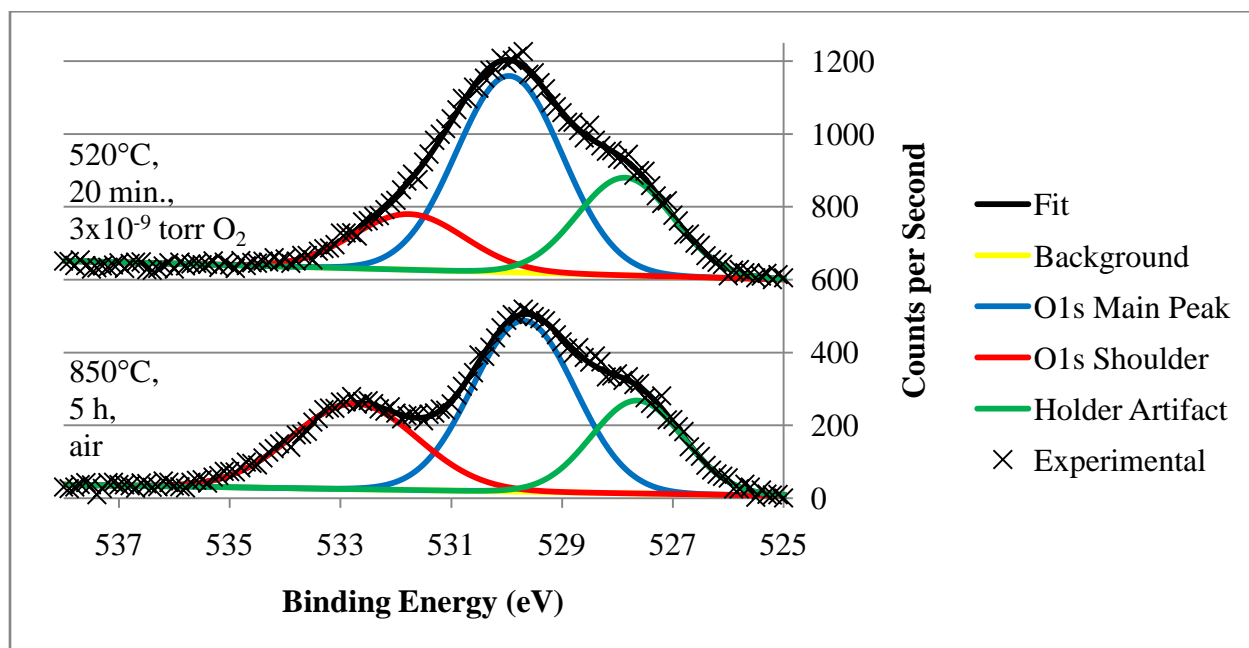


Figure 4.5: O1s peak region of the XPS spectra from a sample which began with the ($\sqrt{13 \times \sqrt{13}}$)-R33.6 reconstruction (bottom) which disappeared (top) upon annealing. Counts per second for each spectra offset by a constant value for ease of viewing. The low binding energy shoulder is an artifact from the sample holder and should be ignored.

Some hydroxide still seemed to be present, as the O1s high binding energy shoulder was significantly larger than the Ti2p low binding energy shoulder. It was therefore concluded that the electron gun, in such a low oxygen environment, had reduced the sample before hydroxide was removed. Conclusions could therefore not yet be drawn as to what role water played in the ($\sqrt{13 \times \sqrt{13}}$)-R33.7° reconstruction.

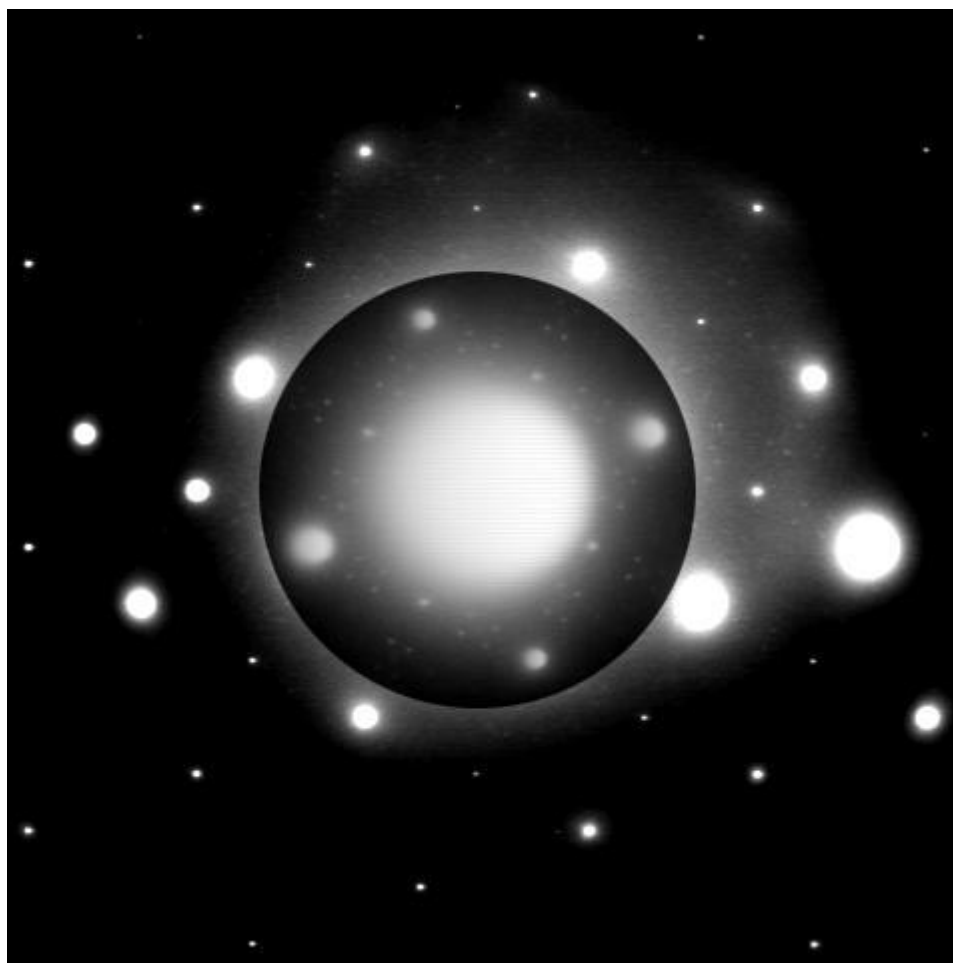


Figure 4.6: $(\sqrt{13} \times \sqrt{13})$ -R33.7° diffraction pattern after annealing in air at 850°C for 5 hours.

A second sample exhibited a $(\sqrt{13} \times \sqrt{13})$ -R33.7° reconstruction (Figure 4.6). This $(\sqrt{13} \times \sqrt{13})$ -R33.7° reconstruction was more distinct than in the previous sample, and the streaking and diffuse (2×1) spots were less intense. Additionally, no Ti^{3+} shoulder was observed in the $\text{Ti}2p$ region, nor did any appear during the course of annealing experiments. There was a significant high binding energy shoulder on the $\text{O}1s$ peak, although smaller than in the previous

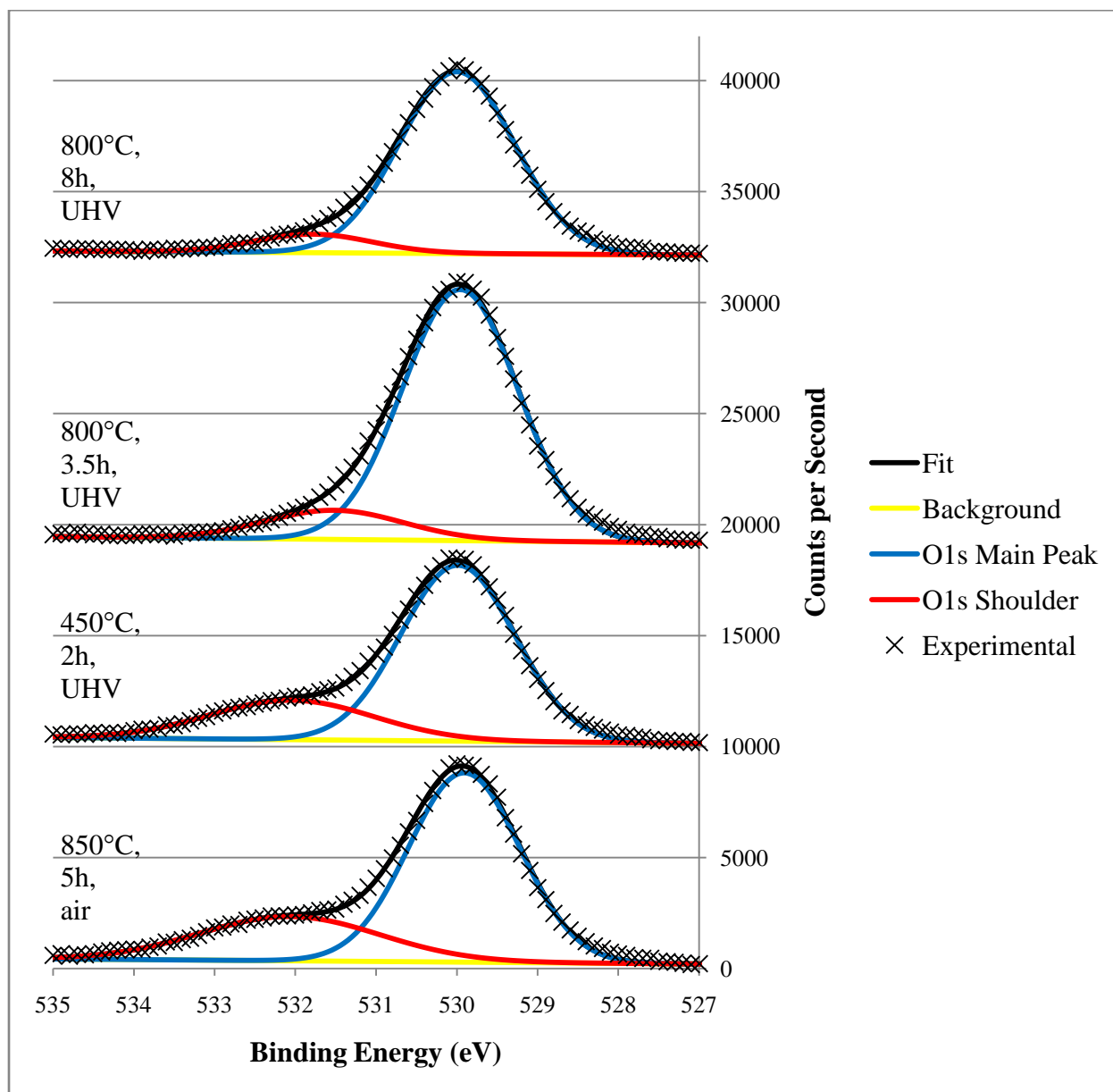


Figure 4.7: O1s peak region of the XPS spectra from a sample which began with the $(\sqrt{13}\times\sqrt{13})$ -R33.6 reconstruction (bottom) and transformed into a streaked (2x1) reconstruction (top) upon annealing. Counts per second for each spectra offset by a constant value for ease of viewing.

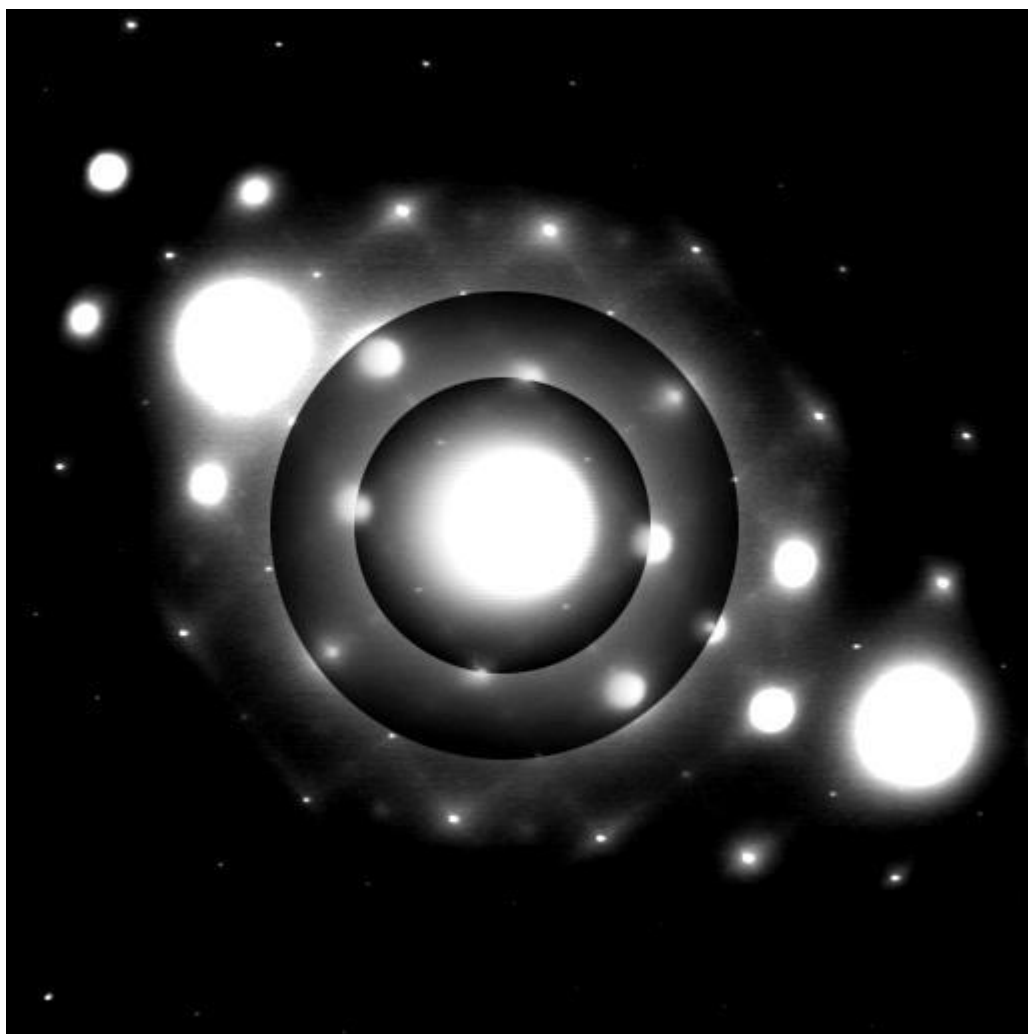


Figure 4.8: Streaked diffraction pattern with higher intensity where (2×1) spots would exist as found after annealing a sample exhibiting the $(\sqrt{13} \times \sqrt{13})\text{-R}33.7^\circ$ reconstruction in UHV.

sample, with area 0.38 relative to the main O1s peak (Figure 4.7). A C1s peak was also present, with area of 0.21 relative to the main O1s peak.

After annealing at $\sim 450^\circ\text{C}$ in the gas cell in UHV for 2 hours, TED showed a slightly fainter $(\sqrt{13} \times \sqrt{13})\text{-R}33.7^\circ$. This decrease in the intensity of the surface diffraction does not

necessarily indicate that the reconstruction is beginning to dissipate, and is more likely the result of the TED being obtained from a slightly thicker area of the sample or a slightly different sample tilt being used. The high binding energy O1s shoulder and C1s peak both shrank slightly, to areas of 0.32 and 0.19, respectively, relative to the main O1s peak (Figure 4.7).

Annealing at $\sim 800^\circ\text{C}$ for 3.5 hours in the gas cell in UHV caused the $(\sqrt{13}\times\sqrt{13})\text{-R}33.7^\circ$ to disappear. The streaking in (001) directions was increased, with significantly higher intensity diffuse (2×1) spots. The high binding energy shoulder on the O1s peak decreased to 0.14 relative to the main O1s peak (Figure 4.7), while that of the C1s peak decreased to an area of 0.13. Annealing at $\sim 800^\circ\text{C}$ for 8 additional hours in gas cell in UHV caused the diffuse (2×1) spots to become more distinct and well resolved (Figure 4.8). The high binding energy shoulder on the O1s peak decreased further to an area of 0.10 relative to the main O1s peak (Figure 4.7). The C1s peak area remained approximately the same, at 0.14 relative to the main O1s peak.

4.3.4: H₂O on the (2x1) reconstruction

A fresh sample with a (2×1) reconstruction (Figure 4.9), similar to that exhibited after annealing the $(\sqrt{13}\times\sqrt{13})\text{-R}33.7^\circ$ sample, was introduced into SPEAR. The sample had been prepared by annealing at 950°C for five hours in air. The TED showed a weak (2×1) reconstruction with some streaking in the (100) directions, with the streaks partially resolving into a series of other spots with a (5×1) periodicity (Figure 4.10). XPS spectra showed a sizable shoulder on the 1.7 eV higher in binding energy than the main O1s peak, with an area of 0.19 relative to the main O1s peak (Figure 4.11). Additionally, there was a sizable C1s peak present, with an area of 0.29 relative to the main O1s peak.

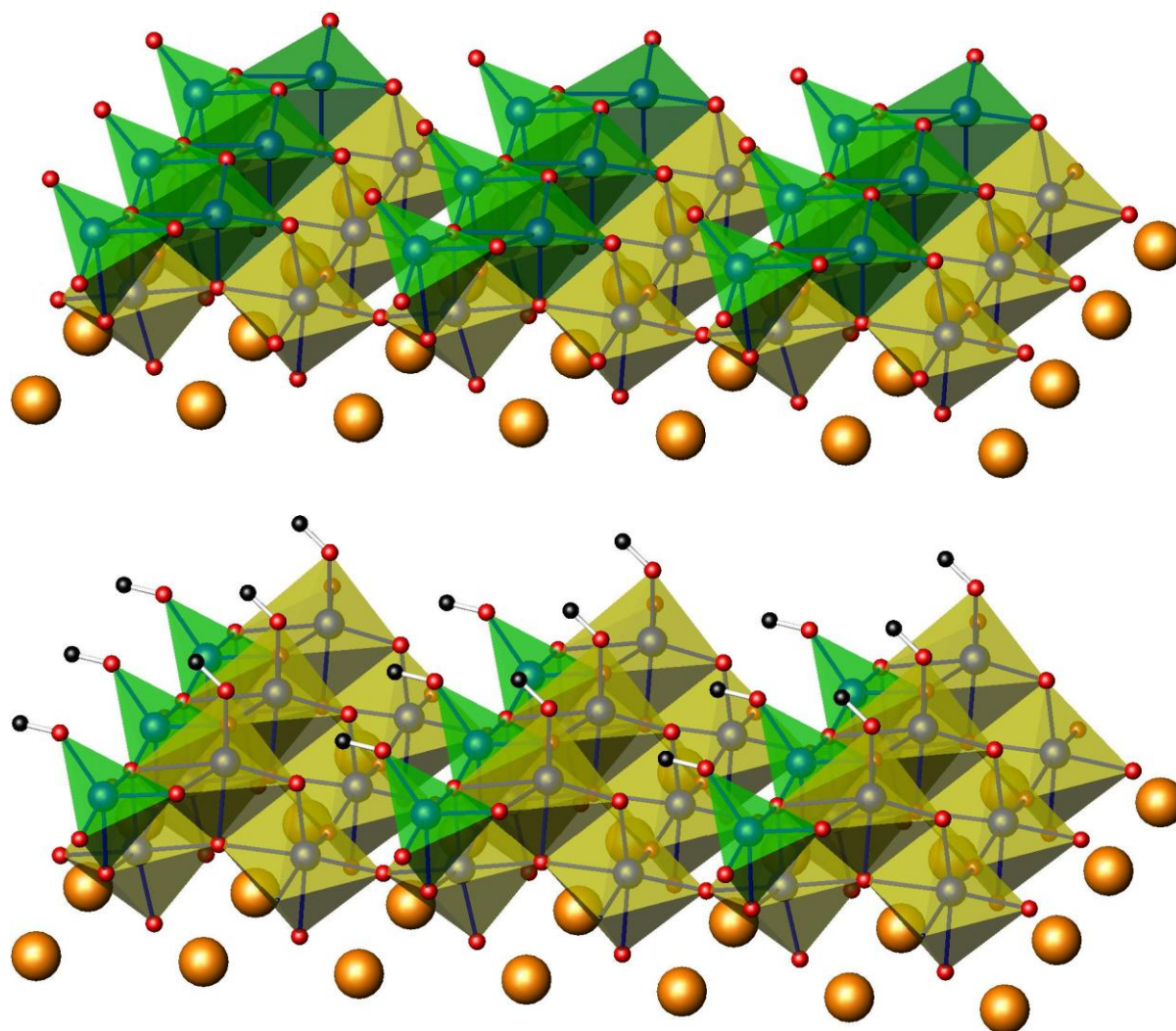


Figure 4.9: (2x1) surface structure with top bulk layer. Top: Clean surface. Bottom: H₂O saturated surface. TiO₅ trigonal bipyramids in blue, TiO₆ octahedra in yellow, strontium cations in orange, oxygen anions in red, and hydrogen cations in black.

Upon annealing the sample in 2×10^{-2} torr O₂ at 750° C for 5 hours in the gas cell, the streaking in the TED pattern went away, as did the incipient (5x1) periodicity present in the streaks. The (2x1) reconstruction became clearer (Figure 4.12). The XPS spectra showed no remaining C1s

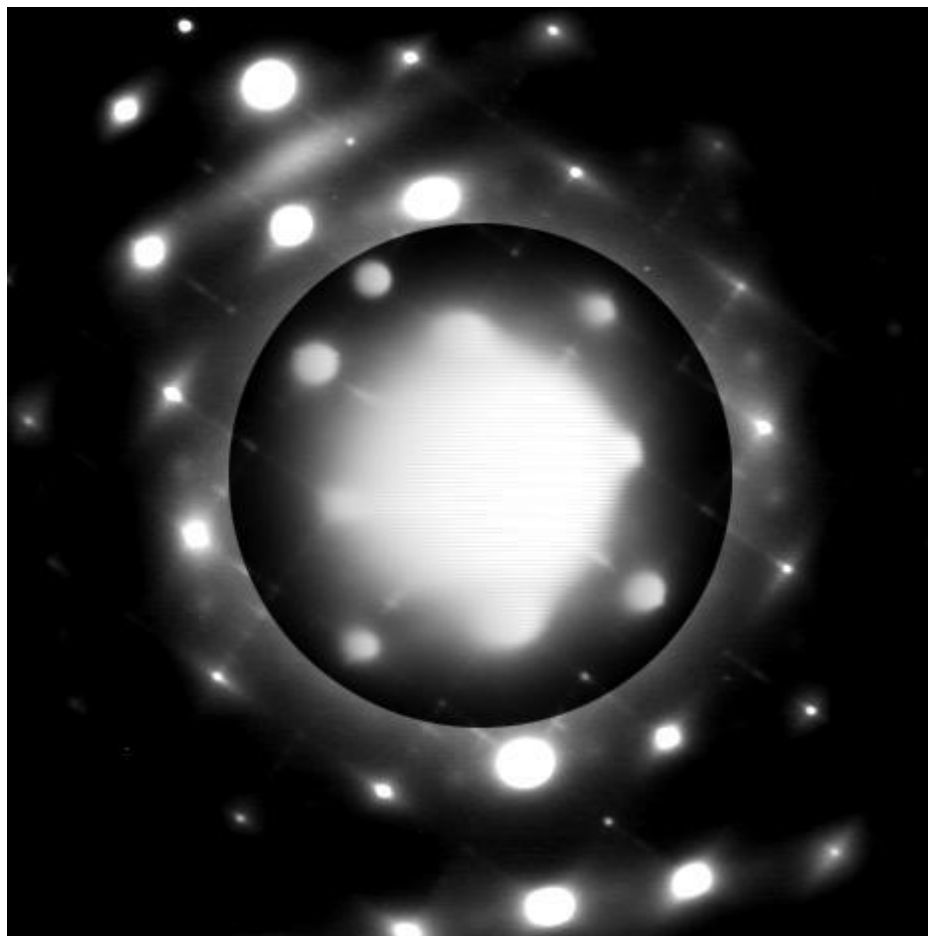


Figure 4.10: (2x1) diffraction pattern with streaks in the (100) directions nearly resolving into a (5x1) reconstruction from a sample annealed in air at 950°C for 5h.

peak. The high binding energy shoulder on the O1s peak remained, only slightly decreased in size relative to the main O1s peak (0.11) (Figure 4.11). It was slightly closer to the main O1s peak, separated by 1.6 eV on the 45° scan and 1.8 eV on the 25° scan. The ratio of the Ti2p:Sr3d peak areas also increased, from 0.99 prior to the anneal, to 1.33. Small particles were observed

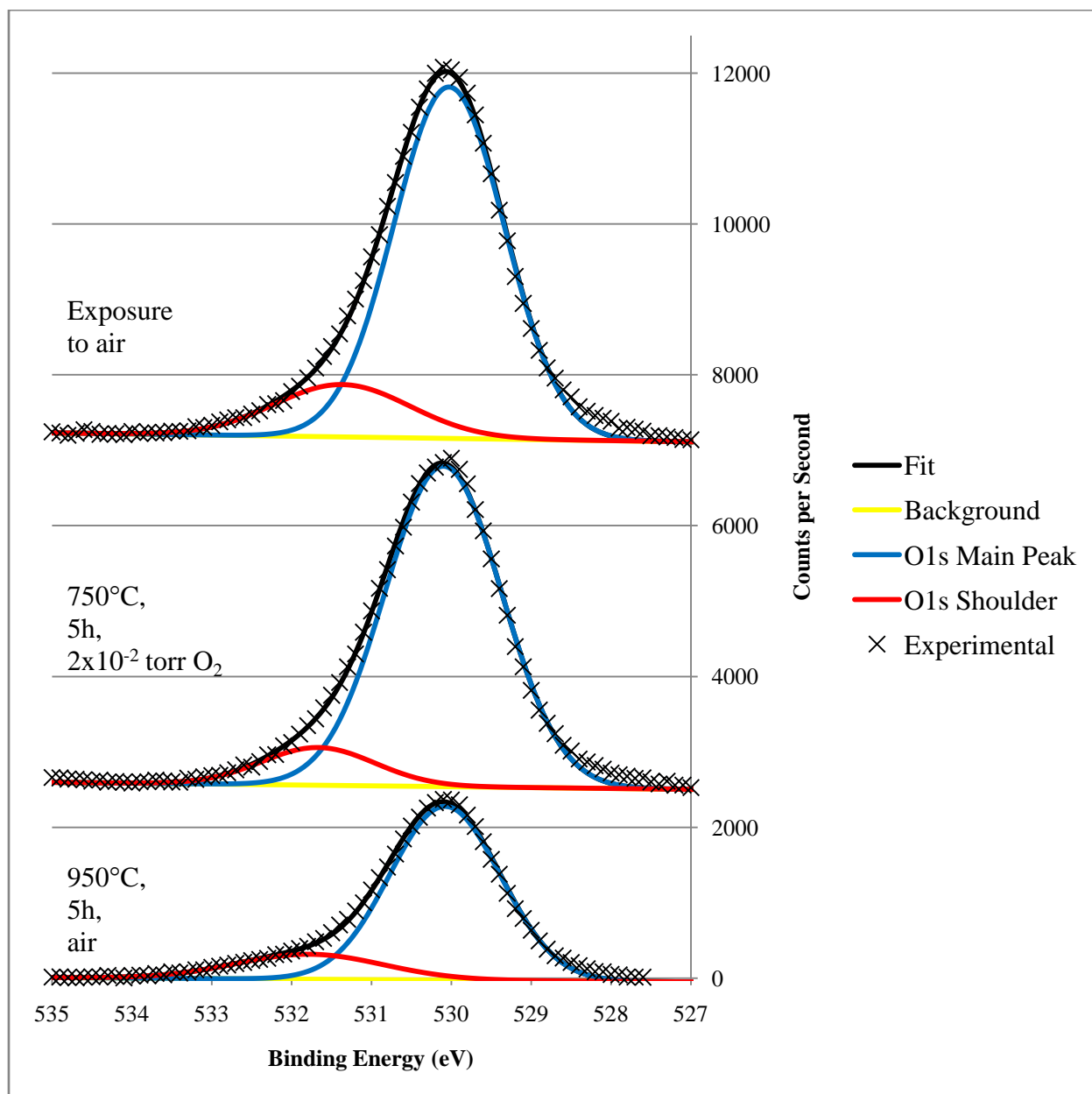


Figure 4.11: O1s peak region of the XPS spectra from a sample which began with the (2x1) reconstruction showing changes in high binding energy shoulder upon annealing and exposure to air. Counts per second for each spectra offset by a constant value for ease of viewing.

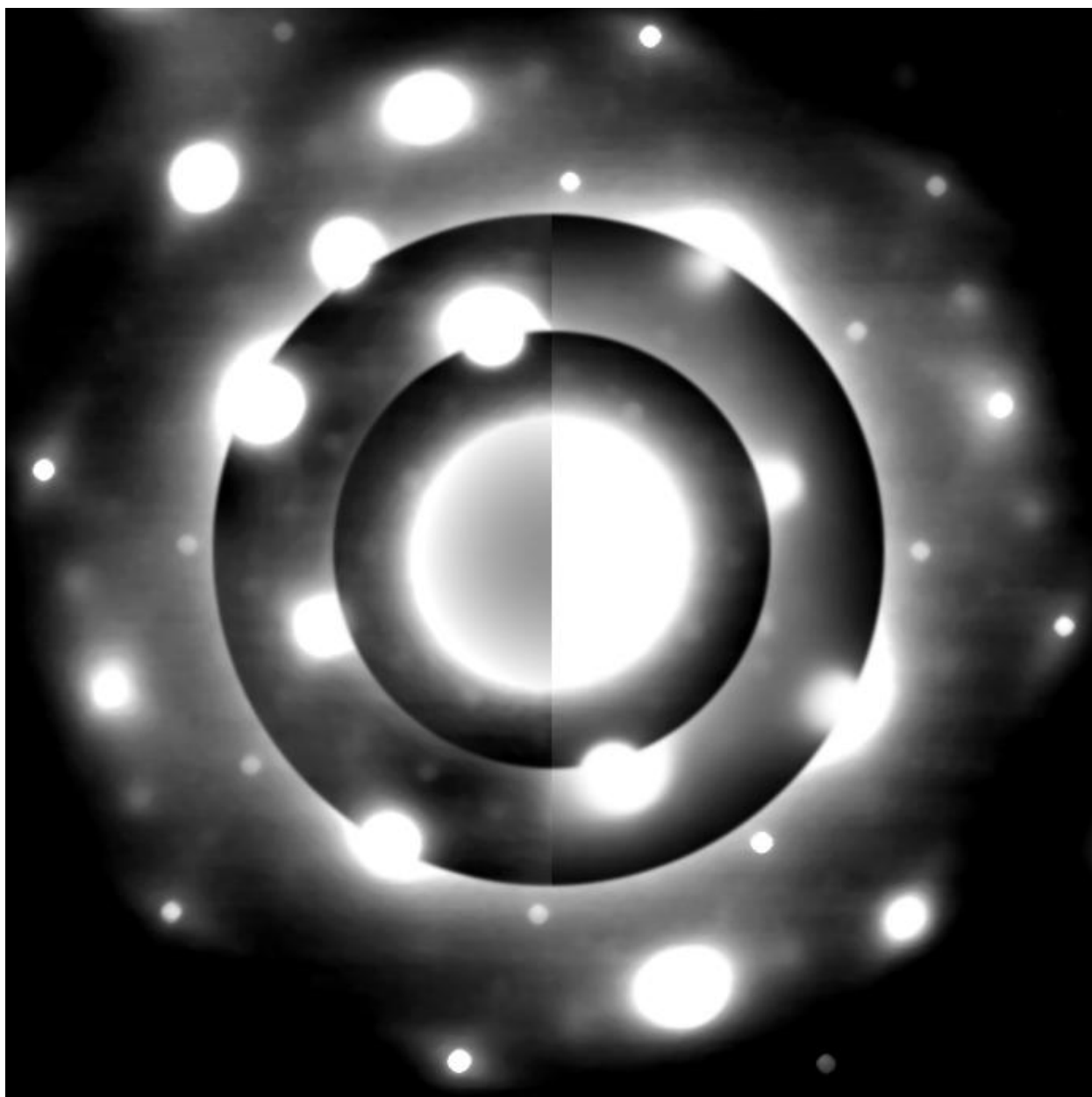


Figure 4.12: (2x1) diffraction pattern with decreased streaking and no indications of a (5x1) reconstruction following annealing at 750°C in 2×10^{-2} torr O₂. High pass filter applied to left half of image to enhance visibility of (2x1) diffraction spots.



Figure 4.13: Dark-field TEM image showing TiO_2 particles growing on the surface of SrTiO_3 .

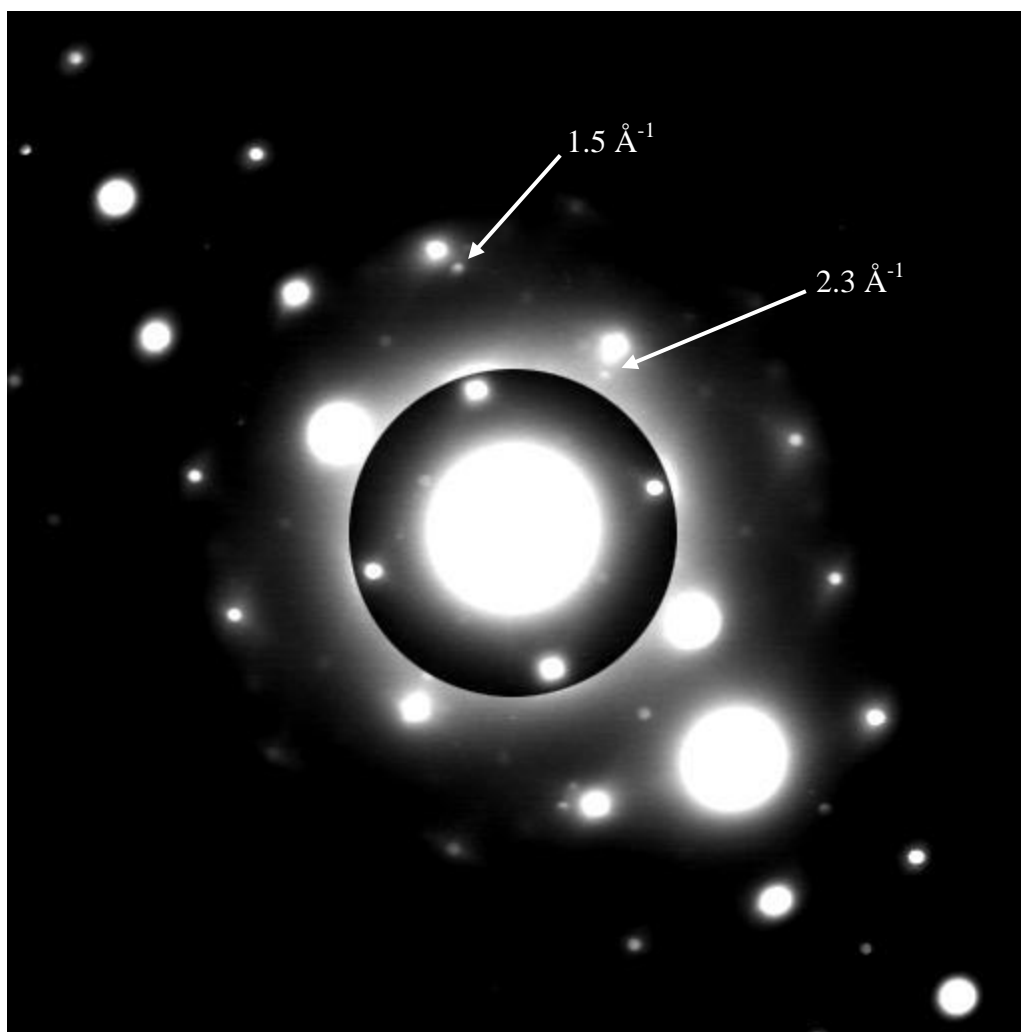


Figure 4.14: TED pattern from an area of the SrTiO₃ sample with TiO₂ particles on the surface.

to grow on the surface during annealing (Figure 4.13). The presence of interference fringes indicated that the particles were crystalline. Similar growth has been reported in the literature, with the particles identified as titanium oxide.^{74,75} TiO₂ rutile has a tetragonal structure (space group $P4_2/mnm$, # 136) with lattice constants $a = b = 4.594 \text{ \AA}$ and $c = 2.959 \text{ \AA}$. Extra spots from the small particles were measured at 1.5 and 2.3 \AA^{-1} on diffraction patterns taken from areas with

these particles (Figure 4.14). This matches well with the expected distances of the TiO₂ (002) and (200) spots of 1.479 Å⁻¹ and 2.297 Å⁻¹, respectively.

The sample was exposed to air and re-introduced to SPEAR, using a cold trap instead of baking. Upon exposing the sample to air for ~1 hour, the XPS of the sample remained largely unchanged. No C1s peak was present, indicating that the sample had not adsorbed CO₂ during the exposure to air. The high binding energy shoulder on the O1s peak grew to an area 0.18 relative to the main O1s peak (Figure 4.11). TED analysis was not completed, as the sample was dropped while attempting to introduce it into the UHV-TEM. However, it is expected that the reconstruction would not have changed as the sample was not raised above room temperature.

4.3.5: Calculations of H₂O and CO₂ on unreconstructed Sr- and Ti-terminations

A total of 20 different possible adsorbate geometries were calculated: four for H₂O on the strontium termination, six for H₂O on the titanium termination, five for CO₂ on the strontium termination, and three for CO₂ on the titanium termination. It was found that water adsorbs and dissociates on the strontium termination, but adsorbs as a molecule on the titanium termination. Carbon dioxide, on either termination, adsorbs by forming a bond between the carbon and a surface oxygen, resulting in a trigonal planar CO₃ species, with the oxygens bonding to surface cations.

On the strontium termination, one H₂O molecule adsorbs per (1x1) surface unit cell. The optimal geometry for H₂O adsorption has a hydroxide group bridging between two surface strontium atoms with the remaining hydrogen bonded to a surface oxygen (Figure 4.15). Each surface strontium is bonded to two hydroxides, and each surface oxygen is bonded to a single

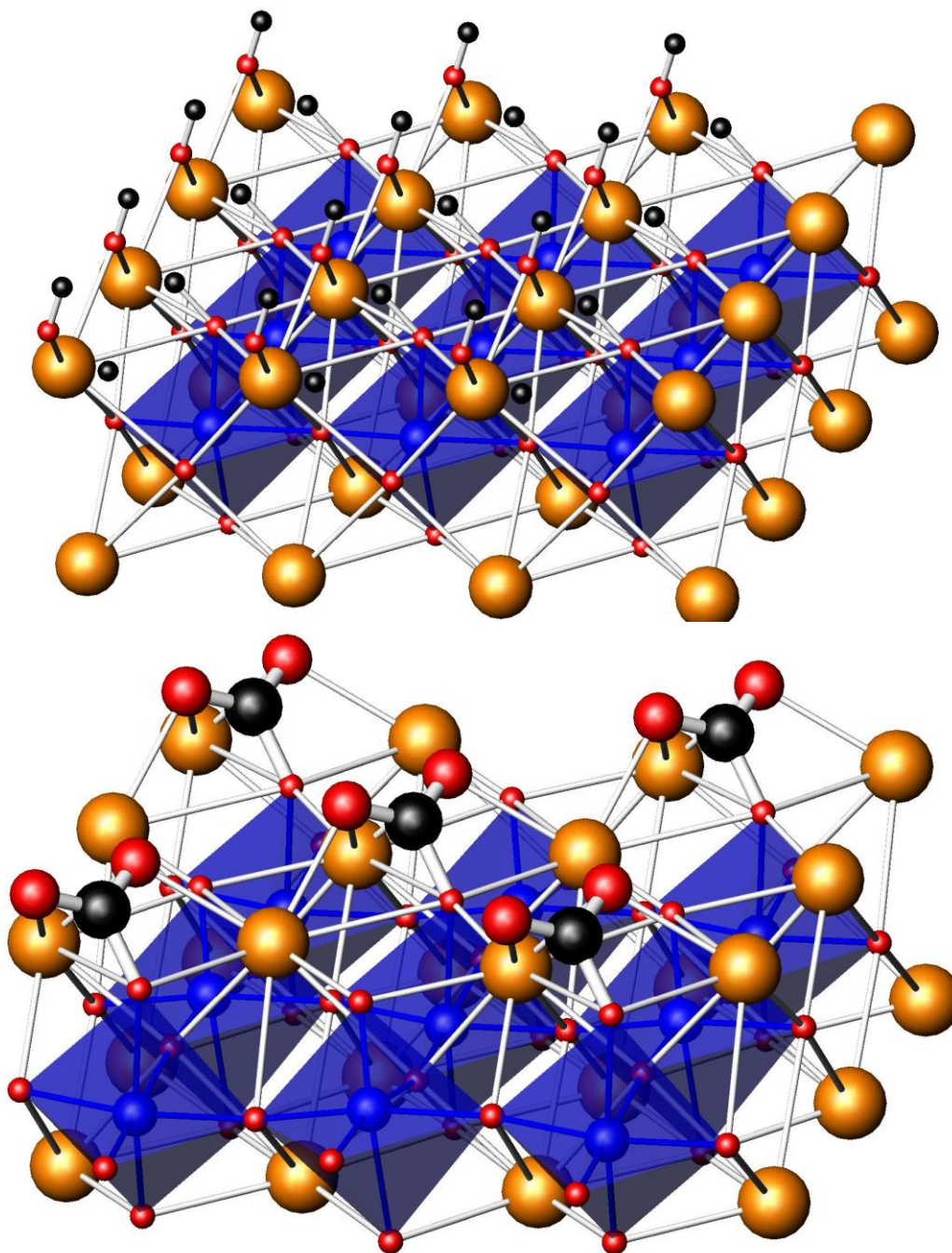


Figure 4.15: SrO (1x1) termination with H₂O (top) and CO₂ (bottom) adsorbed. Titanium octahedral in blue, strontium in orange, oxygen in red, carbon and hydrogen in black.

hydrogen. The hydrogen atom is pointed in the direction of the hydroxide group. The hydrogen of the hydroxide group points nearly straight up from the oxygen, which is shifted slightly towards the other hydrogen. The structure has an energy 0.81 eV lower than that of the clean surface plus a gaseous H₂O molecule. It is also 0.24 eV lower in energy than a H₂O molecularly adsorbed to the surface. Two different starting models arrived at essentially the same final lowest energy configuration, indicating that it is not highly dependent on starting geometry. The fact that molecularly adsorbed H₂O is 0.57 eV lower in energy than the clean surface plus free H₂O indicates that it will readily adsorb. That the dissociated water is significantly lower in energy indicates that it will then dissociate, provided that any kinetic barriers can be overcome.

On the titanium termination, one H₂O adsorbs per unit cell, but it does not dissociate. The oxygen binds to the surface titanium, with the two hydrogen atoms pointed in the direction of the surface oxygen (Figure 4.16). The optimized structure has an energy 0.99 eV lower than that of the clean surface plus a gaseous H₂O molecule. This indicates that H₂O will readily adsorb on the unreconstructed TiO₂ termination.

Carbon dioxide adsorbs on the strontium termination as a CO₃ trigonal planar species. The carbon bonds to a surface oxygen, with the two oxygen atoms from the CO₂ rearranging to create the trigonal planar geometry (Figure 4.15). The oxygen atoms from the CO₂ each bridge two surface strontium atoms. Half the surface oxygen atoms are bonded to a carbon atom, while each surface strontium atom bonds to two oxygen atoms from the CO₂. The optimized structure has an energy 1.15 eV lower than that of the clean surface plus a gaseous CO₂ molecule. It is also 0.91 eV lower in energy than a CO₂ molecularly adsorbed to the surface. Two different

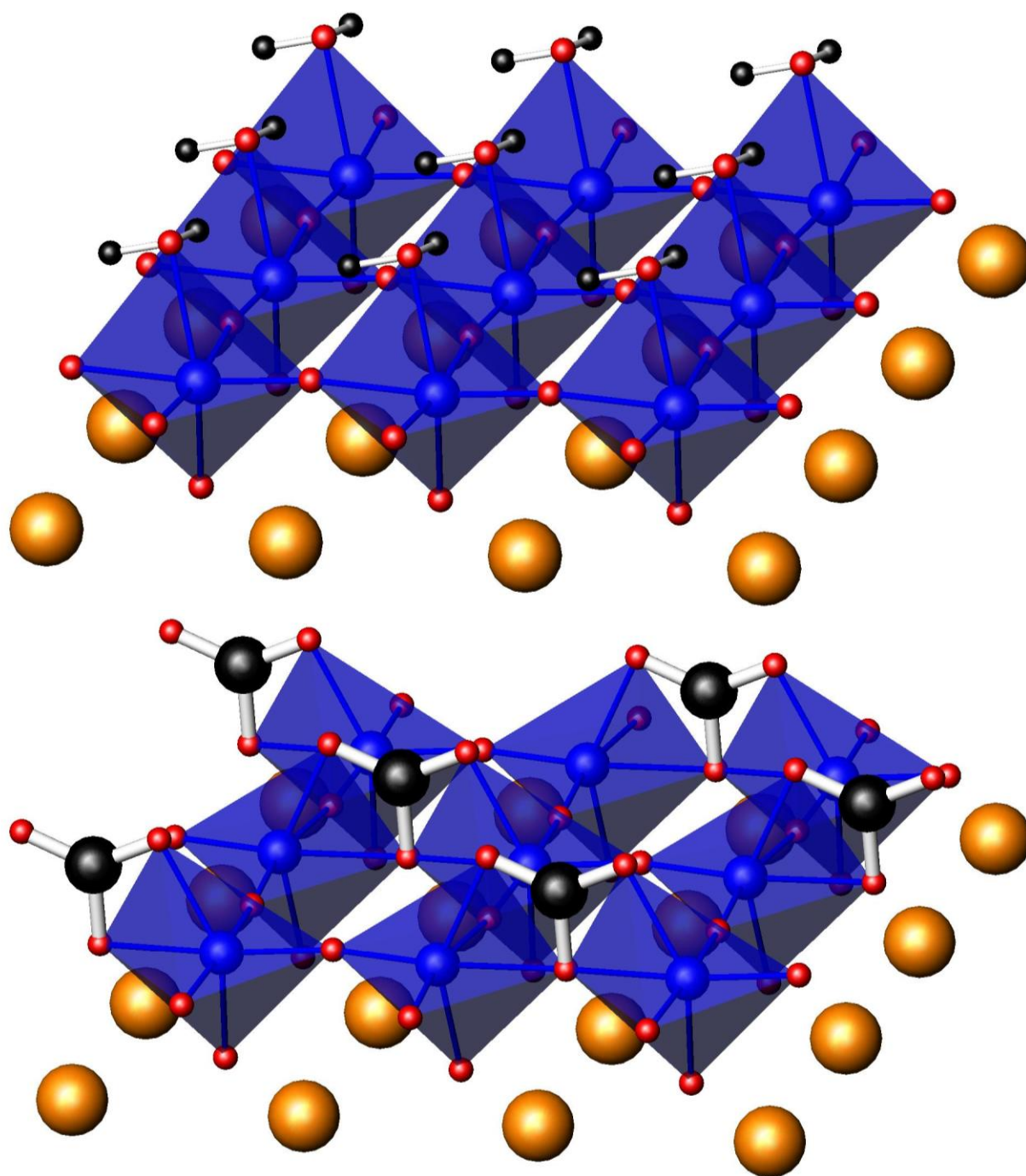


Figure 4.16: TiO_2 (1x1) termination with H_2O (top) and CO_2 (bottom) adsorbed. Titanium octahedral in blue, strontium in orange, oxygen in red, carbon and hydrogen in black.

starting models resulted in CO_2 species of similar geometry, indicating that the structure is in general the most stable configuration, independent of starting geometry. In total, one CO_2 molecule adsorbs every two (1x1) surface unit cells. Doubling the CO_2 coverage caused the energy to increase by 0.88 eV per CO_2 molecule (each only 0.27 eV lower than the clean surface plus a free CO_2 molecule). The fact that the molecularly adsorbed CO_2 was 0.24 eV lower in energy than the clean surface plus a free CO_2 indicates that it will readily adsorb to the surface. The much lower energy of the CO_3 species indicates that it will be the end result of such an interaction, any kinetic barriers notwithstanding.

Carbon dioxide adsorbs on the titanium termination as a CO_3 trigonal planar species as well. The carbon bonds to a surface oxygen, with the two oxygen atoms from the CO_2 rearranging to create the trigonal planar geometry (Figure 4.16). Each then bonds to a surface titanium. Each surface titanium is bonded to one carbon, but only one quarter of the surface oxygen are bonded to an oxygen from the CO_2 . In total, one CO_2 adsorbs for every two (1x1) unit cells. Such a coverage is saturated, as every surface titanium has its coordination sphere fully occupied (distorted but full octahedral coordination). The optimized structure has an energy 1.22 eV lower than the clean surface plus a free CO_2 molecule. Molecularly adsorbed CO_2 is 0.21 eV lower in energy than the clean surface plus a free CO_2 molecule (1.01 eV higher in energy than the CO_3 trigonal planar species). This indicates that, again, CO_2 will readily adsorb to the surface, and then should reconfigure to the CO_3 species, unless prevented by kinetic barriers.

The DFT calculations do not take entropy into account, and gaseous molecules will have greater entropy than molecules adsorbed onto a surface. This would make the adsorbed species somewhat less favored than the numbers from the calculations suggest. The gas phase entropy of CO_2 and H_2O are known to be $213.8 \text{ J/mol}\cdot\text{K}$ and $188.8 \text{ J/mol}\cdot\text{K}$, respectively.⁷⁶ As the entropy of the molecules adsorbed on the surface is not known, the actual difference in free energy at a given temperature cannot be calculated. The temperature at which the free molecule would be equal in free energy (DFT calculated energy plus entropy correction) to the DFT calculated energy of the adsorbed species was calculated to be 412K and 507K for H_2O on the strontium and titanium terminations and 520K and 552K for CO_2 on the strontium and titanium terminations, respectively. This temperature is an estimation of what temperature would be required to remove the adsorbates from the surfaces.

However, the real temperature at which the adsorbed species will be equal in free energy to the free molecules is higher, as there will be a non-zero entropy term in the adsorbed molecules' free energy. To get an idea of how much higher this may be, we can calculate at what temperature the adsorbates would no longer be favorable if the adsorbed species had half the entropy of the bulk species. Note that this is almost certainly an overestimation, and should be taken not as an approximate value but as an upper bound. In such a case, the temperature at which a free molecule would be equal in free energy to the adsorbed species would be 825K and 1014K for H_2O on the strontium and titanium terminations, and 1040K and 1104K for CO_2 on the strontium and titanium terminations, respectively. Preliminary calculations of the vibrational frequencies of the adsorbed species indicate that the adsorbed H_2O species have significantly

higher energy vibrations than the CO_2 species. Thus for the adsorbed H_2O species this may be a reasonable upper boundary for the thermodynamic stability of an adsorbed species. For species which are rigidly bound, such as a CO_3^{2-} group, this is probably a significant overestimation. A more reasonable upper boundary might be to consider if the adsorbed CO_3^{2-} species had one quarter the entropy of the free CO_2 molecule. In such a case, an adsorbed and a free CO_2 molecule will be equal in energy at 693K and 737K on the strontium and titanium terminations, respectively.

Both H_2O and CO_2 bind more strongly to the titanium termination than to the strontium termination. On both terminations, the CO_2 binds more strongly than the H_2O . The difference on the titanium termination is smaller than on the strontium termination. When the entropy of the gaseous molecules is considered, the difference between H_2O and CO_2 on the titanium termination is less than half of the difference between H_2O and CO_2 on the strontium termination. This may be decreased further or even reversed, depending on the entropy of the adsorbed species. However, it seems likely that there could be competition between H_2O and CO_2 as to which will bond to the surface.

4.3.6: Desorption calculations for H_2O on the (2x1) structure

For the (2x1) structure, where wet and dry models both exist, a temperature at which the adsorbed species will be equal in free energy to a gaseous species can be estimated from the known gas phase entropy. An H_2O molecule dissociated on the (2x1) structure was calculated to be 1.44 eV lower in energy per H_2O molecule than a gaseous H_2O molecule and a dry (2x1) structure. Assuming no entropy for the adsorbed species, the energy of the adsorbed and free

H₂O molecules will be equal at 738K. If the adsorbed species had half the entropy of the free molecule, then they would be equal in energy at 1475K.

4.3.7: Bond valence sums for structural models

Bond valence sums were calculated for all structures considered for which atomic level models are available: the unreconstructed titanium and strontium terminated (1x1) surfaces, both clean and with CO₂ and with H₂O adsorbed; the (2x1) surface, both clean and with H₂O adsorbed; and the clean c(4x2) structures. No accurate models for the ($\sqrt{13}\times\sqrt{13}$)-R33.7°, the c(4x2) structure with H₂O adsorbed, or for any reconstruction with CO₂ adsorbed, were available.

The unreconstructed strontium termination is significantly undercoordinated, and adsorbing either CO₂ or H₂O improves the bond valence sums significantly (Table 4.1). The surface instability index of the clean surface is high at 0.29, mainly due to the under-coordinated surface strontium and oxygen (for strontium BVS = 1.78 and for oxygen BVS = -1.50). The coordination of the surface strontium and oxygen is increased and the surface instability is consequently lowered by adsorbing either CO₂ (SII = 0.11, BVS = 2.21 or 2.22 for strontium and BVS = -2.17 or -1.96 for oxygen) or H₂O (SII = 0.13, BVS = 2.02 for strontium and BVS = -2.15 for oxygen).

The unreconstructed titanium termination is less undercoordinated than the strontium termination (SII = 0.24, for titanium BVS = 3.75 and for oxygen BVS = -1.88). The under-coordination is also improved by the adsorption of either CO₂ or H₂O (Table 4.2), but the overall

Table 4.1: Bond valence sums and multiplicity (per (1x1) unit cell) for SrO terminated unreconstructed SrTiO₃ (100) surface, both clean and with H₂O and CO₂ adsorbed, showing surface and top two bulk layers.

SII	Clean 0.29			H ₂ O 0.13			CO ₂ 0.11			
	Atom	Mult.	BVS	Atom	Mult.	BVS	Atom	Mult.	BVS	
Surface				H	1	1.01	C	0.5	3.87	
				H	1	1.03	O	0.5	-2.00	
				O	1	-1.91	O	0.5	-2.00	
		Sr	0.5	1.78	Sr	1	2.02	Sr	0.5	2.21
		Sr	0.5	1.78	O	1	-2.15	Sr	0.5	2.22
		O	0.5	-1.50				O	0.5	-2.17
		O	0.5	-1.49				O	0.5	-1.96
1 st Bulk Layer	Ti	0.5	4.13	Ti	1	4.26	Ti	0.5	4.05	
	Ti	0.5	4.12	O	1	-2.13	Ti	0.5	4.01	
	O	0.5	-2.22	O	1	-2.14	O	0.5	-2.02	
	O	0.5	-2.22				O	0.5	-2.07	
	O	0.5	-2.22				O	0.5	-2.02	
	O	0.5	-2.22				O	0.5	-2.07	
2 nd Bulk Layer	Sr	0.5	2.09	Sr	1	2.18	Sr	0.5	2.12	
	Sr	0.5	2.09	O	1	-2.16	Sr	0.5	2.08	
	O	0.5	-1.98				O	0.5	-2.23	
	O	0.5	-1.98				O	0.5	-1.99	

coordination is better for adsorbed H₂O (SII = 0.15, titanium BVS = 4.13, oxygen BVS = -1.98) than for adsorbed CO₂ (SII = 0.21, titanium BVS = 4.21, oxygen 2.04 > BVS > -2.41).

The c(4x2) structure⁷² is reasonable (SII = 0.17) (Figure 4.1 and Table 4.3). There is a slight over-coordination at the surface, particularly for the oxygen shared by all four titanium polyhedral (BVS = -2.56). No atomic scale model of the surface with adsorbates is available.

Table 4.2: Bond valence sums and multiplicity (per (1x1) unit cell) for TiO₂ terminated unreconstructed SrTiO₃ (100) surface, both clean and with H₂O and CO₂ adsorbed, showing surface and top two bulk layers.

SII	Clean 0.24			H ₂ O 0.15			CO ₂ 0.21		
	Atom	Mult	BVS	Atom	Mult	BVS	Atom	Mult	BVS
Surface	Ti1 O11	1 2	3.75 -1.88	H	1	1.01	C	0.5	3.91
				H	1	1.02	O	0.5	-1.89
				O	1	-2.23	O	0.5	-1.91
				Ti	1	4.13	Ti	0.5	4.2
				O	1	-1.97	Ti	0.5	4.22
				O	1	-1.99	O	0.5	-2.04
				O			O	0.5	-2.05
				O			O	0.5	-2.41
				O			O	0.5	-2.28
				O			O	0.5	-2.28
1 st Bulk Layer	Sr5 O8	1 1	2.25 -2.37	Sr	1	2.22	Sr	0.5	2.26
				O	1	-2.26	Sr	0.5	2.33
				O			O	0.5	-2.15
				O			O	0.5	-2.16
2 nd Bulk Layer	Ti2 O12	1 2	4.23 -2.05	Ti	1	4.23	Ti	0.5	4.15
				O	1	-2.08	Ti	0.5	4.15
				O	1	-2.11	O	0.5	-2.09
				O			O	0.5	-2.09
				O			O	0.5	-2.1
				O			O	0.5	-2.07

The clean (2x1) surface (Figure 4.9)²⁹ is also under-coordinated (SII = 0.22, titanium BVS = 3.92 or 3.65, oxygen BVS = -1.74, Table 4.3). Adsorption of H₂O⁷⁰ improves the coordination of the surface atoms significantly (SII = 0.12, titanium BVS = 4.02 or 4.13, oxygen

Table 4.3: Bond valence sums and multiplicity (per (1x1) unit cell) for (2x1) (both clean and hydroxylated) and c(4x2) structures, showing surface and top two bulk layers.

SII	Clean (2x1)			Hydroxylated (2x1)			c(4x2)		
	Atom	Mult.	BVS	Atom	Mult.	BVS	Atom	Mult.	BVS
Surface				H	0.5	1.00			
				H	0.5	0.99			
				O (H ₂ O)	0.5	-2.01			
	Ti	0.5	3.92	Ti	0.5	4.13	Ti	0.5	4.07
	Ti	0.5	3.65	Ti	0.5	4.02	Ti	0.5	4.03
	O	0.5	-1.74	O	0.5	-2.04	O	1	-1.93
	O	0.5	-1.74	O	0.5	-2.16	O	0.25	-2.20
	O	0.5	-2.25	O	0.5	-2.13	O	0.5	-2.02
1 st Bulk Layer	O	0.5	-2.02	O	0.5	-2.04	O	0.25	-2.56
	Ti	0.5	4.11	Ti	0.5	4.10	Ti	0.25	4.35
	Ti	0.5	4.25	Ti	0.5	4.18	Ti	0.5	4.02
	O	0.5	-2.14	O	0.5	-1.82	Ti	0.25	4.30
	O	0.5	-1.94	O	0.5	-2.18	O	0.5	-2.03
	O	0.5	-1.93	O	0.5	-2.08	O	0.5	-2.15
2 nd Bulk Layer	O	0.5	-2.40	O	0.5	-2.16	O	0.5	-2.20
							O	0.5	-1.94
	Sr	0.5	2.30	Sr	0.5	2.26	Sr	1	2.23
	Sr	0.5	2.42	Sr	0.5	2.38	O	0.25	-2.18
			O	0.5	-2.16	O	0.5	-2.23	
			O	0.5	-2.30	O	0.25	-2.09	

BVS = -2.04 or -2.16, Table 4.3). The bond valence sums for the adsorbed oxygen and hydrogen atoms closely approximate the expected values (hydrogen BVS = 0.99 and 1.00, oxygen BVS = -2.01).

4.4: Discussion

Previous DFT calculations⁷⁰ have indicated that water adsorbs and dissociates on the (2x1) structure very favorably. This is confirmed by bond valence sum calculations, where the bonding of an OH⁻ and H⁺ to the most undercoordinated atoms in the initial structure greatly improves the surface instability index (Table 4.3). The c(4x2) is more stable as a dry surface in DFT calculations.⁷⁰ The bond valence sums show that there are no undercoordinated species at the surface which are likely to adsorb water (Table 4.3). This agrees well with the current XPS and annealing study, where water desorbed easily from the c(4x2) structure, but not from the (2x1) structure. Likely some of the water was removed from the (2x1) structure upon annealing, since the OH peak dropped to about half of its original size. However, following annealing the OH peak on the (2x1), the peak was significantly larger (relative to the main O1s peak) than OH peak on the c(4x2) sample. This suggests that OH is chemically bonded to the (2x1) structure, but on the c(4x2) structure the high binding energy shoulder on the O1s peak comes from physisorbed H₂O.

There exists a (2x2) structure^{77,78} (Figure 4.17) which, like the c(4x2), is predicted to be dry, as there are no significantly under-coordinated ions to which surface species might bond. Due to the presence of a glide plane and the consequent forbidden diffraction spots, the diffraction spots will be in the same locations as those of the (2x1) structure. Without quantifying the intensities, it is impossible to distinguish the (2x1) and (2x2) structures by diffraction methods alone. Other methods, however, such as examining the hydroxyl groups on the surface, will easily distinguish the two reconstructions. In previous experiments where a

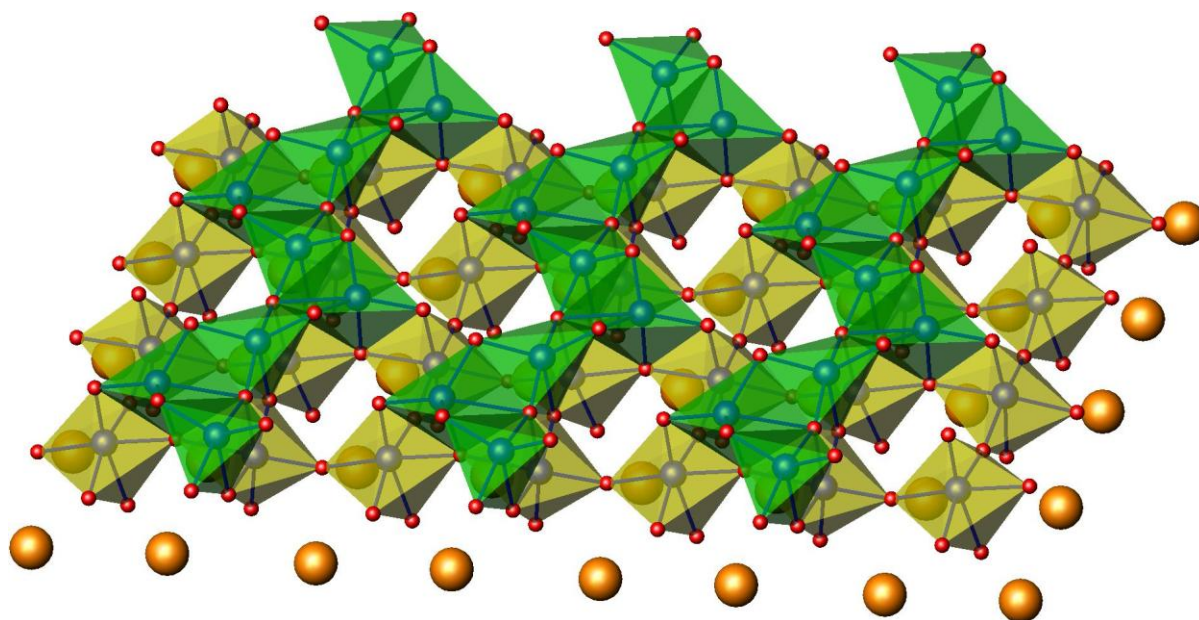


Figure 4.17: SrTiO₃ (2x2) structure with top bulk layer. TiO₅ trigonal bipyramids in blue, TiO₆ octahedra in yellow, strontium cations in orange, oxygen anions in red.

(2x1) diffraction pattern was deduced from the location of diffraction spots only, it may in fact have been a (2x2) structure. This is true as well for the previous sightings of the (2x1) diffraction pattern in this study where XPS spectra were not obtained. The finding that OH is chemically bound to the surface of the sample analyzed here via XPS indicates that this sample is, in fact, the (2x1) and not the (2x2) structure.

The $(\sqrt{13}\times\sqrt{13})\text{-R}33.7^\circ$ structure also has chemically bound OH groups, similar to the (2x1). As there is no definitive model for the $(\sqrt{13}\times\sqrt{13})\text{-R}33.7^\circ$ structure, however, it is difficult to analyze further. The (2x1), (2x2), and c(4x2) all have the same amount of excess TiO₂ at the surface (9.6 TiO₂ / nm²). All preliminary models for the $(\sqrt{13}\times\sqrt{13})\text{-R}33.7^\circ$ have less excess

TiO₂ at the surface. It is proposed, therefore, that the amount of titanium enrichment at the surface is determining whether the ($\sqrt{13}\times\sqrt{13}$)-R33.7° or one of the other reconstruction forms.

Annealing in oxidizing conditions has been seen by previous group members to lead to increased TiO₂ at the surface,⁶⁵ although the mechanism by which it occurs is still unknown. It would not be surprising if longer or hotter annealing led to increased TiO₂ surface enrichment. This would explain why the ($\sqrt{13}\times\sqrt{13}$)-R33.7° reconstruction was replaced by diffuse spots related to a (2x1) pattern, and why TiO₂ grew upon the (2x1) surface following annealing. As the ($\sqrt{13}\times\sqrt{13}$)-R33.7° structure became richer in TiO₂, it transformed into the (2x1) structure (or perhaps a combination of (2x1) and (2x2) structures). The continued presence of the OH shoulder in the XPS spectra indicates that it is not solely the dry (2x2) structure. While some of the hydroxyl groups were removed, many rearranged into a hydroxylated (2x1) structure. When the surface TiO₂ on the (2x1) was enriched through annealing, it presumably could not form a more TiO₂ rich reconstruction. (No reconstructions with more TiO₂ rich structures are known.) Instead, islands of TiO₂ formed on the surface.

Because the conditions at which the ($\sqrt{13}\times\sqrt{13}$)-R33.7° and (2x1) are formed overlap, something beyond the annealing conditions must also effect which reconstruction forms. The titanium enrichment of the surface prior to annealing is probably a primary determinant of which reconstruction forms. Three factors generally determine the amount of titanium enrichment on a sample: the initial state of the sample, the annealing time, and the annealing temperature. Annealing increases the titanium enrichment, with higher temperatures leading to faster rates of enrichment. As the titanium enrichment increases, first a ($\sqrt{13}\times\sqrt{13}$)-R33.7° and then a (2x1)

structure forms. The initial titanium enrichment prior to annealing will determine what additional amount of enrichment is necessary to obtain each structure.

The difference in the titanium enrichment of the initial sample can most likely be traced back to the Ar^+ ion sputtering. During the final stage of sample preparation, Ar^+ ions are used to sputter the sample and do not necessarily effect each sample equally. Preferential sputtering of different elements can occur due to the differences in atomic mass and the surface binding energy of the different elements. Additionally, the sputter yield depends on the incidence angle, the energy of the Ar^+ ions, and the orientation of the sample. A grazing incidence angle is preferred to maximize the thin area, but due to the shadowing effect of the dimple, not all samples are sputtered with the same incidence angle. Initially, 6 kV Ar^+ ions are used, and as the sample becomes thinner, the energy is decreased. The final energy was not always the same from sample to sample, nor was the ion current at a given energy or the time for which the sample was sputtered. Finally, the in-plane sample rotation was not measured, and was certainly different for each sample. All of these variations between samples could result in different initial unreconstructed surfaces for each sample. It is proposed that in future work, they should all be measured to control for these variations.

As mentioned above, the (2×1) , (2×2) , and $c(4 \times 2)$ reconstructions have equal amounts of titanium enrichment. A different mechanism must therefore be responsible for determining which of these reconstructions if formed. The greatest difference in the chemistry of these structures lies in the hydroxyl groups on the surface. On $c(4 \times 2)$ surface, the high binding energy shoulder on the O1s peak is removed by annealing at 300°C , indicating that it is likely from

physisorbed H_2O . The (2×1) reconstructions, on the other hand, has chemisorbed hydroxides, which are not removed by annealing at temperatures as high as 750°C . In the models of each, the dissociated H_2O is bonded to some of the most under-coordinated surface species, and improves the coordination of the surface structure. Unlike the (2×1) reconstruction, the $c(4\times 2)$ has no under-coordinated species on the surface to which adsorbates would be likely to strongly bind. This suggests that hydroxide may be playing an important role in surface structure formation. Similar phenomena have recently been seen on the MgO and NiO (111) surfaces.^{57,58} If hydroxide is influencing surface structure formation, that fact would go a long way towards explaining why different reconstructions are sometimes observed under substantially equivalent preparation conditions.

It is expected that the unreconstructed surface will be hydroxylated. The calculations of CO_2 and H_2O on the unreconstructed surfaces show that both CO_2 and H_2O bond favorably to either termination. On the strontium termination, CO_2 binds significantly more strongly than H_2O . This is supported by the bond valence sums, where CO_2 adsorption improves the surface instability index significantly more than does H_2O adsorption. On the titanium termination the H_2O bonds nearly as strongly as CO_2 . The bond valence sums indicate that while CO_2 improves the surface instability index somewhat, H_2O improves it far more. Considering the entropy of the adsorbed species, it is likely that H_2O is stable to a significantly higher temperature than CO_2 . Even at the upper bound, however, H_2O adsorbed on the titanium (1×1) termination would only be stable to 1014K (741°C), significantly lower than the annealing temperatures used.

Up until some temperature (for the titanium (1x1) surface $T > 234^{\circ}\text{C}$, but probably $T < 741^{\circ}\text{C}$), H_2O will be thermodynamically more favorable as a species adsorbed on a surface than as a free molecule. Above that temperature, not all H_2O would be immediately removed. As H_2O are removed, the remaining H_2O may exhibit increased thermodynamic stability. This likely explains why the OH shoulder in the XPS spectra decreased but did not disappear on the (2x1) sample following annealing in SPEAR. For the unreconstructed terminations, however, H_2O does not bond particularly strongly, and at the annealing temperatures used it is probable that a dry surface plus gaseous H_2O is lower in energy than the (partially) hydroxylated surface. If adsorbed H_2O is thermodynamically unstable on the unreconstructed surface at the annealing temperatures used, then the initially adsorbed species will not lead to a hydroxylated reconstruction.

The surface will not be completely dry when annealed in air (or any other moist atmosphere), even at elevated temperatures, as long as sites to which H_2O can adsorb remain. Instead, a dynamic equilibrium will be established. The adsorbed H_2O molecules will be leaving the surface at some rate, which will depend on the concentration of adsorbed H_2O molecules. (For molecularly adsorbed H_2O it is most likely first order dependent upon $[\text{H}_2\text{O}]$, while for dissociated $\text{OH}+\text{H}$ it may be first order dependent on either $[\text{OH}]$ or $[\text{H}]$, or second order dependent on $[\text{OH}][\text{H}]$. While this dependence will be critical for a quantitative assessment, a qualitative assessment can be made without precise knowledge of the rate law.) At the same time, molecular H_2O from the atmosphere will collide with the surface, forming adsorbed H_2O or $\text{OH}^- + \text{H}^+$. This rate will be dependent on the concentration of H_2O in the annealing atmosphere

and on the number of sites on the surface at which H₂O can adsorb. As H₂O desorbs from the surface, the concentration of adsorbed H₂O on the surface will decrease, and therefore so will the rate at which H₂O leaves the surface. Additionally, the number of locations at which atmospheric H₂O can bind will increase, and consequently so will the rate at which atmospheric H₂O forms adsorbed H₂O. (Any changes in the rate of adsorption due to an increase in the atmospheric H₂O concentration will be minimal for an open system.) As H₂O desorbs, the rate of desorption will decrease and the rate of adsorption will increase. At some point these rates will become equal, and a dynamic equilibrium will be reached. The position of the equilibrium cannot be determined without greater knowledge of the rate laws and the activation energy. However, some further assessments are possible.

The hydroxyl coverage during annealing will be in large part dependent on the rate at which gaseous H₂O molecules strike the surface. Calculating the rate at which gaseous particles collide with the sample surface is straightforward. The root mean square velocity of a gaseous particle is:

$$v_{rms} = \sqrt{\frac{3 \cdot k \cdot T}{m}}$$

while the average velocity of a gaseous particle is:

$$v_{avg} = \sqrt{\frac{8 \cdot k \cdot T}{\pi \cdot m}}$$

where k is Boltzmann's constant ($1.38 \times 10^{-23} \text{ kg} \cdot \text{m}^2/\text{s}^2 \cdot \text{K}$), T is the temperature in Kelvin, and m is the molar mass of the particle. Using a molar mass of 28.97 g/mol (0.02897 kg/mol, the molar

mass of dry air) and a temperature of 950°C (1223K) the average speed of an air particle is 945 m/s. The time (in seconds) between collisions of a particle with a unit area can then be derived from standard pressure calculations to be:

$$t = \frac{m \cdot v_{\perp}}{A \cdot P \cdot N}$$

where v_{\perp} is the velocity perpendicular to the surface (in m/s), A is the area (in m^2), P is the pressure (in $\text{kg/m}\cdot\text{s}^2$), and N is Avogadro's number (6.022×10^{23} particles/mole). v_{\perp} will be $v_{\text{avg}} \cdot \cos(45^{\circ}) = 669 \text{m/s}$ at 950°C, the area of a (1x1) unit cell is $(3.905 \times 10^{-10} \text{ m})^2 = 1.525 \times 10^{-19} \text{ m}^2$, and atmospheric pressure is $101,325 \text{ kg/m}\cdot\text{s}^2$. An air particle will therefore strike each (1x1) unit cell every $2.08 \times 10^{-9} \text{ s}$ at 950°C and atmospheric pressure. 4.80×10^8 air molecules will strike each (1x1) unit cell every second.

The frequency with which a water molecule strikes the surface will also depend on the humidity of the air at the time of the anneal. This can vary greatly. For example, 100% relative humidity at 35°C (95°F) will have an absolute humidity of 5.55%, while 10% relative humidity at -15°C (5°F) will have an absolute humidity of 0.02%, a difference of more than two orders of magnitude. The numbers chosen as illustration are possible in summer and winter, respectively, but are not common. They should be viewed as boundaries of what would be possible when annealing in air. However, differences in atmospheric humidity of an order of magnitude are quite common and differences of two orders of magnitude are possible.

At these two extremes, 2.67×10^7 and 1.13×10^5 atmospheric H_2O molecules will strike each (1x1) unit cell per second, respectively. Many of the molecules will not stick to the surface, striking in the wrong geometry or with insufficient kinetic energy, although at 950°C most will

have sufficient kinetic energy. The sticking coefficient will be the same in both cases, meaning that the rate of H₂O adsorbing will be proportional to the absolute humidity. Thus the amount of H₂O adsorbed on the surface at equilibrium will also be proportional to the absolute humidity.

With $\sim 10^7$ H₂O molecules striking each (1x1) unit cell per second, the surface may well be sufficiently hydroxylated that it will form a structure which stabilizes adsorbed hydroxyl groups. Formation of a dry structure, such as the c(4x2), may only be possible in significantly drier atmospheres. To form a dry structure, there would have to be sufficiently few hydroxyl groups so that the surface would rearrange to a structure on which adsorbed hydroxyl groups are not highly stabilized. Only after the rearrangement occurred and there were no sites at which H₂O would adsorb could the surface become completely dry. During the course of this study, the c(4x2) structure was only found on samples annealed in the colder months, when humidity would have been lower. For example, the c(4x2) sample which is discussed in detail in this chapter was annealed on November 23, 2009. However, the atmospheric conditions were not recorded, and therefore the formation of dry reconstructions only in particularly dry atmospheres cannot be confirmed at this time from these experimental results.

Perhaps more convincing is the fact that in previous studies when the c(4x2) structure was observed reproducibly in this group, it was normally (although not always) annealed in an atmosphere of flowing O₂ rather than air.^{65,72} Although O₂ from a gas cylinder will not be completely void of H₂O, especially when viton seals are used to connect the gas line to the tube furnace, it will be significantly drier than air. In such conditions, the amount of hydroxide on the surface will be far less at the point of dynamic equilibrium. A structure can then form which is

less stable for adsorbed H_2O but more stable without hydroxyl groups. This does not mean that the (2x1) structure cannot be formed in a dry atmosphere. Indeed, it is likely to do so if the temperature is low enough that the initial hydroxyl groups will not desorb.

The (2x2) structure is in some ways an intermediate structure between the (2x1) and c(4x2) structures (Figure 4.18). By moving a single titanium cation per (2x2) unit cell to a nearest neighbor vacant cation site, either the (2x1) or c(4x2) structure can be created. Conversely, to go between the (2x1) and c(4x2) structures by moving titanium cations to nearest-neighbor vacant cation sites would require two such steps, the first of which would form the (2x2) structure. It is thus unlikely that a wet (2x1) structure would transition directly to a c(4x2) even if the hydroxyl groups were removed. More likely, if all the hydroxyl groups were

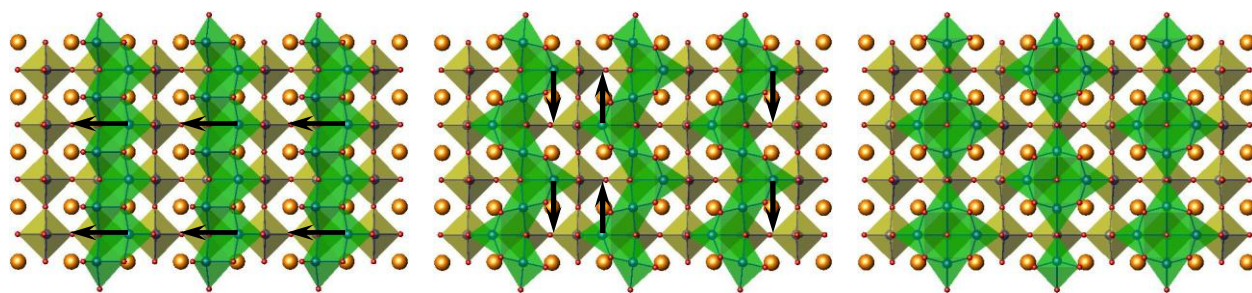


Figure 4.18: Proposed pathway for transformation of (2x1) (left) to c(4x2) (right) with (2x2) (middle) as intermediate. To change from the (2x1) to (2x2) structures, sufficiently few hydroxyl groups must be present to allow the titanium cations to arrange into a structure which is less favorable for hydroxyl groups. TiO_5 trigonal bipyramids in green, TiO_6 octahedra in yellow, strontium cations in orange, oxygen anions in red. Black arrows show titanium cation movements necessary to transform to the next structure.

removed, a (2x1) structure would transform into a (2x2) structure, with the diffraction pattern remaining qualitatively the same. It is likely that any structure with an apparent (2x1) periodicity which transformed to a c(4x2) was in fact a (2x2) reconstruction, and any c(4x2) structures which transformed into a structure with an apparent (2x1) periodicity transformed instead to (2x2) structures.

The hydroxyl groups on the (2x1) structure are significantly more stable than those on the unreconstructed surfaces, as evidenced in this study and by previous DFT calculations⁷⁰. The annealing experiments in this study indicate that hydroxyl groups are bonded equally strongly to the $(\sqrt{13}\times\sqrt{13})\text{-R}33.7^\circ$ structure. Once a hydroxylated structure has formed, it will be even more difficult to remove the hydroxyl groups than it is to remove them from unreconstructed surfaces. In these experiments, annealing in a H₂O free environment at 750–800°C did not remove hydroxyl groups from the (2x1) and $(\sqrt{13}\times\sqrt{13})\text{-R}33.7^\circ$ structures. It is thus highly unlikely that annealing a sample in a moist atmosphere at slightly higher temperatures would cause a hydroxylated structure to transform to a dry structure.

Some of the hydroxide groups were probably removed when samples were annealed in SPEAR, and the $(\sqrt{13}\times\sqrt{13})\text{-R}33.7^\circ$ and (2x1) samples were no longer saturated. However, many hydroxyl groups remained on the $(\sqrt{13}\times\sqrt{13})\text{-R}33.7^\circ$ and (2x1) samples after annealing in SPEAR for prolonged periods. It is possible that the kinetics of water removal are slow enough to prevent the complete removal of hydroxide even after several hours, especially at low hydroxide coverage due to the large distances protons must cross. It will also probably require a higher temperature to remove all the H₂O from the structures than to remove only the first few

H₂O molecules. It is more likely, therefore, that while the temperature was great enough that a saturation coverage with H₂O was no longer stable, a partial H₂O coverage still was stable. Indeed, partial but incomplete removal of H₂O 750–800°C indicates that the previous estimates of desorption temperature using an adsorbed entropy of half the gaseous entropy may not be as great an overestimation as initially expected.

4.5: Conclusions

It has been shown how increasing TiO₂ enrichment can lead to a change in the observed reconstruction. It is further proposed that the initial state of the sample may influence which reconstruction is initially observed. Sample preparation, especially Ar⁺ ion milling, probably leaves different samples in slightly different states. Some samples may be richer in surface TiO₂ than others, which explains why structures of different TiO₂ richness are found following annealing under identical conditions. Water also likely plays a role in determining which reconstruction is observed. Surfaces annealed in humid air should remain sufficiently hydroxylated during annealing to result in a surface structure which is stable with the inclusion of the hydroxyl groups. Formation of a dry structure, on the other hand, requires dry conditions, ranging from air with low humidity to dry flowing oxygen, and sufficient temperature to desorb the hydroxyl groups on the sample prior to annealing.

Chapter 5:

A Chemical Approach to Surface Science:

Bond Valence Analysis of SrTiO₃ Surfaces

5.1: Introduction

For many years an outstanding scientific problem has been how to understand in a general fashion, ideally in a model with predictive power, the structure of solid surfaces. Many theories about the driving forces behind surface structure formation have been put forward, such as a minimization of “dangling bonds”²⁵ or a reduction of Coulomb forces,²⁴ and surface structures have largely been viewed as being inherently different from bulk structures. For polar surfaces in particular there has been much discussion about mechanisms for “charge compensation” and a general belief that such surface structures must be far different from the bulk (see for instance ²⁶⁻²⁸ and references therein). Recent results, however, have made it clear that surface structures share more in common with the bulk than previously believed.⁷⁹

Two fundamental approaches exist for understanding bulk structures: physical and chemical. The former approach is generally based on minimizing the potential energy of a structure, while the latter is based around understanding of localized chemical bonds. In bulk structures, these methods are viewed as complementary, rather than in opposition. The physical theories are often more rigorous, but in their rigor may miss critical insights that are readily apparent in the chemical bonding model. Each, therefore, provides useful and important information necessary for a fuller understanding of material structures.

Investigations of surface structures have been dominated by the physics approach, with relatively little attention paid to a chemical bonding approach. Considering surface structures in the manner that solid state inorganic chemistry considers bulk structures may prove to be a great companion to the physics based investigations potentially leading to predictions of what surface

structures may form and what reactions may occur, just as one can often predict what will form in bulk reactions.

One common metric for analyzing coordination and bonding in solid state chemistry is the bond valence sum (BVS) model,^{4,17,80} which is an outgrowth of Pauling's second crystal rule.⁸¹ The bond valence sum model is simple enough to be taught as part of many undergraduate chemistry curriculums, and yet powerful enough to provide a good understanding of structural chemistry and chemical bonding. A bond valence is assigned to each bond in a structure dependent only on the types of ions involved in the bond and the bond distance. Shorter bonds have higher valence, with the absolute value of the bond valence being relative to the typical bond length between the two ionic species involved.

The bond valence method stems from analyses of accurate structural data for a large number of different oxides. For all atoms the bond valence for each bond is calculated as:

$$BV = e^{\frac{R_0 - R}{b}}$$

where R is the bond distance, R_0 is a standard bond distance for the types of ions involved, and b is an empirically derived constant, normally a universal constant of 0.37. The bond valence sum for an ion is equal to the sum of the bond valences for all the bonds surrounding the ion, with positive values for cations and negative values for anions:

$$|BVS| = \sum BV$$

Lower values indicate reduced species and higher values indicate more oxidized species, while lower absolute values indicate lower coordination and higher absolute values indicate higher coordination.

A useful metric is the global instability index (GII), the root mean square of the deviation of the BVSs from the expected values for all atoms in the unit cell:

$$GII = \sqrt{\frac{\sum(BVS - BVS_0)^2}{N}}$$

Where N is the number of atoms in the unit cell and BVS_0 is the expected bond valence sum. In general, a lower global instability index is preferred, with room temperature structures typically having $GII < 0.2$.^{80,82}

The most common use for bond valence sums is as a tool for structural validation, for which there are literally thousands of examples in the literature. They are also an excellent tool for determining oxidation states of different species in a compound. They have found many other uses as well. For example they have been used to determine whether $NiAl_2O_4$ was a normal or inverse spinel,⁸³ for analyzing and interpreting incommensurate structures,⁸⁴⁻⁸⁶ electronegativities,⁸⁷ ligand field strengths,⁸⁸ nonlinear optical properties,^{89,90} and thermoluminescence,^{91,92} and have aided in the interpretation of multiple experimental methods, including NMR⁹³ and XAFS.⁹⁴

More relevant to the current analysis, the bond valence model has been used in examination of solid-liquid interfaces. Most revolve around O^{2-} anions from solution bonding to cations at a solid surface to compete the coordination sphere of the cations. Depending on solution pH, the O^{2-} may also attract one or more H^+ ions, effectively leading to O^{2-} , OH^- , H_2O or H_3O^+ bonding to the surface, with further hydrogen bonding to the solution.⁹⁵⁻⁹⁹ Additionally, it has been pointed out that the valence sum rule should be obeyed for solid, liquid, and interface,

and that the same types of bonds holding the solid or liquid together also occur at the interface, and the bond valence approach has been used to determine how strongly a solid surface interacts with a solution.¹⁰⁰ It is likely that a similar approach could prove useful in dealing with surface terminations in gaseous atmospheres or even in vacuum, where there is always some small bit of residual gas.

Despite these many demonstrated uses in bulk structures, prior to this current work, bond valence sums have only once been applied to surface structures. Ruberto et. al.^{101,102} use bond valence sums in their analysis of the polar κ -Al₂O₃ (001) and (00-1) surfaces. According to Tasker's rules, the polar κ -Al₂O₃ (001) and (00-1) surfaces should not exist.¹⁰³ For the most stable of the 10 possible κ -Al₂O₃ (001)/(00-1) cleavage planes calculated by Ruberto and coworkers, they found that the bonding essentially eliminated the polarity. They use the bond valence as a measure of the number of electrons donated from a cation (Al³⁺) to an anion (O²⁻). By considering the bonding in this manner, the electrons donated from Al³⁺ to O²⁻ in their relaxed structure lead to an essentially non-polar surface. By cleaving the κ -Al₂O₃ (001)/(00-1), the aluminum on the (00-1) surface breaks one Al–O bond which has a bond valence of 0.69, essentially transferring 0.69 electrons to the (00-1) surface. At the same time, the aluminum on the (001) surface breaks three Al–O bonds with a total bond valence of 0.99, which they see as transferring 0.99 electrons to the (001) surface. The net electron transfer, then, is 0.30 electrons lost at the (00-1) surface and gained at the (001) surface. This total charge difference of 0.60 is very close to the amount (0.69) calculated by DFT as necessary to stabilize the Tasker surface charge.

While Ruberto and coworkers do not publish the full bond valence sums for all atoms in their structure, nor do they publish the full atomic coordinates of their structure to allow for a bond valence sum calculation to be completed by others, the bond valence analysis that they publish is very significant. The fact that the κ -Al₂O₃ (001) and (00-1) are relatively stable, despite the predicted instability due to the Tasker's polarity, goes far in demonstrating that ideas of chemical bonding in general, and the bond valence model in particular, can play an important role in understanding surface structures. This result is strikingly similar to initial physics predictions which would hold that the ionic bonding model of NaCl would collapse into a singularity. The ionic solid NaCl of course does not collapse into a singularity, and the simple ionic bonding model was found to be a very robust model. Similarly the polar κ -Al₂O₃ surface was found to be relatively stable. Just as then modern physics was insufficient to describe NaCl, Ruberto and coworkers find that Tasker's rules are insufficient to describe supposedly polar surfaces. Their study demonstrates how important it is to employ chemistry in conjunction with physics, as one can often easily solve the problems that leave the other stumped.

This chapter first reviews the bond valence method and shows how bond valence sums can work in a complementary manner with DFT surface calculations, similar to how they are known to complement bulk DFT calculations. It then reviews several known and proposed strontium titanate surface structures from a bond valence perspective. (In many cases structures are published in the literature without making the full structure and atomic positions publically available, preventing a full bond valence. As a consequence, with one exception, only those few structures which have been made available publically available^{54,79} or which we have access

to^{29,60,72,104,105} are analyzed.) Finally, it examines a few cases where, similar to solid-liquid interfaces, adsorbates from the atmosphere may be interacting with oxide surfaces. This is not an exhaustive list, rather a representative set. A bond valence analysis will likely prove equally useful to quite a few other surfaces.

5.2: Methods

Bond valence sums were calculated using the KDist program in the Kalvados program suite.¹⁸ Since DFT lattice parameters often differ from true lattice parameters, the volume of structures from DFT calculations was changed isotropically to obtain the correct lattice parameter. Bonding interactions upto 3.5 Å were included in the calculation. A value of $b = 0.37$ was used in all cases. Standard R_0 values of 2.118 Å, 1.791 Å, and 1.815 Å were used for $\text{Sr}^{2+}-\text{O}^{2-}$, $\text{Ti}^{3+}-\text{O}^{2-}$, and $\text{Ti}^{4+}-\text{O}^{2-}$, respectively.¹⁹ A R_0 of 0.957 Å, the O–H bond distance in gaseous H_2O , was used for H^+-O^{2-} .

Hydrogen bonding creates a slight difficulty, requiring different parameters for R_0 and perhaps even b for H–X bonds of different lengths due to the asymmetry of the O–H...O bond, which is best modeled by different values for the short and long portions of the hydrogen bond (see Brown⁴ section 21 for more details). In the case of oxide surfaces, the problem is often reduced, as the hydrogen may be external, not participating in a hydrogen bond. Due to the many different values for R_0 presented in the literature, it is still not immediately clear which are the proper values to use. For this work, $R_0 = 0.957$ Å is used, the length of a O–H bond in gaseous H_2O , which would therefore give bond valence sums of exactly 1.00 and -2.00 for the

hydrogen and oxygen in gas phase H_2O . This was chosen as gas phase H_2O would, similar to the surfaces being considered, not have significant $\text{H}\cdots\text{X}$ interactions. For ease of calculation, $b = 0.37$ was maintained. While determining a R_0 value from a single parameter is far from an optimal solution, it does prove sufficient for the small number of hydroxylated surface structures considered here. A superior method would be determining a R_0 value from a survey of multiple known hydroxylated surfaces, but such is beyond the scope of this current work.

The global instability index (GII), surface instability index (SII), and bulk instability index (BII) were calculated by hand from the bond valence sums and the atomic multiplicities. The surface instability index and bulk instability index are calculated in the same manner as the global instability index, except that only the atoms near the surface or in the central most stoichiometric unit are included, respectively. It is not always easy to determine precisely what atoms should be included in the surface instability index calculation. Generally, in order to include any distorting effects that the surface might impart on the bulk, the surface and top bulk layer were considered. On the SrTiO_3 (110) surface, the top bulk-like O_2^{4-} layer is significantly distorted, and in the case of the (3x1) reconstruction the oxygen positions in that layer were even found from the diffraction refinement. This layer, termed a linking layer as it forms a link between the surface and the bulk, and the top SrTiO^{4+} layer were both included in the surface instability index calculations, except where specifically mentioned otherwise. On other surfaces, no such linking layer is defined, and simply the atoms that are part of the surface structure and the top bulk layer are considered.

Where needed DFT structural relaxations were performed using the all-electron Wien2k⁴⁸ code with an augmented plane wave basis set with the general gradient approximation (GGA) defined by the PBE functional.⁴³ This functional is less accurate than the TPSSh functional used in chapter 3, but is sufficient for the purposes of this analysis, as atomic positions are still well enough converged to complete a relatively accurate bond valence sum analysis.

5.3: Bond valence sums and DFT structural relaxations

The bond valence model is known to provide complementary information to both physical two body potential simulations and density functional theory calculations for bulk structures; for instance it has been used to choose appropriate potentials for two body simulations¹⁰⁶ and to correct DFT bond lengths.⁹⁷ In cases where data is available, physics based calculations, experimental observation, and bond valence analysis all tend to agree. For example, Etxebarria and co-workers found that global instability index calculations and DFT energy calculations were in quantitative agreement when analyzing strain in SrBi₂Ta₂O₉.¹⁰⁷

One clear indication that the bond valence model works well in coordination with common physical models for surface analysis is the complementary nature of bond valence sums and DFT structural convergence. As an example of this, Figure 5.1 shows data during a structural minimization of a hydroxylated MgO (111) surface structure.⁵⁷ The global instability index and energy have nearly identical trends, demonstrating that most of the energy reduction can be attributed to optimization of local bonding primarily at the surface. Note that the bulk

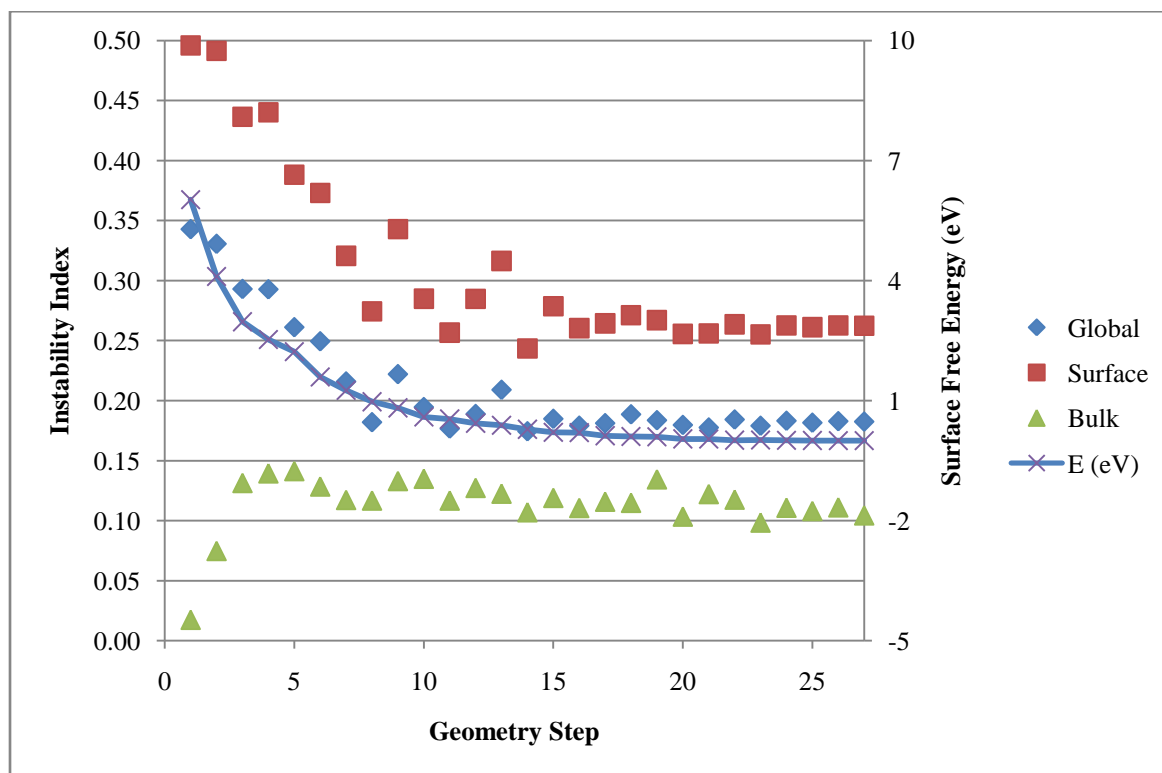


Figure 5.1: Global, surface, and bulk instability indices and energy plotted as a function of geometry optimization step. Energy is relative to the final energy.

instability index gets worse as would be expected; long-range strains from the surface rearrangements perturb the bonding in the center of the slab.

Bond valence sums can also determine whether enough slabs have been used in the DFT surface calculations. If sufficient slabs have been used, then the center will have bond valence sums the same as the bulk structure. If too few slabs have been used, the bond valence sums will differ from those of the bulk structure.

As an example, originally a model of the SrTiO₃ (110) TiO faceted structure was optimized with only 3 bulk SrTiO⁴⁺ and 4 bulk O₂⁴⁻ layers, before expanding the calculations to

the published structure with 5 bulk SrTiO^{4+} and 6 bulk O_2^{4-} .⁷⁹ In the former case, the number of layers was too few as shown from a bond valence sum analysis (Table 5.1). To further the comparison, a case with only 1 bulk SrTiO^{4+} and 2 O_2^{4-} was calculated as well. While the bond valence sums of the surface species were improved for models with smaller numbers of layers, the bulk coordination was not sufficiently close to the bulk bond valence sums. In models that

Table 5.1: Bond valence sums for models of the DFT optimized SrTiO_3 (110) TiO (1x1) surface structure using a model with different numbers of slabs. *The SII includes only the surface and linking layers, not the 1st bulk layer: the 1 SrTiO layer model was so thin that including the top (and only) SrTiO^{4+} layer would make the SII the same as the GII, and thus not a useful metric for comparison in this case.

	5 SrTiO layers		3 SrTiO layers		1 SrTiO layer	
GII	0.31		0.30		0.39	
SII*	0.57		0.44		0.43	
BII	0.10		0.19		0.22	
Layer	Atom	Bond Valence Sum	Atom	Bond Valence Sum	Atom	Bond Valence Sum
Surface	Ti	3.19	Ti	3.52	Ti	3.55
	O	-1.21	O	-1.31	O	-1.34
Linking	O	-2.06	O	-2.20	O	-2.24
1	Sr	2.16	Sr	2.19	Sr	2.24
	Ti	4.06	Ti	4.09	Ti	4.03
	O	-1.96	O	-1.96	O	-1.73
2	O	-2.12	O	-2.15		
3	Sr	2.16	Sr	2.26		
	Ti	4.16	Ti	4.21		
	O	-2.11	O	-2.16		
4	O	-2.09				
5	Sr	2.11				
	Ti	4.14				
	O	-2.07				

are too thin, the surface contains a higher portion of the total atoms, and thus improving the coordination of the surface atoms at the expense of the bulk atoms is favorable. Having bulk atoms at the central layer with bond valence sums similar to the bulk is a necessary, but not sufficient, condition for an accurate model.

Additionally, we have found that moving atomic coordinates to minimize the global instability index can significantly decrease the cost of a DFT structural relaxation, reducing the number of geometry steps by a factor of 2 in some cases. This can be done by hand, changing the position of a few atoms in a structure so they have reasonable BVS values. In principle such a refinement could be carried out in a matter of seconds on a standard laptop computer even for large structures, although at present we are not aware of a code that can do this.

5.4: BVS of model oxide surfaces

5.4.1: *SrTiO₃* (110)

The SrTiO₃ (110) surface was discussed in detail in chapter 3. To briefly review, there were 11 surface structures considered: six members of the homologous series, three stoichiometric models, and two strontium faceted models.

The series of (n×1) reconstructions is composed rings of corner-sharing TiO_{4/2} tetrahedra, with the number of tetrahedral per ring increasing in one dimension with n, until n=∞, where the length of the rings becomes infinite, and therefore the structure becomes infinite chains of corner-sharing tetrahedral.⁷⁹ Alternatively, it can be thought of as composed of chains of corner

sharing $\text{TiO}_{4/2}$ tetrahedra, which are interspersed by rings of corner sharing $\text{TiO}_{4/2}$ tetrahedra after every n tetrahedra in the chain. The pure chain ($n=\infty$) structure is under-coordinated, while the pure ring ($n=2$) structure is over-coordinated, and optimal coordination is achieved by interspersing the chains with rings at the proper interval. The structures which have the best interval between chains and rings ($n=3,4$) have both the best bond valence sums, the best surface instability indices, and are calculated to be the most stable via DFT.

For the first type of stoichiometric structure, half- O_2 (type A), the bond valence sums are close to the bulk values, regardless of which of the two specific configurations of sites the top oxygen occupy. Both had the same surface instability index of 0.21. This implies that structure terminated by a half-filled O_2 layer might be reasonable, and further that it is not highly dependent on the ordering of the missing O. The missing O could potentially be randomly spread out along the surface, which might be expected for a cleaved sample which has not had the opportunity to reconstruct to a more favorable structure. For the much higher energy half- O_2 (type B) structure, the bond valence sums differ significantly from the expected values, with some being over-coordinated and others under-coordinated. The surface instability index is nearly double that of the half- O_2 (type A) surfaces ($\text{SII} = 0.41$). This poor coordination agrees Heifets and coworkers¹⁰⁸ calculations that the half- O_2 (type B) surface is high in energy.

The two Sr faceted models both show that the topmost Sr has a bond valence sum close to the expected value, but that the oxygen from the top O_2 layer bonded to the surface Sr are under-coordinated, while the oxygen on the top SrTiO bulk layer (directly below the surface Sr) are over-coordinated. The degree of this under-coordination for the topmost O and over-

coordination for the next highest O is greater for the (1x2) faceted model than for the (1x1) model. However, on the (1x2) model they represent only half the proportion of the total number of atoms in the structure. The species at the apex of the facet are those which have unfavorable coordination, and therefore the less frequent an apex of the facet occurs, the more stable the structure will be. This, however, is not sufficient to explain why the (1x2) model was calculated to be more stable,³⁵ as the surface instability index remains significantly greater for the (1x2) model (SII = 0.33) than the (1x1) model (SII = 0.26). One possible explanation for this is that the simple bond valence sum calculation does not fully reveal the instability of the strontium at the apex. There are two basic chemical reasons why this would be unstable which are not directly picked up by bond valence sums. First, more than half of the apical strontium's coordination sphere is empty, which would tend to make it unstable. Second, the apical strontium has become unusually close to the titanium in the layer below it (3.00 Å Ti–Sr distance in the (1x1) model and 3.05 Å in the (1x2) model, compared to 3.38 Å in bulk SrTiO₃). While there is no easy way to quantify this using bond valence sums, it is possible that these instabilities could account for the (1x1) structure being calculated to have a higher surface energy than the (1x2) structure.

5.4.2: SrTiO₃ (111)

The only proposed surface structures for SrTiO₃ (111) for which atomic coordinates are available in the literature are the 10 small structures calculated by Marks et. al.^{54,109} For the first sets of comparisons, we will look at the sets of structures with the same stoichiometry, models 5 and 6, and models 7 and 8.

Models 5 and 6 (Figure 5.2) are both stoichiometric structures. For model 5, there are several surface atoms which are under-coordinated, and some bulk atoms which are over-coordinated, but all are within 0.30 of the expected value. The structure could therefore be considered reasonable. For model 6, however, the surface atoms are more drastically under-coordinated. Indeed, one surface titanium is closer to Ti^{3+} than to Ti^{4+} (BVS = 3.37 for $\text{Ti}^{3+}-\text{O}^{2-}$ R_0 and BVS = 3.60 for $\text{Ti}^{4+}-\text{O}^{2-}$ R_0), and that of a sub-surface Sr is 1.34, close to Sr^{1+} . This leads to a significantly better surface instability index for model 5 than for model 6 (0.17 vs. 0.24), which is in agreement with the DFT calculations⁵⁴ where model 6 was found to be higher in energy than model 5 by more than half an eV/1x1 surface unit cell. Not that there is some over-coordination deeper in both structures, indicating that they are likely not quite as good as the surface instability index indicates.

Models 7 and 8 (Figure 5.3) both have an equal amount of excess TiO_2 at the surface. For model 7, all atoms have bond valence sums near the expected value, except for the outer most surface Ti, which is significantly reduced with a bond valence sum of 3.65. This suggests some instability with this structure model, although mainly only in the area of one atom, and not as extreme as have been observed in other model surface structures, and this model has a good surface instability index (SII = 0.14). Model 8 had bond valence sums of bulk atoms which differ significantly from the true bulk values. The innermost two titanium layers, for example, all have bond valence sums > 4.30. The structure was therefore re-optimized via DFT with a larger number of layers, after which the bulk layers matched bulk bond valence sum values almost exactly, with a small change in surface free energy. The surface is somewhat under-

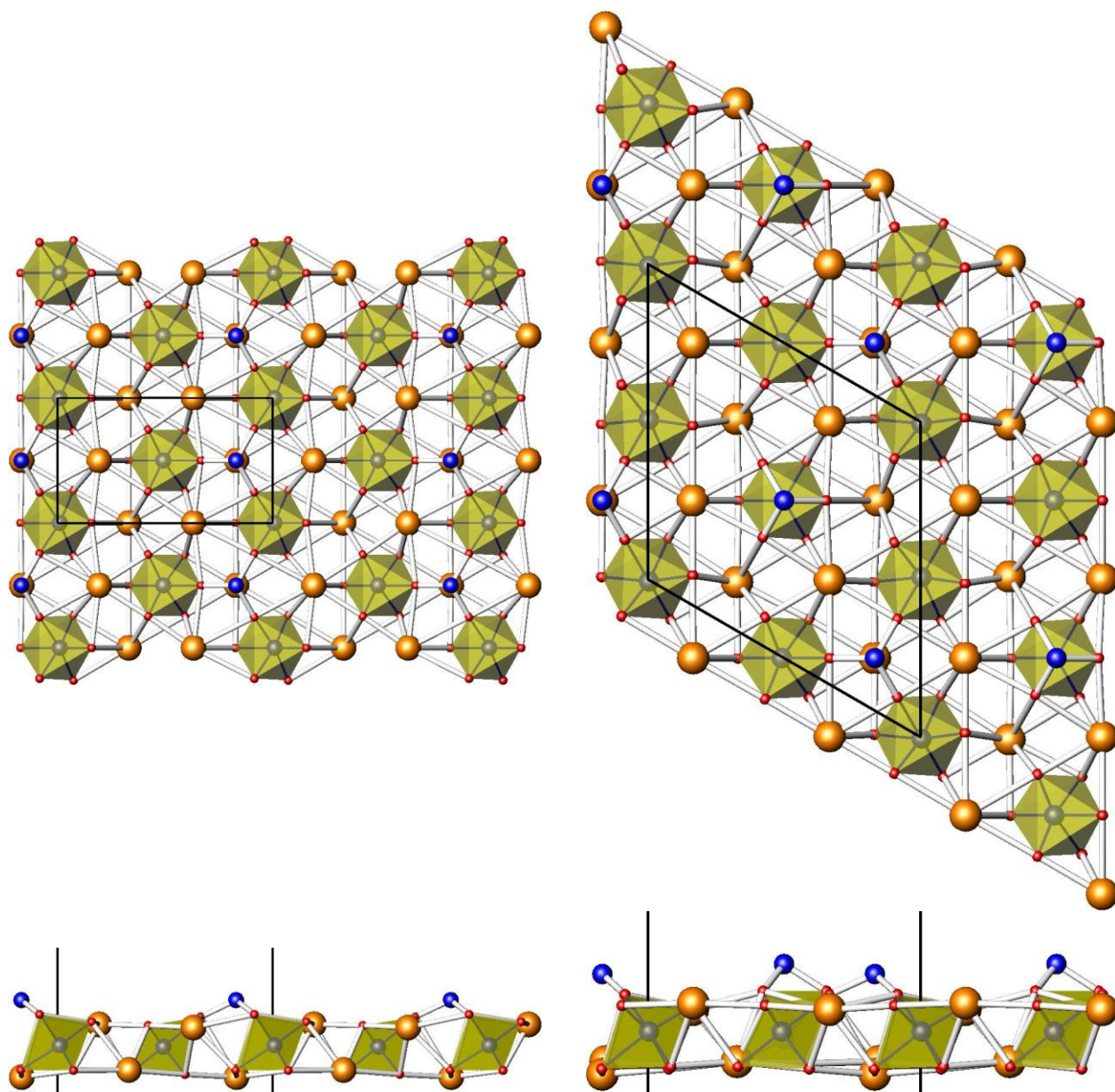


Figure 5.2: SrTiO₃ (111) models 5 (left) and 6 (right). Top: plan view. Bottom: profile view. TiO₆ octahedra as yellow polyhedra, 3-coordinate Ti as blue spheres, Sr as orange spheres, and O as red spheres. Unit cell outlined in black.

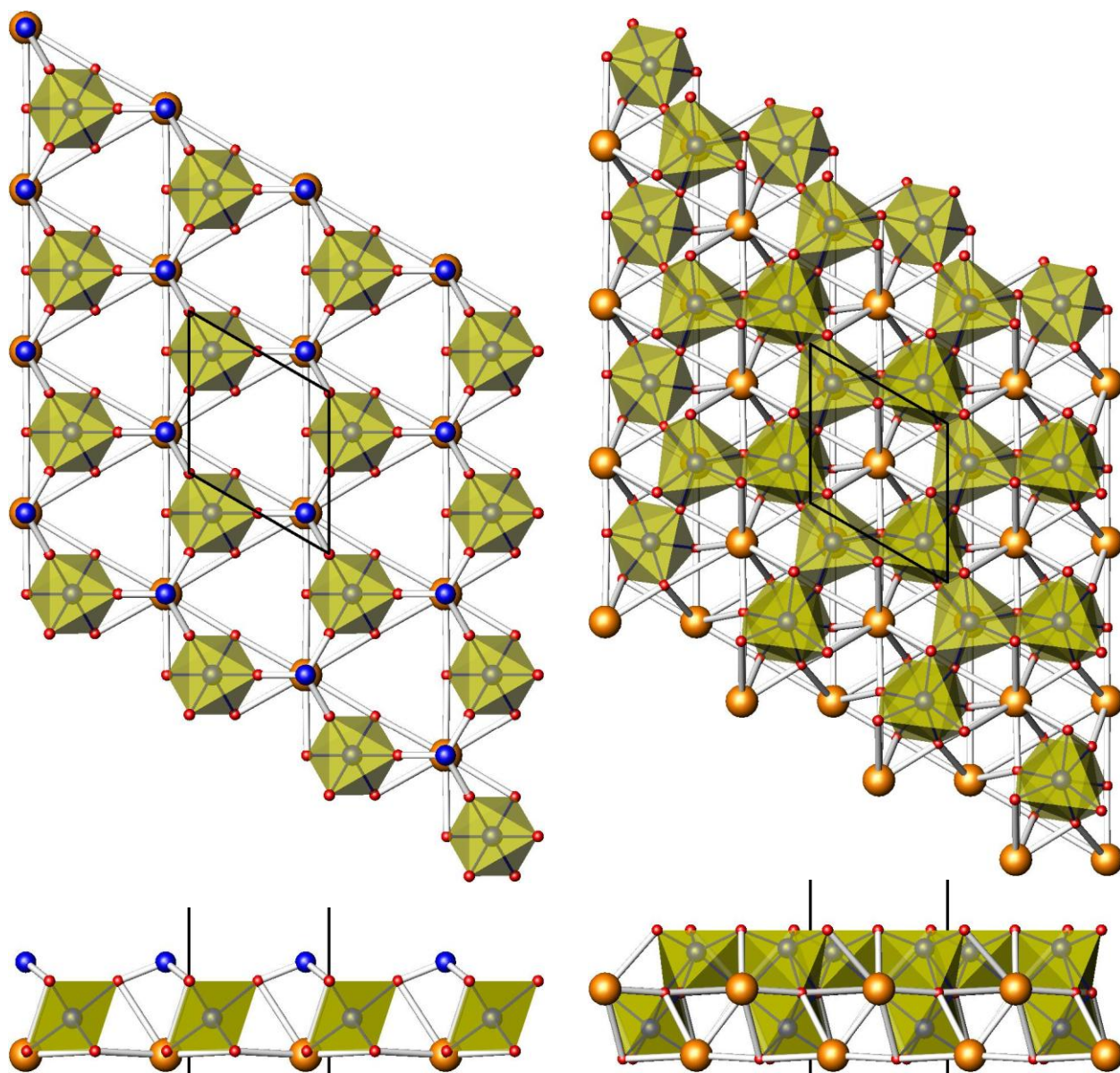


Figure 5.3: SrTiO₃ (111) models 7 (left) and 8 (right), Top: plan view. Bottom: profile view. TiO₆ octahedra as yellow polyhedra, 3-coordinate Ti as blue spheres, Sr as orange spheres, and O as red spheres. Unit cell outlined in black.

coordinated, with bond valence sums of -1.84 for the top-most oxygen and 3.65 and 3.67 for the two surface titanium, which leads to a surface instability index of 0.19. While relatively reasonable, this is not as good as the values for model 7, which is calculated to be significantly higher in energy (>1.5 eV/1x1 surface unit cell). As with the strontium faceted models on the SrTiO₃ (110) surface, the surface instability index and the DFT energies seem to disagree. There are, however, two relatively simple chemical reasons why model 7 might not be as stable as it seems through a bond valence sum analysis. Just as the apical strontium in the SrTiO₃ (110) strontium faceted models had more than half its coordination sphere empty, so too does the top-most titanium on model 7. Additionally, to maintain a reasonable bond valence sum, the three Ti–O bonds formed below the top-most titanium become very short (1.74 Å), which also leaves the titanium unusually close to the strontium directly below it (3.12 Å, as compared to a bulk Ti–Sr distance of 3.38 Å).

Two other models, number 3 and 4 (Figure 5.4), were also valence compensated, i.e. neither oxidized nor reduced. Model 3 is SrO rich at the surface, and has bond valence sums reasonably close to the expected values: the surface Sr and O are only slightly under-coordinated. One O in the top bulk SrO₃ layer is significantly over-coordinated (-2.43), but otherwise the structure is very reasonable (SII = 0.17). Model 4 has one very under-coordinated O at the surface (-1.56), and a slightly under-coordinated Sr in the top bulk layer (1.82). This leads to a high surface instability index of 0.38.

For models 3, 4, 5, 6, 7 and 8 (Table 5.2), the overall best bond valence sums are found in model 7, which as is discussed above, has problems with coordination geometry and Ti–Sr

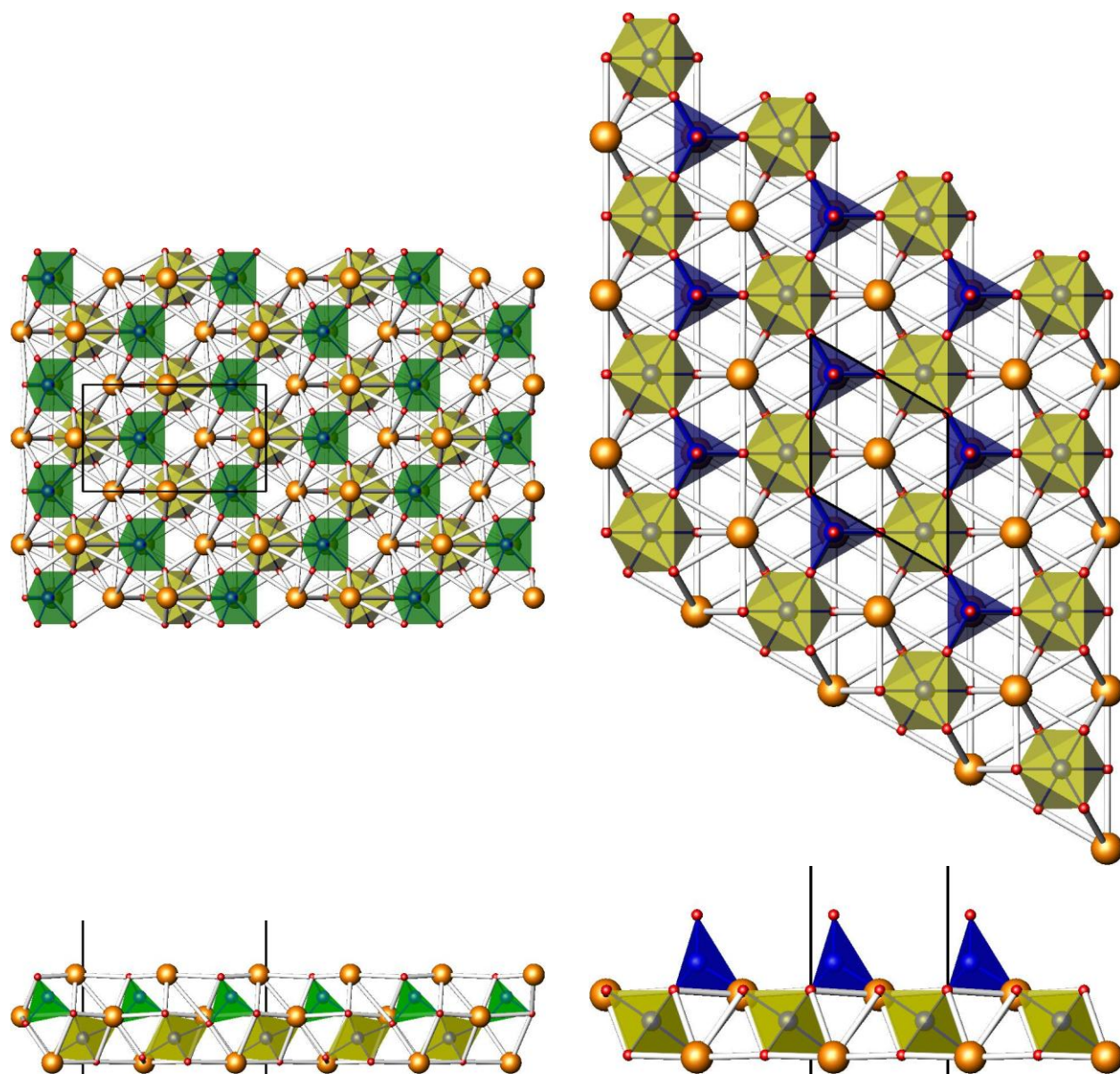


Figure 5.4: SrTiO₃ (111) models 3 (left) and 4 (right), Top: plan view. Bottom: profile view.

TiO₆ octahedra as yellow polyhedra, TiO₅ square-pyramids as green polyhedra, TiO₄ tetrahedra as blue polyhedra, Sr as orange spheres, and O as red spheres. Unit cell outlined in black.

might possibly be present in observed surface reconstructions.⁵⁴ From a bond valence analysis, it seems plausible that the motifs present in models 3 and 8, and possibly model 5, might appear in actual surface reconstruction. Perhaps in some combination they might lead to a superior fit, as was seen with the combination of 6-rings and larger rings in the (nx1) homologous series on the (110) surface of SrTiO₃.

There are also 3 reduced models (models 1, 9 and 10) and one oxidized model (model 2)⁵⁴ (Table 5.3). Model 1 (Figure 5.5) is terminated by a Ti⁴⁺ layer, with titanium atoms in relaxed bulk-like positions. The level of reduction for this structure would require 2 Ti³⁺ per 1x1 surface unit cell, however only one surface Ti is present per unit cell. This Ti is indeed Ti³⁺, but

Table 5.3: Bond valence sums and multiplicity (per 1x1 unit cell) of atoms at the surface and in the top two bulk layers of SrTiO₃ (111) surface models 1, 9, and 10 (oxidized) and model 2 (reduced).

SII	Model 1			Model 9			Model 10			Model 2		
	0.04			0.43			0.20			0.45		
	Atom	Mult.	BVS	Atom	Mult.	BVS	Atom	Mult.	BVS	Atom	Mult.	BVS
Top Surface Layer				Ti	1	3.63	Ti	3	2.88			
				Ti	1	3.89	O	1	-1.78			
				O	3	-2.08	O	1	-1.79			
							O	1	-2.02			
Bottom Surface Layer	Ti	1	3.05	Ti	1	3.06	Ti	1	2.55	Sr	1	1.55
				Ti	1	3.02	Ti	1	3.22	O	3	-1.51
				O	3	-1.62	O	3	-2.03			
1	Sr	1	1.93	Sr	1	2.37	Sr	1	2.42	Ti	1	4.32
	O	3	-2.00	O	3	-2.09	O	3	-2.08			
2	Ti	1	3.99	Ti	1	4.26	Ti	1	4.10	Sr	1	2.20
										O	3	-2.03

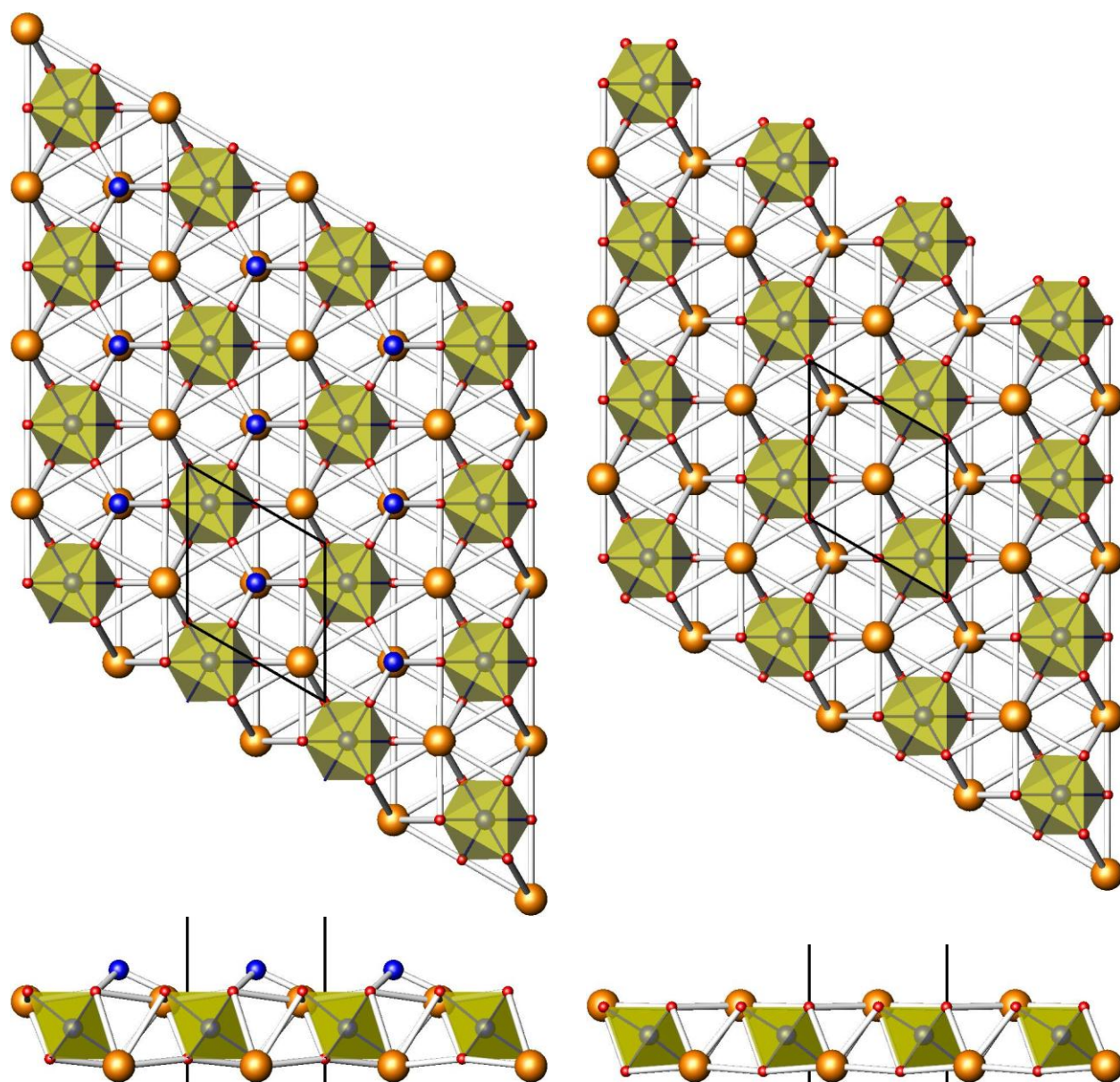


Figure 5.5: SrTiO₃ (111) models 1 (left) and 2 (right), Top: plan view. Bottom: profile view. TiO₆ octahedra as yellow polyhedra, 3-coordinate Ti as blue spheres, Sr as orange spheres, and O as red spheres. Unit cell outlined in black.

additionally every single atom in the structure, except the O nearest the surface Ti, is partially reduced as compared to the expected bulk SrTiO₃ bond valence sums. Even the most central slab shows each atom to be somewhat reduced, suggesting that the reduction is delocalized which is consistent with DFT calculations for a reduced TiO₂ (001).⁵⁶

Model 9 (Figure 5.6) has four Ti per surface unit cell, for an overall Ti₄O₇ stoichiometry, or 2(TiO₂) + Ti₂O₃. With such a stoichiometry, it is expected that in each unit cell there would be 2 Ti³⁺ and 2 Ti⁴⁺. Indeed, this is approximately what is observed. The two top-most Ti are under-coordinated but are closest to Ti⁴⁺ (BVS = 3.63 and 3.89), while the two on the layer just below are clearly Ti³⁺ (BVS = 3.06 and 3.04). The oxygen linking the Ti³⁺ with the Ti⁴⁺ is also under-coordinated (BVS = -1.62). The bulk layers near the surface are somewhat over-coordinated, but the amount of over-coordination drops towards bulk-like values as one moves towards the central layers. The under-coordination observed leads to a high surface instability index (SII = 0.43) which indicates that the surface may be somewhat unstable.

Model 10 (Figure 5.6) is highly reduced, having an overall surface stoichiometry of Ti₅O₇, or 2(Ti₂O₃) + TiO. Thus there must be either a Ti²⁺ at the surface or a Ti³⁺ in the sub-surface region. The BVS shows that the three top-most crystallographically equivalent Ti are Ti³⁺ (BVS = 2.88), the next has a bond valence sum of 2.55, and the fifth is also Ti³⁺ (BVS = 3.22). The top Sr is over-coordinated and somewhat oxidized (BVS = 2.42), while the outermost oxygen are slightly under-coordinated and oxidized (BVS = -1.78 and -1.79). The Ti with the bond valence sum of 2.55 might better be called a Ti²⁺, but it is difficult to say, and R₀ values for Ti²⁺ are not readily available. As this is not completely clear, a surface instability index cannot

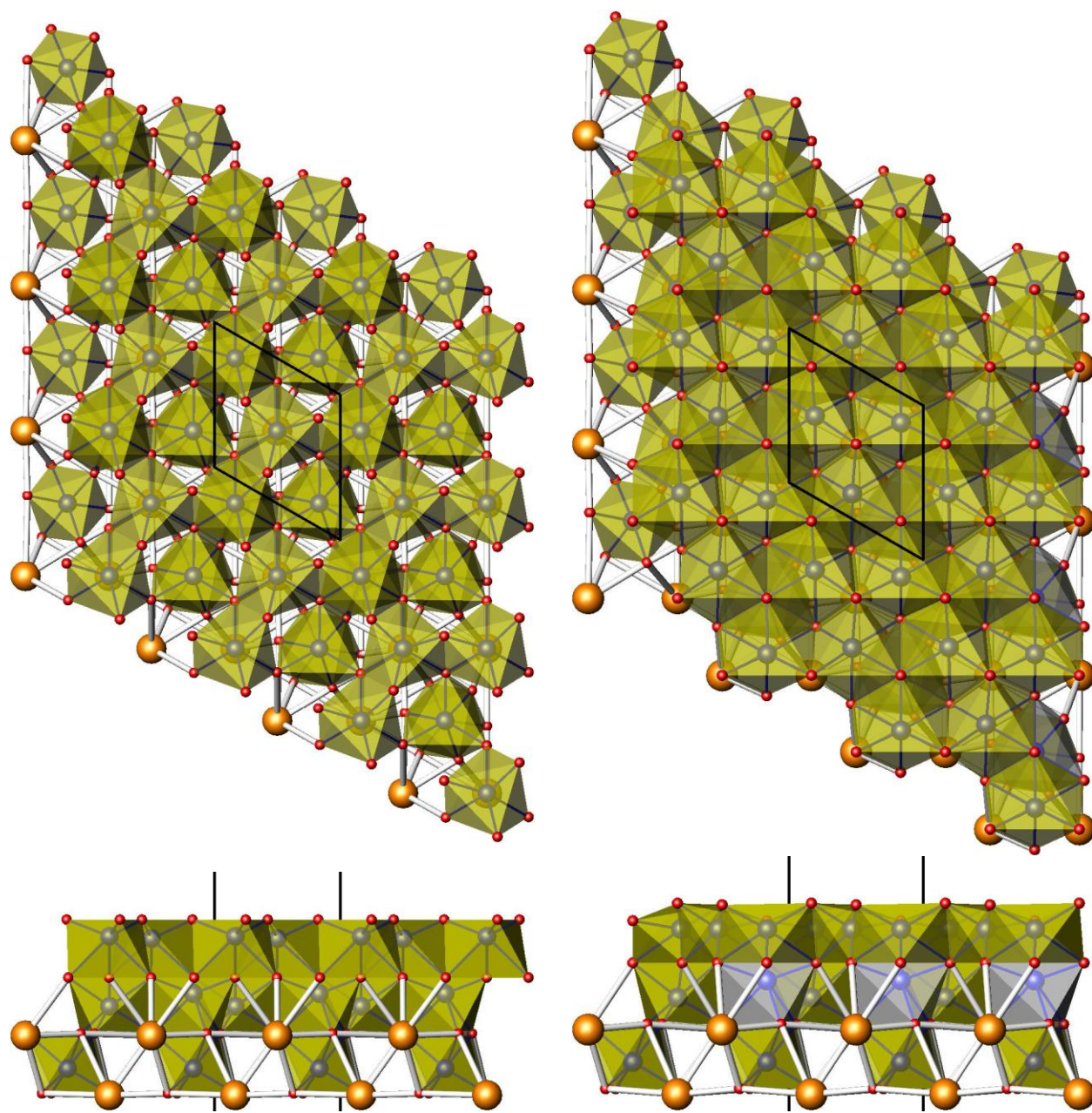


Figure 5.6: SrTiO₃ (111) models 9 (left) and 10 (right), Top: plan view. Bottom: profile view. TiO₆ octahedra as yellow polyhedra, TiO₇ irregular decahedra as silver polyhedra, Sr as orange spheres, and O as red spheres. Unit cell outlined in black.

be calculated. However, it is clear that the reduced species must be at the surface, as the bulk cations all have bond valence sums near the expected values. The under-coordination of the surface O indicate potential instability of such a structure.

The final structure, model 2 (Figure 5.5), is highly oxidized: it is a bulk-like SrO_3 termination, which adds one extra O per surface unit cell beyond what would be present if all species were in bulk-like oxidation states. This is accommodated by having the surface oxygen under-coordinated and oxidized (BVS = -1.51), which leaves the surface strontium highly under-coordinated and reduced (BVS = 1.55). Such an under-coordinated surface would likely be highly unstable.

It is difficult to compare these final four structures to any others, as each is unique in terms of composition and oxidation. Although many are under-coordinated at the surface and therefore likely unstable, this is not to say a structure with similar motifs could not form under the proper conditions. It does imply, however, that if such an under-coordinated structure was formed, it would be highly reactive. Reacting with almost any other species present would likely improve the bond valence sums and be energetically favorable.

5.4.3: SrTiO_3 (100)

Of all the SrTiO_3 surface orientations, the (100) surface is the most studied, and has the most proposed surface structures, both oxidized and reduced. The fully oxidized structures include the crystallographically solved (2×1) ,^{29,60,65,110-112} (2×2) ,^{60,77,78,113} and $c(4 \times 2)$ ^{60,65,72,111,114,115} structures, the bulk-like (1×1) Sr- and Ti-terminations,^{110,116-120} and the calculated $(\sqrt{2} \times \sqrt{2})\text{-R}45^\circ$ ⁵⁶ structures. The (2×1) , $c(4 \times 2)$, and (1×1) structures were discussed in

chapter 4. The reduced structures that have been proposed consist of either Sr-adatoms^{105,121,122} or O vacancies in a Ti-terminated surface.¹²³⁻¹²⁷ Most commonly they have been proposed as solutions to the $(\sqrt{5}\times\sqrt{5})\text{-R}26.6^\circ$ structure, although the Sr-adatom structure type has been proposed for other periodicities as well by Kubo and Nozoye,¹⁰⁵ who also provided the structures of several Sr-adatom models.¹⁰⁴ Other surface reconstructions have been observed, but atomic positions are unknown. The O vacancy model for the $(\sqrt{5}\times\sqrt{5})\text{-R}26.6^\circ$ surface, having been determined important as a point of comparison but without atomic positions available from the literature, was optimized via DFT for this work. The only structure for which atomic coordinates are available to us which is not considered is the $c(6\times 2)$ structure,^{112,115,128,129} for which bond valence sums cannot be easily applied due to the disorder.

Of the two bulk-like (1×1) structures (Table 5.4), the Ti-termination is distinctly better. The surface is somewhat under-coordinated (BVS = -1.88 for O, BVS = 3.75 for Ti) and the SrO layer below slightly over-coordinated (BVS = 2.25 for Sr, BVS = -2.37 for O), leading to a high surface instability index of 0.24. The Sr termination, on the other hand, is severely under-coordinated at the surface, especially for the oxygen (BVS = 1.78 for Sr, BVS = -1.50 for O). The oxygen in the bulk TiO_2 layer below is slightly overcoordinated (BVS = -2.22) due to the proximity of the surface strontium, but the Ti is nearly bulk-like (BVS = 4.12). The surface instability index, at 0.29, is significantly worse than for the strontium termination. While both are under-coordinated at the surface, the Sr termination is far more so, indicating that in general the Ti termination would be more stable. This may help explain why there are more reports of surface reconstructions based on a TiO_2 termination than based on a SrO termination.

Table 5.4: Bond valence sums and multiplicity (per 1x1 unit cell) of atoms at the surface and in the top two bulk layers of SrTiO₃ (100) surface for SrO bulk termination, TiO₂ bulk termination, (2x1), (2x2), ($\sqrt{2}\times\sqrt{2}$)-R45°, and c(4x2) reconstructions.

	SrO (1x1)			TiO ₂ (1x1)			(2x1)			(2x2)			(($\sqrt{2}\times\sqrt{2}$))-R45°			c(4x2)		
SII	0.29			0.24			0.22			0.14			0.15			0.17		
	Atom	Mult.	BVS	Atom	Mult.	BVS	Atom	Mult.	BVS	Atom	Mult.	BVS	Atom	Mult.	BVS	Atom	Mult.	BVS
Surface	Sr	1	1.78	Ti	1	3.75	Ti	0.5	3.92	Ti	0.5	4.03	Ti	1	4.00	Ti	0.5	4.07
	O	1	-1.49	O	1	-1.88	Ti	0.5	3.65	Ti	0.5	3.94	O	1	-1.93	Ti	0.5	4.03
							O	0.5	-1.74	O	1	-1.95	O	1	-2.14	O	1	-1.93
							O	0.5	-1.74	O	0.5	-2.17				O	0.25	-2.20
							O	0.5	-2.25	O	0.5	-2.01				O	0.5	-2.02
							O	0.5	-2.02							O	0.25	-2.56
1 st bulk layer	Ti	1	4.12	Sr	1	2.25	Ti	0.5	4.11	Ti	0.5	3.98	Ti	1	4.21	Ti	0.25	4.35
	O	1	-2.22	O	1	-2.37	Ti	0.5	4.25	Ti	0.5	4.29	O	1	-2.04	Ti	0.5	4.02
							O	0.5	-2.14	O	0.25	-2.03	O	1	-2.25	Ti	0.25	4.30
							O	0.5	-1.94	O	0.25	-2.15				O	0.5	-2.03
							O	0.5	-1.93	O	0.25	-1.92				O	0.5	-2.15
							O	0.5	-2.40	O	0.25	-2.31				O	0.5	-2.20
																O	0.5	-1.94
2 nd bulk layer	Sr	1	2.09	Ti	1	4.23	Sr	0.5	2.30	Sr	1	2.37	Sr	1	2.46	Sr	1	2.23
	O	1	-1.98	O	1	-2.05	Sr	0.5	2.42	O	0.5	-2.15	O	1	-2.24	O	0.25	-2.18
							O	0.5	-2.17	O	0.5	-2.26				O	0.5	-2.23
							O	0.5	-2.26							O	0.25	-2.09

The ($\sqrt{2}\times\sqrt{2}$)-R45° surface structure⁶⁰ (Figure 5.7 and Table 5.4) shows very good BVSs with a surface instability index of 0.15, but has over-coordinated bulk strontium and oxygen (all strontium have BVS ≥ 2.32), which leads to a high global instability index (GII = 0.21). This is far enough from the bulk bond valence sum value to indicate that the structure is not properly converged, and the calculation needs to be repeated with a greater number of layers. It would be expected that when that is done, all the bond valence sums will be lowered somewhat, but to

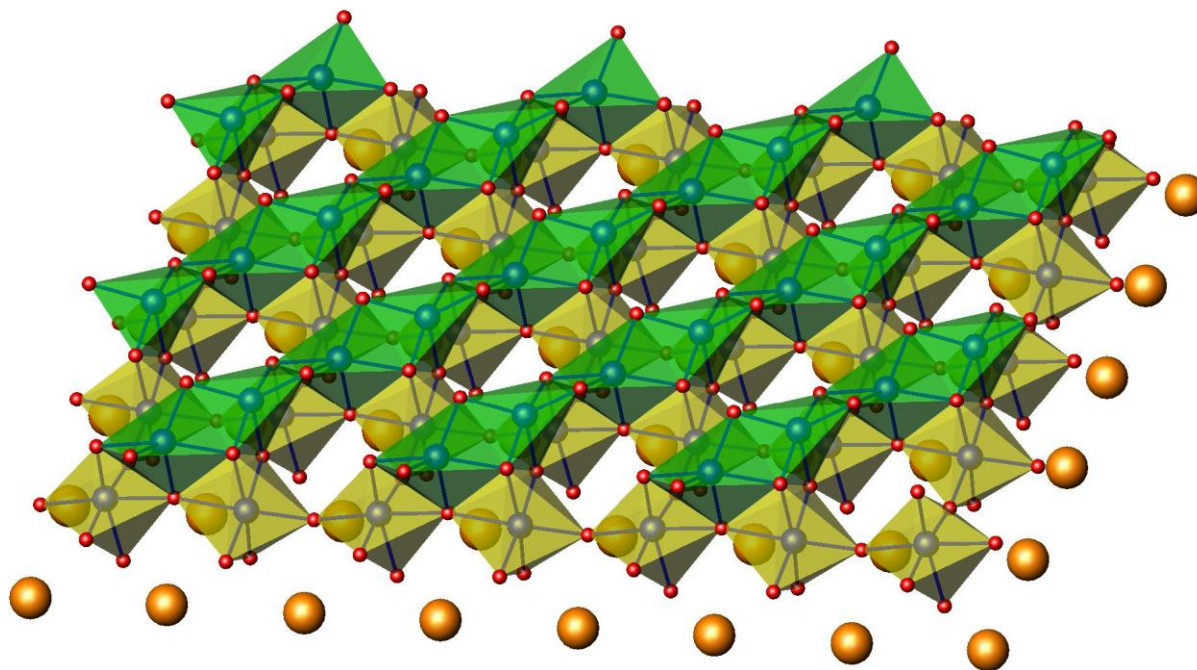


Figure 5.7: $(\sqrt{2}\times\sqrt{2})$ -R45° (bottom) surface structures. TiO₆ octahedra as yellow polyhedra, TiO₅ trigonal bipyramids as green polyhedra, Sr as orange spheres, and O as red spheres.

what degree is unknown, and it cannot be certain whether the surface would still be so close to the expected values. It has never been seen experimentally observed, despite having been calculated to be the lowest in energy.

The (2x1) structure²⁹ (Table 5.4, see also Chapter 4) is surprisingly under-coordinated at the surface for a structure which has been crystallographically solved. The top two surface oxygen, including the “dangling oxygen” are both under-coordinated (both with BVS = -1.74) as is the titanium bonded to the “dangling oxygen” (BVS = 3.65). An oxygen in the top bulk TiO₂ layer is overcoordinated (BVS = -2.40) as are the strontium in the layer below (BVS of 2.30 and

2.42), but otherwise the structure quickly returns to bulk-like coordination. The surface instability index is 0.22, and increases to 0.24 when including the second bulk layer. This is in agreement with DFT calculations, which find the (2x1) structure ~0.6 eV higher in energy than the (2x2) or c(4x2).

The (2x2) structure⁶⁰ (Table 5.4, see also Chapter 4) is fully converged to bulk-like bond valence sums by the second bulk TiO₂ layer. The surface shows nearly ideal bond valence sums, and the top bulk layers are only slightly over-coordinated (BVS = 4.29 for Ti, BVS = -2.31 for O, BVS = 2.37 for Sr), leading to a good surface instability index (SII = 0.14). There are some over-coordinated atoms in the second bulk layer, which lead to an increased instability index of 0.20 when this layer is included. Still, the 2x2 surface structure should be relatively stable.

The c(4x2) structure⁷² (Table 5.4, see also Chapter 4) is also quite reasonable (SII = 0.17). The top bulk TiO₂ layer has some over-coordinated titanium (BVS = 4.35 and 4.30), but in general has very good bond valence sums, except for the oxygen in the middle of all four titanium trigonal bipyramids, which is significantly over-coordinated (BVS = -2.56). It converges more quickly to bulk-like bond valence sums than does the (2x2) structure, and the instability index when including the second bulk layer is 0.18. Overall, the bond valence sums are similar to the 2x2 structure, which agrees well with DFT calculations where the two structures are similar in calculated surface energy (within 0.06 eV).

The oxygen vacancy model was first proposed for the ($\sqrt{5}\times\sqrt{5}$)-R26.6° reconstruction (Figure 5.8), and is reduced. More recent works have focused on the Sr-adatom surfaces for the ($\sqrt{5}\times\sqrt{5}$)-R26.6° structure (Figure 5.8) and it is generally agreed that they fit better with

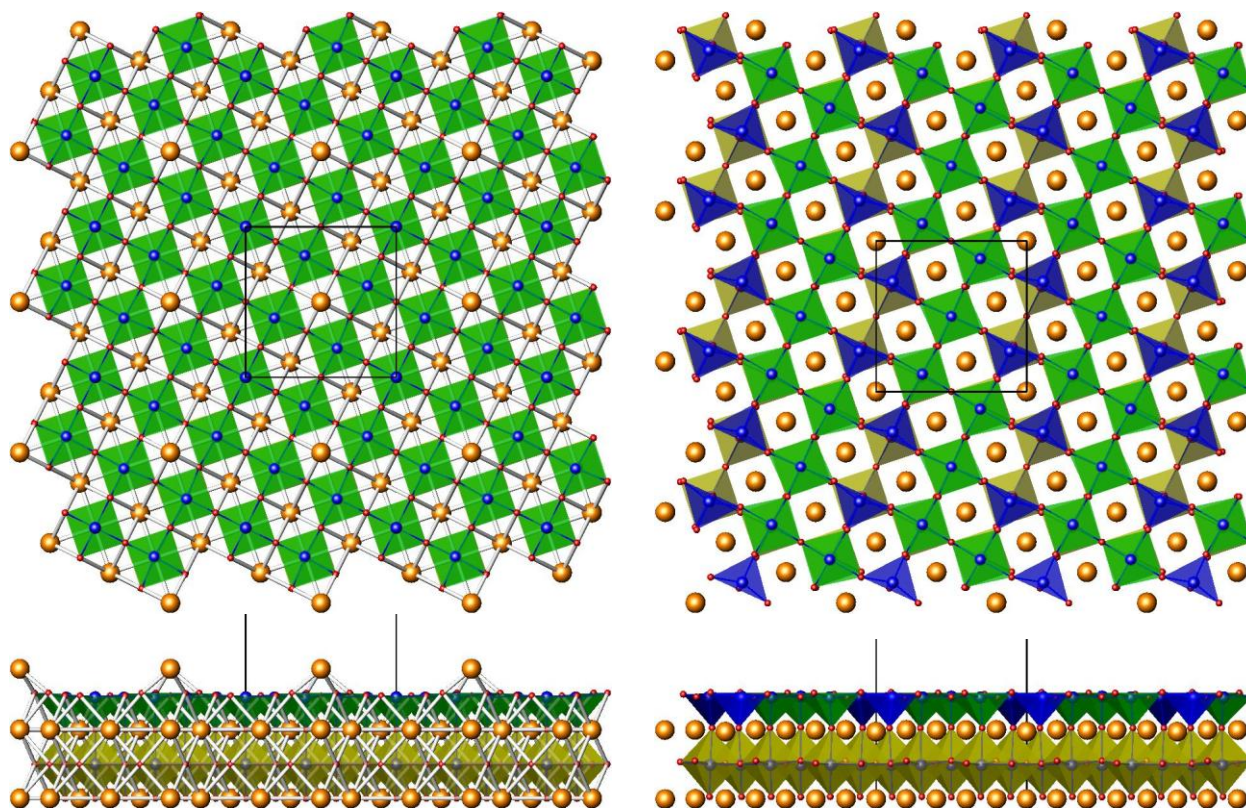


Figure 5.8: SrTiO₃ (100) Sr-atom (left) and O-vacancy (right) models for the $(\sqrt{5}\times\sqrt{5})\text{-R}26.6^\circ$ reconstruction. Top: plan view. Bottom: profile view. TiO₆ octahedra as yellow polyhedra, TiO₅ square-pyramids as green polyhedra, TiO₄ tetrahedra as blue polyhedra, Sr as orange spheres, and O as red spheres. Unit cell outlined in black.

experimental observations than does the oxygen vacancy model. Several other Sr-atom models have also been proposed to fit other observed reconstruction periodicities.¹⁰⁵ As only strontium, not strontium oxide, is added in these models, the more strontium present, the more reduced a structure is. The several Sr-atom structures made available by Kubo¹⁰⁴ are, from least to most reduced (with θ representing the number of Sr-atoms per 1x1 surface unit cell):

coordinated and reduced oxygen on the topmost bulk SrO layer (BVS = -2.42). This highly under-coordinated surface indicates that the structure would be highly unstable. All other structures with $\theta \leq 0.25$ (i.e. no Sr in any two adjacent 1x1 unit cells) have Sr-adatoms on the surface with bond valence sums close to 2 (Table 5.5), and in the case of the $((\sqrt{5} \times \sqrt{5}))\text{-R}26.6^\circ$ even a slightly over-coordinated Sr-adatom (BVS = 2.29). The reduction in these structures is distributed evenly over the titanium in the top bulk layer, which have bond valence sums in the 3.68 – 3.70 range. In the case of the c(4x4)-type A ($\theta=0.125$) structure, this accounts for more than the full amount of reduction needed, and indeed the near-surface oxygen are slightly under-coordinated (oxidized) with bond valence sums of -1.83 – -1.86. For the $((\sqrt{5} \times \sqrt{5}))\text{-R}26.6^\circ$ ($\theta=0.2$) and c(4x2) ($\theta=0.25$) structures, the surface oxygen are not as oxidized ($-1.85 > \text{BVS} > -1.91$), and the oxygen on the bulk SrO layer below is also reduced ($-2.25 > \text{BVS} > -2.31$). In general these structures seem quite reasonable. The fact that the top-most titanium atoms cannot be assigned an oxidation state, being somewhere between Ti^{3+} and Ti^{4+} prevents the calculation of a meaningful surface instability index, and thus prevents a more quantitative assessment. Additionally, the possibility of mixed valence in a surface structure is most interesting, and will be returned to shortly.

For the structures with $\theta > 0.25$, Sr-adatoms must necessarily be present in neighboring unit cells. In these cases, the necessary reduction cannot be accomplished by lowering the coordination of the sub-surface titanium, and for $\theta > 0.5$ there are not enough titanium atoms in that layer to compensate for a reduction by more than 1 electron per surface 1x1 unit cell. In all cases the Sr-adatom is under-coordinated, with the under-coordination getting worse as θ

As the full structure of the oxygen vacancy ($(\sqrt{5}\times\sqrt{5})$ -R26.6° model was not available in the literature, a model was optimized using DFT (Wien2k code).⁴⁸ In the plane of the surface, there are rings composed of 6 titanium and 6 oxygen atoms surrounding the oxygen vacancy. Only the crystallographically distinct titanium at the center of the unit cell is part of two such rings, and it is this titanium which is the most reduced (BVS = 3.36). This and the other corner titanium (BVS = 3.68) have square pyramidal coordination geometries. The titanium closest to the oxygen vacancy adopt a distorted tetrahedral geometry, with only slightly reduced (BVS = 3.69) bond valence sums. The oxygen along the side of the rings are very under-coordinated (BVS = -1.50 and -1.53), while the other surface oxygen are only somewhat under-coordinated ($-1.71 < \text{BVS} > -2.03$). The rather severe under-coordination at the surface suggests that this structure is unstable, and leads to a high surface instability index (SII = 0.29). This structure has the same degree of reduction as the Sr-adatom ($(\sqrt{5}\times\sqrt{5})$ -R26.6° model, and is far more under-coordinated at the surface (Table 5.7). It is thus expected that the Sr-adatom ($(\sqrt{5}\times\sqrt{5})$ -R26.6° model would be preferred over the oxygen vacancy ($(\sqrt{5}\times\sqrt{5})$ -R26.6° model, in agreement with previous studies which show inconsistencies between the oxygen vacancy model and STM images.¹²⁵

We have noted that in the Sr-adatom structures, bond valence sum analysis has revealed mixed valences (e.g. 3 $\text{Ti}^{3.67+}$ instead of 2 Ti^{4+} and 1 Ti^{3+}). Such a phenomenon is indeed known in bulk structures, and bond valence sums have been an excellent method for examining it.¹³⁰⁻¹³² Mixed valence is often very interesting when found in bulk structures, and to our knowledge has never been reported for a surface structure. If these Sr-adatom structures are indeed a case of

Table 5.7: Comparison of bond valence sums for Sr-adatom and O-vacancy models for SrTiO₃ (100) (($\sqrt{5}\times\sqrt{5}$))-R26.6° reconstruction.

Layer	Sr-adatom			O-vacancy		
	Atom	Mult.	BVS	Atom	Mult.	BVS
Surface	Sr	0.2	2.29	Ti1	0.4	3.69
				Ti2	0.4	3.68
				Ti3	0.2	3.36
				O1	0.4	-1.53
				O2	0.4	-2.03
				O3	0.4	-1.50
				O4	0.4	-1.84
1				O5	0.4	-1.71
	Ti	0.2	3.70	Sr1	0.2	2.12
	Ti	0.8	3.67	Sr2	0.400	2.07
	O	0.4	-1.95	Sr3	4.000	2.05
	O	0.4	-1.91	O6	0.4	-2.10
	O	0.2	-1.85	O7	0.400	-2.23
2				O8	0.2	-2.09
	Sr	0.2	2.03	Ti4	0.400	4.01
	Sr	0.8	2.03	Ti5	0.400	4.02
	O	0.2	-2.30	Ti6	0.200	4.03
	O	0.8	-2.31	O9	0.200	-2.01
				O10	0.400	-2.03
				O11	0.400	-2.03
				O12	0.400	-2.02
				O13	0.400	-2.03
			O14	0.200	-2.02	

mixed valence in a surface structure, they would be most interesting. However, it should be noted that in many of these cases, mixed valence has been forced upon the surface structure by the symmetry constraints imposed in the model. For example, for the (($\sqrt{5}\times\sqrt{5}$))-R26.6° model, there are 5 titanium ions on the top layer, four of which are crystallographically identical. Thus

with the symmetry used, there could only be either 0, 1, 4, or 5 Ti^{3+} , not the 2 that would be necessary to maintain integral valence states for titanium. It requires further study to be sure whether the mixed valence is real or if it is a product of the constraints imposed on the structural model.

5.5: Adsorbates on surface structures

As was detailed in chapter 4, there is strong evidence, both from experiment and calculations, that adsorbates play a role in the formation of SrTiO_3 (100) surfaces. For example, the dissociation of water on the SrTiO_3 (100) (2x1) surface structure vastly improves both the energy and bond valence sums. The presence of hydroxide is also supported by XPS data, and it seems to be an integral part of the surface structure, as annealing at temperatures up to 750°C does not completely remove it. Water has also been shown to play a critical role in the formation of the NiO and MgO (111) surface structures.^{57,58} There is every reason to believe, then, that water and other adsorbates, play an important role in oxide surface structures in general. Further, bond valence sums are an ideally suited tool for the study of such phenomena.

As any foreign species adsorbs, it will coordinate to the surface. This will then increase the coordination of the atoms in the surface structure, and a previously under-coordinated surface would be stabilized. It is thus likely that an under-coordinated surface structure, as revealed by a bond valence sum analysis, may indicate a reactive surface, one likely to adsorb foreign species. For example, dissociation of a H_2O molecule onto the SrTiO_3 (100) (2x1) surface improved the energy and surface instability index from 0.22 to 0.12. This parallels the adsorption of O^{2-} (plus

a pH dependent number of H^+) onto metal ions at solid liquid interfaces. In the $SrTiO_3$ (100) (2x1) surface structure, the atoms to which H^+ and OH^- were found to bond were those which were the most under-coordinated in the dry structure.

The bond valence sum analysis can indicate not only to which surfaces a foreign species may adsorb, but at what site. It therefore has the potential to predict active sites at heterogeneous catalysts surfaces. Many of the surfaces which were termed unstable may be stabilized in such a manner. The fact that a surface was termed unstable does not mean that it cannot exist, but such an unstable surface might be more useful than a more stable surface in fields such as heterogeneous catalysis.

Structural models that are most likely to exist as-is are those with the best overall bond valence sums, i.e. the best surface instability index. Structures with bond valence sums that are too high (over-coordinated) can certainly form, as is demonstrated by the high coordination of the central oxygen in the $SrTiO_3$ (100) c(4x2) surface structure. This is especially true if only a small portion of the structure is over-coordinated, in which case the less favorable area would be subordinate to the improvement of the whole, as can be readily seen through the good surface instability index of such structures. Structures which are somewhat under-coordinated may likewise form, although they are likely to adsorb foreign species. A structure without any under-coordinated species on the surface might be more robust and less likely to adsorb any foreign species. Conversely, something on an over-coordinated surface structure might dissociate in order to lower the coordination.

5.6: Conclusions

It has been demonstrated that chemical bonding models of surfaces generally agree with physics based calculations and with experiment, just as they do for bulk structures. Additionally, the bond valence model has been shown to easily describe concepts, such as polar surfaces, which have been most difficult to deal with from a purely physics based approach. Further, bond valence sums show the potential to reveal reactivity of surfaces, which may prove most useful in fields such as heterogeneous catalysis. It is clear that, moving forward, a chemical bonding approach should be a part of any surface study. The complementary nature of the physics based models and the bond valence model can lead to a greatly enhanced understanding of surface structure, chemistry, and reactivity. As with bulk materials, the best way to move forward is to consider the chemistry and physics simultaneously, with each providing insight that is difficult to reach from the alternate approach.

Chapter 6:

Towards Catalytic Applications:

SrTiO₃ Nanocuboids

6.1: Introduction

Because many industrial processes are dependent on catalysis, any advance in catalytic design could provide significant benefits to society. Although catalytic supports are primarily selected for their high surface area or thermal, chemical, and mechanical stability, the support can also affect the selectivity and reactivity of the catalyst.¹³³⁻¹³⁵ Classic catalytic work, for example that of Sinfelt and coworkers,¹³⁶⁻¹³⁹ has shown that changing the support can dramatically alter the catalytic behavior. Many theories have been proposed to explain the influence of supports on catalysts, including sites at the metal-support interface,¹⁴⁰ particle size and surface-structure sensitivities,¹⁴¹ ensemble-size sensitivity,¹⁴² and strong metal-support interactions.¹⁴³ The latter includes concepts such as intermetallic bond formation and charge transfer,^{144,145} diffusion of metal species between support and catalyst,^{133,146,147} geometric decoration,¹⁴⁸⁻¹⁵³ and other electronic effects.^{154,155} However, because high surface area supports of the type normally used in industry have many different surface facets exposed, insights gained from model studies are difficult to extend to industrial catalysts.

One of the more intriguing aspects of support effects is the potential to stabilize a catalyst with the exposed faces carefully controlled. Such a catalyst would be able to take advantage of the differences in selectivity and reactivity of different faces as demonstrated in studies on oriented single crystals (see, for example, ^{41,47,156} and references therein). Catalysts dispersed on high surface area supports are normally found with a wide range of sizes, shapes, orientations and surface structures. There have been many attempts to bridge this gap by creating high surface area nanoparticle catalysts with specific exposed surfaces, but ultimately

with little success. Even when a desired (surface) structure is created by some chemical kinetic path for the initial catalyst, it is invariably a metastable configuration which does not survive catalytic conditions and reverts to the thermodynamically stable structure. This is true particularly if it contains higher-energy more reactive surfaces such as metallic fcc (001). Discovering or engineering a thermodynamically stable, high surface area, nanoparticle catalyst with designed exposed faces would be a significant step forward in catalytic research, but achieving precise control over the exposure of specific faces and their relative ratios remains an important, ongoing challenge.

While at times separated from the catalytic community, much fundamental research has been conducted on the shape and orientation of metal nanoparticles. The shape of free metal nanoparticles has long been known to be governed by the Wulff construction,¹⁵⁷ and that of supported metal nanoparticles by the Winterbottom construction.¹⁵⁸ Indeed, even such complicated aspects as the structure of multiply-twinned metal nanoparticles¹⁵⁹⁻¹⁶² are solved problems, and the surface structures of such metal nanoparticles is well understood.¹⁶³ While many of these studies were motivated by the potential of these types of particles for catalysis,^{164,165} such insights have not been exploited in the design of catalysts.

Recent synthesis of high surface area oriented SrTiO₃ nanocubes^{166,167} opens up new possibilities. When used as a catalytic support, strontium titanate is in powder form, without well defined surface facets exposed. SrTiO₃ nanocubes, however, present primarily the low energy (100) face with a smaller amount of (110) exposed,^{166,168} for which many details of the surface structure are available.^{27,29,65,72,79,128} Note that although they have in the past been termed

nanocubes, they are not truly cubic. The length, width, and depth all vary slightly, making them more accurately resemble a rectangular prism. Further, in addition to the six (100) faces, twelve (110) faces are also exposed, meaning that the nanoparticle actually has eighteen distinct faces exposed. They will therefore be referred to as cuboids, rather than cubes, for the remainder of this work. Note that the mathematical definition of a cuboid requires that the shape have six faces, and therefore these nanocrystals with eighteen faces are not technically cuboids. However, lacking a proper name for such a shape, the term cuboid will be applied for clarity.

This chapter deals with the structure and chemistry of SrTiO₃ nanocuboids and of platinum nanoparticles grown on the SrTiO₃ nanocuboids. The Wulff construction determines the morphology of the SrTiO₃ nanocuboids, and the observation of the particle shape therefore allows for the determination of the surface structure of the nanocuboids. The platinum nanoparticles grown on the SrTiO₃ nanocuboid surfaces have a strong cube-on-cube epitaxy with the predicted Winterbottom shape, consistent with literature values of the interfacial free energy, Pt (001) and Pt (111) surfaces as well as the surface free energy determined for the SrTiO₃ nanocuboid (001) surfaces. As will be discussed, these shapes are *thermodynamically stable*, and expose different surfaces of the platinum nanoparticles than those exposed when supported on polycrystalline supports. As such, we can expect this stable configuration to survive the rigors of catalytic conditions for extended periods of time. In effect we have engineered specific surfaces of the nanoparticles by combining thermodynamics with engineering of the support. This concept is general. In this chapter, methods are proposed through which this concept can be applied to create stable, high surface area, face-selective catalysts.

6.2: Experimental Methods

6.2.1: Sample Preparation

SrTiO₃ nanocuboids were synthesized by Federico Rabuffetti using hydrothermal methods as previously described.¹⁶⁶ Platinum nanoparticles were deposited on the SrTiO₃ nanocuboids by the Elam group at Argonne National Laboratory as previously described.¹⁶⁹

The SrTiO₃ nanocuboids, due to their small size, could not be etched by the normal procedure used for single crystals which consists of dipping the crystal into an acid and removing it. Nor could they be placed in an acid etching solution and removed via filtration, as the nanocuboids would also pass through most filters. An alternate etching scheme was devised and carried out by Federico Rabuffetti, which consisted of placing the SrTiO₃ nanocuboids in a centrifuge tube filled with the etching solution, waiting a period of time for the etching to occur, and centrifuging to separate the nanocuboids from the etching solution. The nanocuboids were then rinsed by adding water to the centrifuge tube and centrifuging again to separate the nanocuboids from the water. The wash step was repeated until a pH of ~6 was reached and Cl⁻ ion concentration was determined to be less than 1 ppm via AgCl precipitation. Two basic types of etching solutions were used: commercially available buffered NH₄F:HF solution (semiconductor grade, Riedel-de Haen, pH = 5.6) used as received, and 3:1 (v/v) solution of HCl:HNO₃ made in house and diluted to the desired concentration with water.

SrTiO₃ nanocuboids were annealed in a fused silica tube within a tub furnace. Samples were dispersed onto a TEM grid for observation. Lacey carbon, lacey SiO_x, and SiN window

TEM supports were all used. Samples dispersed on lacey carbon grids were annealed in an alumina sample boat prior to dispersion. Samples on lacey SiO_x or SiN window supports were annealed after dispersion on the support. Samples dispersed on SiN windows were annealed by Federico Rabuffetti. In all cases, the samples were annealed either in air, or in an atmosphere of flowing O₂.

6.2.2: Transmission Electron Microscopy and Transmission Electron Diffraction

Three different microscopes were used for various portions of this work. Basic TEM, bright-field and dark-field imaging, and TED were carried out on a Hitachi H-8100 TEM. Small probe TED captured on film was carried out on a Hitachi HF-2000 TEM. HREM, small probe TED captured on CCD camera, and thickness mapping were carried out on a JEOL JEM-2100 FasTEM. All three instruments were located in the EPIC facility of the Nuance Center at Northwestern University.

The small size of the nanocuboids required that, in order to avoid obtaining diffraction information from multiple nanocuboids simultaneously, either an isolated nanocuboid had to be found, or a very small probe had to be used. Diffraction patterns were initially taken near to the zone axis to make sure that the nanocuboids were crystalline. When attempting to observe surface reconstructions, the nanocuboid was tilted off the zone axis as described in Chapter 4. The probe in the H-8100 microscope could not be made smaller than the size of a nanocuboid, requiring that an isolated nanocuboid be found. When using the H-8100 diffraction was obtained from the entire cuboid so edge effects could not be avoided. The HF-2000 was preferred when attempting to observe surface reconstructions, as it could form an electron probe smaller than the

nanocuboids and thereby avoid edge effects. The JEOL microscope could likewise form a very small probe, but was not equipped with film, requiring that all images be obtained on a CCD camera. Diffraction patterns were captured on the CCD camera and averaged over several exposures. Images were obtained both of the entire diffraction pattern and of only small areas where surface diffraction spots would be expected.

Bright-field and dark-field imaging were carried out as described in Chapter 4. For HREM imaging, a nanocuboid was first tilted to a (100) zone axis to allow for optimal viewing of the lattice fringes and to obtain a profile view of the edge of the nanocuboids, which was especially important in the case of the platinum nanoparticles grown on the SrTiO₃ nanocuboids. Thickness mapping was carried out using the automated energy-filtered TEM functions in Digital Micrograph. In creating a thickness map, Digital Micrograph takes two images, one unfiltered and one formed only from zero-loss electrons, and creates a third image from the logarithm of the ratio of the intensity at each location in the two original images. In this third image, the contrast is proportional to the mean free path of an electron through the material being imaged.

6.2.3: Wulff and Winterbottom Calculations

The Wulff construction is the thermodynamically stable shape for a nanoparticle. In the Wulff construction, the length of a vector, $d(xyz)$, normal to crystal face (xyz) which connects face (xyz) with the origin is proportional to the surface free energy per unit area of crystal face (xyz). Figure 6.1 shows a Wulff construction for platinum using the literature $\gamma_{Pt(111)} / \gamma_{Pt(001)}$ ratio of 0.84 from Vitos et. al.¹⁷⁰

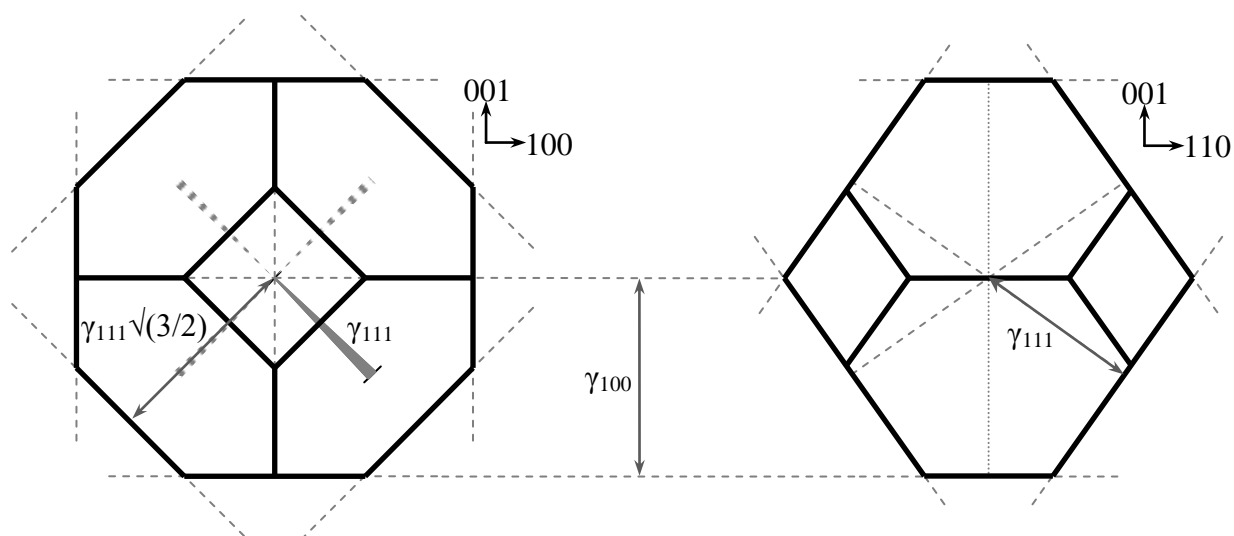


Figure 6.1: Wulff construction¹⁵⁷ for platinum using $\gamma_{(111)}:\gamma_{(001)}$ ratio of 0.84 from Vitos et. al.¹⁷⁰

The SrTiO₃ nanocuboid facets were measured by drawing a line from each facet to the opposite facet perpendicular to those facets and then measuring the length of the line. As the nanocuboids were not perfectly square, the vertical and horizontal directions were averaged, as were the two diagonals. Only cuboids which were imaged near to zone axis were counted. A total of 38 nanocuboids were measured in this manner. The specifics are presented in Table 6.1. The ratio of the $d_{(110)}:d_{(100)}$ was calculated as 1.137:1, with a standard deviation of 0.055.

The SrTiO₃ (110) surface free energies calculated in Chapter 3 cannot be directly compared to previous calculations of the SrTiO₃ (100) surface free energies as they were calculated using different parameters. Values for surface structures on both orientations were calculated by Professor Laurence D. Marks with identical parameters for each surface orientation using a revTPSSh functional.⁷³ The values for each surface orientation can therefore be directly

Table 6.1: $d_{(110)}:d_{(100)}$ ratio for nanocuboids following various annealing conditions.

Annealing Conditions	# Cuboids Measured	$d_{(110)}:d_{(100)}$ Ratio	Standard Deviation
As-prepared	7	1.129	0.027
700°C, 5h, Air	2	1.173	0.032
750°C, 10h, Air	3	1.130	0.039
800°C, 5h, Air	3	1.198	0.038
950°C, 2h, O ₂	8	1.140	0.026
950°C, 5h, O ₂	6	1.160	0.050
950°C, 20h, O ₂	9	1.107	0.086
Total	38	1.137	0.055

compared in those calculations. The calculations by Marks are therefore used for the Wulff analysis of SrTiO₃ nanocuboids.

The calculations by Marks⁷³ do not contain all the (110) surface structures from Chapter 3: only the half-O₂ and (3x1) structures were included. As such, the surface free energies of the other (110) surface structures were extrapolated from their position relative to half-O₂ and (3x1) surface compositions and energies. The change in energy for the half-O₂ and (3x1) structures between the Marks calculations⁷³ and those from Chapter 3 was plotted as a linear function of surface composition. For the (2x1), (4x1), (5x1), (6x1), (1x1) and Sr-terminated surface structures, the appropriate change for that composition was then added to the calculated surface free energy, to obtain a value that could be directly compared to the Marks calculations. The calculations by Marks also did not contain the SrTiO₃ (100) (2x1) structure or any hydroxylated structures. The (2x1) surface free energy was extrapolated from the difference between the (2x1) and the average of the c(4x2) and (2x2) energies in previous calculations by Andres Becerra-Toledo.⁷⁰ The hydroxylated structures were extrapolated using the same differences between the

dry and hydroxylated structures as were found in previous calculations by Danielle Kienzle [($\sqrt{13}\times\sqrt{13}$)-R33.7°]⁷¹ and Andres Becerra-Toledo [(2x1)].⁷⁰ The surface free energies for the calculations by Marks⁷³ and those extrapolated are presented in Figure 6.2. Note that several of the structures are not consistent with experiment exist as DFT calculated models only (e.g. ($\sqrt{13}\times\sqrt{13}$)-R33.7° and ($\sqrt{2}\times\sqrt{2}$)-R45° structures), but for completeness all are included here. None of these were found to be present on the nanocuboid surfacers. The ratios of surface free energies for all possible (110) and (100) pairings were then calculated.

Simply using these ratios, however, is not necessarily enough to determine which pair best matches the observed ratios. A rigorous application of the Wulff construction to the SrTiO₃ nanocuboids requires an extra constraint to account for the difference between the compositions of the surface and the bulk. This constraint will be similar to the bulk starvation energy of a Wulff construction of an alloyed metal nanoparticle.^{171,172} For each excess TiO₂ unit at the surface, the bulk will be deficient by one TiO₂ unit, or could equally be viewed as having one excess SrO unit. The bulk starvation correction is therefore equal to the total excess TiO₂ or SrO at the surface, multiplied by the energy needed to separate a SrTiO₃ unit into SrO and TiO₂ units (1.425 eV).

Next, the contribution of the surface plus bulk starvation to the total free energy of a 60 nm particle of the observed shape was calculated. This was done by multiplying the free energy per unit area of a surface structure by the surface area of that facet in the observed particle shape, summing over all facets, and adding the bulk starvation correction. This was carried out twice:

for nanocuboids which were perfectly stoichiometric when synthesized, and for nanocuboids which were terminated only in TiO_2 when synthesized.

The surface free energies used in the calculation are for the surface structure on a bulk of composition SrTiO_3 . The same surface on a bulk of composition $\text{Sr}_{1-x}\text{TiO}_{3-2x}$ would be slightly

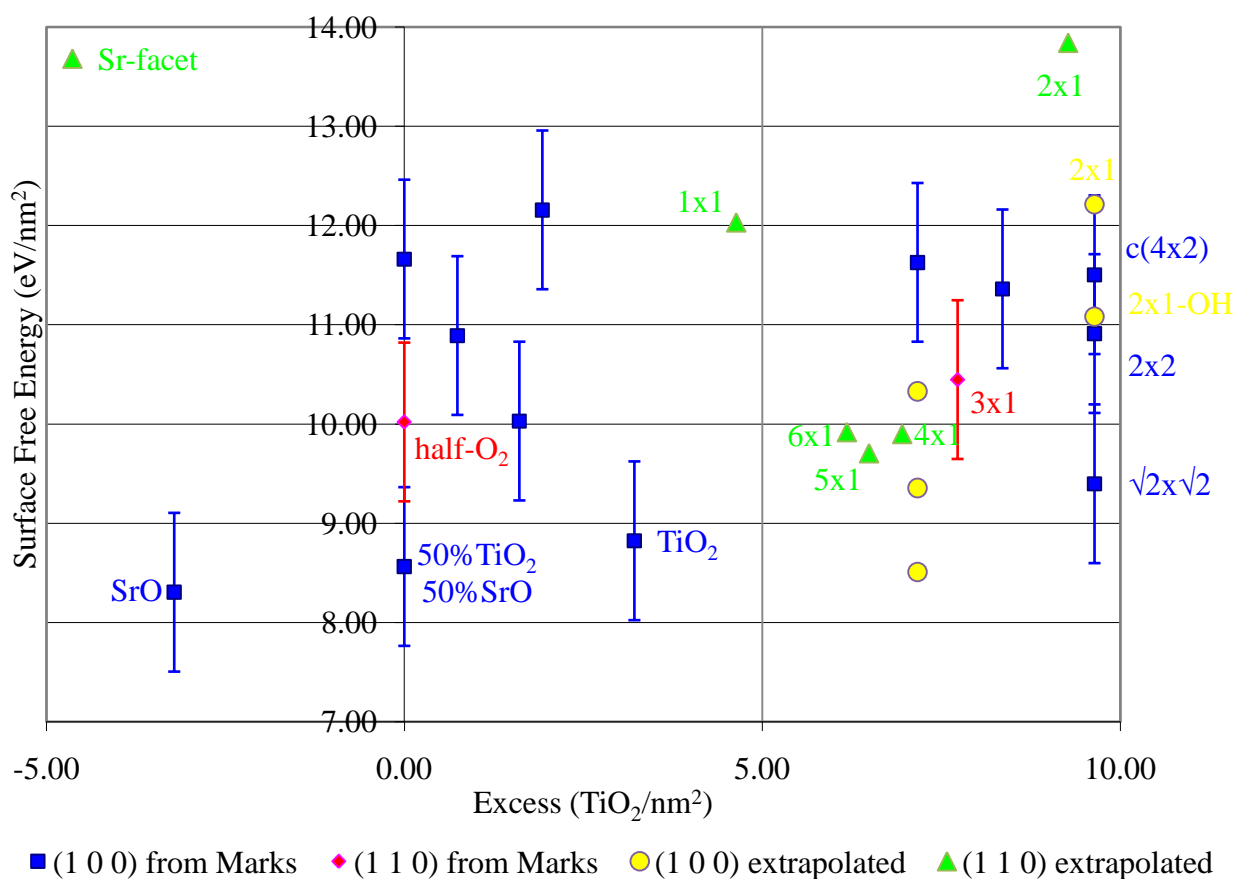


Figure 6.2: Surface free energies and compositions for structures calculated by Professor Marks⁷³ and surface energies extrapolated to match calculation parameters for other structures of interest. Structures which are discussed in this work are labeled. Error bars shown only for calculated structures.

different, and a further correction would be required to be rigorously accurate in the application of the Wulff construction. However, this correction is likely minimal, and an approximation which ignores it should be sufficient.

The Winterbottom construction¹⁵⁸ is similar to the Wulff construction,¹⁵⁷ but includes the interface free energy between the particle and the substrate and the surface free energy of the substrate. The interface free energy can be written as:

$$\gamma_{\text{Int}} = \gamma_{\text{Pt}} + \gamma_{\text{STO}} - \gamma_{\text{Bond}}$$

where γ_{Bond} is the free energy change per unit area associated with bonding across the interface, γ_{Pt} the surface free energy of the relevant Pt face, and γ_{STO} the surface free energy of the relevant SrTiO₃ face. This assumes that the SrTiO₃ surface is rigid and flat, although there have been reports of other nanoparticle systems where this is not true.¹⁷³ The Wulff shape will be truncated at a plane, the location of which is determined by the difference between the interfacial free energy and the substrate free energy (Figure 6.3).¹⁵⁸

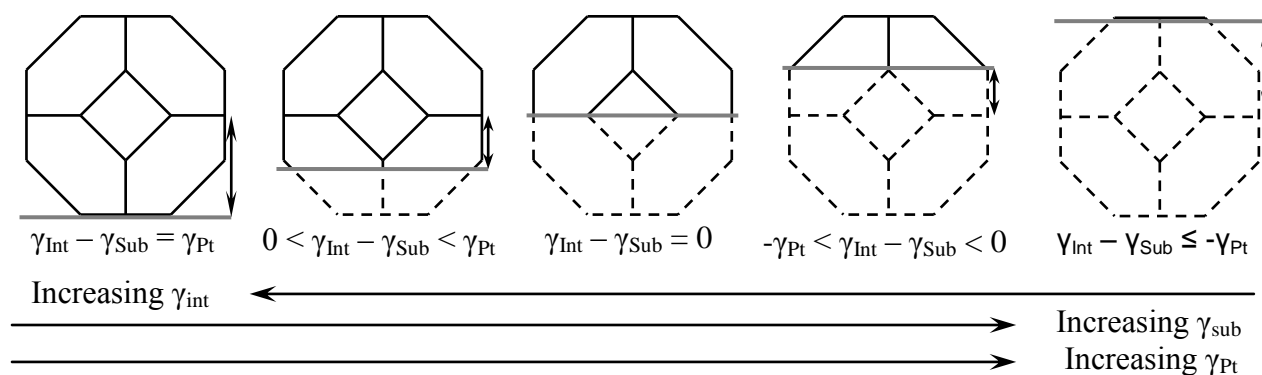


Figure 6.3: Winterbottom construction¹⁵⁸ for platinum on a surface, showing relative energies for different possible degrees of truncation. Wulff shape in black, substrate surface in grey, with arrow indicating magnitude of $\gamma_{\text{Int}} - \gamma_{\text{Sub}}$.

6.3: Results

6.3.1: General nanocuboid morphology and bulk structure

TEM imaging of the SrTiO₃ nanocuboids revealed a general cubic morphology (Figure 6.4). There was some agglomeration of the nanocuboids, which in general decreased with sonication during sample preparation. The SrTiO₃ nanocuboids were each a single crystal, as revealed through small probe electron diffraction (Figure 6.5). The SrTiO₃ nanocuboids have the (100) face primarily exposed, but with slightly rounded corners. HREM revealed that the rounded corners are in fact a combination of the (100) and (110) faces and steps (Figure 6.5).

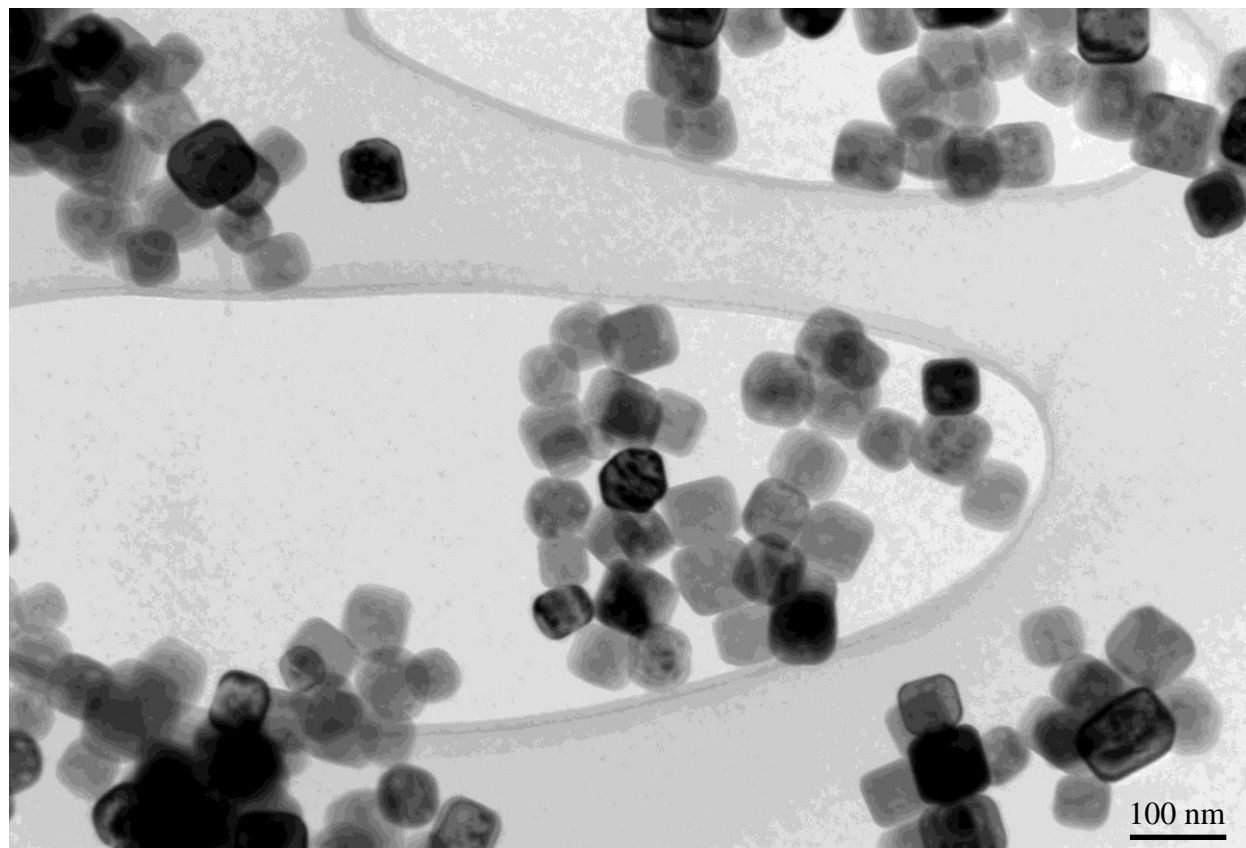


Figure 6.4: Low resolution TEM images of as-prepared SrTiO₃ nanocuboids.

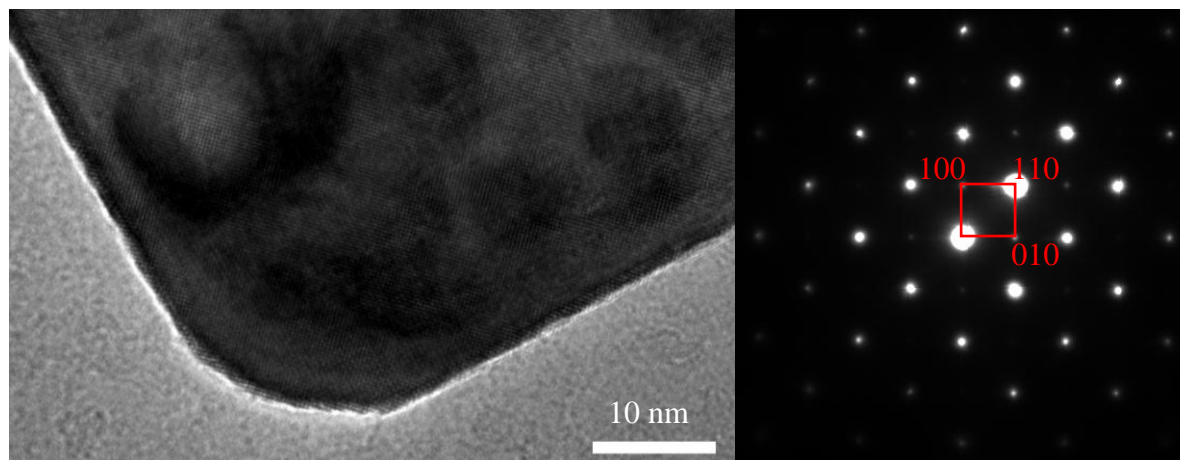


Figure 6.5: Left: HREM image of an as-prepared nanocuboid corner showing (100) and (110) step edges. Right: Near zone axis TED of a single as-prepared nanocuboid.

Additionally, the faces, although appearing flat at low magnifications, have many defects and step edges when viewed in high resolution.

There were features present within the cuboids with roughly the same shape (square with rounded corners) as the nanocuboids. Thickness mapping indicated that the areas with these features were thinner than the rest of the nanocuboids. Since none could be found at the surface, it was inferred that they were voids in the interior of the nanocuboids. Later experiments confirmed this inference.

6.3.2: Nanocuboid annealing and TEM surface characterization

Nanocuboids annealed on SiO_x supports were found to sinter, even at relatively low temperatures (e.g. 600°C). This occurred because SiO_x is a sintering agent for SrTiO_3 . As

individual nanocuboids could not be distinguished following annealing on SiO_x supports, further studies were not attempted.

SrTiO_3 nanocuboids annealed either prior to dispersion or following dispersion on SiN windows showed similar transformations. The major difference between the two was that samples annealed on SiN window supports, being already dispersed, could withstand higher annealing temperatures before sintering made studies difficult. The (110) faceting at the corners becomes more apparent upon annealing (see Figure 6.6 and Figure 6.7). However, the measurement of the ratio of exposed (100) to (110) did not change; only the number of surface

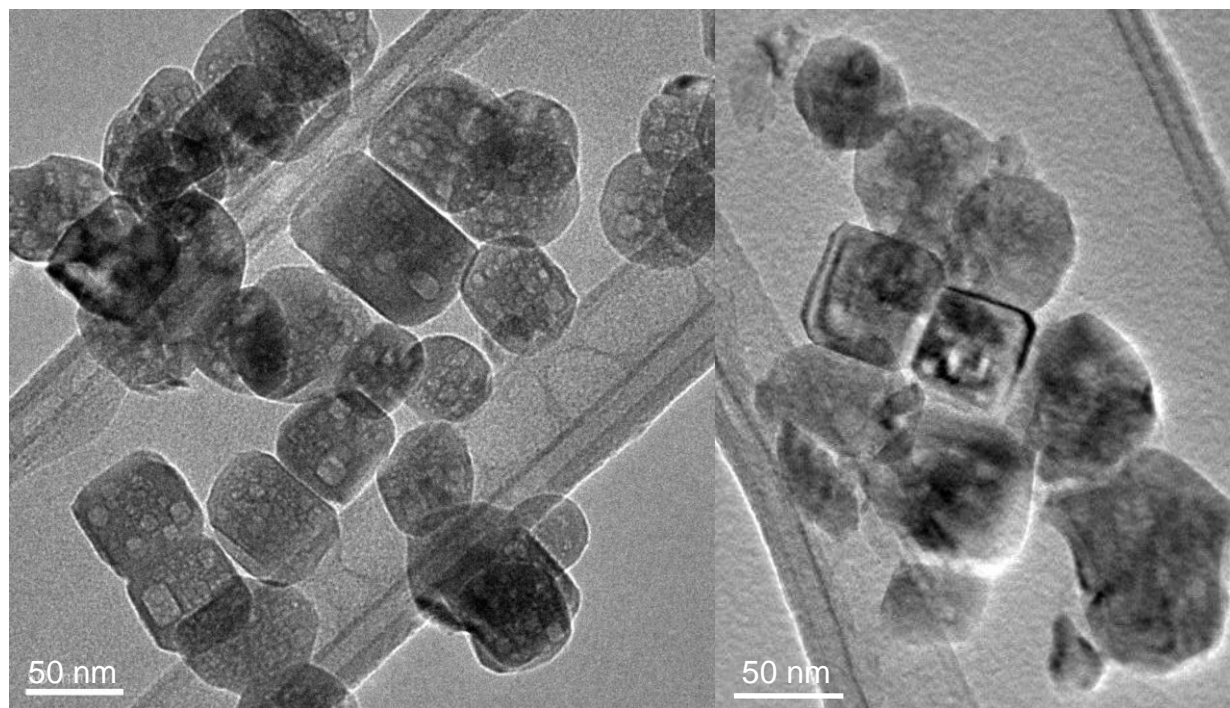


Figure 6.6: Samples annealed prior to dispersion on TEM grid. Left: 700°C for 5 hours in air. Right: 850°C for 1 hour in air.

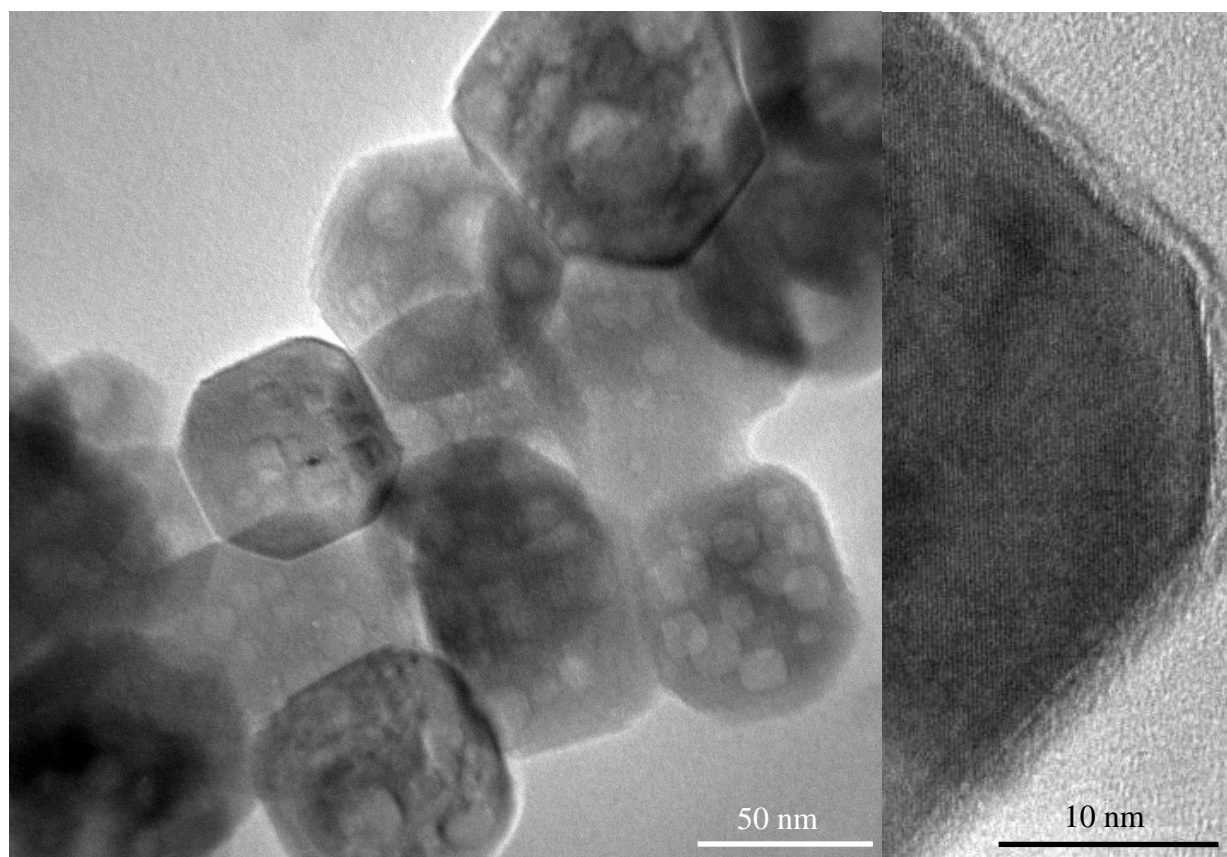


Figure 6.7: Low resolution TEM (left) and HREM (right) images of nanocuboids annealed at 950°C for 20 hours showing smoother (100) faces and distinct (110) faceting at the corners.

steps was reduced upon annealing. The voids showed changes similar to the exterior surface of the nanocuboids: when annealed, the rounded corners of the voids turned into sharp (110) facets.

Nanocuboids annealed at 600°C and 700°C (Figure 6.6) in air for five hours prior to dispersion showed slight irregularities in some cuboids, but by and large remained cuboid. The major change was that the rounded corners became straight (110) facets, both for the exterior surface of the nanocuboids and for the internal voids. Nanocuboids annealed at 750°C in air for

ten hours showed some sintering and some loss of cubic shape. Those annealed at 800°C in air for five hours showed even more sintering and loss of cubic shape. However, in both the 750°C sample and the 800°C sample, the voids retained their cubic shape with pronounced (110) facets at the corners. Samples annealed at 850° (Figure 6.6) and 950°C in air for one hour each showed loss of cubic shape for some nanocuboids, but a significant portion of the nanocuboids retained their cubic shape, especially at 850°C. Additionally, the voids which were present were largely the same as in the samples annealed at lower temperatures.

In general, the nanocuboids annealed on SiN grids showed the same features as those annealed prior to being dispersed: (110) facets formed at the corners of the nanocuboids and at the corners of the voids. The major difference was that the nanocuboids annealed on SiN grids remained dispersed and maintained their cubic shape at higher temperatures. The decreased sintering is likely due only to the fact that each nanocuboid was in proximity to fewer other nanocuboids. Nanocuboids annealed at 950°C in flowing O₂ for two, five, and twenty hours (Figure 6.7) all looked essentially identical. The only major difference between these samples and the as-prepared nanocuboids was the development of (110) facets at the corners of the nanocuboids and of the voids. The exception to this was a single nanocuboid in the 950°C sample which showed a 2x1 superlattice which was clearly visible in both HREM and TED. As the intensity of the 2x1 supercell spots followed the Laue circle, it is concluded that they must be due to a bulk supercell and not a surface reconstruction. As this was found only once, it was assumed to be anomalous. A sample annealed at 1100°C in flowing O₂ for five hours maintained a roughly cubic shape for the nanocuboids. The corners of both the nanocuboids and the voids,

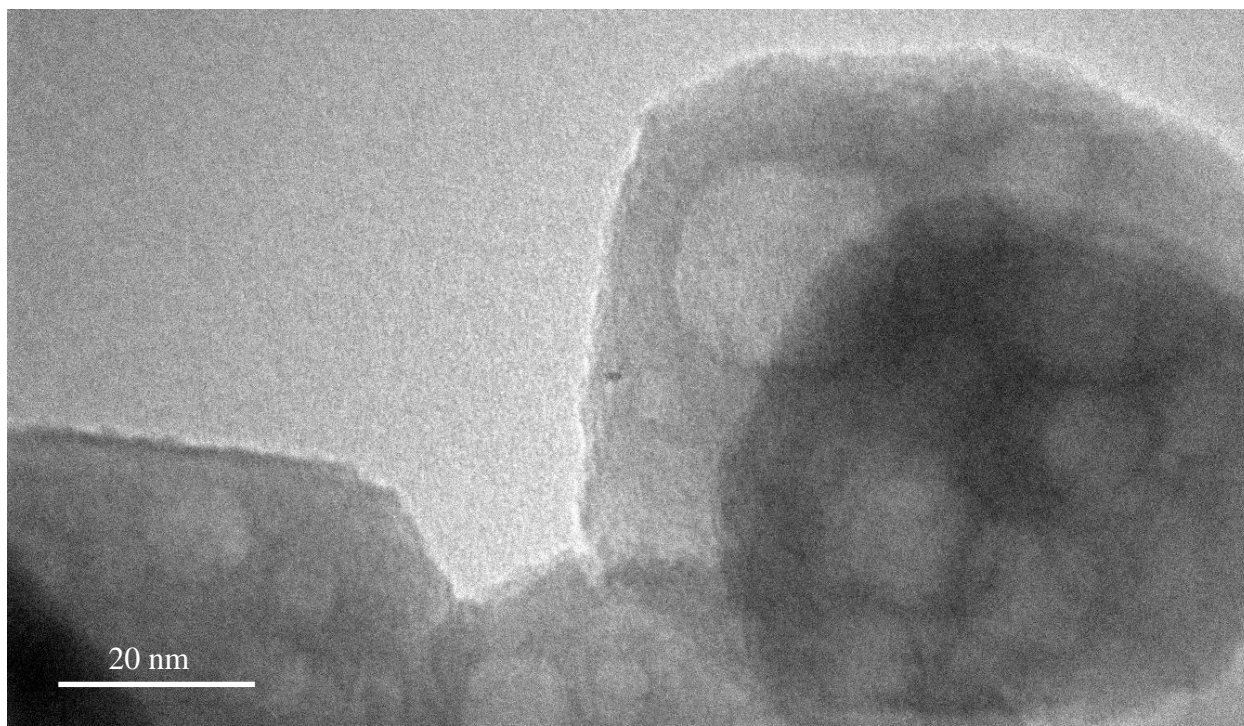


Figure 6.8: TEM of nanocuboids annealed in flowing O_2 for 5 hours at $1100^\circ C$ showing roughening of surface.

however, were somewhat rounded rather than being straight (110) facets. Additionally, the surface was rough, unlike other samples which had relatively flat surfaces (Figure 6.8).

The voids behaved in much the same way as the exterior of the cuboid, which is an indication as to the nature of the voids. That their edges show the same faceting as the exterior surfaces implies that they are essentially interior surfaces. Further, the fact that they do not explode indicates that they are either empty or filled with a gas which is capable of diffusing through $SrTiO_3$ to escape.

At all annealing temperatures, even when the nanocuboids lost their cubic shape, they remained single crystalline, as evidenced by TED. However, at no time was a surface reconstruction observed, either using a CCD camera or using film. Some streaking was observed in TED, but never a clear surface reconstruction. The presence of voids and the edge effects they create in a diffraction pattern are responsible for the streaking, which in turn would likely obscure a surface reconstruction in TED even if one were present.

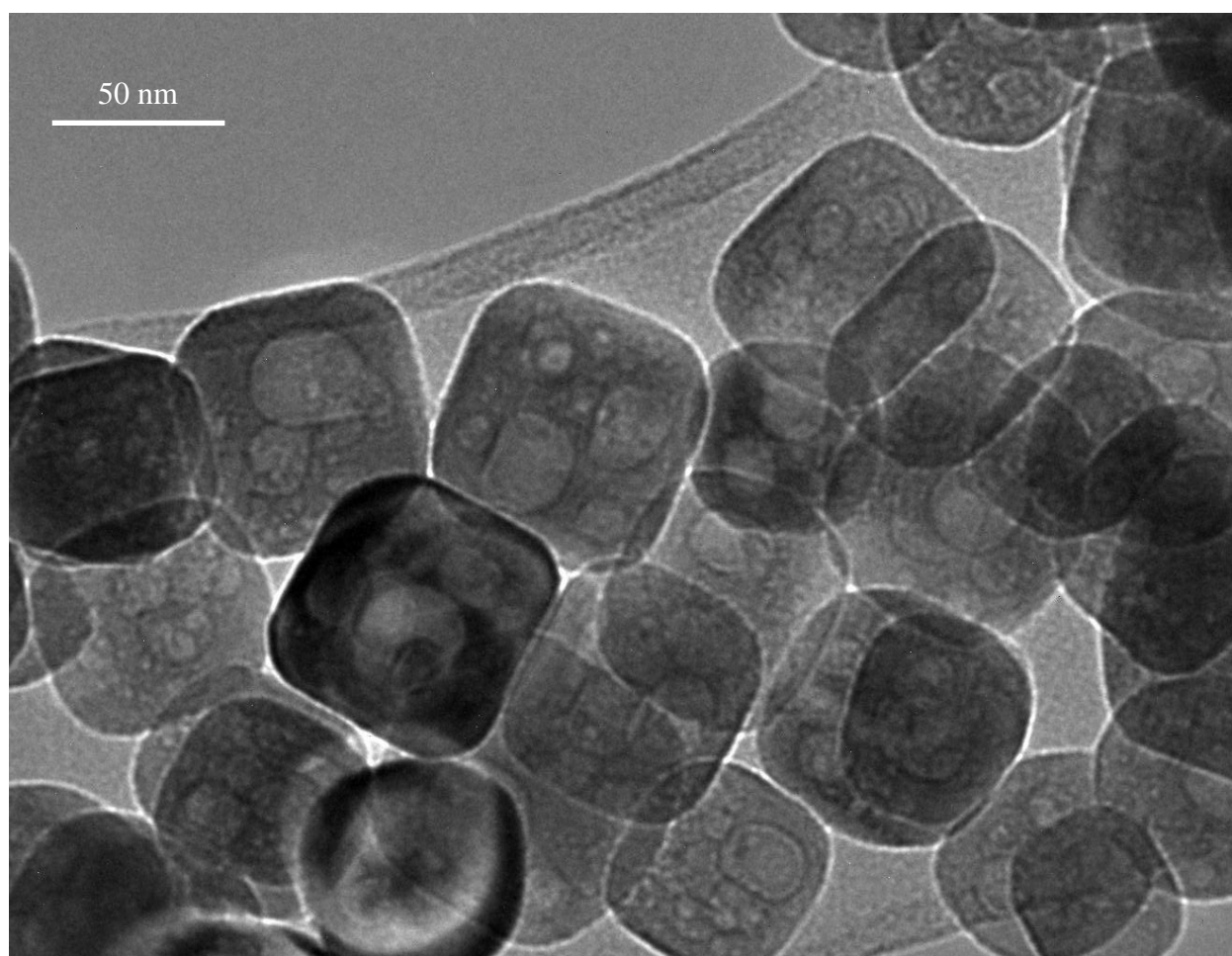


Figure 6.9: TEM of samples etched in 0.3N 3:1 (v/v) HCl:HNO₃ solution for 20 minutes.

6.3.3: Acid etching of SrTiO_3 nanocuboids

Acid etching is expected to remove SrO from the surface of strontium titanate.⁶⁴ Nanocuboids etched in buffered $\text{NH}_4\text{:HF}$ solution for 0.25 hours completely dissolved, yielding only SrF_2 . Nanocuboids etched for 0.3 hours in 0.3M HCl:HNO_3 appeared unchanged from the as-prepared nanocuboids (Figure 6.9). Nanocuboids etched for twelve hours in 0.3M HCl:HNO_3 did not retain cubic shape (Figure 6.10). However, the (100) facets were still predominantly exposed, simply with more corners and step edges. Nanocuboids etched in 3M HCl:HNO_3 for 0.75 hours were even less regular in shape (Figure 6.10). They too retained predominantly (100) facets. The loss of cubic morphology was attributed to the acid removing material and exposing

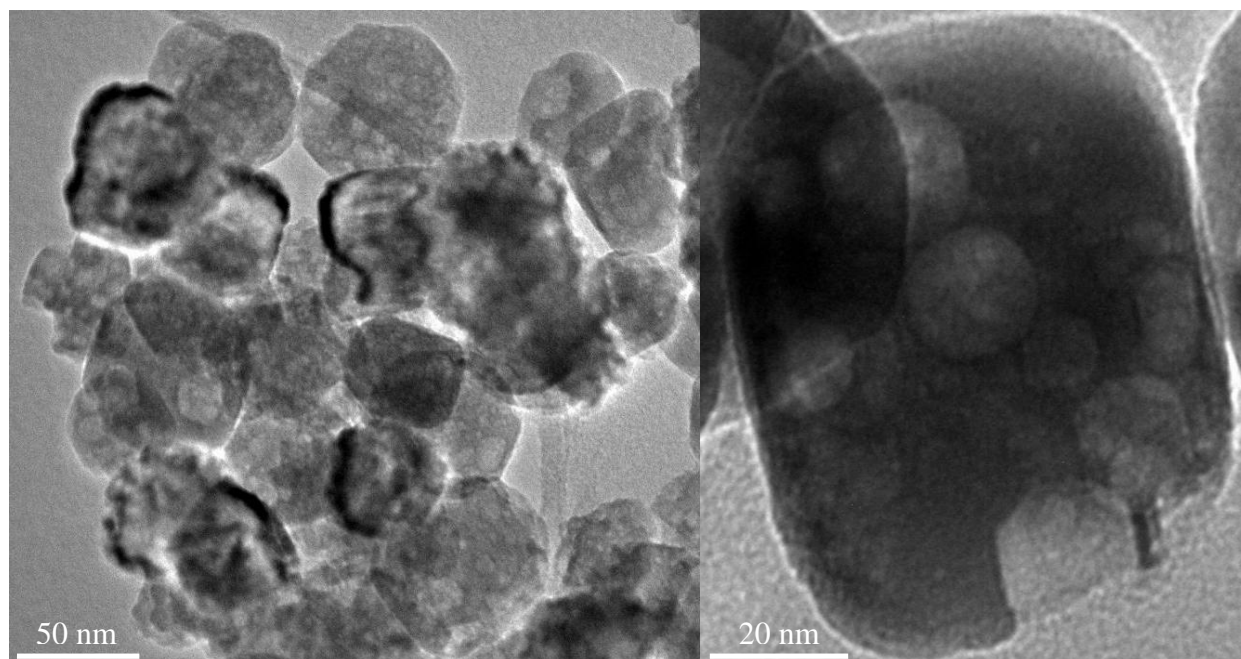


Figure 6.10: TEM image of sample etched in 3:1 (v/v) HCl:HNO_3 solution. Left: 0.3N for 12 hours. Right: 3.0N for 15 minutes, showing a void which has become an exterior surface.

the interior voids. This accounts for the facets remaining while the shape changed. The voids, which were interior surfaces with the same facets exposed, became exterior surfaces.

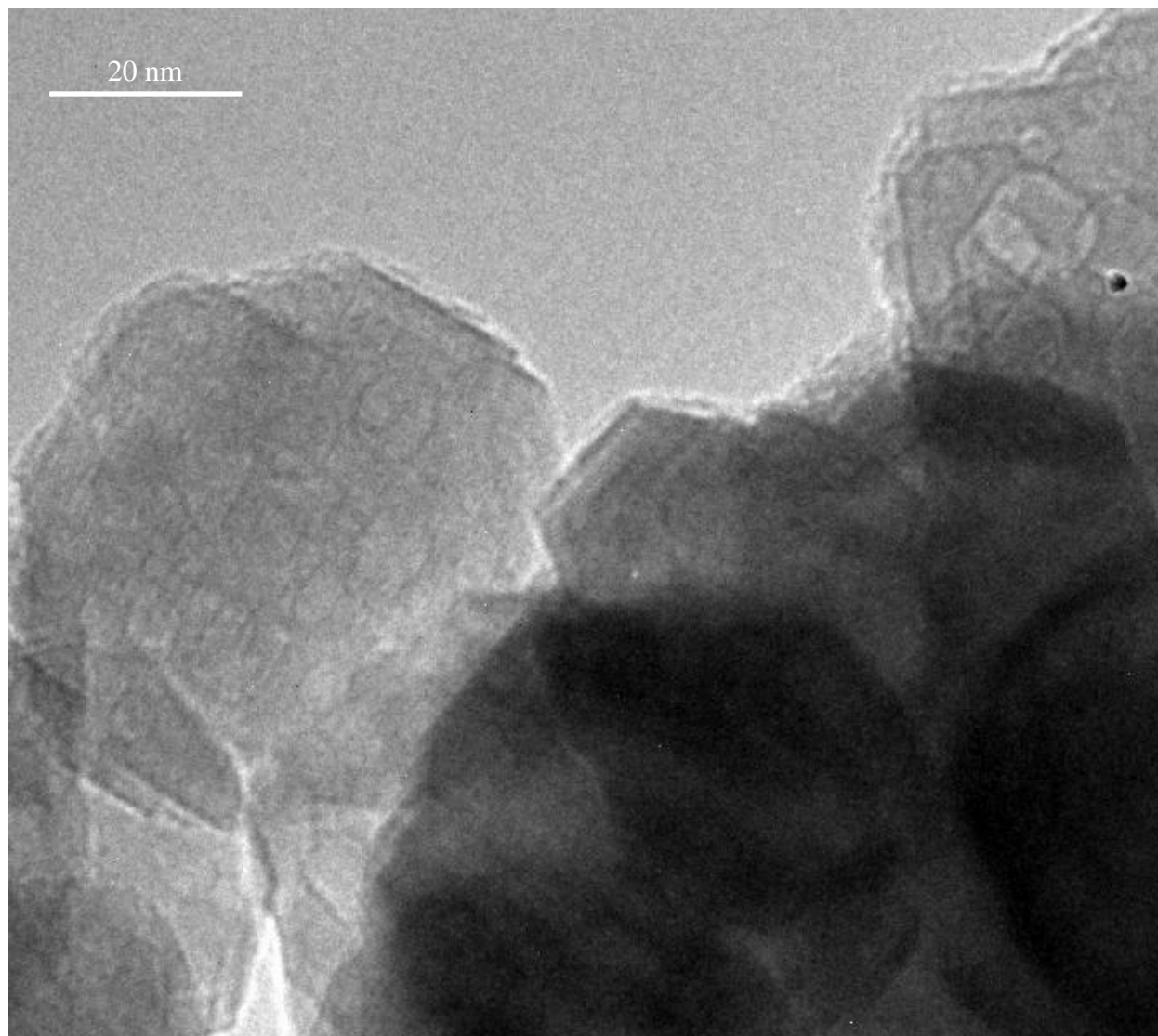


Figure 6.11: TEM of sample etched in 0.3N 3:1 (v/v) HCl:HNO₃ solution for 12 hours then annealed at 950°C for 5 hours in flowing O₂ showing irregular shape but well defined (100) and (110) facets.

6.3.4: Annealing of acid etched nanocuboids

Samples of acid etched nanocuboids which were not already dispersed on a SiN grid could not be obtained for further experimentation. Annealing of acid etched samples dispersed on SiN grids met with mixed results. The SiN grids in these cases tended to fall apart upon annealing, possibly due to an interaction with some acid remaining on the nanocuboids. Some nanocuboids were found to image, usually near the corners of the window, but as the support was unstable high quality images could not be obtained. The best images were obtained for samples etched in 0.3M HCl:HNO₃ for twelve hours and annealed at 950°C in flowing oxygen for 5h (Figure 6.11). While the etched nanocuboids showed more step edges and smaller plateau sizes than the unetched and annealed nanocuboids, the (100) and (110) facets were very flat and in approximately the same proportions.

6.3.5: Wulff Construction for SrTiO₃ Nanocuboids

The formation of well defined, stable facets upon annealing indicates that the shape of the nanocuboids is determined by a Wulff construction.¹⁵⁷ To determine the relative surface energies and surface composition, the $d_{(110)}:d_{(100)}$ was counted for a total of 38 nanocuboids annealed at various temperatures (Table 6.1). The ratio of $d_{(110)}:d_{(100)}$ was in this manner determined to be 1.137:1, with a standard deviation of 0.055.

To determine what pair of (110) and (100) surface structures best accounts for the observed shape, the ratio of $\gamma_{(110)}:\gamma_{(100)}$ was calculated (Table 6.2) for each pair of surface structures as described in section 6.2.3: using the energies supplied by Professor Marks⁷³ and the

Table 6.2: $\gamma_{(110)}:\gamma_{(100)}$ ratios from calculations by Professor Marks⁷³ and extrapolated energies.

Values within one standard deviation of experiment are highlighted.

	(1 1 0)							
	Sr facet	half-O ₂	(1x1)	(6x1)	(5x1)	(4x1)	(3x1)	(2x1)
SrO (1x1)	1.648	1.207	1.449	1.194	1.169	1.192	1.258	1.667
50% SrO (1x1) 50% TiO ₂ (1x1)	1.598	1.170	1.405	1.158	1.133	1.156	1.220	1.616
2 $\sqrt{2}\times\sqrt{2}$ -R45°	1.173	0.859	1.032	0.850	0.832	0.849	0.896	1.187
($\sqrt{13}\times\sqrt{13}$)-R33.7° on SrO termination	1.256	0.920	1.105	0.911	0.891	0.909	0.959	1.271
4 $\sqrt{2}\times\sqrt{2}$ -R45°	1.364	0.999	1.200	0.989	0.968	0.987	1.042	1.380
($\sqrt{5}\times\sqrt{5}$)-R26.6° on SrO termination	1.125	0.824	0.990	0.816	0.798	0.814	0.859	1.138
TiO ₂ (1x1)	1.551	1.136	1.364	1.124	1.100	1.122	1.184	1.569
($\sqrt{13}\times\sqrt{13}$)-R33.7°	1.177	0.862	1.035	0.853	0.835	0.851	0.898	1.190
($\sqrt{5}\times\sqrt{5}$)-R26.6°	1.204	0.882	1.059	0.873	0.854	0.871	0.919	1.218
$\sqrt{2}\times\sqrt{2}$ -R45°	1.456	1.066	1.280	1.055	1.033	1.053	1.112	1.473
c(4x2)	1.189	0.871	1.046	0.862	0.844	0.860	0.908	1.203
(2x2)	1.254	0.918	1.103	0.909	0.889	0.907	0.957	1.269
Dry (2x1)	1.120	0.820	0.985	0.812	0.795	0.811	0.855	1.133
(2x1) H ₂ O	1.235	0.904	1.086	0.895	0.876	0.893	0.943	1.249
($\sqrt{13}\times\sqrt{13}$)-R33.7° 2 H ₂ O	1.325	0.970	1.165	0.960	0.940	0.958	1.011	1.340
($\sqrt{13}\times\sqrt{13}$)-R33.7° 4 H ₂ O	1.463	1.071	1.286	1.060	1.037	1.058	1.117	1.480
($\sqrt{13}\times\sqrt{13}$)-R33.7° 6 H ₂ O	1.608	1.178	1.414	1.166	1.141	1.163	1.228	1.627

other extrapolated energies. There are several pairs of surfaces which match the experimentally observed $d_{(110)}:d_{(100)}$ ratio. The total energy of a particle with the observed shape and a given pair of (110) and (100) surface structures is necessary to distinguish which pairs of surfaces are possible. The total energy contribution to a nanocuboid from the surface and the associated bulk

Table 6.3: Total contribution (in keV) to the free energy from surface free energies (eV) and bulk starvation for a stoichiometric 60nm diameter SrTiO₃ nanocuboids with the observed $d_{(110)}:d_{(100)}$ ratio. Values within 10 keV of the lowest energy value are highlighted.

	(1 1 0)							
	Sr facet	half-O ₂	(1x1)	(6x1)	(5x1)	(4x1)	(3x1)	(2x1)
SrO (1x1)	286	232	208	186	182	180	177	193
50% SrO (1x1) 50% TiO ₂ (1x1)	226	172	217	217	219	223	232	261
2√2x√2-R45°	269	215	260	261	262	266	275	304
(√13x√13)-R33.7° on SrO termination	243	219	264	265	266	270	279	308
4√2x√2-R45°	214	224	269	270	271	276	284	313
(√5x√5)-R26.6° on SrO termination	245	261	306	306	307	312	320	350
TiO ₂ (1x1)	224	240	285	285	286	291	299	329
(√13x√13)-R33.7°	342	357	403	403	404	409	417	446
(√5x√5)-R26.6°	362	377	422	423	424	429	437	466
√2x√2-R45°	360	375	421	421	422	427	435	465
c(4x2)	390	405	450	450	452	456	465	494
(2x2)	381	397	442	442	443	448	456	486
Dry (2x1)	399	415	460	460	462	466	475	504
(2x1) H ₂ O	384	399	444	445	446	450	459	488
(√13x√13)-R33.7° 2 H ₂ O	324	339	384	385	386	390	399	428
(√13x√13)-R33.7° 4 H ₂ O	310	326	371	371	372	377	385	415
(√13x√13)-R33.7° 6 H ₂ O	298	314	359	359	361	365	374	403

starvation was calculated for a stoichiometric nanocuboid (Table 6.3) and one which began with a titanium termination (Table 6.4).

Table 6.4: Total contribution (in keV) to the free energy from surface free energies (eV) and bulk starvation for a 60nm diameter SrTiO₃ nanocuboids with the observed $d_{(110)}:d_{(100)}$ ratio synthesized with a titanium rich surface. Values within 10 keV of the lowest energy value are highlighted.

	(1 1 0)							
	Sr facet	half-O ₂	(1x1)	(6x1)	(5x1)	(4x1)	(3x1)	(2x1)
SrO (1x1)	350	296	272	250	246	244	241	247
50% SrO (1x1) 50% TiO ₂ (1x1)	290	236	212	189	186	183	181	197
2√2x√2-R45°	333	279	255	233	229	227	224	240
(√13x√13)-R33.7° on SrO termination	307	254	230	207	204	206	215	244
4√2x√2-R45°	278	224	206	206	207	212	220	249
(√5x√5)-R26.6° on SrO termination	301	248	242	242	243	248	256	286
TiO ₂ (1x1)	229	176	221	221	222	227	235	265
(√13x√13)-R33.7°	278	294	339	339	340	345	353	383
(√5x√5)-R26.6°	298	313	358	359	360	365	373	402
√2x√2-R45°	296	312	357	357	358	363	371	401
c(4x2)	326	341	386	386	388	392	401	430
(2x2)	317	333	378	378	379	384	392	422
Dry (2x1)	335	351	396	396	398	402	411	440
(2x1) H ₂ O	320	335	380	381	382	386	395	424
(√13x√13)-R33.7° 2 H ₂ O	260	275	320	321	322	327	335	364
(√13x√13)-R33.7° 4 H ₂ O	246	262	307	307	308	313	322	351
(√13x√13)-R33.7° 6 H ₂ O	235	250	295	295	297	301	310	339

Previous studies indicated that SrCO₃ formed upon annealing the nanocuboids.¹⁷⁴ Upon annealing for 20 hours, the SrCO₃ increased to 0.3% of the total mass by weight.¹⁷⁵ If it was being formed from SrO leaving the nanocuboids, this would constitute ~18,000 SrO units

removed from a 60 nm nanoparticle of the observed shape. This is far less than the number of excess TiO_2 units on a pair of TiO_2 rich surfaces. For example, a cuboid of the same size terminated by the (3×1) structure on the (110) facets and the $(\sqrt{2} \times \sqrt{2})\text{-}45^\circ$ structure on the (100) facets would have a total of $\sim 175,000$ excess TiO_2 units. Even if the formation of SrCO_3 leads to titanium enrichment on the surface and reduces the starvation energy, it is an order of magnitude too small to cancel out the starvation energy. Therefore, unless the nanocuboids are formed already nonstoichiometric, or titanium or strontium is removed in some other way, for example by acid etching, the bulk starvation energy will have an effect and must be included in the calculations. Due to the similarities between the nanocuboids as-prepared and those following acid etching (which should be TiO_2 terminated⁶⁴), the possibility that the nanocuboids are initially titanium terminated must be considered.

Since the change in energy to the particle due to the bulk starvation energy is significantly larger than the change due to the different surface free energy, the overall surface composition of an annealed nanocuboid will be similar to the surface composition of the as-prepared nanocuboid. If, for example, the as-prepared nanocuboid is stoichiometric, the lowest energy particle will have (100) facets with a 50%/50% mixture SrO (1×1) and TiO_2 (1×1) terminations and the (110) facets will have the half- O_2 structure (Table 6.3). If, on the other hand, the initial surface of an as-prepared nanocuboid is an unreconstructed TiO_2 surface, then the overall lowest energy structure will be the TiO_2 (1×1) structure on the (100) facets and the half- O_2 structure on the (110) facets (Table 6.4). The surface structure after annealing will be determined by the dominant species in the nanocuboids as they are prepared. This in turn will

depend upon the preparation conditions, such as the acidity of the solution in which they are formed and what (if any) surfactant is used.

6.3.6: Platinum Nanoparticles on SrTiO₃ Nanocuboids

Images of nanocuboids after one cycle of platinum ALD showed that platinum nanoparticles approximately 1.5 – 2.5 nm in diameter were formed (Figure 6.12). High-resolution imaging shows that the particles are metallic Pt and that the lattice fringes of the platinum nanoparticles were aligned with those of the strontium titanate with cube-on-cube epitaxy. A strong epitaxy is unsurprising, as the lattice mismatch between platinum and strontium titanate is only 0.4% (3.920 Å for platinum and 3.905 Å for strontium titanate). The platinum was observed to grow only in the (100) direction and not the (111) direction, which implies that the SrTiO₃ nanocuboids were TiO₂ terminated,¹⁷⁶ in agreement with our characterization of the nanocuboid surfaces above. Such interfaces are known to have strong Pt–O bonds between the metal and the oxide support.^{176,177}

The observed shape of the platinum particles matches the Winterbottom construction.¹⁵⁸ The Wulff construction for platinum using the literature $\gamma_{Pt(111)} / \gamma_{Pt(001)}$ of 0.84 from Vitos et al.¹⁷⁰ is shown in Figure 6.1. By comparing the truncation in the experimental images to the Pt Wulff construction, it can be seen that slightly more than half of the Wulff shape was exposed above the substrate surface (Figure 6.13). Exactly half the particle would be exposed when the substrate surface free energy and the interface energy are equal, i.e. $(\gamma_{interface} - \gamma_{substrate}) = 0$, while the entire Wulff construction would be exposed if the interface energy were greater than or equal to the sum of the particle surface free energy plus the substrate surface free energy, i.e.

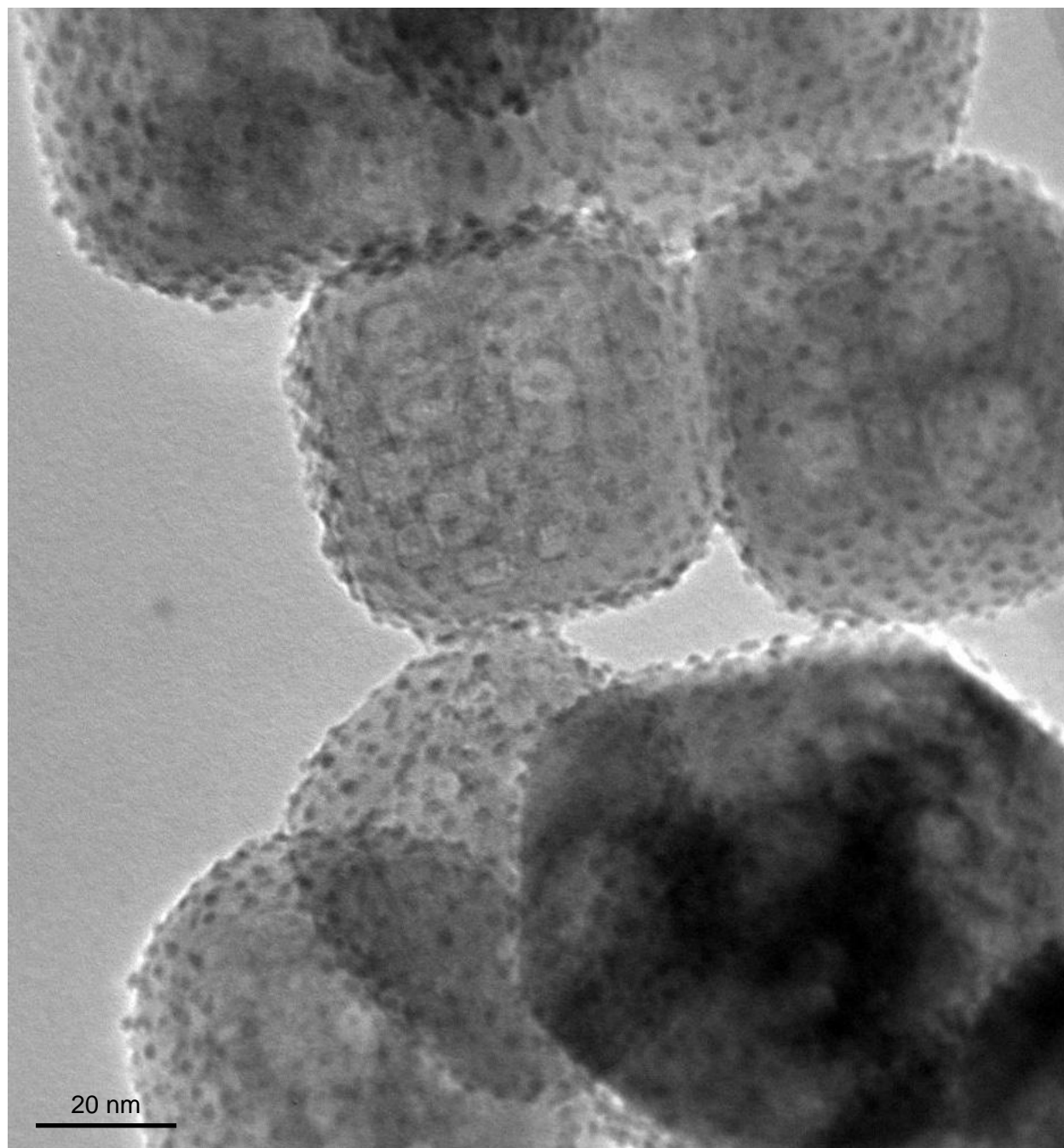


Figure 6.12: TEM image of platinum nanoparticles on strontium titanate nanocuboids.

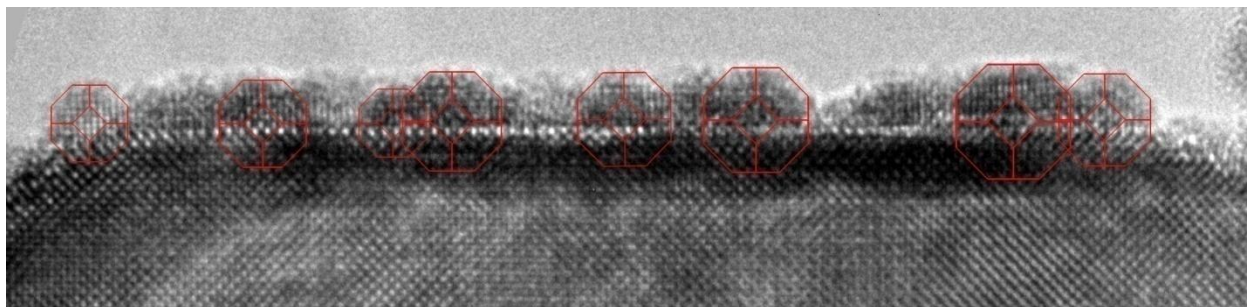


Figure 6.13: HREM image of platinum nanoparticles on the (100) face of a strontium titanate nanocuboid. Near perfect alignment of Pt (100) and SrTiO₃ (100) lattice fringes indicates a strong epitaxy. Wulff construction shapes for platinum are overlaid upon the platinum nanoparticles in red, showing that slightly more than half of the Wulff construction shape exists above the substrate surface.

$(\gamma_{interface} - \gamma_{substrate}) \geq \gamma_{particle}$. Between 50% and 100% of the Wulff construction would be exposed when the interface energy is between the sum of the substrate surface free energy and the substrate surface free energy plus the particle surface free energy, i.e. $0 < (\gamma_{interface} - \gamma_{substrate}) < \gamma_{particle}$.¹⁵⁸ The experimental data shows that barely more than half of the particle is exposed, hence the interface energy is slightly greater than the substrate surface free energy, consistent with previous literature reports.¹⁷⁸

It was determined in section 6.3.5: (and will be discussed in more detail in section 6.4.3:) that the (100) faces of the SrTiO₃ nanocuboids are most likely terminated by a mix of SrO and TiO₂ terminations, or possibly entirely by a TiO₂ termination. If the former, then the platinum is likely growing on regions with TiO₂ termination, since the epitaxy indicates that it is growing on

a TiO_2 surface. The TiO_2 (1x1) structure has a surface free energy of $0.088 \text{ eV}/\text{\AA}^2$ when using the revTPSSh functional,⁷³ and $0.063 \text{ eV}/\text{\AA}^2$ when using a simple PBE (GGA) functional.⁷⁰ The absolute surface free energy for the (111) and (100) surfaces of platinum calculated by Vitos et. al. using a GGA functional are $0.143 \text{ eV}/\text{\AA}^2$ and $0.171 \text{ eV}/\text{\AA}^2$, respectively.¹⁷⁰ According to the experimental data the interface free energy between the SrTiO_3 nanocuboids and the Pt nanoparticles is slightly greater than the SrTiO_3 (100) surface free energy. This is in good agreement with (1) the GGA calculations by Asthagiri and Sholl, where the work of separation between Pt and TiO_2 terminated SrTiO_3 (001) was calculated to be $0.061 - 0.066 \text{ eV}/\text{\AA}^2$ for 2-5 monolayers of Pt,^{177,179} and (2) GGA calculations by Iddir et. al., where the work of separation was calculated to be $0.066 \text{ eV}/\text{\AA}^2$.¹⁷⁸

6.4: Discussion

6.4.1: Voids in SrTiO_3 nanocuboids

Within the nanocuboids are multiple voids (see, for example, Figure 6.4, Figure 6.6, and Figure 6.7), the edges of which are interior surfaces. These voids are visible as square features with rounded corners inside the as-prepared nanocuboids. These areas were thinner than the rest of the nanocuboids, implying that they were voids. That the voids behaved the same as the exterior of the nanocuboids upon annealing supported that inference. Confirmation of their nature came from the acid etching experiments. As the material separating the voids from the surface was etched away, the voids became exposed. This resulted in the irregular shapes that were observed after acid etching as the interior surface of the voids became exterior surfaces.

The annealing experiments also implied that the voids could not be filled with a liquid or gas. If they were filled with a gas or liquid, expansion during annealing would have caused the nanocuboids to explode. Alternatively if they were not vacant, then whatever was inside must have diffused through the SrTiO₃ and escaped.

The voids are most likely a product of the nanocuboid formation mechanism. The cubic crystal structure of SrTiO₃ should mean that as proto-nanocuboids form in solution, they would assume an approximately cubic shape. Such proto-nanocuboids can grow in one of two ways: additional species from solution can be deposited, or they can join with other proto-nanocuboids. When proto-nanocuboids join, their lattices will align, but it is unlikely that their edges will be perfectly flush. Non-aligned edges will result in gaps wherever multiple proto-nanocuboids join in this way. The gaps will vary in size, but will all have 90° angles at their corners, forming rectangular prism shaped voids. Upon annealing, the voids will assume the same shape as the cuboid exterior in order to minimize their energy.

During any acid etch, the (100) and (110) surfaces remained exposed in the same ratios. Even when the shape of the particles had changed significantly from their original cubic shape by exposing the voids, those voids had the same (100) and (110) exposed surfaces and the overall surface orientation was therefore unchanged. While irregular shapes would make many direct surface studies difficult, the surfaces of highly etched particles should remain same as the nanocuboids etched for shorter time periods which retained their cubic shape. Therefore, it is reasonable to conclude that what is learned about the regular shaped nanocuboids may be applied to these less regular shapes. Additionally, the high surface area of these irregularly shaped

particles makes them far better suited to catalytic studies. Recognizing this relationship may be a useful step in the direction of connecting surface studies with catalysis.

6.4.2: *SrTiO₃ nanocuboid surfaces*

Annealing at temperatures from 600°C to 950°C had similar effect on the SrTiO₃ nanocuboids. As described above, the surfaces formed well defined (100) and (110) facets. No further change to the surface structure was conclusively determined to occur for annealing at temperatures up to 950°C for as long as 20 hours. At temperatures of 1100°C, however, the surface was observed to roughen (Figure 6.8). It is well known that at higher temperatures oxygen chemical potential is reduced, and even an oxygen atmosphere becomes somewhat reducing at high enough temperatures. Indeed, the SrTiO₃ (100) c(6x2) surface reconstruction which was found at 1100°C was also found to be slightly reduced.¹²⁸ It is therefore likely that the nanocuboid surfaces become reduced when annealed at such high temperatures, leading to the observed surface roughness.

SrTiO₃ nanocuboids acid etched then subsequently annealed maintained the same (100) and (110) facets. The acid etched cuboids, according to the literature,⁶⁴ should have the surface strontium preferentially removed, and therefore be titanium oxide terminated. The fact that the as-prepared and acid etched nanocuboids displayed similar faceting suggests that the surfaces are titanium rich. However, the data from the acid etched and annealed nanocuboids is not good enough to actually measure the $d_{(110)}:d_{(100)}$ ratio. It cannot be confirmed, therefore, whether the same structures are present as in the nanocuboids that were annealed without an acid wash. Further studies, such as annealing acid washed nanocuboids before depositing them on a TEM

grid in order to avoid damaging the support, will be necessary before definite conclusions can be drawn.

The platinum growth also indicated that the nanocuboids were titanium terminated. The platinum grew epitaxially in the (100) direction on the SrTiO₃ (100), indicating that the platinum was growing on titanium terminated SrTiO₃ (100). If the nanocuboids were strontium terminated, a mix of (100) and (111) oriented platinum would have been observed.¹⁷⁶ This is also not completely conclusive, however. If the (100) surface were 50% TiO₂ (1x1) and 50% SrO (1x1), then the platinum might be growing only on the areas terminated by TiO₂. If such were the case, a higher interface energy between the SrO termination and platinum might aid in keeping the platinum particles separated.

The existence of the stable (110) facet indicates that the surface is either titanium rich or stoichiometric. DFT studies have shown that the strontium rich (110) surface would be stabilized by forming (100) facets, with the stability improving as the size of the (100) facets increased.³⁵ Because annealing leads to the (110) facets becoming well defined rather than disappearing, they must not be strontium terminated.

Application of the Wulff construction¹⁵⁷ with inclusion of a bulk starvation energy^{171,172} indicated that the bulk starvation energy has a much larger effect on the overall nanoparticle energy than does the specific energy of the surface. If the as-prepared nanocuboids are completely stoichiometric, then the lowest energy structure for that composition has the half-O₂ structure on the (110) facets and a 50%/50% mixture of the TiO₂ (1x1) and SrO (1x1) structures on the (100) facets (Table 6.3). The ratio of $\gamma_{(110)}:\gamma_{(100)}$ in this case is 1.170 (example by acid

etching, the bulk starvation energy will have an effect and must be included in t), within one standard deviation of the observed $d_{(110)}:d_{(100)}$ ratio (1.137 with a standard deviation of 0.055). The only other pairs of terminations which are close in energy (within 10,000 eV per nanoparticle) are the (3x1) or (4x1) structure on the (110) facets and the SrO (1x1) termination on the (100) facets (Table 6.3). The ratios of $\gamma_{(110)}:\gamma_{(100)}$ are 1.258 and 1.192, respectively, still relatively close to the observed $d_{(110)}:d_{(100)}$ ratio. However, such structures can be ruled out because the platinum epitaxy indicates that there is some TiO_2 on the (100) facets.

The nanocuboids are not necessarily stoichiometric when they form. If they are enriched in either SrO or TiO_2 , the large effect of the bulk starvation energy will force them to form surfaces rich in that same species. The existence of stable (110) facets indicates that they are not strontium rich, and the platinum epitaxy indicates that the (100) facets are not strontium rich either. A strontium rich nanocuboid can therefore be ruled out. A titanium rich nanocuboid, however, cannot. If strontium was slightly more soluble in the solution from which the nanocuboids were prepared or if slightly more titanium were present in the solution, then titanium rich nanocuboids would be formed. However, it is unlikely that the amount of titanium enrichment would exceed that of a nanocuboid with strontium removed from the surface.

With such an amount of titanium enrichment, the overall lowest energy structure for the nanocuboids would be a TiO_2 (1x1) reconstruction on the (100) facets and a half- O_2 structure on the (110) facets (Table 6.4). The $\gamma_{(110)}:\gamma_{(100)}$ in this case would be 1.136 (example by acid etching, the bulk starvation energy will have an effect and must be included in t), almost identical to the observed $d_{(110)}:d_{(100)}$ ratio of 1.137. The only other (110) and (100) surface

pairings to have an energy contribution within 10,000 eV per nanoparticle are the (3x1) or (4x1) structures on the (110) facets and a 50%/50% mixture of the TiO₂ (1x1) and SrO (1x1) structures on the (100) facets (Table 6.4). These structures have $\gamma_{(110)}:\gamma_{(100)}$ ratios of 1.220 and 1.156, respectively (example by acid etching, the bulk starvation energy will have an effect and must be included in t), close to the observed $d_{(110)}:d_{(100)}$ ratio. However, the total energy contribution to the nanoparticle from using either of these pairings is more than 5,000 eV per nanoparticle, indicating that they are unlikely.

Taken together, this indicates that the (110) facets are likely to be terminated by a half-O₂ structure, whether the nanocuboid is stoichiometric or titanium enriched. Depending upon the amount of titanium enrichment, the (100) facet will be terminated by a TiO₂ (1x1) structure or a mixture of TiO₂ (1x1) and SrO (1x1) structures. If the nanocuboids were enriched in strontium, then it is likely that the proportion of the (100) facet composed of the SrO (1x1) termination would be increased.

The presence of both strontium and titanium at the surface is in agreement with previous studies by collaborators.¹⁷⁴ The vibrational spectra of CO₂ and of pyridine adsorbed to the nanocuboids indicated that both strontium and titanium were present.¹⁷⁴ The precise method by which atmospheric species bonded to the surface could not in most cases be determined from the vibrational spectra, due to the lack of appropriate models and associated calculated vibrational spectra. Preliminary vibrational spectra calculations from the unreconstructed SrTiO₃ (100) titanium and strontium terminations calculated in Chapter 4 indicate that CO₂ and H₂O on both titanium and strontium terminations have vibrations in the region where most of the vibrational

signals were observed. Currently determination of whether the surface is TiO_2 or SrO terminated or of whether H_2O or CO_2 is bonding cannot be made from vibrational spectra. If the preliminary modeling of the vibrational spectra is sufficiently improved upon, however, such spectra may confirm the current analysis of the nanocuboid surfaces, and may provide a path to determining surface composition and structure of nanocuboids synthesized in the future.

The surface structure depends highly upon the initial stoichiometry of the nanocuboid. Varying the nanocuboid composition even slightly should change which surface structure is present. Altering the composition of the nanocuboids might be accomplished during particle synthesis through varying precursor stoichiometry, changing in solvent, solution pH, or using a surfactant, among other possibilities. Additionally, post-synthesis processing, such as acid etching or deposition of a TiO_2 or SrO thin film, could be used to change the stoichiometry. By controlling the composition in such a way, the surface structure can be similarly controlled. This in turn will lead to differences in the ability to bond adsorbates and to different interfaces between the nanocuboids and any particles or films grown on them.

No periodic surface reconstruction was definitively observed, as the surface is most likely composed of a mix of TiO_2 and SrO (1x1) terminations. Even if a surface termination with a different periodicity were created, it would be difficult to resolve on the nanocuboids described herein. In addition to the technical difficulties of seeing surface diffraction from an area only 60 nm across and those involved with seeing surface diffraction from a sample as thick as 60 nm, the voids within the cuboids create further difficulties. The voids get in way of seeing a reconstruction by adding edge effects to the diffraction pattern, which are strong enough to make

weak surface spots nearly impossible to observe. Experiments are underway to synthesize nanocuboids without voids. At the same time, cuboids such as those used in these experiments can continue to find use, particularly as catalytic substrates after acid etching to expose the voids and creating high surface area, oriented nanoparticles. Even though no surface reconstructions were ultimately observed, the experiments did yield information about the surface structure, and likely structures were determined despite the fact that no reconstruction was observed.

6.4.3: Platinum nanoparticles on SrTiO₃ nanocuboids

The platinum nanoparticles on the SrTiO₃ nanocuboids are unconditionally metallic platinum. Such interfaces are known to have strong Pt–O bonds between the metal and the oxide support.^{176,177} Additionally, there can be dissociative chemisorption of O₂ on exposure to air¹⁸⁰ forming a PtO shell at the surface. Hence bulk averaging techniques might interpret these nanoparticles as PtO. For example, a nanoparticle consisting of 4 unit cells of platinum arranged in a square on the substrate surface would have 38 platinum atoms, 29 at the surface, 13 at the support interface (8 both at the surface and at the support interface), leaving only 4 (10%) in the interior. Such a particle would have a length of 1.063 nm (2 unit cells plus 2 atomic radii) and a height of 0.670 nm (1 unit cell plus 2 atomic radii), with 90% of the platinum bonded to an oxygen atom. This is consistent with results from Setthapun and coworkers,¹⁸¹ who reported that after 1 cycle of Pt ALD on SrTiO₃ nanocuboids, the platinum nanoparticles were 5% metallic platinum and 95% PtO and after 2 cycles 45% metallic platinum and 55% PtO; as well as Christensen and coworkers¹⁶⁹, who reported that the amount of oxidation scaled with surface to volume ratio.

The observed shape of the platinum nanoparticles on the strontium titanate nanocuboids is the thermodynamically favored structure, as determined by the Winterrbottom construction.¹⁵⁸ Unlike metastable structures, which cannot survive extended catalytic use, thermodynamically stable structures such as these will be stable and maintain their configuration. Indeed, platinum in a different, metastable geometry will eventually reconfigure to this thermodynamically stable shape.

The shape of the platinum nanoparticles is controlled by the interfacial free energy and the surface free energy of the support. Changing these alters the ratio of exposed Pt (111) to Pt (100) which in turn will change face-selective catalytic performance. This is relatively simple to do. Perovskite nanocuboids of other compositions (e.g. BaTiO₃¹⁸²) have also been synthesized, as have oriented nanoparticles of other materials (e.g. MgO smoke nanocuboids^{183,184}). For example, by switching to a support with a greater lattice mismatch such as BaTiO₃ (a=b=3.992Å, c=4.036Å; 2.2% lattice mismatch), the interface energy would be expected to increase. Since the platinum grows on the TiO₂ termination, switching the A-site cation should not have a direct bonding effect on the interface, and the difference in lattice mismatch would be the only major change. This could be fine tuned by having mixed ions on the A-site, e.g. Sr_{1-x}Ba_xTiO₃. By changing the B-site cation, by changing the surface of the nanocuboids as described above, or by changing the material entirely, larger changes in the interface and substrate surface free energies will lead to associated changes in the exposed facets and face-selective catalysis.

Since the platinum particle shape is the thermodynamically favorable structure, it will be maintained during catalytic use, provided that the thermodynamics are not altered by poisoning or coking. Even if the particle size increases via sintering, the shape and the ratio of different surface facets will be maintained. Such a method for controlling a nanoparticle catalyst surface can be applied to any catalytic system, not just platinum, and tuned as discussed above while maintaining thermodynamically stability.

6.5: Conclusions

The structure of the interior and exterior of hydrothermally synthesized SrTiO_3 nanocuboids has been elucidated. Matching the Wulff construction with TEM images has revealed the TiO_2 (1x1) structure or a mix of the TiO_2 (1x1) and SrO (1x1) structures as the most likely candidates for the structure of the main surfaces of the SrTiO_3 nanocuboids, and the half- O_2 structure as the most likely termination of the (110) facets. The surface structure depends on the nanocrystal stoichiometry, and precise control over the stoichiometry will allow for control over the surface structure. The titanium rich (100) termination for the nanocuboids analyzed herein fits with the observation of titanium rich terminations on single crystal SrTiO_3 following annealing in oxidizing environments (see Chapter 4), and with the cube-on-cube epitaxy exhibited by platinum nanoparticles grown on the SrTiO_3 nanocuboids. The voids within the nanocuboids have the same surfaces as the exterior of the cuboids. Exposure of these voids through acid etching could lead to particles with higher surface areas while keeping the advantage of the oriented surfaces.

The analysis of platinum nanoparticles on strontium titanate nanocuboids has shown that they are of thermodynamically stable shapes, as governed by the Wulff construction. Further analysis has illuminated a method by which stable, high surface area, oriented catalysts can be created. Control of the support surface allows one to engineer such catalysts with precise control over which nanoparticle surface orientation is exposed, thus enabling precise modification of selectivity and yield for structure sensitive catalytic reactions. By combining thermodynamics with control over the support, stable, high surface area, face selective catalysts may be created.

Chapter 7:

Conclusions

This work began with an examination of the inorganic chemistry of the complex $\text{La}_4\text{Cu}_3\text{MoO}_{12}$ structure. Tools similar to those used to analyze the bulk $\text{La}_4\text{Cu}_3\text{MoO}_{12}$ structure were then turned on the (110) surface of SrTiO_3 , and it was shown that the same principles of coordination and chemical bonding applied to the surface as to the bulk. It then considered adsorbates on the SrTiO_3 (100) surface, and found that, yet again, the same basic chemical rules apply. A thorough review of many known and proposed surface structures confirmed that the bond valence method allows not only an understanding of surface structures, but the ability to predict them as well. Finally, attention turned from large single crystals to nanocrystals, and it was shown that control over a support surface may lead to fine control over structure sensitive catalytic reactions.

There were two major goals for this work. The first was to develop a better chemistry based understanding of surface structures. The second was to apply that knowledge to enhance the understanding of catalysis at the atomic scale. The former was accomplished by showing that the same chemical principles governing bulk structures control surface structures as well, and by showing that bonding principles, such as bond valence sums, can be used to predict surface structures. The latter was accomplished by showing that adsorbates on surfaces can also be understood and predicted through chemical bonding methods. Finally, the enhanced understanding of surfaces and interfaces combined with nanoparticle thermodynamics was used to suggest a method by which catalytic selectivity and activity can be precisely controlled in structure sensitive reactions.

The rules of solid state chemistry that govern bulk structures apply equally to surface structures and to adsorbates on surface structures. The chemical bonding principles are general to all surfaces, and even have predictive power. Through an understanding of surface chemistry, we can predict and perhaps even control what structures will form and what species may interact with the surface. In future surface studies, both chemistry and physics ought to be considered in order to arrive at the most complete understanding of surface structure and interactions. Finally, through the control of the surface that this knowledge allows, one may control and manipulate the potential active sites of supported heterogeneous catalysts.

References

- 1 Boyle, R. *The sceptical chymist; or, Chymico-physical doubts & paradoxes, touching the spagyrist's principles commonly call'd hypostatical, as they are wont to be propos'd and defended by the generality of alchymists. Whereunto is præmis'd part of another discourse relating to the same subject.* (Printed by F. Cadwell for F. Crooke Dawson of Pall Mall, 1661).
- 2 Chang, R. *Chemistry*. 6th edn, (McGraw-Hill, 1998).
- 3 Bragg, W. H. & Bragg, W. L. The Reflection of X-rays by Crystals. *Proceedings of the Royal Society of London, Series A: Mathematical, Physical and Engineering Sciences* **88**, 428-438, (1913).
- 4 Brown, I. D. Recent Developments in the Methods and Applications of the Bond Valence Model. *Chemical Reviews* **109**, 6858-6919, (2009).
- 5 Ramirez, A. P. Strongly Geometrically Frustrated Magnets. *Annual Review of Materials Science* **24**, 453-480, (1994).
- 6 Vander Griend, D. A. *et al.* $\text{La}_4\text{Cu}_3\text{MoO}_{12}$: A novel cuprate with unusual magnetism. *J. Am. Chem. Soc.* **121**, 4787-4792, (1999).
- 7 Azuma, M. *et al.* Antiferromagnetic ordering of $S=1/2$ triangles in $\text{La}_4\text{Cu}_3\text{MoO}_{12}$. *Phys. Rev. B: Condens. Matter* **62**, R3588-R3591, (2000).
- 8 Wessel, S. & Haas, S. Phase diagram and thermodynamic properties of the square lattice of antiferromagnetic spin-1/2 triangles in $\text{La}_4\text{Cu}_3\text{MoO}_{12}$. *Phys. Rev. B: Condens. Matter* **63**, 140403, (2001).
- 9 Wang, H. T. Elementary excitations in the spin-tube and spin-orbit models. *Phys. Rev. B: Condens. Matter* **64**, 174410, (2001).
- 10 Qiu, Y. *et al.* Spin-trimer antiferromagnetism in $\text{La}_4\text{Cu}_3\text{MoO}_{12}$. *Phys. Rev. B: Condens. Matter* **71**, 214439, (2005).
- 11 Changkang, C. Physico-Chemical Investigations on Crystal Growth of Oxide Superconductors. *Prog. Cryst. Growth Charact. Mater.* **24**, 213-267, (1992).
- 12 Own, C. S.-Y. *System Design and Verification of the Precession Electron Diffraction Technique* Ph.D. thesis, Northwestern University, (2005).

- 13 Own, C. S., Subramanian, A. K. & Marks, L. D. Quantitative analyses of precession diffraction data for a large cell oxide. *Microsc. Microanal.* **10**, 396-396, (2004).
- 14 Own, C. S., Subramanian, A. K. & Marks, L. D. Quantitative analyses of precession diffraction data for a large cell oxide. *Microsc. Microanal.* **10**, 96-104, (2004).
- 15 SHELXTL (Bruker-AXS, Inc., Madison, WI, 1997).
- 16 Sheldrick, G. M. in *SHELXTL Reference Manual* Ch. 6, (Bruker-AXS, Inc., 1997).
- 17 Brown, I. D. & Altermatt, D. Bond-Valence Parameters Obtained from a Systematic Analysis of the Inorganic Crystal-Structure Database. *Acta Crystallographica Section B-Structural Science* **41**, 244-247, (1985).
- 18 Knížek, K. *Kalvados*, <<http://www.fzu.cz/~knizek/kalvados/index.html>> (2010).
- 19 Brown, I. D. <http://www.ccp14.ac.uk/ccp/web-mirrors/i_d_brown/bond_valence_param/bvparm2009.cif> (2009).
- 20 Heier, K. R. & Poeppelmeier, K. R. Reinvestigation of $\text{CuNbOF}_5 \cdot 4\text{H}_2\text{O}$. *J. Solid State Chem.* **133**, 576-579, (1997).
- 21 Chen, M. D., Zhou, Z. H. & Hu, S. Z. Bond valence parameters linearly dependent on the molybdenum oxidation states. *Chin. Sci. Bull.* **47**, 978-981, (2002).
- 22 Malo, S., Vander Griend, D. A., Poeppelmeier, K. R., Wang, Y. G. & Dravid, V. P. Crystal symmetry of $\text{La}_3\text{Cu}_2\text{VO}_9$ and $\text{La}_4\text{Cu}_3\text{MoO}_{12}$ derived from the YAlO_3 hexagonal structure by transmission electron microscopy. *Solid State Sci.* **3**, 17-23, (2001).
- 23 Vander Griend, D. A. *et al.* $\text{La}_3\text{Cu}_2\text{VO}_9$: A surprising variation on the YAlO_3 structure-type with 2D copper clusters of embedded triangles. *Solid State Sci.* **3**, 569-579, (2001).
- 24 Wolf, D. Reconstruction of NaCl surfaces from a dipolar solution to the Madelung problem. *Phys. Rev. Lett.* **68**, 3315-3318, (1992).
- 25 Pashley, M. D. Electron counting model and its application to island structures on molecular-beam epitaxy grown GaAs(001) and ZnSe(001). *Phys. Rev. B: Condens. Matter* **40**, 10481-10487, (1989).
- 26 Goniakowski, J., Finocchi, F. & Noguera, C. Polarity of oxide surfaces and nanostructures. *Reports on Progress in Physics* **71**, 016501, (2008).

- 27 Deak, D. S. Strontium titanate surfaces. *Mater. Sci. Technol.* **23**, 127-136, (2007).
- 28 Noguera, C. Polar oxide surfaces. *J. Phys.: Condens. Matter* **12**, R367-R410, (2000).
- 29 Erdman, N. *et al.* The structure and chemistry of the TiO₂-rich surface of SrTiO₃(001). *Nature* **419**, 55-58, (2002).
- 30 Russell, B. C. & Castell, M. R. Reconstructions on the polar SrTiO₃ (110) surface: Analysis using STM, LEED, and AES. *Phys. Rev. B: Condens. Matter* **77**, 254414, (2008).
- 31 Brunen, J. & Zegenhagen, J. Investigation of the SrTiO₃ (110) surface by means of LEED, scanning tunneling microscopy and Auger spectroscopy. *Surf. Sci.* **389**, 349-365, (1997).
- 32 Bando, H., Aiura, Y., Haruyama, Y., Shimizu, T. & Nishihara, Y. Structure and electronic states on reduced SrTiO₃(110) surface observed by scanning-tunneling-microscopy and spectroscopy. *J. Vac. Sci. Technol., B* **13**, 1150-1154, (1995).
- 33 Kotomin, E. A. *et al.* Comparative study of polar perovskite surfaces. *Surf. Sci.* **566**, 231-235, (2004).
- 34 Heifets, E., Goddard, W. A., Kotomin, E. A., Eglitis, R. I. & Borstel, G. Ab initio calculations of the SrTiO₃ (110) polar surface. *Phys. Rev. B: Condens. Matter* **69**, 035408, (2004).
- 35 Bottin, F., Finocchi, F. & Noguera, C. Facetting and (nx1) reconstructions of SrTiO₃(110) surfaces. *Surf. Sci.* **574**, 65-76, (2005).
- 36 Eglitis, R. I. & Vanderbilt, D. First-principles calculations of atomic and electronic structure of SrTiO₃ (001) and (011) surfaces. *Phys. Rev. B: Condens. Matter* **77**, 195408, (2008).
- 37 Jayaram, G., Xu, P. & Marks, L. D. Structure of Si(100)-(2x1) surface using UHV transmission electron-diffraction. *Phys. Rev. Lett.* **71**, 3489-3492, (1993).
- 38 Xu, P., Jayaram, G. & Marks, L. D. Cross-correlation method for intensity measurement of transmission electron-diffraction patterns. *Ultramicroscopy* **53**, 15-18, (1994).
- 39 Chiamonti, A. N. & Marks, L. D. Atomic resolution transmission electron microscopy of surfaces. *J. Mater. Res.* **20**, 1619-1627, (2005).

- 40 Marks, L. D., Sinkler, W. & Landree, E. A feasible set approach to the crystallographic phase problem. *Acta Crystallogr., Sect. A: Found. Crystallogr.* **55**, 601-612, (1999).
- 41 Kohn, W. & Sham, L. J. Self-Consistent Equations Including Exchange and Correlation Effects. *Phys Rev* **140**, 1133-&, (1965).
- 42 Perdew, J. P. & Wang, Y. Accurate and Simple Analytic Representation of the Electron-Gas Correlation-Energy. *Phys. Rev. B: Condens. Matter* **45**, 13244-13249, (1992).
- 43 Perdew, J. P., Burke, K. & Ernzerhof, M. Generalized gradient approximation made simple. *Phys. Rev. Lett.* **77**, 3865-3868, (1996).
- 44 Mattsson, T. R. & Mattsson, A. E. Calculating the vacancy formation energy in metals: Pt, Pd, and Mo. *Phys. Rev. B: Condens. Matter* **66**, 214110, (2002).
- 45 Mattsson, A. E. & Jennison, D. R. Computing accurate surface energies and the importance of electron self-energy in metal/metal-oxide adhesion. *Surf. Sci.* **520**, L611-L618, (2002).
- 46 Armiento, R. & Mattsson, A. E. Functional designed to include surface effects in self-consistent density functional theory. *Phys. Rev. B: Condens. Matter* **72**, 085108, (2005).
- 47 Perdew, J. P. *et al.* Restoring the density-gradient expansion for exchange in solids and surfaces. *Phys. Rev. Lett.* **100**, 136406, (2008).
- 48 Blaha, P., Schwarz, K., Madsen, G. K. H., Kvasnicka, D. & Luitz, J. *WIEN2k, An Augmented Plane Wave Plus Local Orbitals Program for Calculating Crystal Properties.* (Technical University of Vienna, 2001).
- 49 Yu, R. C., Singh, D. & Krakauer, H. All-Electron and Pseudopotential Force Calculations Using the Linearized-Augmented-Plane-Wave Method. *Phys. Rev. B: Condens. Matter* **43**, 6411-6422, (1991).
- 50 Perdew, J. P., Ernzerhof, M. & Burke, K. Rationale for mixing exact exchange with density functional approximations. *J. Chem. Phys.* **105**, 9982-9985, (1996).
- 51 Adamo, C. & Barone, V. Toward reliable density functional methods without adjustable parameters: The PBE0 model. *J. Chem. Phys.* **110**, 6158-6170, (1999).
- 52 Tao, J. M., Perdew, J. P., Staroverov, V. N. & Scuseria, G. E. Climbing the density functional ladder: Nonempirical meta-generalized gradient approximation designed for molecules and solids. *Phys. Rev. Lett.* **91**, 146401, (2003).

- 53 Staroverov, V. N., Scuseria, G. E., Tao, J. M. & Perdew, J. P. Comparative assessment of a new nonempirical density functional: Molecules and hydrogen-bonded complexes. *J. Chem. Phys.* **119**, 12129-12137, (2003).
- 54 Marks, L. D., Chiaramonti, A. N., Tran, F. & Blaha, P. The small unit cell reconstructions of SrTiO₃(111). *Surf. Sci.* **603**, 2179-2187, (2009).
- 55 Tersoff, J. & Hamann, D. R. Theory of the scanning tunneling microscope. *Phys. Rev. B: Condens. Matter* **31**, 805-813, (1985).
- 56 Warschkow, O., Wang, Y., Subramanian, A., Asta, M. & Marks, L. D. Structure and local-equilibrium thermodynamics of the c(2x2) reconstruction of rutile TiO₂ (100). *Phys. Rev. Lett.* **100**, 86102, (2008).
- 57 Ciston, J., Subramanian, A. & Marks, L. D. Water-driven structural evolution of the polar MgO (111) surface: An integrated experimental and theoretical approach. *Phys. Rev. B: Condens. Matter* **79**, 085421, (2009).
- 58 Ciston, J., Subramanian, A., Kienzle, D. & Marks, L. D. Why the case for clean surfaces does not hold water: Structure and morphology of hydroxylated nickel oxide (111). *Surf. Sci.* **604**, 155-164, (2010).
- 59 Wolf, D. Structure of Ionic Interfaces from an Absolutely Convergent Solution of the Madelung Problem. *Solid State Ionics* **75**, 3-11, (1995).
- 60 Warschkow, O. *et al.* TiO₂-rich reconstructions of SrTiO₃(001): a theoretical study of structural patterns. *Surf. Sci.* **573**, 446-456, (2004).
- 61 Lazarov, V. K. *et al.* Structure of the hydrogen-stabilized MgO(111)-(1x1) polar surface: Integrated experimental and theoretical studies. *Phys. Rev. B: Condens. Matter* **71**, 115434, (2005).
- 62 Bluhm, H. Photoelectron spectroscopy of surfaces under humid conditions. *J. Electron Spectrosc. Relat. Phenom.* **177**, 71-84, (2010).
- 63 Yamamoto, S. *et al.* In situ x-ray photoelectron spectroscopy studies of water on metals and oxides at ambient conditions. *Journal of Physics-Condensed Matter* **20**, 184025, (2008).
- 64 Kawasaki, M. *et al.* Atomic Control of the SrTiO₃ Crystal-Surface. *Science* **266**, 1540-1542, (1994).

- 65 Erdman, N. & Marks, L. D. SrTiO₃(001) surface structures under oxidizing conditions. *Surf. Sci.* **526**, 107-114, (2003).
- 66 XPSPEAK 95 v. 2.0 (Hong Kong, 1996).
- 67 Mayer, J. T., Diebold, U., Madey, T. E. & Garfunkel, E. Titanium and Reduced Titania Overlayers on Titanium Dioxide(110). *J. Electron Spectrosc. Relat. Phenom.* **73**, 1-11, (1995).
- 68 Wang, L. Q., Baer, D. R. & Engelhard, M. H. Creation of Variable Concentrations of Defects on TiO₂(110) Using Low-Density Electron-Beams. *Surf. Sci.* **320**, 295-306, (1994).
- 69 Xu, P., Dunn, D., Zhang, J. P. & Marks, L. D. Atomic Imaging of Surfaces in Plan View. *Surf. Sci.* **285**, L479-L485, (1993).
- 70 Becerra-Toledo, A. E. <e-mail> (2010)
- 71 Kienzle, D. <e-mail> (2010)
- 72 Erdman, N. *et al.* Surface structures of SrTiO₃ (001): A TiO₂-rich reconstruction with a c(4 x 2) unit cell. *J. Am. Chem. Soc.* **125**, 10050-10056, (2003).
- 73 Marks, L. D. <e-mail> (2010)
- 74 Kazimirov, A., Goodner, D. M., Bedzyk, M. J., Bai, J. & Hubbard, C. R. X-ray surface diffraction analysis of structural transformations on the (001) surface of oxidized SrTiO₃. *Surf. Sci.* **492**, L711-L716, (2001).
- 75 Szot, K. & Speier, W. Surfaces of reduced and oxidized SrTiO₃ from atomic force microscopy. *Phys. Rev. B: Condens. Matter* **60**, 5909-5926, (1999).
- 76 McQuarrie, D. A. & Simon, J. D. *Physical chemistry : a molecular approach.* (University Science Books, 1997).
- 77 Herger, R. *et al.* Surface of strontium titanate. *Phys. Rev. Lett.* **98**, 076102, (2007).
- 78 Herger, R. *et al.* Surface structure of SrTiO₃(001). *Phys. Rev. B: Condens. Matter* **76**, 195435, (2007).

- 79 Enterkin, J. A. *et al.* A homologous series of structures on the surface of SrTiO₃(110). *Nat. Mater.* **9**, 245-248, (2010).
- 80 Brown, I. D. *The chemical bond in inorganic chemistry : the bond valence model.* (Oxford University Press, 2002).
- 81 Pauling, L. The principles determining the structure of complex ionic crystals. *J. Am. Chem. Soc.* **51**, 1010-1026, (1929).
- 82 Brown, I. D. Chemical and Steric Constraints in Inorganic Solids. *Acta Crystallographica Section B-Structural Science* **48**, 553-572, (1992).
- 83 Tabira, Y. & Withers, R. L. Cation ordering in NiAl₂O₄ spinel by a 111 systematic row CBED technique. *Phys. Chem. Miner.* **27**, 112-118, (1999).
- 84 van Smaalen, S., Dinnebier, R., Sofin, M. & Jansen, M. Structures of incommensurate and commensurate composite crystals Na_xCuO₂ (x=1.58, 1.6, 1.62). *Acta Crystallographica Section B-Structural Science* **63**, 17-25, (2007).
- 85 Isobe, M. *et al.* Low-temperature crystal and magnetic structures of the chain-ladder composite material Sr_{0.4}Ca_{13.6}CU_{24+y}O_{41+z}: Hole redistribution and antiferromagnetic order. *Phys. Rev. B: Condens. Matter* **62**, 11667-11676, (2000).
- 86 Tamazyan, R., van Smaalen, S., Vasilyeva, I. G. & Arnold, H. Two-dimensionally modulated structure of the rare-earth polysulfide GdS_{2-x} (x=0.18 similar or equal to 13/72). *Acta Crystallographica Section B-Structural Science* **59**, 709-719, (2003).
- 87 Xue, D. F., Zuo, S. & Ratajczak, H. Electronegativity and structural characteristics of lanthanides. *Physica B-Condensed Matter* **352**, 99-104, (2004).
- 88 Albuquerque, R. Q., Rocha, G. B., Malta, O. L. & Porcher, P. On the charge factors of the simple overlap model for the ligand field in lanthanide coordination compounds. *Chem. Phys. Lett.* **331**, 519-525, (2000).
- 89 Xue, D. F. & Zhang, S. Y. Chemical bond analysis of the correlation between crystal structure and nonlinear optical properties of complex crystals. *Physica B* **262**, 78-83, (1999).
- 90 Xue, D., Betzler, K. & Hesse, H. Chemical-bond analysis of the nonlinear optical properties of the borate crystals LiB₃O₅, CsLiB₆O₁₀, and CsB₃O₅. *Applied Physics a-Materials Science & Processing* **74**, 779-782, (2002).

- 91 Holovey, V. M., Sidey, V. I., Lyamayev, V. I. & Birov, M. M. Influence of different annealing conditions on the luminescent properties of $\text{Li}_2\text{B}_4\text{O}_7 : \text{Mn}$ single crystals. *J. Phys. Chem. Solids* **68**, 1305-1310, (2007).
- 92 Holovey, V. M., Sidey, V. I., Lyamayev, V. I. & Puga, P. P. Influence of reducing annealing on the luminescent properties of $\text{Li}_2\text{B}_4\text{O}_7 : \text{Cu}$ single crystals. *J. Lumin.* **126**, 408-412, (2007).
- 93 Adams, S. & Swenson, J. Predictability of ion transport properties from the structure of solid electrolytes. *Ionics* **10**, 317-326, (2004).
- 94 Newville, M. Using Bond Valence sums as restraints in XAFS analysis. *Phys. Scr.* **T115**, 159-161, (2005).
- 95 Hiemstra, T., Vanriemsdijk, W. H. & Bolt, G. H. Multisite Proton Adsorption Modeling at the Solid-Solution Interface of (Hydr)Oxides - a New Approach .1. Model Description and Evaluation of Intrinsic Reaction Constants. *J. Colloid Interface Sci.* **133**, 91-104, (1989).
- 96 Hiemstra, T., Venema, P. & VanRiemsdijk, W. H. Intrinsic proton affinity of reactive surface groups of metal (hydr)oxides: The bond valence principle. *J. Colloid Interface Sci.* **184**, 680-692, (1996).
- 97 Bickmore, B. R., Rosso, K. M., Nagy, K. L., Cygan, R. T. & Tadanier, C. J. Ab initio determination of edge surface structures for dioctahedral 2 : 1 phyllosilicates: Implications for acid-base reactivity. *Clays Clay Miner.* **51**, 359-371, (2003).
- 98 Bickmore, B. R., Rosso, K. M., Tadanier, C. J., Bylaska, E. J. & Doud, D. Bond-valence methods for pK_a prediction. II. Bond-valence, electrostatic, molecular geometry, and solvation effects. *Geochim. Cosmochim. Acta* **70**, 4057-4071, (2006).
- 99 Bickmore, B. R., Tadanier, C. J., Rosso, K. M., Monn, W. D. & Eggett, D. L. Bond-Valence methods for pK_a prediction: critical reanalysis and a new approach. *Geochim. Cosmochim. Acta* **68**, 2025-2042, (2004).
- 100 Schindler, M., Mutter, A., Hawthorne, F. C. & Putnis, A. Prediction of crystal morphology of complex uranyl-sheet minerals. I. Theory. *Can. Mineral.* **42**, 1629-1649, (2004).
- 101 Ruberto, C., Yourdshahyan, Y. & Lundqvist, B. I. Stability of a flexible polar ionic crystal surface: Metastable alumina and one-dimensional surface metallicity. *Phys. Rev. Lett.* **88**, 226101, (2002).

- 102 Ruberto, C., Yourdshahyan, Y. & Lundqvist, B. I. Surface properties of metastable alumina: A comparative study of kappa- and alpha-Al₂O₃. *Phys. Rev. B: Condens. Matter* **67**, 195412, (2003).
- 103 Tasker, P. W. Stability of Ionic-Crystal Surfaces. *Journal of Physics C-Solid State Physics* **12**, 4977-4984, (1979).
- 104 Kubo, T. <e-mail> (2010)
- 105 Kubo, T. & Nozoye, H. Surface structure of SrTiO₃(100). *Surf. Sci.* **542**, 177-191, (2003).
- 106 Rossano, R., Farges, F., Ramos, A., Delaye, J. M. & Brown, G. E. Bond valence in silicate glasses. *J. Non-Cryst. Solids* **304**, 167-173, (2002).
- 107 Etxebarria, I. *et al.* Comparison of empirical bond-valence and first-principles energy calculations for a complex structural instability. *Phys. Rev. B: Condens. Matter* **72**, 174108, (2005).
- 108 Heifets, E., Kotomin, E. A. & Maier, J. Semi-empirical simulations of surface relaxation for perovskite titanates. *Surf. Sci.* **462**, 19-35, (2000).
- 109 <http://www.wien2k.at/Depository/SurfSci_STO111_Marks/> (
- 110 Johnston, K., Castell, M. R., Paxton, A. T. & Finnis, M. W. SrTiO₃(001)(2x1) reconstructions: First-principles calculations of surface energy and atomic structure compared with scanning tunneling microscopy images. *Phys. Rev. B: Condens. Matter* **70**, 085415, (2004).
- 111 Castell, M. R. Scanning tunneling microscopy of reconstructions on the SrTiO₃(001) surface. *Surf. Sci.* **505**, 1-13, (2002).
- 112 Naito, M. & Sato, H. Reflection High-Energy Electron-Diffraction Study on the SrTiO₃ Surface-Structure. *Physica C (Amsterdam, Neth.)* **229**, 1-11, (1994).
- 113 Jiang, Q. D. & Zegenhagen, J. SrTiO₃(001) Surfaces and Growth of Ultra-Thin GdBa₂Cu₃O_{7-x} Films Studied by LEED/AES and UHV-STM. *Surf. Sci.* **338**, L882-L888, (1995).
- 114 Castell, M. R. Nanostructures on the SrTiO₃(001) surface studied by STM. *Surf. Sci.* **516**, 33-42, (2002).

- 115 Jiang, Q. D. & Zegenhagen, J. c(6x2) and c(4x2) reconstruction of SrTiO₃(001). *Surf. Sci.* **425**, 343-354, (1999).
- 116 Cheng, C., Kunc, K. & Lee, M. H. Structural relaxation and longitudinal dipole moment of SrTiO₃(001)(1X1) surfaces. *Phys. Rev. B: Condens. Matter* **62**, 10409-10418, (2000).
- 117 Heifets, E., Dorfman, S., Fuks, D., Kotomin, E. & Gordon, A. Atomistic simulation of SrTiO₃(001) surface relaxation. *J. Phys.: Condens. Matter* **10**, L347-L353, (1998).
- 118 Heifets, E., Eglitis, R. I., Kotomin, E. A., Maier, J. & Borstel, G. Ab initio modeling of surface structure for SrTiO₃ perovskite. *Phys. Rev. B: Condens. Matter* **64**, 235417, (2001).
- 119 Li, Z. Q., Zhu, J. L., Wu, C. Q., Tang, Z. & Kawazoe, Y. Relaxations of TiO₂- and SrO-terminated SrTiO₃ (001) surfaces. *Phys. Rev. B: Condens. Matter* **58**, 8075-8078, (1998).
- 120 Charlton, G. *et al.* Surface relaxation of SrTiO₃(001). *Surf. Sci.* **457**, L376-L380, (2000).
- 121 Kubo, T. & Nozoye, H. Surface structure of SrTiO₃(100)-(√5x√5)-R26.6°. *Phys. Rev. Lett.* **86**, 1801-1804, (2001).
- 122 Liborio, L. M., Sanchez, C. G., Paxton, A. T. & Finnis, M. W. Stability of Sr adatom model structures for SrTiO₃(001) surface reconstructions. *J. Phys.: Condens. Matter* **17**, L223-L230, (2005).
- 123 Matsumoto, T., Tanaka, H., Kouguchi, K., Kawai, T. & Kawai, S. A Scanning-Tunneling-Microscopy Study of Laser Molecular-Beam Epitaxy on SrTiO₃(100) Surface. *Surf. Sci.* **312**, 21-30, (1994).
- 124 Tanaka, H., Matsumoto, T., Kawai, T. & Kawai, S. Surface-Structure and Electronic Property of Reduced SrTiO₃(100) Surface Observed by Scanning Tunneling Microscopy Spectroscopy. *Jpn. J. Appl. Phys., Part 1* **32**, 1405-1409, (1993).
- 125 Seo, D. K., Perdue, K., Ren, J. & Whangbo, M. H. Study of scanning tunneling microscopy images and probable relaxations of the SrTiO₃(100) surface by electronic structure calculations. *Surf. Sci.* **370**, 245-251, (1997).
- 126 Kimura, S. & Tsukada, M. Electronic structure of the (001) surface of reduced SrTiO₃. *Appl. Surf. Sci.* **121**, 195-199, (1997).
- 127 Stashans, A., Erazo, F., Ortiz, J. & Valverde, P. Oxygen-vacancy defects on the SrTiO₃(001) surface: a quantum-chemical, study. *Philos. Mag. B* **81**, 1977-1988, (2001).

- 128 Lanier, C. H. *et al.* Atomic-scale structure of the SrTiO₃(001)-c(6x2) reconstruction: Experiments and first-principles calculations. *Phys. Rev. B: Condens. Matter* **76**, 045421, (2007).
- 129 Jiang, Q. D. & Zegenhagen, J. SrTiO₃(001)-c(6x2): A long-range, atomically ordered surface stable in oxygen and ambient air. *Surf. Sci.* **367**, L42-L46, (1996).
- 130 Van Smaalen, S. & Ludecke, J. The valence states of vanadium in the low-temperature superstructure of NaV₂O₅. *Europhys. Lett.* **49**, 250-254, (2000).
- 131 Bernert, A., Chatterji, T., Thalmeier, P. & Fulde, P. Structure determination, valence, and superexchange in the dimerized low temperature phase of α' -NaV₂O₅. *European Physical Journal B* **21**, 535-546, (2001).
- 132 Karen, P., Gustafsson, K. & Linden, J. EuBaFe₂O₅: Extent of charge ordering by Mossbauer spectroscopy and high-intensity high-resolution powder diffraction. *J. Solid State Chem.* **180**, 138-147, (2007).
- 133 Haller, G. L. & Resasco, D. E. Metal Support Interaction - Group-VIII Metals and Reducible Oxides. *Adv. Catal.* **36**, 173-235, (1989).
- 134 Verykios, X. E. in *Catalysis and Electrocatalysis at Nanoparticle Surfaces* (eds Andrezej Wieckowski, Elena R. Savinova, & Constantino G. Vayenas) Ch. 20, (CRC Press, 2003).
- 135 Coq, B. & Figueras, F. in *Catalysis and Electrocatalysis at Nanoparticle Surfaces* (eds Andrezej Wieckowski, Elena R. Savinova, & Constantino G. Vayenas) Ch. 23, (CRC Press, 2003).
- 136 Sinfelt, J. H. Hydrogenolysis of Ethane over Supported Platinum. *J. Phys. Chem.* **68**, 344, (1964).
- 137 Taylor, W. F., Yates, D. J. C. & Sinfelt, J. H. Catalysis over Supported Metals .2. Effect of Support on Catalytic Activity of Nickel for Ethane Hydrogenolysis. *J. Phys. Chem.* **68**, 2962, (1964).
- 138 Taylor, W. F., Sinfelt, J. H. & Yates, D. J. C. Catalysis over Supported Metals .4. Ethane Hydrogenolysis over Dilute Nickel Catalysts. *J. Phys. Chem.* **69**, 3857, (1965).
- 139 Yates, D. J. C., Sinfelt, J. H. & Taylor, W. F. Chemisorption and Catalysis Studies over Supported Cobalt. *Transactions of the Faraday Society* **61**, 2044, (1965).

- 140 Hayek, K., Kramer, R. & Paal, Z. Metal-support boundary sites in catalysis. *Applied Catalysis a-General* **162**, 1-15, (1997).
- 141 Che, M. & Bennett, C. O. The Influence of Particle-Size on the Catalytic Properties of Supported Metals. *Adv. Catal.* **36**, 55-172, (1989).
- 142 Ponec, V. Catalysis by Alloys in Hydrocarbon Reactions. *Adv. Catal.* **32**, 149-214, (1983).
- 143 Tauster, S. J., Fung, S. C., Baker, R. T. K. & Horsley, J. A. Strong-Interactions in Supported-Metal Catalysts. *Science* **211**, 1121-1125, (1981).
- 144 Dauscher, A. & Maire, G. Isomerization and Hydrogenolysis Reactions of Hexanes over Platinum Catalysts Supported on Physical Mixtures of TiO₂ and CeO₂. *J. Mol. Catal.* **69**, 259-270, (1991).
- 145 Dauscher, A., Muller, W. & Maire, G. Catalytic Behavior of Polycrystalline Pt₃Ti in Relation to Strong Metal-Support Interaction Phenomenon. *Catal. Lett.* **2**, 139-144, (1989).
- 146 Bond, G. C., Rajaram, R. R. & Burch, R. Hydrogenolysis of Propane, Normal-Butane, and Isobutane over Various Pretreated Ru/TiO₂ Catalysts. *J. Phys. Chem.* **90**, 4877-4881, (1986).
- 147 Burch, R. in *Hydrogen Effects in Catalysis* (eds Zoltan Paal & P. G. Menon) Ch. 13, 347 (Marcel Dekker, Inc., 1988).
- 148 Sadeghi, H. R. & Henrich, V. E. SMSI in Rh/TiO₂ Model Catalysts - Evidence for Oxide Migration. *J. Catal.* **87**, 279-282, (1984).
- 149 Simoens, A. J., Baker, R. T. K., Dwyer, D. J., Lund, C. R. F. & Madon, R. J. A Study of the Nickel-Titanium Oxide Interaction. *J. Catal.* **86**, 359-372, (1984).
- 150 Bernal, S. *et al.* Metal-Support Interaction Phenomena in Rhodium Ceria and Rhodium Titania Catalysts - Comparative-Study by High-Resolution Transmission Electron-Spectroscopy. *Applied Catalysis a-General* **99**, 1-8, (1993).
- 151 Ko, C. S. & Gorte, R. J. Evidence for Diffusion of a Partially Oxidized Titanium Species into Bulk Platinum. *J. Catal.* **90**, 59-64, (1984).

- 152 Logan, A. D., Braunschweig, E. J., Datye, A. K. & Smith, D. J. Direct Observation of the Surfaces of Small Metal Crystallites - Rhodium Supported on TiO₂. *Langmuir* **4**, 827-830, (1988).
- 153 Bernal, S. *et al.* High-resolution electron microscopy investigation of metal-support interactions in Rh/TiO₂. *Journal of the Chemical Society-Faraday Transactions* **92**, 2799-2809, (1996).
- 154 Belzunegui, J. P., Rojo, J. M. & Sanz, J. H-1-NMR Procedure to Estimate the Extent of Metal-Surface Covered by TiO_x Overlayers in Reduced Rh/TiO₂ Catalysts. *J. Phys. Chem.* **95**, 3463-3465, (1991).
- 155 Belzunegui, J. P., Sanz, J. & Rojo, J. M. Contribution of Physical Blocking and Electronic Effect to Establishment of Strong Metal Support Interaction in Rh/TiO₂ Catalysts. *J. Am. Chem. Soc.* **114**, 6749-6754, (1992).
- 156 Spencer, N. D., Schoonmaker, R. C. & Somorjai, G. A. Structure Sensitivity in the Iron Single-Crystal Catalyzed Synthesis of Ammonia. *Nature* **294**, 643-644, (1981).
- 157 Wulff, G. On the question of speed of growth and dissolution of crystal surfaces. *Zeitschrift fur Kristallographie und Mineralogie* **34**, 449-530, (1901).
- 158 Winterbottom, W. L. Equilibrium Shape of a Small Particle in Contact with a Foreign Substrate. *Acta Metallurgica* **15**, 303, (1967).
- 159 Marks, L. D. Surface-Structure and Energetics of Multiply Twinned Particles. *Philosophical Magazine a-Physics of Condensed Matter Structure Defects and Mechanical Properties* **49**, 81-93, (1984).
- 160 Howie, A. & Marks, L. D. Elastic Strains and the Energy-Balance for Multiply Twinned Particles. *Philosophical Magazine a-Physics of Condensed Matter Structure Defects and Mechanical Properties* **49**, 95-109, (1984).
- 161 Marks, L. D. Modified Wulff Constructions for Twinned Particles. *J. Cryst. Growth* **61**, 556-566, (1983).
- 162 Marks, L. D. & Smith, D. J. HREM and STEM of Defects in Multiply-Twinned Particles. *Journal of Microscopy-Oxford* **130**, 249-261, (1983).
- 163 Marks, L. D. & Smith, D. J. Direct Surface Imaging in Small Metal Particles. *Nature* **303**, 316-317, (1983).

- 164 Howie, A., Marks, L. D. & Pennycook, S. J. New Imaging Methods for Catalyst Particles. *Ultramicroscopy* **8**, 163-174, (1982).
- 165 Marks, L. D. & Howie, A. Multiply-Twinned Particles in Silver Catalysts. *Nature* **282**, 196-198, (1979).
- 166 Rabuffetti, F. A. *et al.* Synthesis-dependent first-order Raman scattering in SrTiO₃ nanocubes at room temperature. *Chem. Mater.* **20**, 5628-5635, (2008).
- 167 Banerjee, S. *et al.* Observation of Fano asymmetry in Raman spectra of SrTiO₃ and Ca_xSr_{1-x}TiO₃ perovskite nanocubes. *Appl. Phys. Lett.* **89**, 223130, (2006).
- 168 Enterkin, J. A., Poeppelmeier, K. R. & Marks, L. D. TEM investigations of SrTiO₃ nanocube surfaces. *In Preparation*, (2010).
- 169 Christensen, S. T. *et al.* Controlled Growth of Platinum Nanoparticles on Strontium Titanate Nanocubes by Atomic Layer Deposition. *Small* **5**, 750-757, (2009).
- 170 Vitos, L., Ruban, A. V., Skriver, H. L. & Kollar, J. The surface energy of metals. *Surf. Sci.* **411**, 186-202, (1998).
- 171 Ringe, E., Van Duyne, R. P. & Marks, L. D. Size-dependent Wulff construction for alloy nanoparticles. *In Preparation*, (2010).
- 172 Ringe, E. <e-mail> (2010)
- 173 Ajayan, P. M. & Marks, L. D. Evidence for Sinking of Small Particles into Substrates and Implications for Heterogeneous Catalysis. *Nature* **338**, 139-141, (1989).
- 174 Rabuffetti, F. A., Stair, P. C. & Poeppelmeier, K. R. Synthesis-Dependent Surface Acidity and Structure of SrTiO₃ Nanoparticles. *J. Phys. Chem. C* **114**, 11056-11067, (2010).
- 175 Rabuffetti, F. A. <e-mail> (2010)
- 176 Polli, A. D., Wagner, T., Gemming, T. & Ruhle, M. Growth of platinum on TiO₂- and SrO-terminated SrTiO₃(100). *Surf. Sci.* **448**, 279-289, (2000).
- 177 Asthagiri, A. & Sholl, D. S. First principles study of Pt adhesion and growth on SrO- and TiO₂-terminated SrTiO₃(100). *J. Chem. Phys.* **116**, 9914-9925, (2002).

- 178 Iddir, H., Komanicky, V., Ogut, S., You, H. & Zapol, P. Shape of platinum nanoparticles supported on SrTiO₃: Experiment and theory. *J. Phys. Chem. C* **111**, 14782-14789, (2007).
- 179 Asthagiri, A. & Sholl, D. S. DFT study of Pt adsorption on low index SrTiO₃ surfaces: SrTiO₃(100), SrTiO₃(111) and SrTiO₃(110). *Surf. Sci.* **581**, 66-87, (2005).
- 180 Georgopoulos, P. & Cohen, J. B. Study of Supported Platinum Catalysts by Anomalous Scattering. *J. Catal.* **92**, 211-215, (1985).
- 181 Setthapun, W. *et al.* Genesis and Evolution of Surface Species during Pt Atomic Layer Deposition on Oxide Supports Characterized by in Situ XAFS Analysis and Water-Gas Shift Reaction. *J. Phys. Chem. C* **114**, 9758-9771, (2010).
- 182 Miao, J., Hu, C. G., Liu, H. & Xiong, Y. F. BaTiO₃ nanocubes: Size-selective formation and structure analysis. *Mater. Lett.* **62**, 235-238, (2008).
- 183 Turkevich, J. & Hillier, J. Electron Microscopy of Colloidal Systems. *Anal. Chem.* **21**, 475-485, (1949).
- 184 Ardenne, M. v. & Beischer, D. Untersuchungen von Katalysatoren mit dem Universal-Elektronenmikroskop. *Angew. Chem.* **53**, 103, (1940).

Appendices

A.1: XPS Peak Fits for All XPS Spectra in Chapter 4

Appendix A.1 contains the fitted peaks for all spectra used in Chapter 4, for the oxygen, titanium, strontium, and carbon energy regions. Peak position, full-width at half-maximum, and areas are listed. The angle listed is the angle from the XPS detector to the sample face, i.e. 90° is normal to the surface. Peaks that were not present or were too small to accurately fit are marked with an X.

Table A.1.1: Peak fitting for O1s peak region, including main O1s peak, the high binding energy shoulder (hydroxyl shoulder) and, when applicable, the holder artifact.

Treatment	Reconstruction	Angle	O1s			O1s Shoulder			Holder Artifact		
			BE	FWHM	Area	BE	FWHM	Area	BE	FWHM	Area
850°C, 5h, Air	$(\sqrt{13}\times\sqrt{13})$ -R33.7°	45°	529.7	2.2	1093	532.7	2.7	667	527.6	2.0	532
		75°	529.5	2.4	1108	532.5	2.6	817	527.1	2.2	647
520°C, 20 min, e ⁻ gun, 3x10 ⁻⁹ torr O ₂	None	45°	530.0	2.3	1290	531.8	2.4	383	527.9	2.0	582
		75°	530.1	2.3	1480	531.8	2.3	394	527.6	2.3	810
850°C, 5h, Air	$(\sqrt{13}\times\sqrt{13})$ -R33.7°	45°	529.9	1.6	14705	532.1	2.6	5560	X	X	X
		80°	529.9	1.7	18653	532.0	2.6	4722	X	X	X
450°C, 2h, Gas Cell, UHV	$(\sqrt{13}\times\sqrt{13})$ -R33.7°	20°	530.1	1.9	7778	532.3	2.3	3599	528.1	1.2	504
		45°	530.0	1.7	14029	532.1	2.3	4202	X	X	X
		85°	530.0	1.7	16072	532.1	2.5	3954	X	X	X
800°C, 3.5h, Gas Cell, UHV	(2x1) streaky	20°	530.1	1.8	11053	532.1	2.5	4245	X	X	X
		45°	530.0	1.7	20220	531.5	2.0	2785	X	X	X
		85°	530.0	1.7	24359	531.8	1.6	1835	X	X	X
800°C, 8h, Gas Cell, UHV	(2x1) streaky	20°	530.1	1.9	9020	532.0	2.0	2164	X	X	X
		45°	530.0	1.7	14639	531.8	1.7	1498	X	X	X
		85°	529.9	1.7	17026	531.8	1.6	1082	X	X	X
950°C, 5h, Air	(2x1) + (5x1) streaky	25°	530.0	1.7	3312	532.1	2.3	806	X	X	X
		45°	530.1	1.6	3999	531.8	2.2	767	X	X	X
750°C, 5h, Gas Cell, 2x10 ⁻² torr O ₂	(2x1)	25°	530.2	1.9	5756	531.9	2.6	1307	528.0	0.7	42
		45°	530.1	1.7	7777	531.7	1.7	888	X	X	X
Air Exposure	Unknown	25°	530.1	1.8	6768	531.9	1.5	632	528.0	1.0	141
		45°	530.0	1.6	8083	531.4	2.0	1476	X	X	X
950°C, 5h, Air	c(4x2), very strong	45°	529.8	2.3	1572	532.0	2.4	537	527.6	2.3	1005
		75°	530.1	2.1	1606	532.0	2.1	571	527.3	2.8	965
400°C, 20 min, e ⁻ gun, 8x10 ⁻⁷ torr O ₂	c(4x2)	45°	530.4	2.2	2097	532.3	2.2	1150	X	X	X
		75°	530.2	2.1	1997	532.1	2.0	381	527.3	2.8	1142
300°C, 3h, e ⁻ gun, 4x10 ⁻⁶ torr O ₂	c(4x2)	45°	529.7	2.7	2011	532.0	2.5	165	527.6	1.6	292
		75°	529.9	2.3	1376	532.2	1.5	100	527.8	2.5	1018
800°C, 20 min, e ⁻ gun, 9x10 ⁻⁷ torr O ₂	c(4x2), weak	45°	529.8	2.9	1941	532.3	1.9	142	527.2	2.0	646
		75°	530.3	2.1	1467	532.3	2.0	320	527.3	3.0	1179

Table A.1.2: Peak fitting for Ti2p peak region, including Ti2p^{3/2} and Ti2p^{1/2} peaks and, when applicable, reduced titanium peaks.

Treatment	Reconstruction Angle	Angle	Ti2p ^{3/2}			Ti2p ^{1/2}			Reduced Ti2p ^{3/2}			Reduced Ti2p ^{1/2}		
			BE	FWHM	Area	BE	FWHM	Area	BE	FWHM	Area	BE	FWHM	Area
850°C, 5h, Air	(√13x√13) -R33.7°	45°	458.8	1.6	210	464.1	3.2	119	455.9	2.0	49	X	X	X
		75°	458.8	1.6	332	464.2	3.1	196	455.3	1.3	30	X	X	X
520°C, 20 min, e ⁻ gun, 3x10 ⁻⁹ torr O ₂	None	45°	458.8	1.8	230	464.5	2.1	87	456.3	1.8	67	462.1	3.9	67
		75°	458.8	1.4	303	464.7	2.0	138	456.5	3.1	65	460.8	4.2	104
850°C, 5h, Air	(√13x√13) -R33.7°	45°	458.8	1.6	9004	464.4	2.7	5192	X	X	X	X	X	X
		80°	458.8	1.6	10934	464.5	2.7	6201	X	X	X	X	X	X
450°C, 2h, Gas Cell, UHV	(√13x√13) -R33.7°	20°	458.8	1.6	4315	464.5	2.8	2493	X	X	X	X	X	X
		45°	458.8	1.6	9160	464.4	2.8	5208	X	X	X	X	X	X
		85°	458.9	1.6	10058	464.5	2.7	5832	X	X	X	X	X	X
800°C, 3.5h, Gas Cell, UHV	(2x1) streaky	20°	458.8	1.7	6300	464.4	2.9	3682	X	X	X	X	X	X
		45°	458.8	1.6	12896	464.4	2.8	7414	X	X	X	X	X	X
		85°	458.8	1.6	13910	464.5	2.9	8184	X	X	X	X	X	X
800°C, 8h, Gas Cell, UHV	(2x1) streaky	20°	458.8	1.6	4575	464.4	2.8	2689	X	X	X	X	X	X
		45°	458.8	1.6	9944	464.4	2.8	5897	X	X	X	X	X	X
		85°	458.8	1.6	9696	464.4	2.9	5679	X	X	X	X	X	X
950°C, 5h, Air	(2x1) + (5x1) streaky	25°	458.8	1.6	2098	464.4	2.7	1211	X	X	X	X	X	X
		45°	458.9	1.6	2684	464.5	2.7	1564	X	X	X	X	X	X
750°C, 5h, Gas Cell, 2x10 ⁻² torr O ₂	(2x1)	25°	458.8	1.5	3222	464.5	2.7	1840	X	X	X	X	X	X
		45°	458.8	1.6	4335	464.5	2.7	2489	X	X	X	X	X	X
Air Exposure	Unknown	25°	458.8	1.6	3977	464.5	2.7	2263	X	X	X	X	X	X
		45°	458.9	1.6	4389	464.5	2.8	2619	X	X	X	X	X	X
950°C, 5h, Air	c(4x2), very strong	45°	458.9	1.9	448	464.4	2.7	212	X	X	X	X	X	X
		75°	458.8	1.8	605	464.5	1.8	247	X	X	X	X	X	X
400°C, 20 min, e ⁻ gun, 8x10 ⁻⁷ torr O ₂	c(4x2)	45°	458.7	1.7	614	464.2	2.5	314	X	X	X	X	X	X
		75°	458.9	1.7	794	464.4	2.9	411	X	X	X	X	X	X
300°C, 3h, e ⁻ gun, 4x10 ⁻⁶ torr O ₂	c(4x2)	45°	458.9	1.5	298	464.5	2.6	186	456.3	1.9	192	461.4	2.2	130
		75°	458.8	1.6	352	464.6	2.1	164	455.6	1.9	162	461.4	3.3	147
800°C, 20 min, e ⁻ gun, 9x10 ⁻⁷ torr O ₂	c(4x2), weak	45°	458.7	1.7	359	464.4	2.4	143	455.9	1.9	64	461.5	2.6	65
		75°	458.9	1.4	310	464.4	2.7	213	457.6	4.9	148	460.1	3.1	92

Table A.1.3: Peak fitting for Sr3d and C1s peak regions, including Sr3d^{5/2} and Sr3d^{3/2} peaks, C1s peak and, when applicable, the non-charging C1s peak from the sample holder.

Treatment	Reconstruction	Angle	Sr3d ^{5/2}			Sr3d ^{3/2}			C1s			Holder C1s		
			BE	FWHM	Area	BE	FWHM	Area	BE	FWHM	Area	position	FWHM	area
850°C, 5h, Air	(√13x√13) -R33.7°	45°	133.8	1.2	115	135.5	1.5	122	285.8	3.2	538	X	X	X
		75°	133.6	1.3	244	135.4	1.6	222	285.8	2.8	490	X	X	X
520°C, 20 min, e ⁻ gun, 3x10 ⁻⁹ torr O ₂	None	45°	133.7	1.2	111	135.5	2.0	186	284.3	2.1	399	X	X	X
		75°	133.8	1.3	284	135.5	1.6	260	284.2	1.9	345	X	X	X
850°C, 5h, Air	(√13x√13) -R33.7°	45°	133.6	1.4	6385	135.3	1.5	5238	285.7	1.8	3114	X	X	X
		80°	133.7	1.4	8407	135.4	1.5	6491	285.7	1.9	2167	X	X	X
450°C, 2h, Gas Cell, UHV	(√13x√13) -R33.7°	20°	133.5	1.4	2252	135.2	1.8	2520	285.4	2.0	3254	X	X	X
		45°	133.5	1.4	6399	135.3	1.5	5044	285.6	2.0	2633	X	X	X
		85°	133.6	1.4	8550	135.4	1.5	6887	285.6	2.0	2109	X	X	X
800°C, 3.5h, Gas Cell, UHV	(2x1) streaky	20°	133.5	1.5	3725	135.3	1.7	3406	284.9	2.2	5908	X	X	X
		45°	133.5	1.4	8632	135.2	1.6	7124	284.6	2.5	2637	X	X	X
		85°	133.6	1.5	11784	135.3	1.5	8777	284.5	2.8	2099	X	X	X
800°C, 8h, Gas Cell, UHV	(2x1) streaky	20°	133.6	1.4	2961	135.3	1.7	2711	284.5	2.3	3505	X	X	X
		45°	133.6	1.4	7129	135.3	1.5	5656	284.7	2.5	2013	X	X	X
		85°	133.5	1.5	8063	135.3	1.5	5895	284.5	2.9	1519	X	X	X
950°C, 5h, Air	(2x1) + (5x1) streaky	25°	133.5	1.3	1782	135.3	1.6	1565	285.1	1.9	1292	X	X	X
		45°	133.6	1.4	2458	135.3	1.5	1980	285.2	2.0	1144	X	X	X
750°C, 5h, Gas Cell, 2x10 ⁻² torr O ₂	(2x1)	25°	133.5	1.4	2153	135.3	1.5	1663	X	X	X	X	X	X
		45°	133.5	1.4	3547	135.3	1.5	2735	X	X	X	X	X	X
Air Exposure	Unknown	25°	133.5	1.3	2613	135.2	1.5	2056	285.0	4.0	187	X	X	X
		45°	133.6	1.4	3679	135.3	1.4	2604	X	X	X	X	X	X
950°C, 5h, Air	c(4x2), very strong	45°	133.7	1.4	342	135.4	2.0	439	284.3	2.7	530	281.7	2.1	697
		75°	133.7	1.5	683	135.5	1.5	535	284.5	1.8	343	X	X	X
400°C, 20 min, e ⁻ gun, 8x10 ⁻⁷ torr O ₂	c(4x2)	45°	133.8	1.6	384	135.6	1.9	408	284.7	2.1	621	X	X	X
		75°	133.8	1.5	568	135.6	1.5	456	284.1	2.0	380	281.1	2.8	663
300°C, 3h, e ⁻ gun, 4x10 ⁻⁶ torr O ₂	c(4x2)	45°	133.7	1.4	346	135.5	1.4	227	284.1	2.5	300	282.4	1.9	961
		75°	133.6	1.4	470	135.3	1.5	356	283.4	2.4	195	281.7	1.7	528
800°C, 20 min, e ⁻ gun, 9x10 ⁻⁷ torr O ₂	c(4x2), weak	45°	133.7	1.5	294	135.5	1.9	310	284.1	2.6	356	281.6	2.2	497
		75°	133.8	1.4	380	135.5	1.7	372	284.2	2.7	359	X	X	X

A.2: CIFs for All Structures, Including Bond Valence Sums

Appendix A.2 contains Crystallographic Information Files (CIF) for all structures analyzed in this work. In addition to the standard information, such as unit cell dimensions and atomic coordinates, bond valence sums for each atom are included. Due to the length of the CIFs as they are deposited with all the experimental parameters and tables of bond lengths and angles, only unit cell parameters, atomic coordinates, occupancies, and bond valence sums are included.

A.2.1: CIFs for $La_4Cu_3MoO_{12}$

The complete crystallographic information files can be obtained from the Fachinformationzentrum Karlsruhe, 76344 Eggenstein-Leopoldshafen, Germany (e-mail: crysdta@fiz.karlsruhe.de) on quoting the Registry nos. CSD-421355 (disordered refinement in Pm) and CSD-421356 (twinned refinement in Pm).

A.2.1.1: $La_4Cu_3MoO_{12}$ with two disordered fractions

data_LCMO_Disordered	
_cell_length_a	6.8560(6)
_cell_length_b	10.9802(10)
_cell_length_c	7.9147(7)
_cell_angle_alpha	90.00
_cell_angle_beta	90.0160(10)
_cell_angle_gamma	90.00
_cell_volume	595.82(9)
_cell_formula_units_Z	2
_symmetry_cell_setting	Monoclinic
_symmetry_space_group_name_H-M	Pm
loop_	

_symmetry_equiv_pos_as_xyz									
'x, y, z'									
'x, -y, z'									
loop_									
_atom_site_label									
_atom_site_type_symbol									
_atom_site_fract_x									
_atom_site_fract_y									
_atom_site_fract_z									
_atom_site_U_iso_or_equiv									
_atom_site_adp_type									
_atom_site_occupancy									
_atom_site_symmetry_multiplicity									
_atom_site_disorder_group									
Mo2A	Mo	0.5913(17)	0.5000	0.1251(16)	0.025(2)	Uani	0.427(12)	2	1
Cu4A	Cu	0.5512(17)	0.5000	0.6253(18)	0.000(2)	Uiso	0.427(12)	2	1
Cu5A	Cu	0.1069(15)	0.5000	0.8440(16)	0.025(2)	Uiso	0.427(12)	2	1
Cu6A	Cu	0.1220(15)	0.5000	0.3943(15)	0.022(2)	Uiso	0.427(12)	2	1
O13A	O	0.256(7)	0.5000	0.629(6)	0.014(11)	Uiso	0.427(12)	2	1
O14A	O	0.303(5)	0.5000	0.122(4)	0.000(7)	Uiso	0.427(12)	2	1
O15A	O	0.732(4)	0.5000	0.921(4)	0.001(5)	Uiso	0.427(12)	2	1
O16A	O	0.715(5)	0.5000	0.323(4)	0.010(6)	Uiso	0.427(12)	2	1
Mo2B	Mo	0.5897(14)	0.5000	0.6168(13)	0.0148(14)	Uani	0.573(12)	2	2
Cu4B	Cu	0.5480(13)	0.5000	0.1211(14)	0.0000(14)	Uiso	0.573(12)	2	2
Cu5B	Cu	0.1164(12)	0.5000	0.3409(13)	0.0204(15)	Uiso	0.573(12)	2	2
Cu6B	Cu	0.1110(12)	0.5000	0.8983(12)	0.0148(14)	Uiso	0.573(12)	2	2
O13B	O	0.250(5)	0.5000	0.113(4)	0.013(8)	Uiso	0.573(12)	2	2
O14B	O	0.306(5)	0.5000	0.619(4)	0.006(6)	Uiso	0.573(12)	2	2
O15B	O	0.725(3)	0.5000	0.419(3)	0.001(4)	Uiso	0.573(12)	2	2
O16B	O	0.720(3)	0.5000	0.815(3)	0.006(5)	Uiso	0.573(12)	2	2
La1	La	0.25064(17)	0.74998(6)	0.11452(13)	0.0065(4)	Uani	1	1	.
La2	La	0.24841(16)	0.75036(6)	0.62688(13)	0.0066(4)	Uani	1	1	.
La3	La	0.76687(13)	0.74836(6)	0.36988(16)	0.0067(4)	Uani	1	1	.
La4	La	0.75349(15)	0.75127(6)	0.87158(18)	0.0061(3)	Uani	1	1	.
Mo1	Mo	0.4196(9)	1.0000	0.3710(9)	0.0040(3)	Uani	1	2	.
Cu1	Cu	0.4712(9)	1.0000	0.8708(9)	0.0142(6)	Uiso	1	2	.
Cu2	Cu	0.8957(9)	1.0000	0.0870(9)	0.0029(5)	Uiso	1	2	.
Cu3	Cu	0.8940(9)	1.0000	0.6543(9)	0.0028(5)	Uiso	1	2	.
O1	O	0.4183(18)	0.8263(7)	0.3709(19)	0.0096(18)	Uiso	1	1	.
O2	O	0.4109(18)	0.8363(7)	0.8690(18)	0.0081(17)	Uiso	1	1	.
O3	O	0.9157(18)	0.8342(8)	0.1192(18)	0.009(2)	Uiso	1	1	.
O4	O	0.9157(19)	0.8328(9)	0.6195(19)	0.012(2)	Uiso	1	1	.

O5	O	0.0796(16)	0.6647(7)	0.8703(17)	0.0070(19)	Uiso	1	1	.
O6	O	0.5831(17)	0.6708(7)	0.6203(16)	0.0059(18)	Uiso	1	1	.
O7	O	0.5820(17)	0.6698(7)	0.1233(16)	0.0076(18)	Uiso	1	1	.
O8	O	0.0836(16)	0.6642(7)	0.3708(16)	0.0044(18)	Uiso	1	1	.
O9	O	0.763(2)	1.0000	0.867(2)	0.009(3)	Uiso	1	2	.
O10	O	0.681(2)	1.0000	0.3688(19)	0.007(3)	Uiso	1	2	.
O11	O	0.292(2)	1.0000	0.5700(18)	0.010(3)	Uiso	1	2	.
O12	O	0.289(2)	1.0000	0.1727(17)	0.007(2)	Uiso	1	2	.

loop_

_atom_site_label

_atom_bond_valence_sum_part_1

_atom_bond_valence_sum_part_2

Mo2A	5.54	.
Cu4A	1.68	.
Cu5A	1.93	.
Cu6A	1.83	.
O13A	-1.60	.
O14A	-1.43	.
O15A	-1.59	.
O16A	-1.91	.
Mo2B	.	5.66
Cu4B	.	1.67
Cu5B	.	1.86
Cu6B	.	1.94
O13B	.	-1.68
O14B	.	-1.47
O15B	.	-1.79
O16B	.	-1.80
La1	3.13	3.14
La2	3.18	3.17
La3	3.22	3.23
La4	3.14	3.13
Mo1	6.00	6.00
Cu1	1.83	1.83
Cu2	1.86	1.86
Cu3	1.87	1.87
O1	-2.24	-2.24
O2	-2.05	-2.05
O3	-2.09	-2.09
O4	-2.07	-2.07
O5	-2.13	-2.12
O6	-1.89	-2.41

O7	-2.47	-1.94
O8	-2.07	-2.07
O9	-1.86	-1.86
O10	-1.84	-1.84
O11	-1.82	-1.82
O12	-1.80	-1.80

A.2.1.2: $\text{La}_4\text{Cu}_3\text{MoO}_{12}$ twinned model

data_LCMO_Twinned					
_cell_length_a				6.8560(6)	
_cell_length_b				10.9802(10)	
_cell_length_c				7.9147(7)	
_cell_angle_alpha				90.00	
_cell_angle_beta				90.0160(10)	
_cell_angle_gamma				90.00	
_cell_volume				595.82(9)	
_cell_formula_units_Z				2	
_symmetry_cell_setting				Monoclinic	
_symmetry_space_group_name_H-M				Pm	
loop_					
_symmetry_equiv_pos_as_xyz					
'x, y, z'					
'x, -y, z'					
loop_					
_atom_site_label					
_atom_site_type_symbol					
_atom_site_fract_x					
_atom_site_fract_y					
_atom_site_fract_z					
_atom_site_U_iso_or_equiv					
Mo2	Mo	0.5855(19)	0.5000	0.6210(16)	0.0133(10)
Cu4	Cu	0.547(2)	0.5000	0.1206(17)	0.0101(10)
Cu5	Cu	0.119(2)	0.5000	0.3410(17)	0.0176(14)
Cu6	Cu	0.115(2)	0.5000	0.8981(17)	0.0158(13)
O13	O	0.254(3)	0.5000	0.120(3)	0.000(3)
O14	O	0.322(3)	0.5000	0.618(3)	0.000(3)
O15	O	0.724(3)	0.5000	0.420(3)	0.000(3)
O16	O	0.731(4)	0.5000	0.822(3)	0.000(4)
La1	La	0.2547(5)	0.74896(10)	0.1155(3)	0.0035(6)
La2	La	0.2443(4)	0.75091(11)	0.6258(3)	0.0026(9)
La3	La	0.7656(4)	0.74843(10)	0.3668(3)	0.0045(9)

La4	La	0.7553(5)	0.75073(10)	0.8745(4)	0.0038(5)
Mo1	Mo	0.4233(19)	1.0000	0.3717(16)	0.0031(6)
Cu1	Cu	0.463(2)	1.0000	0.8663(17)	0.0080(9)
Cu2	Cu	0.901(2)	1.0000	0.0907(16)	0.0063(11)
Cu3	Cu	0.892(2)	1.0000	0.6519(16)	0.0068(11)
O1	O	0.421(3)	0.8227(11)	0.370(3)	0.009(3)
O2	O	0.418(4)	0.8340(11)	0.868(3)	0.009(3)
O3	O	0.919(3)	0.8366(12)	0.123(3)	0.008(4)
O4	O	0.921(4)	0.8363(13)	0.623(3)	0.009(4)
O5	O	0.082(3)	0.6670(10)	0.875(3)	0.003(3)
O6	O	0.582(3)	0.6700(11)	0.625(3)	0.000(3)
O7	O	0.589(3)	0.6651(11)	0.126(3)	0.001(3)
O8	O	0.088(3)	0.6677(10)	0.374(3)	0.000(3)
O9	O	0.743(6)	1.0000	0.847(5)	0.052(9)
O10	O	0.685(6)	1.0000	0.340(4)	0.055(9)
O11	O	0.321(7)	1.0000	0.620(5)	0.124(17)
O12	O	0.305(4)	1.0000	0.186(3)	0.018(6)
loop_					
_atom_site_label					
_atom_bond_valence_sum					
Mo2		5.78			
Cu4		1.86			
Cu5		1.77			
Cu6		1.80			
O13		-1.71			
O14		-1.83			
O15		-1.67			
O16		-1.59			
La1		3.12			
La2		3.22			
La3		3.16			
La4		3.13			
Mo1		5.56			
Cu1		2.09			
Cu2		1.77			
Cu3		2.06			
O1		-2.21			
O2		-2.03			
O3		-2.11			
O4		-2.08			
O5		-2.12			
O6		-2.36			

O7	-2.02
O8	-2.05
O9	-1.80
O10	-1.80
O11	-1.29
O12	-2.28

A.2.2: CIFs for $SrTiO_3$ (1 1 0) surface structures

The complete crystallographic information files for the homologous series can be obtained from the Fachinformationzentrum Karlsruhe, 76344 Eggenstein-Leopoldshafen, Germany (e-mail: crysdata@fiz.karlsruhe.de) on quoting the Registry nos. 421515 (2x1), 421516 (3x1), 421517 (4x1), 421518 (5x1), 421519 (6x1) , and 421520 (∞ x1).

A.2.2.1: $SrTiO_3$ (1 1 0) (2x1)

```

data_2x1
_cell_length_a          31.6930
_cell_length_b          5.5225
_cell_length_c          7.8103
_cell_angle_alpha      90.000000
_cell_angle_beta       90.000000
_cell_angle_gamma      90.000000
_symmetry_space_group_name_H-M 'P112/m'
_symmetry_space_group_number    10
loop_
_symmetry_equiv_pos_as_xyz
  +x,+y,+z
  -x,-y,-z
  -x,-y,+z
  +x,+y,-z
loop_
_atom_site_label
_atom_site_type_symbol
_atom_site_fract_x
_atom_site_fract_y

```

_atom_site_fract_z				
Ti1	Ti	0.26908166	0.46369036	0.20372541
Ti2	Ti	0.26466576	0.95912707	0.28867199
O1	O	0.29964692	0.18554077	0.19689980
O2	O	0.29537748	0.69103463	0.33222640
O3	O	0.27608298	0.60711281	0.00000000
O4	O	0.25093825	0.06945368	0.50000000
O5	O	0.21886347	0.26510923	0.22178493
O6	O	0.21766479	0.75750637	0.22967158
Sr1	Sr	0.17397298	0.00477160	0.00000000
Sr2	Sr	0.17181690	0.00855645	0.50000000
Ti3	Ti	0.17295470	0.50703452	0.24828505
O7	O	0.16541716	0.51945750	0.00000000
O8	O	0.17407118	0.50379076	0.50000000
O9	O	0.13100855	0.25195067	0.25571897
O10	O	0.13036550	0.75986240	0.26326286
Sr3	Sr	0.08612970	0.50174175	0.00000000
Sr4	Sr	0.08720667	0.50240269	0.50000000
Ti4	Ti	0.08665083	0.00337790	0.25074362
O11	O	0.08849455	0.00051225	0.00000000
O12	O	0.08424757	0.01161457	0.50000000
O13	O	0.04404761	0.25643430	0.24512106
O14	O	0.04297618	0.75495035	0.24845891
Sr5	Sr	0.00000000	0.00000000	0.00000000
Sr6	Sr	0.00000000	0.00000000	0.50000000
Ti5	Ti	0.00000000	0.50000000	0.24909958
O15	O	0.00000000	0.50000000	0.00000000
O16	O	0.00000000	0.50000000	0.50000000

loop_

_atom_site_label
_atom_bond_valence_sum

Ti1	4.08
Ti2	4.12
O1	-1.99
O2	-2.05
O3	-2.21
O4	-2.39
O5	-1.95
O6	-2.01
Sr1	2.12
Sr2	2.20
Ti3	4.03

O7 -2.06
 O8 -1.86
 O9 -2.12
 O10 -2.15
 Sr3 2.23
 Sr4 2.17
 Ti4 4.17
 O11 -2.06
 O12 -2.14
 O13 -2.13
 O14 -2.09
 Sr5 2.13
 Sr6 2.14
 Ti5 4.17
 O15 -2.14
 O16 -2.05

A.2.2.2: $SrTiO_3$ (1 1 0) (3x1)

data_3x1
 _cell_length_a 5.5225
 _cell_length_b 31.6930
 _cell_length_c 11.7155
 _cell_angle_alpha 90.000000
 _cell_angle_beta 90.000000
 _cell_angle_gamma 90.000000
 _symmetry_space_group_name_H-M 'P112/m'
 _symmetry_space_group_number 10
 loop_
 _symmetry_equiv_pos_as_xyz
 +x,+y,+z
 -x,-y,+z
 -x,-y,-z
 +x,+y,-z
 loop_
 _atom_site_label
 _atom_site_type_symbol
 _atom_site_fract_x
 _atom_site_fract_y
 _atom_site_fract_z
 Ti1 Ti 0.66064561 0.72910552 0.13918190
 Ti2 Ti 0.15728454 0.72456532 0.23063868

Ti3	Ti	0.99752689	0.74625921	0.50000000
O1	O	0.94707022	0.70239649	0.12719430
O2	O	0.45358900	0.70032586	0.23095697
O3	O	0.51878025	0.73721590	0.00000000
O4	O	0.01223065	0.71680505	0.36716758
O5	O	0.72662304	0.78273290	0.18318738
O6	O	0.22496543	0.77954502	0.19511327
O7	O	0.22536483	0.78807083	0.50000000
O8	O	0.74914236	0.78278316	0.50000000
Sr1	Sr	0.48664804	0.82112313	0.00000000
Sr2	Sr	0.49054080	0.82234667	0.33756886
Ti4	Ti	0.98889655	0.82579503	0.16875942
Ti5	Ti	0.97640656	0.83401798	0.50000000
O9	O	0.99806916	0.82079262	0.00000000
O10	O	0.97536108	0.83439403	0.33348833
O11	O	0.24491439	0.86753728	0.16134499
O12	O	0.73964401	0.86832561	0.15530356
O13	O	0.20111363	0.87859206	0.50000000
O14	O	0.68494921	0.86487116	0.50000000
Sr3	Sr	0.99506100	0.91160892	0.00000000
Sr4	Sr	0.99846895	0.91481249	0.32672459
Ti6	Ti	0.49448449	0.91201802	0.16476619
Ti7	Ti	0.49413502	0.91485362	0.50000000
O15	O	0.48827144	0.91449346	0.00000000
O16	O	0.49483066	0.91286388	0.33154500
O17	O	0.24396673	0.95578155	0.16639122
O18	O	0.74593890	0.95645112	0.16595227
O19	O	0.28113346	0.96309843	0.50000000
O20	O	0.77957811	0.95106812	0.50000000
Sr5	Sr	0.50000000	0.00000000	0.00000000
Sr6	Sr	0.50000000	0.00000000	0.32492588
Ti8	Ti	0.00000000	0.00000000	0.16507412
Ti9	Ti	0.00000000	0.00000000	0.50000000
O21	O	0.00000000	0.00000000	0.00000000
O22	O	0.00000000	0.00000000	0.33299201
loop_				
_atom_site_label				
_atom_bond_valence_sum				
Ti1	4.08			
Ti2	4.04			
Ti3	4.04			
O1	-2.03			

O2	-2.02
O3	-2.19
O4	-2.04
O5	-2.11
O6	-1.99
O7	-2.06
O8	-2.01
Sr1	1.93
Sr2	2.12
Ti4	4.01
Ti5	4.18
O9	-1.75
O10	-2.04
O11	-2.04
O12	-2.09
O13	-2.19
O14	-2.35
Sr3	2.15
Sr4	2.30
Ti6	4.10
Ti7	4.15
O15	-2.11
O16	-1.99
O17	-2.15
O18	-2.09
O19	-2.11
O20	-2.04
Sr5	2.15
Sr6	2.18
Ti8	4.12
Ti9	4.09
O21	-2.12
O22	-2.11

A.2.2.3: $SrTiO_3$ (1 1 0) (4x1)

data_4x1	
_cell_length_a	5.5225
_cell_length_b	31.6930
_cell_length_c	15.6207
_cell_angle_alpha	90.000000
_cell_angle_beta	90.000000

```

_cell_angle_gamma          90.000000
_symmetry_space_group_name_H-M 'P112/m'
_symmetry_space_group_number 10
loop_
_symmetry_equiv_pos_as_xyz
  +x,+y,+z
  -x,-y,+z
  -x,-y,-z
  +x,+y,-z
loop_
_atom_site_label
_atom_site_type_symbol
_atom_site_fract_x
_atom_site_fract_y
_atom_site_fract_z
  Ti1  Ti    0.34541875  0.27078492  0.10591785
  Ti2  Ti    0.84702541  0.27548472  0.18402595
  Ti3  Ti    0.99271693  0.25444852  0.39097788
  O1   O     0.05738453  0.29720749  0.10587751
  O2   O     0.55053977  0.29912693  0.17648320
  O3   O     0.96798341  0.28435934  0.29136684
  O4   O     0.47908651  0.26278771  0.00000000
  O5   O     0.98623461  0.27683586  0.50000000
  O6   O     0.27538982  0.21740059  0.13829880
  O7   O     0.77788156  0.22137718  0.15055547
  O8   O     0.24120322  0.21827903  0.38192057
  O9   O     0.76995380  0.21221431  0.38150837
  Sr1  Sr    0.51377473  0.17789188  0.00000000
  Sr2  Sr    0.50955005  0.17798926  0.25538969
  Sr3  Sr    0.50132982  0.18206312  0.50000000
  Ti4  Ti    0.01108613  0.17457241  0.12683354
  Ti5  Ti    0.02117827  0.16665803  0.37601957
  O10  O     0.00060182  0.17934366  0.00000000
  O11  O     0.02699557  0.16670928  0.25173334
  O12  O     0.01816166  0.16451079  0.50000000
  O13  O     0.25690651  0.13153605  0.11623452
  O14  O     0.75248515  0.13328441  0.12129457
  O15  O     0.31469363  0.13557784  0.37752282
  O16  O     0.79491215  0.12237868  0.37297463
  Sr4  Sr    0.00392165  0.08828706  0.00000000
  Sr5  Sr    0.00253230  0.08565487  0.24514288
  Sr6  Sr    0.99821344  0.08345864  0.50000000

```

Ti6	Ti	0.50554396	0.08794603	0.12379687
Ti7	Ti	0.50699886	0.08601332	0.37475965
O17	O	0.50336957	0.08799295	0.24804062
O18	O	0.51401035	0.08535467	0.00000000
O19	O	0.51017800	0.08337132	0.50000000
O20	O	0.25466224	0.04353255	0.12388876
O21	O	0.75667605	0.04455548	0.12527619
O22	O	0.22366834	0.04850864	0.37203136
O23	O	0.72470044	0.03774017	0.37213439
Sr7	Sr	0.50000000	0.00000000	0.00000000
Sr8	Sr	0.50000000	0.00000000	0.24694640
Sr9	Sr	0.50000000	0.00000000	0.50000000
Ti8	Ti	0.00000000	0.00000000	0.12378047
Ti9	Ti	0.00000000	0.00000000	0.37273261
O24	O	0.00000000	0.00000000	0.00000000
O25	O	0.00000000	0.00000000	0.24811676
O26	O	0.00000000	0.00000000	0.50000000

loop_

_atom_site_label

_atom_bond_valence_sum

Ti1	4.07
Ti2	3.97
Ti3	3.94
O1	-2.03
O2	-2.02
O3	-1.94
O4	-2.13
O5	-1.84
O6	-2.10
O7	-1.95
O8	-2.04
O9	-2.11
Sr1	1.91
Sr2	2.06
Sr3	2.14
Ti4	3.94
Ti5	4.21
O10	-1.74
O11	-2.00
O12	-2.07
O13	-2.07
O14	-2.02

O15	-2.29
O16	-2.22
Sr4	2.15
Sr5	2.30
Sr6	2.38
Ti6	4.10
Ti7	4.16
O17	-2.00
O18	-2.11
O19	-2.02
O20	-2.06
O21	-2.13
O22	-2.08
O23	-2.17
Sr7	2.15
Sr8	2.18
Sr9	2.24
Ti8	4.14
Ti9	4.08
O24	-2.12
O25	-2.16
O26	-2.09

A.2.2.4: $SrTiO_3$ (1 1 0) (5x1)

```

data_5x1
_cell_length_a      5.5225
_cell_length_b     29.7122
_cell_length_c     19.5259
_cell_angle_alpha  90.000000
_cell_angle_beta   90.000000
_cell_angle_gamma  90.000000
_symmetry_space_group_name_H-M 'P112/m'
_symmetry_space_group_number    10
loop_
_symmetry_equiv_pos_as_xyz
  +x,+y,+z
  -x,-y,+z
  -x,-y,-z
  +x,+y,-z
loop_
_atom_site_label

```

_atom_site_type_symbol		_atom_site_fract_x	_atom_site_fract_y	_atom_site_fract_z
Ti1	Ti	0.34932916	0.28853237	0.08732390
Ti2	Ti	0.84822459	0.29492560	0.15626873
Ti3	Ti	0.97587200	0.27261228	0.32340493
Ti4	Ti	0.98289965	0.27205230	0.50000000
O1	O	0.46477894	0.28231043	0.00000000
O2	O	0.06520144	0.31784698	0.09512391
O3	O	0.55105907	0.31883554	0.14457062
O4	O	0.94659193	0.30509480	0.24391503
O5	O	0.96588146	0.29613542	0.41180244
O6	O	0.28410656	0.23065772	0.11054561
O7	O	0.78697304	0.23744834	0.12695440
O8	O	0.22749148	0.23492526	0.31199815
O9	O	0.75947929	0.22676268	0.30977324
O10	O	0.23279976	0.23351558	0.50000000
O11	O	0.76448862	0.22636367	0.50000000
Sr1	Sr	0.50757809	0.18962421	0.00000000
Sr2	Sr	0.51015296	0.18844765	0.20487774
Sr3	Sr	0.49404913	0.19395884	0.40253935
Ti5	Ti	0.00650939	0.18741234	0.10236142
Ti6	Ti	0.01620891	0.17904221	0.30205475
Ti7	Ti	0.01370297	0.17696439	0.50000000
O12	O	0.99290460	0.19285483	0.00000000
O13	O	0.02844297	0.17829185	0.20303773
O14	O	0.01393280	0.17490643	0.40193662
O15	O	0.24586699	0.13973842	0.09302699
O16	O	0.74357547	0.14468562	0.09838456
O17	O	0.30781028	0.14475182	0.30418346
O18	O	0.79138044	0.13099262	0.29881439
O19	O	0.31015106	0.14347140	0.50000000
O20	O	0.79073618	0.12930940	0.50000000
Sr4	Sr	0.00226146	0.09447068	0.00000000
Sr5	Sr	0.00283521	0.09182643	0.19670855
Sr6	Sr	0.00051415	0.08918995	0.39915972
Ti8	Ti	0.50111150	0.09451426	0.09930520
Ti9	Ti	0.50479679	0.09192016	0.30048633
Ti10	Ti	0.50592780	0.09098362	0.50000000
O21	O	0.51461770	0.09248689	0.00000000
O22	O	0.49857301	0.09531116	0.19820995

O23	O	0.50772104	0.08827665	0.39927696
O24	O	0.25913782	0.04581583	0.09885951
O25	O	0.76000571	0.04870736	0.10032277
O26	O	0.22544046	0.05148691	0.29675976
O27	O	0.72518076	0.04064448	0.29625935
O28	O	0.22609645	0.05061724	0.50000000
O29	O	0.72862417	0.04015302	0.50000000
Sr7	Sr	0.50000000	0.00000000	0.00000000
Sr8	Sr	0.50000000	0.00000000	0.19759170
Sr9	Sr	0.50000000	0.00000000	0.39941978
Ti11	Ti	0.00000000	0.00000000	0.09897856
Ti12	Ti	0.00000000	0.00000000	0.29753297
Ti13	Ti	0.00000000	0.00000000	0.50000000
O30	O	0.00000000	0.00000000	0.00000000
O31	O	0.00000000	0.00000000	0.19816280
O32	O	0.00000000	0.00000000	0.39835612

loop_
 _atom_site_label
 _atom_bond_valence_sum

Ti1	4.04
Ti2	3.97
Ti3	3.85
Ti4	3.82
O1	-2.10
O2	-2.02
O3	-2.03
O4	-1.93
O5	-1.75
O6	-2.10
O7	-1.96
O8	-1.97
O9	-2.08
O10	-2.02
O11	-2.12
Sr1	1.90
Sr2	2.05
Sr3	2.10
Ti5	3.90
Ti6	4.14
Ti7	4.22
O12	-1.66
O13	-1.99

O14	-2.10
O15	-2.07
O16	-2.01
O17	-2.25
O18	-2.20
O19	-2.22
O20	-2.25
Sr4	2.12
Sr5	2.28
Sr6	2.43
Ti8	4.04
Ti9	4.15
Ti10	4.21
O21	-2.09
O22	-2.00
O23	-2.06
O24	-2.05
O25	-2.06
O26	-2.10
O27	-2.15
O28	-2.16
O29	-2.23
Sr7	2.11
Sr8	2.18
Sr9	2.30
Ti11	4.09
Ti12	4.11
Ti13	4.16
O30	-2.12
O31	-2.17
O32	-2.12

A.2.2.5: $SrTiO_3$ (1 1 0) (6x1)

data_6x1	
_cell_length_a	5.575998
_cell_length_b	29.999988
_cell_length_c	23.657991
_cell_angle_alpha	90.000000
_cell_angle_beta	90.000000
_cell_angle_gamma	90.000000
_symmetry_space_group_name_H-M	'P112/m'

```

_symmetry_space_group_number      10
loop_
_symmetry_equiv_pos_as_xyz
  +x,+y,+z
  -x,-y,+z
  -x,-y,-z
  +x,+y,-z
loop_
_atom_site_label
_atom_site_type_symbol
_atom_site_fract_x
_atom_site_fract_y
_atom_site_fract_z
  Ti1  Ti    0.34825868    0.28874944    0.07280412
  Ti2  Ti    0.84849942    0.29522341    0.13130408
  Ti3  Ti    0.97342466    0.27272744    0.27199763
  Ti4  Ti    0.97788481    0.27210576    0.42323014
  O1   O     0.46384296    0.28274017    0.00000000
  O2   O     0.06317101    0.31756807    0.07948574
  O3   O     0.55214851    0.31899313    0.12022437
  O4   O     0.94543398    0.30452230    0.20514458
  O5   O     0.96215547    0.29449225    0.34756246
  O6   O     0.96771327    0.29301157    0.50000000
  O7   O     0.78876640    0.23801050    0.10642879
  O8   O     0.28595166    0.23054477    0.09170706
  O9   O     0.22590498    0.23553646    0.26084288
  O10  O     0.75794904    0.22714826    0.25855550
  O11  O     0.22930422    0.23425924    0.42002234
  O12  O     0.75770174    0.22680453    0.42017178
  Sr1  Sr    0.50529938    0.18961387    0.00000000
  Sr2  Sr    0.50951630    0.18862029    0.17073794
  Sr3  Sr    0.49363622    0.19445705    0.33631438
  Sr4  Sr    0.49401860    0.19444948    0.50000000
  Ti5  Ti    0.00604720    0.18745402    0.08519919
  Ti6  Ti    0.01593513    0.17950163    0.74840159
  Ti7  Ti    0.01188376    0.17793933    0.41740017
  O13  O     0.99050984    0.19314487    0.00000000
  O14  O     0.02908787    0.17838773    0.16929165
  O15  O     0.01180522    0.17617066    0.33580623
  O16  O     0.01486386    0.17605098    0.50000000
  O17  O     0.24290375    0.13955110    0.07738924
  O18  O     0.74108169    0.14514143    0.08223816

```

O19	O	0.30686530	0.14518560	0.25381213
O20	O	0.79087973	0.13150525	0.24904028
O21	O	0.30735817	0.14450004	0.41740595
O22	O	0.78920312	0.13031913	0.41713037
Sr4	Sr	0.00135467	0.09449040	0.00000000
Sr6	Sr	0.00237235	0.09202570	0.16401600
Sr7	Sr	0.99964272	0.08970135	0.33275586
Sr8	Sr	0.99962908	0.08931883	0.50000000
Ti8	Ti	0.50151645	0.09444775	0.08287334
Ti9	Ti	0.50460649	0.09209608	0.25065883
Ti10	Ti	0.50477766	0.09169117	0.41702698
O23	O	0.51505514	0.09283732	0.00000000
O24	O	0.49768745	0.09540152	0.16517443
O25	O	0.50735066	0.08897759	0.33269487
O26	O	0.50516854	0.08886554	0.50000000
O27	O	0.26057665	0.04551420	0.08226136
O28	O	0.76138227	0.04912596	0.08355615
O29	O	0.22497145	0.05162177	0.24723883
O30	O	0.72471916	0.04079972	0.24673959
O31	O	0.22507831	0.05103894	0.41591835
O32	O	0.72749754	0.04039762	0.41605093
Sr9	Sr	0.50000000	0.00000000	0.00000000
Sr10	Sr	0.50000000	0.00000000	0.16457798
Sr11	Sr	0.50000000	0.00000000	0.33274631
Sr12	Sr	0.50000000	0.00000000	0.50000000
Ti11	Ti	0.00000000	0.00000000	0.08256313
Ti12	Ti	0.00000000	0.00000000	0.24803775
Ti13	Ti	0.00000000	0.00000000	0.41628476
O33	O	0.00000000	0.00000000	0.00000000
O34	O	0.00000000	0.00000000	0.16489293
O35	O	0.00000000	0.00000000	0.33134691
O36	O	0.00000000	0.00000000	0.50000000

loop_

_atom_site_label

_atom_bond_valence_sum

Ti1	4.03
Ti2	3.96
Ti3	3.80
Ti4	3.68
O1	-2.09
O2	-2.02
O3	-2.03

O4	-1.90
O5	-1.63
O6	-1.57
O7	-1.95
O8	-2.09
O9	-1.95
O10	-2.07
O11	-2.02
O12	-2.13
Sr1	1.91
Sr2	2.04
Sr3	2.04
Sr4	2.05
Ti5	3.87
Ti6	4.10
Ti7	4.20
O13	-1.66
O14	-1.99
O15	-2.05
O16	-2.08
O17	-2.06
O18	-2.00
O19	-2.22
O20	-2.19
O21	-2.19
O22	-2.25
Sr4	2.13
Sr6	2.28
Sr7	2.39
Sr8	2.44
Ti8	4.03
Ti9	4.12
Ti10	4.17
O23	-2.08
O24	-2.00
O25	-2.05
O26	-2.06
O27	-2.05
O28	-2.07
O29	-2.09
O30	-2.14
O31	-2.15

O32 -2.20
 Sr9 2.11
 Sr10 2.17
 Sr11 2.28
 Sr12 2.32
 Ti11 4.08
 Ti12 4.10
 Ti13 4.13
 O33 -2.11
 O34 -2.16
 O35 -2.12
 O36 -2.17

A.2.2.6: $SrTiO_3$ (1 1 0) ($\infty x 1$)

```

data_1x1
_cell_length_a          3.9052
_cell_length_b          5.5225
_cell_length_c          31.6930
_cell_angle_alpha       90.000000
_cell_angle_beta        90.000000
_cell_angle_gamma       90.000000
_symmetry_space_group_name_H-M 'Pmmm'
_symmetry_space_group_number 47
loop_
_symmetry_equiv_pos_as_xyz
  +x,+y,+z
  -x,-y,+z
  -x,+y,-z
  +x,-y,-z
  -x,-y,-z
  +x,+y,-z
  +x,-y,+z
  -x,+y,+z
loop_
_atom_site_label
_atom_site_type_symbol
_atom_site_fract_x
_atom_site_fract_y
_atom_site_fract_z
  Ti1  Ti    0.50000000  0.00000000  0.25406892
  Ti2  Ti    0.50000000  0.50000000  0.17403745
  
```

Ti3	Ti	0.50000000	0.00000000	0.08685943
Ti4	Ti	0.50000000	0.50000000	0.00000000
O1	O	0.00000000	0.00000000	0.26821875
O2	O	0.50000000	0.76192819	0.21625846
O3	O	0.00000000	0.50000000	0.17131976
O4	O	0.50000000	0.24970224	0.13048312
O5	O	0.00000000	0.00000000	0.08727830
O6	O	0.50000000	0.24966670	0.04348745
O7	O	0.00000000	0.50000000	0.00000000
Sr1	Sr	0.00000000	0.00000000	0.17230020
Sr2	Sr	0.00000000	0.50000000	0.08743482
Sr3	Sr	0.00000000	0.00000000	0.00000000

loop_
 _atom_site_label
 _atom_bond_valence_sum

Ti1	3.19
Ti2	4.06
Ti3	4.16
Ti4	4.14
O1	-1.21
O2	-2.07
O3	-1.96
O4	-2.11
O5	-2.11
O6	-2.09
O7	-2.07
Sr1	2.16
Sr2	2.16
Sr3	2.11

A.2.3: CIFs for SrTiO₃ (1 0 0) surface structures

A.2.3.1: SrO (1x1)

data_SrO_1x1	
_cell_length_a	5.5225
_cell_length_b	5.5225
_cell_length_c	35.6629
_cell_angle_alpha	90.0000
_cell_angle_beta	90.0000

_cell_angle_gamma				90.0000		
_cell_formula_units_Z				1		
_symmetry_space_group_name_H-M				'P-1'		
loop_						
_atom_site_label						
_atom_site_type_symbol						
_atom_site_fract_x						
_atom_site_fract_y						
_atom_site_fract_z						
_atom_site_occupancy						
_atom_site_B_iso_or_equiv						
Sr1	Sr	0.007486	0.008803	0.323007	1.0000	0.000
Sr2	Sr	0.503158	0.505170	0.322982	1.0000	0.000
O1	O	0.501105	0.013006	0.329318	1.0000	0.000
O2	O	0.010521	0.505046	0.329413	1.0000	0.000
Ti1	Ti	0.504564	0.006553	0.276267	1.0000	0.000
Ti2	Ti	0.004559	0.506593	0.276294	1.0000	0.000
O3	O	0.756563	0.759357	0.275629	1.0000	0.000
O4	O	0.256390	0.259338	0.274279	1.0000	0.000
O5	O	0.755883	0.258593	0.274997	1.0000	0.000
O6	O	0.255723	0.758652	0.274918	1.0000	0.000
Sr3	Sr	0.001259	0.004110	0.217734	1.0000	0.000
Sr4	Sr	0.501456	0.504326	0.217663	1.0000	0.000
O7	O	0.506490	0.006498	0.219388	1.0000	0.000
O8	O	0.003855	0.508843	0.219402	1.0000	0.000
Ti3	Ti	0.499014	0.002244	0.165061	1.0000	0.000
Ti4	Ti	0.998737	0.502500	0.165074	1.0000	0.000
O9	O	0.753696	0.755877	0.164757	1.0000	0.000
O10	O	0.254118	0.256361	0.164858	1.0000	0.000
O11	O	0.754224	0.256615	0.164778	1.0000	0.000
O12	O	0.253943	0.756826	0.164793	1.0000	0.000
Sr5	Sr	0.999004	0.001648	0.109417	1.0000	0.000
O13	O	0.503817	0.004878	0.109804	1.0000	0.000
Sr6	Sr	0.499017	0.501712	0.109415	1.0000	0.000
O14	O	0.003368	0.505341	0.109786	1.0000	0.000
Ti5	Ti	0.497522	0.999586	0.054982	1.0000	0.000
O15	O	0.753500	0.754310	0.054915	1.0000	0.000
O16	O	0.752105	0.254404	0.054967	1.0000	0.000
Ti6	Ti	0.997451	0.499643	0.054993	1.0000	0.000
O17	O	0.252314	0.253097	0.054952	1.0000	0.000
O18	O	0.253258	0.753340	0.054959	1.0000	0.000
Sr7	Sr	0.000000	0.000000	0.000000	1.0000	0.000

Sr8	Sr	0.500000	0.500000	0.000000	1.0000	0.000
O19	O	0.500000	0.000000	0.000000	1.0000	0.000
O20	O	0.000000	0.500000	0.000000	1.0000	0.000

loop_
 _atom_site_label
 _atom_bond_valence_sum

Sr1	1.78
Sr2	1.78
O1	-1.50
O2	-1.49
Ti1	4.13
Ti2	4.12
O3	-2.22
O4	-2.22
O5	-2.22
O6	-2.22
Sr3	2.09
Sr4	2.09
O7	-1.98
O8	-1.98
Ti3	4.14
Ti4	4.14
O9	-2.12
O10	-2.11
O11	-2.12
O12	-2.12
Sr5	2.10
O13	-2.04
Sr6	2.10
O14	-2.04
Ti5	4.12
O15	-2.08
O16	-2.09
Ti6	4.12
O17	-2.08
O18	-2.09
Sr7	2.09
Sr8	2.09
O19	-2.05
O20	-2.05

A.2.3.2: *SrO* (1x1) – *CO*₂

data_SrCO2						
_cell_length_a			5.5225			
_cell_length_b			5.5225			
_cell_length_c			35.6619			
_cell_angle_alpha			90.0000			
_cell_angle_beta			90.0000			
_cell_angle_gamma			90.0000			
_cell_formula_units_Z			1			
_symmetry_space_group_name_H-M			'P-1'			
loop_						
_atom_site_label						
_atom_site_type_symbol						
_atom_site_fract_x						
_atom_site_fract_y						
_atom_site_fract_z						
_atom_site_occupancy						
_atom_site_B_iso_or_equiv						
C1	C	0.598148	0.008401	0.365686	1.0000	0.000
O1	O	0.684737	0.210862	0.375642	1.0000	0.000
O2	O	0.687913	0.805580	0.375203	1.0000	0.000
Sr1	Sr	0.006391	0.006403	0.328780	1.0000	0.000
Sr2	Sr	0.509918	0.507630	0.331704	1.0000	0.000
O3	O	0.426405	0.008297	0.338344	1.0000	0.000
O4	O	0.056123	0.502031	0.328330	1.0000	0.000
Ti1	Ti	0.505722	0.004031	0.270863	1.0000	0.000
Ti2	Ti	0.010462	0.503666	0.279728	1.0000	0.000
O5	O	0.749906	0.759400	0.280651	1.0000	0.000
O6	O	0.253935	0.248202	0.270917	1.0000	0.000
O7	O	0.747982	0.251389	0.280445	1.0000	0.000
O8	O	0.256007	0.759010	0.271713	1.0000	0.000
Sr3	Sr	0.005093	0.000163	0.219166	1.0000	0.000
Sr4	Sr	0.500510	0.501569	0.219606	1.0000	0.000
O9	O	0.537866	0.002593	0.220208	1.0000	0.000
O10	O	0.974783	0.506064	0.218527	1.0000	0.000
Ti3	Ti	0.500410	0.997887	0.162263	1.0000	0.000
Ti4	Ti	0.994645	0.497551	0.166667	1.0000	0.000
O11	O	0.752813	0.754152	0.162398	1.0000	0.000
O12	O	0.256571	0.252228	0.166823	1.0000	0.000
O13	O	0.754075	0.251310	0.162632	1.0000	0.000
O14	O	0.256687	0.755117	0.166667	1.0000	0.000

Sr5	Sr	0.997616	0.997353	0.109420	1.0000	0.000
O15	O	0.493014	0.003264	0.109877	1.0000	0.000
Sr6	Sr	0.496893	0.497854	0.109573	1.0000	0.000
O16	O	0.011775	0.502044	0.109007	1.0000	0.000
Ti5	Ti	0.494911	0.996965	0.054079	1.0000	0.000
O17	O	0.751082	0.753726	0.055353	1.0000	0.000
O18	O	0.748671	0.252271	0.055313	1.0000	0.000
Ti6	Ti	0.996331	0.496490	0.055585	1.0000	0.000
O19	O	0.250634	0.247906	0.054514	1.0000	0.000
O20	O	0.254433	0.751676	0.054655	1.0000	0.000
Sr7	Sr	0.000000	0.000000	0.000000	1.0000	0.000
Sr8	Sr	0.500000	0.500000	0.000000	1.0000	0.000
O21	O	0.500000	0.000000	0.000000	1.0000	0.000
O22	O	0.000000	0.500000	0.000000	1.0000	0.000
loop_						
_atom_site_label						
_atom_bond_valence_sum						
C1		3.87				
O1		-2.00				
O2		-2.00				
Sr1		2.21				
Sr2		2.22				
O3		-2.17				
O4		-1.96				
Ti1		4.05				
Ti2		4.01				
O5		-2.02				
O6		-2.07				
O7		-2.02				
O8		-2.07				
Sr3		2.12				
Sr4		2.08				
O9		-2.23				
O10		-1.99				
Ti3		4.19				
Ti4		4.09				
O11		-2.10				
O12		-2.03				
O13		-2.11				
O14		-2.05				
Sr5		2.12				
O15		-2.19				

Sr6	2.11
O16	-2.01
Ti5	4.20
O17	-2.07
O18	-2.08
Ti6	4.10
O19	-2.10
O20	-2.10
Sr7	2.09
Sr8	2.09
O21	-2.17
O22	-1.98

A.2.3.3: SrO (1x1) – H₂O

data_SrOHc						
_cell_length_a			3.905018			
_cell_length_b			3.905018			
_cell_length_c			35.662084			
_cell_angle_alpha			90.0000			
_cell_angle_beta			90.0000			
_cell_angle_gamma			90.0000			
_cell_formula_units_Z			1			
_symmetry_space_group_name_H-M			'P-1'			
loop_						
_atom_site_label						
_atom_site_type_symbol						
_atom_site_fract_x						
_atom_site_fract_y						
_atom_site_fract_z						
_atom_site_occupancy						
_atom_site_B_iso_or_equiv						
H1	H	0.586327	0.186167	0.398291	1.0000	0.000
H2	H	0.532722	0.353932	0.350414	1.0000	0.000
O1	O	0.579636	0.097760	0.373297	1.0000	0.000
Sr1	Sr	0.033983	0.960146	0.325863	1.0000	0.000
O2	O	0.487499	0.518793	0.324959	1.0000	0.000
Ti1	Ti	0.523938	0.472034	0.270931	1.0000	0.000
O3	O	0.001863	0.494932	0.270871	1.0000	0.000
O4	O	0.505950	0.998497	0.270961	1.0000	0.000
Sr2	Sr	0.017955	0.982099	0.216607	1.0000	0.000
O5	O	0.496559	0.501220	0.216719	1.0000	0.000

Ti2	Ti	0.517001	0.483624	0.162575	1.0000	0.000
O6	O	0.998963	0.498650	0.162502	1.0000	0.000
O7	O	0.500595	0.000116	0.162509	1.0000	0.000
Sr3	Sr	0.012739	0.989877	0.108295	1.0000	0.000
O8	O	0.497280	0.501789	0.108382	1.0000	0.000
Ti3	Ti	0.511440	0.490108	0.054202	1.0000	0.000
O9	O	0.998332	0.499914	0.054186	1.0000	0.000
O10	O	0.498952	0.000418	0.054186	1.0000	0.000
Sr4	Sr	0.000000	0.000000	0.000000	1.0000	0.000
O11	O	0.500000	0.500000	0.000000	1.0000	0.000
loop_						
_atom_site_label						
_atom_bond_valence_sum						
H1		1.01				
H2		1.03				
O1		-1.91				
Sr1		2.02				
O2		-2.15				
Ti1		4.26				
O3		-2.13				
O4		-2.14				
Sr2		2.18				
O5		-2.16				
Ti2		4.24				
O6		-2.13				
O7		-2.13				
Sr3		2.18				
O8		-2.16				
Ti3		4.23				
O9		-2.12				
O10		-2.12				
Sr4		2.16				
O11		-2.15				

A.2.3.4: TiO_2 (1x1)

data_TiO2_1x1	
_cell_length_a	3.9050
_cell_length_b	3.9050
_cell_length_c	38.4232
_cell_angle_alpha	90.0000
_cell_angle_beta	90.0000

```

_cell_angle_gamma          90.0000
_cell_formula_units_Z      1
_symmetry_space_group_name_H-M 'P4/mmm'
loop_
_atom_site_label
_atom_site_type_symbol
_atom_site_fract_x
_atom_site_fract_y
_atom_site_fract_z
_atom_site_occupancy
_atom_site_B_iso_or_equiv
  Ti1  Ti  0.000000  0.000000  0.202243  1.0000  0.000
  Ti2  Ti  0.000000  0.000000  0.300496  1.0000  0.000
  Ti3  Ti  0.000000  0.000000  0.400133  1.0000  0.000
  Ti4  Ti  0.000000  0.000000  0.500000  1.0000  0.000
  Sr5  Sr  0.500000  0.500000  0.245802  1.0000  0.000
  Sr6  Sr  0.500000  0.500000  0.349261  1.0000  0.000
  Sr7  Sr  0.500000  0.500000  0.449893  1.0000  0.000
  O8   O   0.000000  0.000000  0.249466  1.0000  0.000
  O9   O   0.000000  0.000000  0.349920  1.0000  0.000
  O10  O   0.000000  0.000000  0.450003  1.0000  0.000
  O11  O   0.500000  0.000000  0.200088  1.0000  0.000
  O12  O   0.500000  0.000000  0.300090  1.0000  0.000
  O13  O   0.500000  0.000000  0.400076  1.0000  0.000
  O14  O   0.500000  0.000000  0.500000  1.0000  0.000
loop_
_atom_site_label
_atom_bond_valence_sum
  Ti1  3.75
  Ti2  4.23
  Ti3  4.25
  Ti4  4.26
  Sr5  2.25
  Sr6  2.20
  Sr7  2.20
  O8   -2.37
  O9   -2.23
  O10  -2.21
  O11  -1.88
  O12  -2.05
  O13  -2.11
  O14  -2.12

```

A.2.3.5: $TiO_2 (1x1) - CO_2$

```

data_TiOH
_cell_length_a      3.905010
_cell_length_b      3.905010
_cell_length_c      35.662059
_cell_angle_alpha   90.0000
_cell_angle_beta    90.0000
_cell_angle_gamma   90.0000
_cell_formula_units_Z 1
_symmetry_space_group_name_H-M 'P -1'
loop_
_atom_site_label
_atom_site_type_symbol
_atom_site_fract_x
_atom_site_fract_y
_atom_site_fract_z
_atom_site_occupancy
_atom_site_B_iso_or_equiv
  H1      H      0.797728    0.497603    0.675840    1.0000    0.000
  O1      O      0.554724    0.526929    0.670042    1.0000    0.000
  H2      H      0.520790    0.770478    0.674727    1.0000    0.000
  Ti1     Ti      0.444708    0.422968    0.730347    1.0000    0.000
  O2      O      0.478654    0.960204    0.728401    1.0000    0.000
  O3      O      0.984570    0.454126    0.728468    1.0000    0.000
  Sr1     Sr      0.955677    0.938463    0.779844    1.0000    0.000
  O4      O      0.487187    0.465105    0.782384    1.0000    0.000
  Ti2     Ti      0.461984    0.449371    0.837356    1.0000    0.000
  O5      O      0.485687    0.969657    0.836975    1.0000    0.000
  O6      O      0.989076    0.466406    0.836978    1.0000    0.000
  Sr2     Sr      0.971740    0.963673    0.890803    1.0000    0.000
  O7      O      0.496447    0.481544    0.891259    1.0000    0.000
  Ti3     Ti      0.479994    0.477038    0.945753    1.0000    0.000
  O8      O      0.496442    0.991317    0.945771    1.0000    0.000
  O9      O      0.998387    0.489573    0.945761    1.0000    0.000
  Sr3     Sr      0.000000    0.000000    0.000000    1.0000    0.000
  O10     O      0.500000    0.500000    0.000000    1.0000    0.000
loop_
_atom_site_label
_atom_bond_valence_sum
  H1      1.01
  O1      -2.23

```

H2	1.02
Ti1	4.13
O2	-1.97
O3	-1.99
Sr1	2.22
O4	-2.26
Ti2	4.23
O5	-2.08
O6	-2.11
Sr2	2.17
O7	-2.15
Ti3	4.22
O8	-2.10
O9	-2.12
Sr3	2.16
O10	-2.14

A.2.3.6: $TiO_2 (1 \times 1) - H_2O$

data_TiCO2						
_cell_length_a			5.5225			
_cell_length_b			5.5225			
_cell_length_c			35.6619			
_cell_angle_alpha			90.0000			
_cell_angle_beta			90.0000			
_cell_angle_gamma			90.0000			
_cell_formula_units_Z			1			
_symmetry_space_group_name_H-M			'P-1'			
loop_						
_atom_site_label						
_atom_site_type_symbol						
_atom_site_fract_x						
_atom_site_fract_y						
_atom_site_fract_z						
_atom_site_occupancy						
_atom_site_B_iso_or_equiv						
C1	C	0.744621	0.243961	0.309671	1.0000	0.000
O1	O	0.599431	0.095301	0.324322	1.0000	0.000
O2	O	0.893519	0.389965	0.324054	1.0000	0.000
Ti1	Ti	0.498263	0.953392	0.272302	1.0000	0.000
Ti2	Ti	0.034834	0.489145	0.272206	1.0000	0.000
O3	O	0.735921	0.739454	0.268477	1.0000	0.000

O4	O	0.245515	0.248767	0.268539	1.0000	0.000
O5	O	0.743645	0.243340	0.271046	1.0000	0.000
O6	O	0.240137	0.746669	0.274084	1.0000	0.000
Sr1	Sr	0.996399	0.992288	0.219361	1.0000	0.000
Sr2	Sr	0.504693	0.483275	0.218577	1.0000	0.000
O7	O	0.498056	0.997519	0.218975	1.0000	0.000
O8	O	0.994013	0.490960	0.218821	1.0000	0.000
Ti3	Ti	0.498431	0.992918	0.164140	1.0000	0.000
Ti4	Ti	0.999266	0.493743	0.164139	1.0000	0.000
O9	O	0.748805	0.744650	0.163925	1.0000	0.000
O10	O	0.248420	0.244088	0.163710	1.0000	0.000
O11	O	0.748938	0.244051	0.164201	1.0000	0.000
O12	O	0.249164	0.743807	0.164825	1.0000	0.000
Sr3	Sr	0.998996	0.996561	0.109683	1.0000	0.000
O13	O	0.498883	0.995546	0.109579	1.0000	0.000
Sr4	Sr	0.499274	0.496157	0.109640	1.0000	0.000
O14	O	0.999764	0.497382	0.109533	1.0000	0.000
Ti5	Ti	0.499426	0.998094	0.054771	1.0000	0.000
O15	O	0.749229	0.748285	0.054633	1.0000	0.000
O16	O	0.749242	0.248509	0.054940	1.0000	0.000
Ti6	Ti	0.999539	0.498323	0.054757	1.0000	0.000
O17	O	0.249244	0.248271	0.054675	1.0000	0.000
O18	O	0.249320	0.748505	0.054887	1.0000	0.000
Sr5	Sr	0.000000	0.000000	0.000000	1.0000	0.000
Sr6	Sr	0.500000	0.500000	0.000000	1.0000	0.000
O19	O	0.500000	0.000000	0.000000	1.0000	0.000
O20	O	0.000000	0.500000	0.000000	1.0000	0.000

loop_

_atom_site_label

_atom_bond_valence_sum

C1	3.91
O1	-1.89
O2	-1.91
Ti1	4.20
Ti2	4.22
O3	-2.04
O4	-2.05
O5	-2.41
O6	-2.28
Sr1	2.26
Sr2	2.33
O7	-2.15

O8	-2.16
Ti3	4.15
Ti4	4.15
O9	-2.09
O10	-2.09
O11	-2.10
O12	-2.07
Sr3	2.12
O13	-2.09
Sr4	2.11
O14	-2.09
Ti5	4.13
O15	-2.08
O16	-2.08
Ti6	4.13
O17	-2.08
O18	-2.08
Sr5	2.11
Sr6	2.11
O19	-2.08
O20	-2.08

A.2.3.7: (2x1)

data_Dry_2x1						
_cell_length_a			39.05060			
_cell_length_b			7.8098			
_cell_length_c			3.9050			
_cell_angle_alpha			90.0000			
_cell_angle_beta			90.0000			
_cell_angle_gamma			90.0000			
_cell_formula_units_Z			1			
_symmetry_space_group_name_H-M			'P112/m'			
loop_						
_atom_site_label						
_atom_site_type_symbol						
_atom_site_fract_x						
_atom_site_fract_y						
_atom_site_fract_z						
_atom_site_occupancy						
_atom_site_B_iso_or_equiv						
O1	O	0.339967	0.598542	0.500000	1.0000	0.000

O2	O	0.312120	0.972475	0.500000	1.0000	0.000
Ti1	Ti	0.306928	0.721753	0.500000	1.0000	0.000
Ti2	Ti	0.299653	0.018785	0.000000	1.0000	0.000
O3	O	0.296491	0.749599	0.000000	1.0000	0.000
O4	O	0.295110	0.241779	0.000000	1.0000	0.000
O5	O	0.252584	0.999408	0.000000	1.0000	0.000
O6	O	0.249858	0.730352	0.500000	1.0000	0.000
Ti3	Ti	0.247083	0.263672	0.000000	1.0000	0.000
Ti4	Ti	0.245315	0.732419	0.000000	1.0000	0.000
O7	O	0.241572	0.253506	0.500000	1.0000	0.000
O8	O	0.238805	0.499291	0.000000	1.0000	0.000
O9	O	0.198759	0.779069	0.000000	1.0000	0.000
Sr1	Sr	0.198836	0.005440	0.500000	1.0000	0.000
Sr2	Sr	0.196270	0.491629	0.500000	1.0000	0.000
O10	O	0.196253	0.223566	0.000000	1.0000	0.000
O11	O	0.151184	0.501125	0.000000	1.0000	0.000
O12	O	0.148750	0.749776	0.500000	1.0000	0.000
Ti5	Ti	0.148439	0.245930	0.000000	1.0000	0.000
Ti6	Ti	0.147360	0.750545	0.000000	1.0000	0.000
O13	O	0.147069	0.250516	0.500000	1.0000	0.000
O14	O	0.144052	0.998703	0.000000	1.0000	0.000
O15	O	0.099018	0.736856	0.000000	1.0000	0.000
O16	O	0.098256	0.261923	0.000000	1.0000	0.000
Sr3	Sr	0.098593	0.498775	0.500000	1.0000	0.000
Sr4	Sr	0.098445	0.000634	0.500000	1.0000	0.000
O17	O	0.047485	0.500016	0.000000	1.0000	0.000
O18	O	0.048942	0.249187	0.500000	1.0000	0.000
Ti7	Ti	0.048785	0.749850	0.000000	1.0000	0.000
Ti8	Ti	0.049818	0.250659	0.000000	1.0000	0.000
O19	O	0.049620	0.749938	0.500000	1.0000	0.000
O20	O	0.051035	0.999333	0.000000	1.0000	0.000
O21	O	0.999815	0.241773	0.000000	1.0000	0.000
Sr5	Sr	0.000000	0.500000	0.500000	1.0000	0.000
Sr6	Sr	0.000000	0.000000	0.500000	1.0000	0.000

loop_

_atom_site_label

_atom_bond_valence_sum

O1	-1.74
O2	-1.74
Ti1	3.92
Ti2	3.65
O3	-2.25

O4	-2.02
O5	-2.14
O6	-1.94
Ti3	4.11
Ti4	4.25
O7	-1.93
O8	-2.40
O9	-2.17
Sr1	2.30
Sr2	2.42
O10	-2.26
O11	-2.09
O12	-2.06
Ti5	4.22
Ti6	4.16
O13	-2.15
O14	-2.15
O15	-2.19
O16	-2.20
Sr3	2.20
Sr4	2.23
O17	-2.13
O18	-2.13
Ti7	4.23
Ti8	4.24
O19	-2.12
O20	-2.11
O21	-2.19
Sr5	2.21
Sr6	2.19

A.2.3.8: (2x1) – OH

data_Wet_2x1	
_cell_length_a	39.050632
_cell_length_b	7.809971
_cell_length_c	3.904985
_cell_angle_alpha	90.0000
_cell_angle_beta	90.0000
_cell_angle_gamma	90.0000
_cell_formula_units_Z	1
_symmetry_space_group_name_H-M	'P-1'

loop_						
_atom_site_label						
_atom_site_type_symbol						
_atom_site_fract_x						
_atom_site_fract_y						
_atom_site_fract_z						
_atom_site_occupancy						
_atom_site_B_iso_or_equiv						
O	O	0.342946	0.634711	0.499881	1.0000	0.000
O	O	0.307747	0.980948	0.499186	1.0000	0.000
Ti	Ti	0.303314	0.751350	0.499796	1.0000	0.000
Ti	Ti	0.306604	0.051482	0.997703	1.0000	0.000
O	O	0.297925	0.756711	0.999863	1.0000	0.000
O	O	0.295346	0.267623	0.999796	1.0000	0.000
O	O	0.252739	0.007327	0.000869	1.0000	0.000
O	O	0.253278	0.738787	0.500142	1.0000	0.000
Ti	Ti	0.247126	0.268948	0.029142	1.0000	0.000
Ti	Ti	0.245613	0.751503	0.000257	1.0000	0.000
O	O	0.241627	0.262922	0.494874	1.0000	0.000
O	O	0.239894	0.511777	0.000512	1.0000	0.000
O	O	0.199110	0.784122	0.000184	1.0000	0.000
Sr	Sr	0.199331	0.017123	0.502829	1.0000	0.000
Sr	Sr	0.197052	0.497515	0.503751	1.0000	0.000
O	O	0.196195	0.233811	0.997794	1.0000	0.000
O	O	0.151268	0.505722	0.000412	1.0000	0.000
O	O	0.149495	0.754074	0.500301	1.0000	0.000
Ti	Ti	0.148428	0.251374	0.000421	1.0000	0.000
Ti	Ti	0.147384	0.754665	0.000484	1.0000	0.000
O	O	0.146961	0.254352	0.500018	1.0000	0.000
O	O	0.144335	0.002968	0.000152	1.0000	0.000
O	O	0.099171	0.739069	0.000111	1.0000	0.000
O	O	0.098226	0.266049	0.000024	1.0000	0.000
Sr	Sr	0.098815	0.500508	0.500054	1.0000	0.000
Sr	Sr	0.098740	0.002996	0.500065	1.0000	0.000
O	O	0.047023	0.501189	0.000013	1.0000	0.000
O	O	0.048746	0.250494	0.500021	1.0000	0.000
Ti	Ti	0.048900	0.750457	0.000013	1.0000	0.000
Ti	Ti	0.049718	0.250873	0.000023	1.0000	0.000
O	O	0.049944	0.750641	0.500015	1.0000	0.000
O	O	0.051574	0.000654	0.000014	1.0000	0.000
O	O	0.999730	0.238944	0.999998	1.0000	0.000
Sr	Sr	0.000000	0.500000	0.500000	1.0000	0.000

Sr	Sr	0.000000	0.000000	0.500000	1.0000	0.000
O	O	0.352789	0.073068	0.999917	1.0000	0.000
H	H	0.370412	0.987656	0.999998	1.0000	0.000
H	H	0.347810	0.513979	0.498967	1.0000	0.000
loop_						
_atom_site_label						
_atom_bond_valence_sum						
O		-2.04				
O		-2.16				
Ti		4.13				
Ti		4.02				
O		-2.13				
O		-2.04				
O		-1.82				
O		-2.18				
Ti		4.10				
Ti		4.18				
O		-2.08				
O		-2.16				
O		-2.16				
Sr		2.26				
Sr		2.38				
O		-2.30				
O		-2.09				
O		-2.04				
Ti		4.23				
Ti		4.15				
O		-2.16				
O		-2.13				
O		-2.19				
O		-2.20				
Sr		2.19				
Sr		2.22				
O		-2.12				
O		-2.12				
Ti		4.22				
Ti		4.23				
O		-2.11				
O		-2.11				
O		-2.19				
Sr		2.21				
Sr		2.19				

O	-2.01
H	1.00
H	0.99

A.2.3.9: $c(4x2)$

data_c(4x2)						
_cell_length_a			7.8099			
_cell_length_b			15.6197			
_cell_length_c			39.0500			
_cell_angle_alpha			90.0000			
_cell_angle_beta			90.0000			
_cell_angle_gamma			90.0000			
_cell_formula_units_Z			1			
_symmetry_space_group_name_H-M			'Cmmm'			
loop_						
_atom_site_label						
_atom_site_type_symbol						
_atom_site_fract_x						
_atom_site_fract_y						
_atom_site_fract_z						
_atom_site_occupancy						
_atom_site_B_iso_or_equiv						
Ti1	Ti	0.761712	0.000000	0.304155	1.0000	0.000
O1	O	0.206403	0.397245	0.322262	1.0000	0.000
Ti2	Ti	0.000000	0.364339	0.303032	1.0000	0.000
O2	O	0.000000	0.000000	0.298042	1.0000	0.000
O3	O	0.000000	0.251883	0.296215	1.0000	0.000
O4	O	0.500000	0.000000	0.295738	1.0000	0.000
O5	O	0.000000	0.376232	0.252874	1.0000	0.000
O6	O	0.752374	0.000000	0.253634	1.0000	0.000
Ti3	Ti	0.500000	0.000000	0.246111	1.0000	0.000
Ti4	Ti	0.000000	0.239586	0.249150	1.0000	0.000
Ti5	Ti	0.000000	0.000000	0.245144	1.0000	0.000
O7	O	0.000000	0.122489	0.242020	1.0000	0.000
O8	O	0.250000	0.250000	0.242227	1.0000	0.000
O9	O	0.000000	0.000000	0.197968	1.0000	0.000
O10	O	0.000000	0.256960	0.196460	1.0000	0.000
Sr1	Sr	0.249947	0.131572	0.197857	1.0000	0.000
O11	O	0.500000	0.000000	0.199762	1.0000	0.000
O12	O	0.000000	0.125396	0.148586	1.0000	0.000
Ti6	Ti	0.500000	0.000000	0.146701	1.0000	0.000

Ti7	Ti	0.000000	0.000000	0.147759	1.0000	0.000
O13	O	0.250000	0.250000	0.146917	1.0000	0.000
O14	O	0.500000	0.123333	0.147332	1.0000	0.000
O15	O	0.250298	0.000000	0.149179	1.0000	0.000
Ti8	Ti	0.000000	0.250441	0.148696	1.0000	0.000
O16	O	0.000000	0.000000	0.099162	1.0000	0.000
Sr2	Sr	0.249644	0.126199	0.098561	1.0000	0.000
O17	O	0.000000	0.250282	0.098303	1.0000	0.000
O18	O	0.500000	0.000000	0.098627	1.0000	0.000
O19	O	0.000000	0.124605	0.049416	1.0000	0.000
Ti9	Ti	0.500000	0.000000	0.048988	1.0000	0.000
Ti10	Ti	0.000000	0.000000	0.049186	1.0000	0.000
O20	O	0.250000	0.250000	0.049000	1.0000	0.000
O21	O	0.500000	0.124706	0.049124	1.0000	0.000
O22	O	0.249956	0.000000	0.049655	1.0000	0.000
Ti11	Ti	0.000000	0.250122	0.049545	1.0000	0.000
O23	O	0.000000	0.000000	0.000000	1.0000	0.000
Sr3	Sr	0.249570	0.126172	0.000000	1.0000	0.000
O24	O	0.000000	0.249390	0.000000	1.0000	0.000
O25	O	0.500000	0.000000	0.000000	1.0000	0.000

loop_

_atom_site_label

_atom_bond_valence_sum

Ti1	4.07
O1	-1.93
Ti2	4.03
O2	-2.20
O3	-2.02
O4	-2.56
O5	-2.03
O6	-2.15
Ti3	4.35
Ti4	4.02
Ti5	4.30
O7	-2.20
O8	-1.94
O9	-2.18
O10	-2.23
Sr1	2.23
O11	-2.09
O12	-2.09
Ti6	4.20

Ti7	4.20
O13	-2.18
O14	-2.11
O15	-2.01
Ti8	4.24
O16	-2.17
Sr2	2.18
O17	-2.18
O18	-2.24
O19	-2.12
Ti9	4.26
Ti10	4.23
O20	-2.15
O21	-2.12
O22	-2.09
Ti11	4.25
O23	-2.19
Sr3	2.19
O24	-2.18
O25	-2.21

A.2.3.10: (2x2)

data_Dry_2x2					
_cell_length_a			7.809971		
_cell_length_b			39.050632		
_cell_length_c			7.809971		
_cell_angle_alpha			90.0000		
_cell_angle_beta			90.0000		
_cell_angle_gamma			90.0000		
_cell_formula_units_Z			1		
_symmetry_space_group_name_H-M			'Pccm'		
loop_					
_atom_site_label					
_atom_site_type_symbol					
_atom_site_fract_x					
_atom_site_fract_y					
_atom_site_fract_z					
_atom_site_occupancy					
_atom_site_B_iso_or_equiv					
O1	O	0.296513	0.323107	0.796214	1.0000 0.000

Ti1	Ti	0.500000	0.303353	0.750000	1.0000	0.000
Ti2	Ti	0.779212	0.304446	0.500000	1.0000	0.000
O2	O	0.477280	0.296129	0.500000	1.0000	0.000
O3	O	0.005168	0.297005	0.500000	1.0000	0.000
O4	O	0.753481	0.256347	0.500000	1.0000	0.000
O5	O	0.500000	0.252813	0.750000	1.0000	0.000
Ti3	Ti	0.010891	0.249861	0.500000	1.0000	0.000
Ti4	Ti	0.484512	0.245913	0.500000	1.0000	0.000
O6	O	0.000000	0.243040	0.750000	1.0000	0.000
O7	O	0.254152	0.238676	0.500000	1.0000	0.000
O8	O	0.536217	0.199775	0.500000	1.0000	0.000
Sr1	Sr	0.762365	0.197984	0.746312	1.0000	0.000
O9	O	0.972679	0.196931	0.500000	1.0000	0.000
O10	O	0.251684	0.153011	0.500000	1.0000	0.000
O11	O	0.500000	0.150171	0.750000	1.0000	0.000
Ti5	Ti	0.999158	0.149310	0.500000	1.0000	0.000
Ti6	Ti	0.501663	0.148040	0.500000	1.0000	0.000
O12	O	0.000000	0.147728	0.750000	1.0000	0.000
O13	O	0.748918	0.144053	0.500000	1.0000	0.000
O14	O	0.484916	0.099607	0.500000	1.0000	0.000
O15	O	0.014707	0.098669	0.500000	1.0000	0.000
Sr2	Sr	0.247514	0.098985	0.749385	1.0000	0.000
O16	O	0.250922	0.048024	0.500000	1.0000	0.000
O17	O	0.749242	0.050841	0.500000	1.0000	0.000
O18	O	0.000000	0.049200	0.750000	1.0000	0.000
Ti7	Ti	0.498416	0.049458	0.500000	1.0000	0.000
Ti8	Ti	0.000979	0.049783	0.500000	1.0000	0.000
O19	O	0.500000	0.050314	0.750000	1.0000	0.000
O20	O	0.000000	0.000000	0.500000	1.0000	0.000
Sr3	Sr	0.247519	0.000000	0.750000	1.0000	0.000
O21	O	0.500000	0.000000	0.500000	1.0000	0.000

loop_

_atom_site_label

_atom_bond_valence_sum

O1	-1.95
Ti1	4.03
Ti2	3.94
O2	-2.17
O3	-2.01
O4	-2.03
O5	-2.15
Ti3	3.98

Ti4	4.29
O6	-1.92
O7	-2.31
O8	-2.15
Sr1	2.37
O9	-2.26
O10	-2.05
O11	-2.02
Ti5	4.18
Ti6	4.11
O12	-2.19
O13	-2.16
O14	-2.17
O15	-2.15
Sr2	2.19
O16	-2.15
O17	-2.07
O18	-2.14
Ti7	4.18
Ti8	4.21
O19	-2.08
O20	-2.14
Sr3	2.16
O21	-2.14

A.2.3.11: ($\sqrt{2}\times\sqrt{2}$)-R45°

data_Dry_Rt2xRt2R45	
_cell_length_a	5.5225
_cell_length_b	34.1045
_cell_length_c	5.5225
_cell_angle_alpha	90.0000
_cell_angle_beta	90.0000
_cell_angle_gamma	90.0000
_cell_formula_units_Z	1
_symmetry_space_group_name_H-M	'Pmma'
loop_	
_atom_site_label	
_atom_site_type_symbol	
_atom_site_fract_x	
_atom_site_fract_y	
_atom_site_fract_z	

_atom_site_occupancy						
_atom_site_B_iso_or_equiv						
O1	O	0.250000	0.000000	0.710976	1.0000	0.000
O2	O	0.000000	0.051541	0.000000	1.0000	0.000
O3	O	0.500000	0.060758	0.500000	1.0000	0.000
O4	O	0.250000	0.112448	0.791832	1.0000	0.000
O5	O	0.750000	0.225006	0.301584	1.0000	0.000
O6	O	0.000000	0.173835	0.000000	1.0000	0.000
O7	O	0.500000	0.163350	0.500000	1.0000	0.000
O8	O	0.000000	0.287587	0.500000	1.0000	0.000
O9	O	0.500000	0.272803	0.000000	1.0000	0.000
O10	O	0.750000	0.663885	0.252182	1.0000	0.000
O11	O	0.250000	0.632465	0.335897	1.0000	0.000
Ti1	Ti	0.250000	0.056213	0.750354	1.0000	0.000
Ti2	Ti	0.250000	0.168712	0.749769	1.0000	0.000
Ti3	Ti	0.750000	0.280660	0.228316	1.0000	0.000
Ti4	Ti	0.000000	0.655492	0.500000	1.0000	0.000
Sr5	Sr	0.250000	0.112257	0.251725	1.0000	0.000
Sr6	Sr	0.750000	0.224785	0.746766	1.0000	0.000
Sr7	Sr	0.250000	0.000000	0.249021	1.0000	0.000

loop_

_atom_site_label	
_atom_bond_valence_sum	
O1	-2.22
O2	-2.15
O3	-2.14
O4	-2.22
O5	-2.24
O6	-2.12
O7	-2.15
O8	-2.04
O9	-2.25
O10	-2.14
O11	-1.93
Ti1	4.18
Ti2	4.14
Ti3	4.21
Ti4	4.00
Sr5	2.33
Sr6	2.46
Sr7	2.32

A.2.3.12: *O*-vacancy ($\sqrt{5} \times \sqrt{5}$)-*R*26.6°

data_Rt5_Ovac_Ti						
_cell_length_a			8.731842			
_cell_length_b			8.731842			
_cell_length_c			39.049985			
_cell_angle_alpha			90.0000			
_cell_angle_beta			90.0000			
_cell_angle_gamma			90.0000			
_cell_formula_units_Z			1			
_symmetry_space_group_name_H-M			'P112/m'			
loop_						
_atom_site_label						
_atom_site_type_symbol						
_atom_site_fract_x						
_atom_site_fract_y						
_atom_site_fract_z						
_atom_site_occupancy						
_atom_site_B_iso_or_equiv						
Ti1	Ti	0.610387	0.231166	0.698317	1.0000	0.000
Ti2	Ti	0.807236	0.617154	0.698623	1.0000	0.000
Ti3	Ti	0.000000	0.000000	0.697349	1.0000	0.000
O1	O	0.599397	0.733150	0.691177	1.0000	0.000
O2	O	0.692481	0.417763	0.697773	1.0000	0.000
O3	O	0.779887	0.094283	0.693761	1.0000	0.000
O4	O	0.912059	0.801745	0.692040	1.0000	0.000
O5	O	0.000000	0.500000	0.697887	1.0000	0.000
Sr1	Sr	0.500000	0.500000	0.749359	1.0000	0.000
Sr2	Sr	0.700917	0.905504	0.746714	1.0000	0.000
Sr3	Sr	0.902378	0.301358	0.747010	1.0000	0.000
O6	O	0.588726	0.193547	0.743968	1.0000	0.000
O7	O	0.795126	0.623169	0.744041	1.0000	0.000
O8	O	0.000000	0.000000	0.743049	1.0000	0.000
Ti4	Ti	0.600417	0.200149	0.798830	1.0000	0.000
Ti5	Ti	0.800269	0.601138	0.798983	1.0000	0.000
Ti6	Ti	0.000000	0.000000	0.799310	1.0000	0.000
O9	O	0.500000	0.000000	0.796603	1.0000	0.000
O10	O	0.598582	0.697138	0.797190	1.0000	0.000
O11	O	0.702122	0.399669	0.792966	1.0000	0.000
O12	O	0.800846	0.099855	0.794605	1.0000	0.000
O13	O	0.899755	0.800548	0.796494	1.0000	0.000
O14	O	0.000000	0.500000	0.792788	1.0000	0.000

Sr4	Sr	0.500000	0.500000	0.849783	1.0000	0.000
Sr5	Sr	0.699711	0.899980	0.849466	1.0000	0.000
Sr6	Sr	0.900321	0.299413	0.849728	1.0000	0.000
O15	O	0.606588	0.203232	0.846199	1.0000	0.000
O16	O	0.804014	0.593296	0.846197	1.0000	0.000
O17	O	0.000000	0.000000	0.846594	1.0000	0.000
Ti7	Ti	0.600329	0.200191	0.899695	1.0000	0.000
Ti8	Ti	0.800253	0.599757	0.899910	1.0000	0.000
Ti9	Ti	0.000000	0.000000	0.899776	1.0000	0.000
O18	O	0.500000	0.000000	0.896787	1.0000	0.000
O19	O	0.600422	0.700376	0.896918	1.0000	0.000
O20	O	0.699416	0.400227	0.898293	1.0000	0.000
O21	O	0.800119	0.100000	0.898014	1.0000	0.000
O22	O	0.899931	0.799599	0.897490	1.0000	0.000
O23	O	0.000000	0.500000	0.898527	1.0000	0.000
Sr7	Sr	0.500000	0.500000	0.950061	1.0000	0.000
Sr8	Sr	0.700185	0.900153	0.950016	1.0000	0.000
Sr9	Sr	0.899925	0.299929	0.950097	1.0000	0.000
O24	O	0.598153	0.199057	0.948680	1.0000	0.000
O25	O	0.798830	0.601408	0.948828	1.0000	0.000
O26	O	0.000000	0.000000	0.948839	1.0000	0.000
Ti10	Ti	0.599621	0.199797	0.000000	1.0000	0.000
Ti11	Ti	0.799784	0.600370	0.000000	1.0000	0.000
Ti12	Ti	0.000000	0.000000	0.000000	1.0000	0.000
O27	O	0.500000	0.000000	0.000000	1.0000	0.000
O28	O	0.599803	0.699824	0.000000	1.0000	0.000
O29	O	0.700062	0.399679	0.000000	1.0000	0.000
O30	O	0.799723	0.100050	0.000000	1.0000	0.000
O31	O	0.899993	0.800030	0.000000	1.0000	0.000
O32	O	0.000000	0.500000	0.000000	1.0000	0.000

loop_

_atom_site_label

_atom_bond_valence_sum

Ti1	3.69
Ti2	3.68
Ti3	3.36
O1	-1.53
O2	-2.03
O3	-1.50
O4	-1.84
O5	-1.71
Sr1	2.12

Sr2	2.07
Sr3	2.05
O6	-2.10
O7	-2.23
O8	-2.09
Ti4	4.01
Ti5	4.02
Ti6	4.03
O9	-2.01
O10	-2.03
O11	-2.03
O12	-2.02
O13	-2.03
O14	-2.02
Sr4	2.02
Sr5	2.01
Sr6	2.03
O15	-2.09
O16	-2.09
O17	-2.11
Ti7	3.98
Ti8	3.99
Ti9	3.99
O18	-2.06
O19	-2.07
O20	-2.08
O21	-2.08
O22	-2.07
O23	-2.08
Sr7	2.00
Sr8	2.00
Sr9	2.00
O24	-2.07
O25	-2.08
O26	-2.08
Ti10	3.97
Ti11	3.97
Ti12	3.97
O27	-2.09
O28	-2.09
O29	-2.08
O30	-2.08

O31 -2.09
O32 -2.07

A.2.3.13: Sr-adatom c(4x4) ($\theta=0.125$)

```

data_STOc4x4
_audit_creation_date          2010-06-02
_audit_creation_method        'Materials Studio'
_symmetry_space_group_name_H-M 'P4/MMM'
_symmetry_Int_Tables_number   123
_symmetry_cell_setting        tetragonal
loop_
_symmetry_equiv_pos_as_xyz
  x,y,z
  -x,-y,z
  -y,x,z
  y,-x,z
  -x,y,-z
  x,-y,-z
  y,x,-z
  -y,-x,-z
  -x,-y,-z
  x,y,-z
  y,-x,-z
  -y,x,-z
  x,-y,z
  -x,y,z
  -y,-x,z
  y,x,z
_cell_length_a                11.0450
_cell_length_b                11.0450
_cell_length_c                23.4300
_cell_angle_alpha             90.0000
_cell_angle_beta              90.0000
_cell_angle_gamma             90.0000
loop_
_atom_site_label
_atom_site_type_symbol
_atom_site_fract_x
_atom_site_fract_y
_atom_site_fract_z
_atom_site_U_iso_or_equiv

```

_atom_site_adp_type							
_atom_site_occupancy							
O1	O	0.87516	-0.37516	-0.41677	0.00000	Uiso	1.00
O2	O	0.87600	-0.37551	-0.24606	0.00000	Uiso	1.00
Sr3	Sr	0.50000	-0.50000	-0.50000	0.00000	Uiso	1.00
Sr4	Sr	0.00000	0.00000	-0.50000	0.00000	Uiso	1.00
Sr5	Sr	1.00000	-0.50000	-0.50000	0.00000	Uiso	1.00
O6	O	0.75032	-0.50000	-0.50000	0.00000	Uiso	1.00
Sr7	Sr	0.75000	-0.75000	-0.50000	0.00000	Uiso	1.00
O8	O	1.00000	-0.25032	-0.50000	0.00000	Uiso	1.00
Sr9	Sr	0.00000	0.00000	-0.33376	0.00000	Uiso	1.00
Sr10	Sr	0.00000	0.00000	-0.18070	0.00000	Uiso	1.00
Sr11	Sr	0.50000	-0.50000	-0.32859	0.00000	Uiso	1.00
Sr12	Sr	1.00000	-0.50000	-0.32847	0.00000	Uiso	1.00
Ti13	Ti	1.00000	-0.25032	-0.41677	0.00000	Uiso	1.00
Ti14	Ti	1.00000	-0.25934	-0.25154	0.00000	Uiso	1.00
O15	O	1.00000	-0.24671	-0.32922	0.00000	Uiso	1.00
O16	O	0.87484	-0.87484	-0.41677	0.00000	Uiso	1.00
Sr17	Sr	0.74869	-0.74869	-0.32652	0.00000	Uiso	1.00
O18	O	0.87716	-0.87716	-0.23861	0.00000	Uiso	1.00
O19	O	0.62516	-0.62516	-0.41677	0.00000	Uiso	1.00
O20	O	0.62451	-0.62451	-0.24585	0.00000	Uiso	1.00
Ti21	Ti	0.75032	-0.50000	-0.41677	0.00000	Uiso	1.00
Ti22	Ti	0.74720	-0.50000	-0.25127	0.00000	Uiso	1.00
O23	O	0.74984	-0.50000	-0.32930	0.00000	Uiso	1.00
loop_							
_atom_site_label							
_atom_bond_valence_sum							
O1		-2.01					
O2		-1.86					
Sr3		2.10					
Sr4		2.10					
Sr5		2.13					
O6		-2.09					
Sr7		2.12					
O8		-2.09					
Sr9		1.91					
Sr10		2.14					
Sr11		2.00					
Sr12		1.98					
Ti13		3.98					
Ti14		3.70					

O15	-2.19
O16	-2.02
Sr17	1.94
O18	-1.83
O19	-2.00
O20	-1.83
Ti21	3.98
Ti22	3.68
O23	-2.21

A.2.3.14: *Sr-adatom* ($\sqrt{5} \times \sqrt{5}$)- $R26.6^\circ$ ($\theta=0.2$)

data_STOsqrt5	
_audit_creation_date	2010-06-02
_audit_creation_method	'Materials Studio'
_symmetry_space_group_name_H-M	'P4/M'
_symmetry_Int_Tables_number	83
_symmetry_cell_setting	tetragonal
loop_	
_symmetry_equiv_pos_as_xyz	
x,y,z	
-x,-y,z	
-y,x,z	
y,-x,z	
-x,-y,-z	
x,y,-z	
y,-x,-z	
-y,x,-z	
_cell_length_a	8.7318
_cell_length_b	8.7318
_cell_length_c	27.3350
_cell_angle_alpha	90.0000
_cell_angle_beta	90.0000
_cell_angle_gamma	90.0000
loop_	
_atom_site_label	
_atom_site_type_symbol	
_atom_site_fract_x	
_atom_site_fract_y	
_atom_site_fract_z	
_atom_site_U_iso_or_equiv	
_atom_site_adp_type	

<u>_atom_site_occupancy</u>							
Ti1	Ti	0.10000	-1.70000	-0.57143	0.00000	Uiso	1.00
O2	O	0.09958	-1.70137	-0.64370	0.00000	Uiso	1.00
Sr3	Sr	0.39915	-1.79796	-0.64356	0.00000	Uiso	1.00
O4	O	0.30000	-1.60000	-0.57143	0.00000	Uiso	1.00
O5	O	0.20000	-1.90000	-0.57143	0.00000	Uiso	1.00
Ti6	Ti	0.10702	-1.69191	-0.71049	0.00000	Uiso	1.00
O7	O	0.30020	-1.59976	-0.71454	0.00000	Uiso	1.00
O8	O	0.19008	-1.90320	-0.72035	0.00000	Uiso	1.00
Sr9	Sr	0.00000	-1.00000	-0.50000	0.00000	Uiso	1.00
O10	O	-0.50000	-0.50000	-0.50000	0.00000	Uiso	1.00
O11	O	0.10000	-1.70000	-0.50000	0.00000	Uiso	1.00
Sr12	Sr	0.40000	-1.80000	-0.50000	0.00000	Uiso	1.00
Ti13	Ti	-0.50000	-0.50000	-0.57143	0.00000	Uiso	1.00
O14	O	-0.50000	-0.50000	-0.64411	0.00000	Uiso	1.00
Ti15	Ti	-0.50000	-0.50000	-0.71134	0.00000	Uiso	1.00
Sr16	Sr	0.00000	-1.00000	-0.64421	0.00000	Uiso	1.00
Sr17	Sr	0.00000	-1.00000	-0.77121	0.00000	Uiso	1.00
O18	O	0.00000	-1.50000	-0.57143	0.00000	Uiso	1.00
O19	O	0.00000	-1.50000	-0.71440	0.00000	Uiso	1.00

loop_

_atom_site_label

_atom_bond_valence_sum

Ti1	4.10
O2	-2.31
Sr3	2.03
O4	-2.08
O5	-2.06
Ti6	3.67
O7	-1.91
O8	-1.95
Sr9	2.11
O10	-2.08
O11	-2.08
Sr12	2.11
Ti13	4.08
O14	-2.30
Ti15	3.70
Sr16	2.03
Sr17	2.29
O18	-2.06
O19	-1.85

A.2.3.15: Sr-adatom (2x2)-type A ($\theta=0.25$)

data_STO2x2							
_audit_creation_date							2010-06-02
_audit_creation_method							'Materials Studio'
_symmetry_space_group_name_H-M							'P4/MMM'
_symmetry_Int_Tables_number							123
_symmetry_cell_setting							tetragonal
loop_							
_symmetry_equiv_pos_as_xyz							
x,y,z							
-x,-y,z							
-y,x,z							
y,-x,z							
-x,y,-z							
x,-y,-z							
y,x,-z							
-y,-x,-z							
-x,-y,-z							
x,y,-z							
y,-x,-z							
-y,x,-z							
x,-y,z							
-x,y,z							
-y,-x,z							
y,x,z							
_cell_length_a							7.8100
_cell_length_b							7.8100
_cell_length_c							23.4300
_cell_angle_alpha							90.0000
_cell_angle_beta							90.0000
_cell_angle_gamma							90.0000
loop_							
_atom_site_label							
_atom_site_type_symbol							
_atom_site_fract_x							
_atom_site_fract_y							
_atom_site_fract_z							
_atom_site_U_iso_or_equiv							
_atom_site_adp_type							
_atom_site_occupancy							
Sr1	Sr	0.50000	0.50000	0.50000	0.00000	Uiso	1.00

O2	O	0.75048	0.50000	0.75084	0.00000	Uiso	1.00
O3	O	0.74968	0.50000	0.58323	0.00000	Uiso	1.00
Sr4	Sr	0.50000	0.00000	0.50000	0.00000	Uiso	1.00
O5	O	0.75488	-0.00000	0.75335	0.00000	Uiso	1.00
O6	O	0.74968	0.00000	0.58323	0.00000	Uiso	1.00
Sr7	Sr	0.50000	0.50000	0.66726	0.00000	Uiso	1.00
O8	O	0.74968	0.74968	0.50000	0.00000	Uiso	1.00
Sr9	Sr	0.00000	0.00000	0.50000	0.00000	Uiso	1.00
Sr10	Sr	0.00000	0.00000	0.66639	0.00000	Uiso	1.00
Sr11	Sr	0.00000	0.00000	0.82913	0.00000	Uiso	1.00
Sr12	Sr	0.50000	0.00000	0.66741	0.00000	Uiso	1.00
Ti13	Ti	0.74968	0.74968	0.58323	0.00000	Uiso	1.00
O14	O	0.75038	0.75038	0.66898	0.00000	Uiso	1.00
Ti15	Ti	0.74312	0.74312	0.74450	0.00000	Uiso	1.00
loop_							
_atom_site_label							
_atom_bond_valence_sum							
Sr1		2.13					
O2		-1.92					
O3		-2.08					
Sr4		2.12					
O5		-1.72					
O6		-2.07					
Sr7		2.07					
O8		-2.09					
Sr9		2.10					
Sr10		2.06					
Sr11		1.06					
Sr12		2.02					
Ti13		4.04					
O14		-2.42					
Ti15		3.84					

A.2.3.16: Sr-adatom $c(4 \times 2)$ ($\theta=0.25$)

```

data_STOc4x2b
_audit_creation_date      2010-06-02
_audit_creation_method    'Materials Studio'
_symmetry_space_group_name_H-M ''
_symmetry_Int_Tables_number 0
_symmetry_cell_setting    orthorhombic
loop_

```

```

_symmetry_equiv_pos_as_xyz
  x,y,z
  -x,-y,z
  y,x,-z
  -y,-x,-z
  -x,-y,-z
  x,y,-z
  -y,-x,z
  y,x,z
_cell_length_a      8.7318
_cell_length_b      8.7318
_cell_length_c     23.4300
_cell_angle_alpha   90.0000
_cell_angle_beta    90.0000
_cell_angle_gamma   53.1301
loop_
_atom_site_label
_atom_site_type_symbol
_atom_site_fract_x
_atom_site_fract_y
_atom_site_fract_z
_atom_site_U_iso_or_equiv
_atom_site_adp_type
_atom_site_occupancy
  O1  O   -0.36691  1.12180  0.66956  0.00000  Uiso  1.00
  Ti2 Ti   -0.37500  1.12500  0.58323  0.00000  Uiso  1.00
  Ti3 Ti   -0.38322  1.12784  0.74724  0.00000  Uiso  1.00
  O4  O    0.37466  0.37466  0.75181  0.00000  Uiso  1.00
  O5  O    0.37500  0.37500  0.58323  0.00000  Uiso  1.00
  O6  O   -0.12414  0.87586  0.76042  0.00000  Uiso  1.00
  O7  O   -0.12500  0.87500  0.58323  0.00000  Uiso  1.00
  Sr8 Sr   -0.24885  0.75115  0.66922  0.00000  Uiso  1.00
  Sr9 Sr    0.00000  0.00000  0.50000  0.00000  Uiso  1.00
  Sr10 Sr  -0.25000  0.75000  0.50000  0.00000  Uiso  1.00
  O11 O   -0.37500  1.12500  0.50000  0.00000  Uiso  1.00
  Sr12 Sr  0.00000  0.00000  0.81733  0.00000  Uiso  1.00
  Sr13 Sr  0.00000  0.00000  0.66188  0.00000  Uiso  1.00
  Sr14 Sr  -0.50000  0.50000  0.50000  0.00000  Uiso  1.00
  Sr15 Sr  -0.50000  0.50000  0.66970  0.00000  Uiso  1.00
  O16 O   -0.75000  0.75000  0.58323  0.00000  Uiso  1.00
  O17 O   -0.75187  0.75187  0.75940  0.00000  Uiso  1.00
  O18 O   -0.50000  1.00000  0.58323  0.00000  Uiso  1.00

```

O19	O	-0.50000	1.00000	0.75099	0.00000	Uiso	1.00
-----	---	----------	---------	---------	---------	------	------

loop_
 _atom_site_label
 _atom_bond_valence_sum

O1	-2.01
Ti2	3.12
Ti3	2.89
O4	-0.90
O5	-0.98
O6	-1.28
O7	-1.38
Sr8	0.81
Sr9	0.53
Sr10	0.53
O11	-1.18
Sr12	1.04
Sr13	0.82
Sr14	0.53
Sr15	0.79
O16	-0.72
O17	-0.73
O18	-0.98
O19	-0.91

A.2.3.17: *c(4x4)-type B* ($\theta=0.375$)

data_STOc4x4a	
_audit_creation_date	2010-06-02
_audit_creation_method	'Materials Studio'
_symmetry_space_group_name_H-M	'P4/MMM'
_symmetry_Int_Tables_number	123
_symmetry_cell_setting	tetragonal

loop_
 _symmetry_equiv_pos_as_xyz

x,y,z
-x,-y,z
-y,x,z
y,-x,z
-x,y,-z
x,-y,-z
y,x,-z
-y,-x,-z

-x,-y,-z							
x,y,-z							
y,-x,-z							
-y,x,-z							
x,-y,z							
-x,y,z							
-y,-x,z							
y,x,z							
_cell_length_a		11.0450					
_cell_length_b		11.0450					
_cell_length_c		23.4300					
_cell_angle_alpha		90.0000					
_cell_angle_beta		90.0000					
_cell_angle_gamma		90.0000					
loop_							
_atom_site_label							
_atom_site_type_symbol							
_atom_site_fract_x							
_atom_site_fract_y							
_atom_site_fract_z							
_atom_site_U_iso_or_equiv							
_atom_site_adp_type							
_atom_site_occupancy							
O1	O	0.62270	0.87776	0.24161	0.00000	Uiso	1.00
O2	O	0.62484	0.87516	0.41677	0.00000	Uiso	1.00
O3	O	0.87516	0.87516	0.41677	0.00000	Uiso	1.00
O4	O	0.62379	0.62379	0.24840	0.00000	Uiso	1.00
O5	O	0.87781	0.87781	0.24264	0.00000	Uiso	1.00
Sr6	Sr	0.74944	0.74944	0.66780	0.00000	Uiso	1.00
O7	O	0.62484	0.62484	0.41677	0.00000	Uiso	1.00
Sr8	Sr	0.00000	0.00000	0.17450	0.00000	Uiso	1.00
Sr9	Sr	0.00000	0.00000	0.33731	0.00000	Uiso	1.00
Sr10	Sr	0.50000	0.50000	0.33333	0.00000	Uiso	1.00
Sr11	Sr	0.50000	0.50000	0.50000	0.00000	Uiso	1.00
Sr12	Sr	0.00000	0.00000	0.50000	0.00000	Uiso	1.00
O13	O	0.75405	0.50000	0.33078	0.00000	Uiso	1.00
Ti14	Ti	0.75000	0.50000	0.41677	0.00000	Uiso	1.00
Ti15	Ti	0.74355	0.50000	0.25309	0.00000	Uiso	1.00
O16	O	0.75000	0.00000	0.50000	0.00000	Uiso	1.00
Sr17	Sr	0.50000	0.00000	0.50000	0.00000	Uiso	1.00
Sr18	Sr	0.50000	0.00000	0.33711	0.00000	Uiso	1.00
Sr19	Sr	0.50000	0.00000	0.17912	0.00000	Uiso	1.00

Ti20	Ti	0.75000	0.00000	0.41677	0.00000	Uiso	1.00
Ti21	Ti	0.74919	0.00000	0.25210	0.00000	Uiso	1.00
O22	O	0.74985	0.00000	0.33018	0.00000	Uiso	1.00
O23	O	0.75000	0.50000	0.50000	0.00000	Uiso	1.00
Sr24	Sr	0.75000	0.75000	0.50000	0.00000	Uiso	1.00

loop_
 _atom_site_label
 _atom_bond_valence_sum

O1	-1.92
O2	-2.11
O3	-2.10
O4	-1.90
O5	-1.91
Sr6	1.89
O7	-2.08
Sr8	1.47
Sr9	1.98
Sr10	2.00
Sr11	2.12
Sr12	2.12
O13	-2.27
Ti14	4.03
Ti15	3.67
O16	-2.09
Sr17	2.12
Sr18	2.00
Sr19	1.82
Ti20	4.01
Ti21	3.63
O22	-2.22
O23	-2.09
Sr24	2.11

A.2.3.18: (2×1) ($\theta=0.5$)

data_STO2x1b
 _audit_creation_date 2010-06-02
 _audit_creation_method 'Materials Studio'
 _symmetry_space_group_name_H-M 'PMMM'
 _symmetry_Int_Tables_number 47
 _symmetry_cell_setting orthorhombic
 loop_

```

_symmetry_equiv_pos_as_xyz
  x,y,z
  -x,-y,z
  -x,y,-z
  x,-y,-z
  -x,-y,-z
  x,y,-z
  x,-y,z
  -x,y,z
_cell_length_a          7.8100
_cell_length_b          3.9050
_cell_length_c          23.4300
_cell_angle_alpha       90.0000
_cell_angle_beta        90.0000
_cell_angle_gamma       90.0000
loop_
_atom_site_label
_atom_site_type_symbol
_atom_site_fract_x
_atom_site_fract_y
_atom_site_fract_z
_atom_site_U_iso_or_equiv
_atom_site_adp_type
_atom_site_occupancy
  O1  O    0.75000  0.50000  0.50000  0.00000  Uiso  1.00
  Ti2 Ti    0.73987  0.50000  0.74700  0.00000  Uiso  1.00
  Ti3 Ti    0.75000  0.50000  0.58323  0.00000  Uiso  1.00
  O4  O    0.76446  0.50000  0.66939  0.00000  Uiso  1.00
  O5  O    0.50000  0.50000  0.58323  0.00000  Uiso  1.00
  O6  O    0.50000  0.50000  0.74324  0.00000  Uiso  1.00
  O7  O    0.00000  0.50000  0.76499  0.00000  Uiso  1.00
  O8  O    0.00000  0.50000  0.58323  0.00000  Uiso  1.00
  Sr9  Sr    0.00000  0.00000  0.66252  0.00000  Uiso  1.00
  Sr10 Sr    0.00000  0.00000  0.82558  0.00000  Uiso  1.00
  Sr11 Sr    0.00000  0.00000  0.50000  0.00000  Uiso  1.00
  Sr12 Sr    0.50000  0.00000  0.50000  0.00000  Uiso  1.00
  Sr13 Sr    0.50000  0.00000  0.66292  0.00000  Uiso  1.00
  O14  O    0.75322  0.00000  0.75906  0.00000  Uiso  1.00
  O15  O    0.75000  0.00000  0.58323  0.00000  Uiso  1.00
loop_
_atom_site_label
_atom_bond_valence_sum

```

O1	-2.09
Ti2	3.38
Ti3	4.02
O4	-2.18
O5	-2.15
O6	-1.99
O7	-1.97
O8	-2.15
Sr9	2.04
Sr10	1.65
Sr11	2.12
Sr12	2.12
Sr13	1.97
O14	-1.78
O15	-2.15

A.2.3.19: (2x2)-type B ($\theta=0.75$)

data_STO2x2a2	
_audit_creation_date	2010-06-02
_audit_creation_method	'Materials Studio'
_symmetry_space_group_name_H-M	'P4/MMM'
_symmetry_Int_Tables_number	123
_symmetry_cell_setting	tetragonal
loop_	
_symmetry_equiv_pos_as_xyz	
	x,y,z
	-x,-y,z
	-y,x,z
	y,-x,z
	-x,y,-z
	x,-y,-z
	y,x,-z
	-y,-x,-z
	-x,-y,-z
	x,y,-z
	y,-x,-z
	-y,x,-z
	x,-y,z
	-x,y,z
	-y,-x,z
	y,x,z

_cell_length_a	7.8100						
_cell_length_b	7.8100						
_cell_length_c	23.4300						
_cell_angle_alpha	90.0000						
_cell_angle_beta	90.0000						
_cell_angle_gamma	90.0000						
loop_							
_atom_site_label							
_atom_site_type_symbol							
_atom_site_fract_x							
_atom_site_fract_y							
_atom_site_fract_z							
_atom_site_U_iso_or_equiv							
_atom_site_adp_type							
_atom_site_occupancy							
Sr1	Sr	0.50000	0.50000	0.50000	0.00000	Uiso	1.00
O2	O	0.75860	0.50000	0.75520	0.00000	Uiso	1.00
O3	O	0.74968	0.50000	0.58323	0.00000	Uiso	1.00
Sr4	Sr	0.50000	0.00000	0.50000	0.00000	Uiso	1.00
O5	O	0.74969	0.00000	0.75683	0.00000	Uiso	1.00
O6	O	0.74968	0.00000	0.58323	0.00000	Uiso	1.00
Sr7	Sr	0.50000	0.50000	0.66438	0.00000	Uiso	1.00
O8	O	0.74968	0.74968	0.50000	0.00000	Uiso	1.00
Sr9	Sr	0.00000	0.00000	0.50000	0.00000	Uiso	1.00
Sr10	Sr	0.00000	0.00000	0.66435	0.00000	Uiso	1.00
Sr11	Sr	0.00000	0.00000	0.82470	0.00000	Uiso	1.00
Ti12	Ti	0.74968	0.74968	0.58323	0.00000	Uiso	1.00
O13	O	0.75137	0.75137	0.66754	0.00000	Uiso	1.00
Ti14	Ti	0.74588	0.74588	0.74726	0.00000	Uiso	1.00
Sr15	Sr	0.50000	0.00000	0.66391	0.00000	Uiso	1.00
Sr16	Sr	0.50000	0.00000	0.82815	0.00000	Uiso	1.00
loop_							
_atom_site_label							
_atom_bond_valence_sum							
Sr1	2.13						
O2	-1.93						
O3	-2.13						
Sr4	2.12						
O5	-2.01						
O6	-2.11						
Sr7	1.89						
O8	-2.09						

Sr9	2.10
Sr10	1.96
Sr11	1.35
Ti12	4.10
O13	-2.16
Ti14	3.32
Sr15	1.99
Sr16	1.22

A.2.3.20: (1x1) ($\theta=1.0$)

data_STOp1x1b	
_audit_creation_date	2010-06-02
_audit_creation_method	'Materials Studio'
_symmetry_space_group_name_H-M	'P4/MMM'
_symmetry_Int_Tables_number	123
_symmetry_cell_setting	tetragonal
loop_	
_symmetry_equiv_pos_as_xyz	
	x,y,z
	-x,-y,z
	-y,x,z
	y,-x,z
	-x,y,-z
	x,-y,-z
	y,x,-z
	-y,-x,-z
	-x,-y,-z
	x,y,-z
	y,-x,-z
	-y,x,-z
	x,-y,z
	-x,y,z
	-y,-x,z
	y,x,z
_cell_length_a	3.9050
_cell_length_b	3.9050
_cell_length_c	23.4300
_cell_angle_alpha	90.0000
_cell_angle_beta	90.0000
_cell_angle_gamma	90.0000
loop_	

```

_atom_site_label
_atom_site_type_symbol
_atom_site_fract_x
_atom_site_fract_y
_atom_site_fract_z
_atom_site_U_iso_or_equiv
_atom_site_adp_type
_atom_site_occupancy
  O1  O      0.50000  -0.50000  -0.33177  0.00000  Uiso  1.00
  Ti2 Ti      0.50000  -0.50000  -0.25198  0.00000  Uiso  1.00
  Ti3 Ti      0.50000  -0.50000  -0.41677  0.00000  Uiso  1.00
  Sr4 Sr      0.00000   0.00000  -0.17344  0.00000  Uiso  1.00
  Sr5 Sr      0.00000   0.00000  -0.33886  0.00000  Uiso  1.00
  O6  O      1.00000   0.50000  -0.41677  0.00000  Uiso  1.00
  O7  O      1.00000   0.50000  -0.24305  0.00000  Uiso  1.00
  O8  O      0.50000  -0.50000  -0.50000  0.00000  Uiso  1.00
  Sr9 Sr      0.00000   0.00000  -0.50000  0.00000  Uiso  1.00
loop_
_atom_site_label
_atom_bond_valence_sum
  O1  -2.12
  Ti2  3.32
  Ti3  4.07
  Sr4  1.26
  Sr5  1.98
  O6  -2.18
  O7  -2.08
  O8  -2.09
  Sr9  2.12

```

A.2.4: CIFs for SrTiO₃ (1 1 1) surface structures

A.2.4.1: Model 1

```

data_Model_1
_cell_length_a      5.522461
_cell_length_b      5.522461
_cell_length_c     20.290814
_cell_angle_alpha   90.0000
_cell_angle_beta    90.0000

```

```

_cell_angle_gamma          120.0000
_cell_formula_units_Z      1
_symmetry_space_group_name_H-M 'P-3m1'
loop_
_atom_site_label
_atom_site_type_symbol
_atom_site_fract_x
_atom_site_fract_y
_atom_site_fract_z
_atom_site_occupancy
_atom_site_B_iso_or_equiv
  Sr1  Sr  0.000000  0.000000  0.159652  1.0000  0.800
  Sr2  Sr  0.333333  0.666667  0.270021  1.0000  0.800
  Sr3  Sr  0.666667  0.333333  0.054040  1.0000  0.800
  Ti1  Ti  0.000000  0.000000  0.000000  1.0000  0.800
  Ti2  Ti  0.333333  0.666667  0.111400  1.0000  0.800
  Ti3  Ti  0.666667  0.333333  0.224115  1.0000  0.800
  Ti4  Ti  0.000000  0.000000  0.324055  1.0000  0.800
  O1   O   0.833707  0.667413  0.943079  1.0000  0.800
  O2   O   0.168917  0.831083  0.713263  1.0000  0.800
  O3   O   0.499612  0.500388  0.171879  1.0000  0.800

```

```

loop_
_atom_site_label
_atom_bond_valence_sum
  Sr1  2.04
  Sr2  1.93
  Sr3  1.97
  Ti1  3.99
  Ti2  3.90
  Ti3  3.99
  Ti4  3.05
  O1   -2.16
  O2   -2.00
  O3   -2.13

```

A.2.4.2: Model 2

```

data_Model_2
_cell_length_a          5.522461
_cell_length_b          5.522461
_cell_length_c          20.290814

```

_cell_angle_alpha				90.0000		
_cell_angle_beta				90.0000		
_cell_angle_gamma				120.0000		
_cell_formula_units_Z				1		
_symmetry_space_group_name_H-M				'P-3m1'		
loop_						
_atom_site_label						
_atom_site_type_symbol						
_atom_site_fract_x						
_atom_site_fract_y						
_atom_site_fract_z						
_atom_site_occupancy						
_atom_site_B_iso_or_equiv						
Sr1	Sr	0.000000	0.000000	0.000000	1.0000	0.800
Sr2	Sr	0.333333	0.666667	0.112703	1.0000	0.800
Sr3	Sr	0.666667	0.333333	0.229360	1.0000	0.800
Sr4	Sr	0.000000	0.000000	0.333160	1.0000	0.800
Ti1	Ti	0.333333	0.666667	0.282244	1.0000	0.800
Ti2	Ti	0.666667	0.333333	0.055909	1.0000	0.800
Ti3	Ti	0.000000	0.000000	0.167415	1.0000	0.800
O1	O	0.834521	0.669042	0.779573	1.0000	0.800
O2	O	0.166082	0.833918	0.890120	1.0000	0.800
O3	O	0.500000	0.500000	0.000000	1.0000	0.800
O4	O	0.498440	0.996880	0.330471	1.0000	0.800

loop_	
_atom_site_label	
_atom_bond_valence_sum	
Sr1	2.18
Sr2	2.15
Sr3	2.20
Sr4	1.55
Ti1	4.32
Ti2	4.19
Ti3	4.26
O1	-2.03
O2	-2.03
O3	-2.04
O4	-1.51

A.2.4.3: Model 3

```

data_Model_3
_cell_length_a          9.565183
_cell_length_b         20.290814
_cell_length_c          5.522461
_cell_angle_alpha      90.0000
_cell_angle_beta       90.0000
_cell_angle_gamma      90.0000
_cell_formula_units_Z  1
_symmetry_space_group_name_H-M 'B112/m'
loop_
_atom_site_label
_atom_site_type_symbol
_atom_site_fract_x
_atom_site_fract_y
_atom_site_fract_z
_atom_site_occupancy
_atom_site_B_iso_or_equiv
  Sr1  Sr  0.500000  0.500000  0.000000  1.0000  0.800
  Sr2  Sr  0.833731  0.723438  0.000000  1.0000  0.800
  Sr3  Sr  0.166191  0.604991  0.000000  1.0000  0.800
  Sr4  Sr  0.539419  0.830665  0.000000  1.0000  0.800
  Ti1  Ti  0.837884  0.557036  0.000000  1.0000  0.800
  Ti2  Ti  0.188977  0.773418  0.000000  1.0000  0.800
  Ti3  Ti  0.500841  0.667922  0.000000  1.0000  0.800
  O1   O   0.675265  0.618641  0.000000  1.0000  0.800
  O2   O   0.811849  0.705336  0.500000  1.0000  0.800
  O3   O   0.927476  0.607623  0.250136  1.0000  0.800
  O4   O   0.051783  0.730992  0.249078  1.0000  0.800
  O5   O   0.750000  0.500000  0.250000  1.0000  0.800
  O6   O   0.000000  0.500000  0.000000  1.0000  0.800
  O7   O   0.246833  0.824799  0.246870  1.0000  0.800

loop_
_atom_site_label
_atom_bond_valence_sum
  Sr1  2.16
  Sr2  2.23
  Sr3  2.28
  Sr4  1.84
  Ti1  4.09

```

Ti2	4.03
Ti3	4.08
O1	-2.03
O2	-2.43
O3	-2.11
O4	-2.09
O5	-2.06
O6	-2.26
O7	-1.79

A.2.4.4: Model 4

```

data_Model_4
_cell_length_a          5.522461
_cell_length_b          5.522461
_cell_length_c         26.746224
_cell_angle_alpha       90.0000
_cell_angle_beta        90.0000
_cell_angle_gamma       120.0000
_cell_formula_units_Z   1
_symmetry_space_group_name_H-M 'P-3m1'
loop_
_atom_site_label
_atom_site_type_symbol
_atom_site_fract_x
_atom_site_fract_y
_atom_site_fract_z
_atom_site_occupancy
_atom_site_B_iso_or_equiv
O1  O  0.666667  0.333333  0.350161  1.0000  0.800
O2  O  0.497736  0.502264  0.252407  1.0000  0.800
O3  O  0.165559  0.834441  0.168537  1.0000  0.800
O4  O  0.833082  0.666163  0.083980  1.0000  0.800
O5  O  0.500000  0.000000  0.000000  1.0000  0.800
Ti1 Ti  0.333333  0.666667  0.711566  1.0000  0.800
Ti2 Ti  0.000000  0.000000  0.873975  1.0000  0.800
Ti3 Ti  0.333333  0.666667  0.958294  1.0000  0.800
Ti4 Ti  0.666667  0.333333  0.787276  1.0000  0.800
Sr1 Sr  0.666667  0.333333  0.915146  1.0000  0.800
Sr2 Sr  0.000000  0.000000  0.753487  1.0000  0.800
Sr3 Sr  0.333333  0.666667  0.834146  1.0000  0.800
Sr4 Sr  0.000000  0.000000  0.000000  1.0000  0.800

```

```

loop_
  _atom_site_label
  _atom_bond_valence_sum
    O1   -1.56
    O2   -2.13
    O3   -2.10
    O4   -2.11
    O5   -2.10
    Ti1   4.07
    Ti2   4.15
    Ti3   4.18
    Ti4   4.26
    Sr1   2.10
    Sr2   1.82
    Sr3   2.11
    Sr4   2.13

```

A.2.4.5: Model 5

```

data_Model_5
  _cell_length_a          9.565183
  _cell_length_b         17.335515
  _cell_length_c          5.522461
  _cell_angle_alpha      90.0000
  _cell_angle_beta       90.0000
  _cell_angle_gamma      90.0000
  _cell_formula_units_Z  1
  _symmetry_space_group_name_H-M 'P112/m'
loop_
  _atom_site_label
  _atom_site_type_symbol
  _atom_site_fract_x
  _atom_site_fract_y
  _atom_site_fract_z
  _atom_site_occupancy
  _atom_site_B_iso_or_equiv
    Sr1  Sr  0.000000  0.000000  0.000000  1.0000  0.800
    O1   O   0.739265  0.002757  0.744668  1.0000  0.800
    O2   O   0.000000  0.000000  0.500000  1.0000  0.800
    Sr2  Sr  0.500000  0.000000  0.500000  1.0000  0.800
    O3   O   0.500000  0.000000  0.000000  1.0000  0.800

```

Ti1	Ti	0.168717	0.064446	0.500000	1.0000	0.800
Ti2	Ti	0.664898	0.066058	0.000000	1.0000	0.800
O4	O	0.327743	0.137220	0.500000	1.0000	0.800
O5	O	0.092893	0.126158	0.244334	1.0000	0.800
Sr3	Sr	0.332911	0.119242	0.000000	1.0000	0.800
O6	O	0.831046	0.126074	0.000000	1.0000	0.800
O7	O	0.574071	0.136139	0.239581	1.0000	0.800
Sr4	Sr	0.831259	0.137331	0.500000	1.0000	0.800
Ti3	Ti	0.991842	0.196256	0.000000	1.0000	0.800
Ti4	Ti	0.509651	0.200176	0.500000	1.0000	0.800
O8	O	0.658216	0.259754	0.500000	1.0000	0.800
O9	O	0.415481	0.279044	0.746307	1.0000	0.800
O10	O	0.166667	0.272439	0.000000	1.0000	0.800
Sr5	Sr	0.132425	0.245464	0.500000	1.0000	0.800
O11	O	0.921131	0.250715	0.247538	1.0000	0.800
Sr6	Sr	0.692881	0.253530	0.000000	1.0000	0.800
Ti5	Ti	0.330887	0.315457	0.000000	1.0000	0.800

loop_

_atom_site_label

_atom_bond_valence_sum

Sr1	2.07
O1	-2.13
O2	-1.95
Sr2	2.08
O3	-2.27
Ti1	4.10
Ti2	4.21
O4	-1.87
O5	-2.16
Sr3	2.17
O6	-2.30
O7	-2.09
Sr4	2.11
Ti3	4.26
Ti4	4.06
O8	-1.71
O9	-1.88
O10	-2.03
Sr5	2.14
O11	-2.05
Sr6	1.81

Ti5 3.70

A.2.4.6: Model 6

data_Model_6						
_cell_length_a				11.044902		
_cell_length_b				11.044902		
_cell_length_c				17.335515		
_cell_angle_alpha				90.0000		
_cell_angle_beta				90.0000		
_cell_angle_gamma				120.0000		
_cell_formula_units_Z				1		
_symmetry_space_group_name_H-M				'P-3m1'		
loop_						
_atom_site_label						
_atom_site_type_symbol						
_atom_site_fract_x						
_atom_site_fract_y						
_atom_site_fract_z						
_atom_site_occupancy						
_atom_site_B_iso_or_equiv						
Ti1	Ti	0.000000	0.000000	0.337730	1.0000	0.800
Ti2	Ti	0.333333	0.666667	0.317826	1.0000	0.800
O1	O	0.405147	0.069537	0.254831	1.0000	0.800
Sr1	Sr	0.666667	0.333333	0.259472	1.0000	0.800
O2	O	0.415883	0.831767	0.276726	1.0000	0.800
O3	O	0.922937	0.845875	0.283601	1.0000	0.800
Sr2	Sr	0.167471	0.832529	0.246390	1.0000	0.800
Ti3	Ti	0.991303	0.495651	0.202439	1.0000	0.800
Ti4	Ti	0.000000	0.000000	0.187144	1.0000	0.800
O4	O	0.584653	0.415347	0.132638	1.0000	0.800
Sr3	Sr	0.827412	0.172588	0.142284	1.0000	0.800
O5	O	0.092583	0.423421	0.127675	1.0000	0.800
Sr4	Sr	0.333333	0.666667	0.116867	1.0000	0.800
O6	O	0.083413	0.916587	0.138618	1.0000	0.800
Ti5	Ti	0.666667	0.333333	0.070487	1.0000	0.800
Ti6	Ti	0.170945	0.829055	0.061087	1.0000	0.800
O7	O	0.749794	0.499588	0.004452	1.0000	0.800
O8	O	0.754197	0.000000	0.000000	1.0000	0.800
Sr5	Sr	0.000000	0.500000	0.000000	1.0000	0.800
Sr6	Sr	0.000000	0.000000	0.000000	1.0000	0.800

```

loop_
  _atom_site_label
  _atom_bond_valence_sum
    Ti1    3.37
    Ti2    3.75
    O1     -1.78
    Sr1     1.34
    O2     -2.05
    O3     -1.81
    Sr2     2.06
    Ti3     4.14
    Ti4     4.07
    O4     -2.28
    Sr3     2.11
    O5     -2.03
    Sr4     2.22
    O6     -2.22
    Ti5     4.39
    Ti6     4.12
    O7     -2.23
    O8     -1.94
    Sr5     2.06
    Sr6     1.95

```

A.2.4.7: Model 7

```

data_Model_7
  _cell_length_a      5.522461
  _cell_length_b      5.522461
  _cell_length_c      20.290814
  _cell_angle_alpha   90.0000
  _cell_angle_beta    90.0000
  _cell_angle_gamma   120.0000
  _cell_formula_units_Z 1
  _symmetry_space_group_name_H-M 'P-3m1'
loop_
  _atom_site_label
  _atom_site_type_symbol
  _atom_site_fract_x
  _atom_site_fract_y
  _atom_site_fract_z
  _atom_site_occupancy

```

_atom_site_B_iso_or_equiv						
Sr1	Sr	0.000000	0.000000	0.000000	1.0000	0.800
Ti1	Ti	0.000000	0.000000	0.830348	1.0000	0.800
O1	O	0.342310	0.171155	0.779512	1.0000	0.800
O2	O	0.166667	0.333333	0.888467	1.0000	0.800
Sr2	Sr	0.333333	0.666667	0.785663	1.0000	0.800
Sr3	Sr	0.666667	0.333333	0.890008	1.0000	0.800
Ti2	Ti	0.333333	0.666667	0.944526	1.0000	0.800
Ti3	Ti	0.666667	0.333333	0.725012	1.0000	0.800
O3	O	0.000000	0.500000	0.000000	1.0000	0.800
Ti4	Ti	0.333333	0.666667	0.631990	1.0000	0.800
O4	O	0.994132	0.497066	0.663332	1.0000	0.800

loop_

_atom_site_label	
_atom_bond_valence_sum	
Sr1	2.09
Ti1	4.07
O1	-2.05
O2	-2.09
Sr2	2.11
Sr3	2.19
Ti2	4.11
Ti3	4.15
O3	-2.10
Ti4	3.65
O4	-1.92

A.2.4.8: Model 8

data_Model_8_expanded	
_cell_length_a	5.522505
_cell_length_b	5.522505
_cell_length_c	41.605580
_cell_angle_alpha	90.0000
_cell_angle_beta	90.0000
_cell_angle_gamma	120.0000
_cell_formula_units_Z	1
_symmetry_space_group_name_H-M	'P-3'
loop_	
_atom_site_label	
_atom_site_type_symbol	

_atom_site_fract_x						
_atom_site_fract_y						
_atom_site_fract_z						
_atom_site_occupancy						
_atom_site_B_iso_or_equiv						
O000	O	0.625429	0.619546	0.377108	1.0000	0.800
Ti00	Ti	0.333333	0.666667	0.361974	1.0000	0.800
Ti00	Ti	0.666667	0.333333	0.358857	1.0000	0.800
Sr00	Sr	0.000000	0.000000	0.328039	1.0000	0.800
O000	O	0.013557	0.566180	0.324786	1.0000	0.800
Ti00	Ti	0.333333	0.666667	0.295070	1.0000	0.800
Sr00	Sr	0.666667	0.333333	0.272752	1.0000	0.800
O000	O	0.665676	0.796270	0.269753	1.0000	0.800
Ti00	Ti	0.000000	0.000000	0.242932	1.0000	0.800
O001	O	0.814974	0.147517	0.216176	1.0000	0.800
Sr01	Sr	0.333333	0.666667	0.215445	1.0000	0.800
Ti01	Ti	0.666667	0.333333	0.189624	1.0000	0.800
O001	O	0.500310	0.500457	0.162270	1.0000	0.800
Sr01	Sr	0.000000	0.000000	0.161807	1.0000	0.800
Ti01	Ti	0.333333	0.666667	0.135333	1.0000	0.800
Sr01	Sr	0.666667	0.333333	0.107993	1.0000	0.800
O001	O	0.666880	0.830690	0.108205	1.0000	0.800
Ti01	Ti	0.000000	0.000000	0.081202	1.0000	0.800
O001	O	0.825472	0.159372	0.054208	1.0000	0.800
Sr02	Sr	0.333333	0.666667	0.054225	1.0000	0.800
Ti02	Ti	0.666667	0.333333	0.027068	1.0000	0.800
O002	O	0.500000	0.500000	0.000000	1.0000	0.800
Sr02	Sr	0.000000	0.000000	0.000000	1.0000	0.800

loop_

_atom_site_label	
_atom_bond_valence_sum	
O000	-1.85
Ti00	3.67
Ti00	3.65
Sr00	2.18
O000	-1.99
Ti00	4.12
Sr00	2.17
O000	-2.12
Ti00	4.14
O001	-2.09

Sr01 2.19
 Ti01 4.14
 O001 -2.09
 Sr01 2.13
 Ti01 4.15
 Sr01 2.13
 O001 -2.10
 Ti01 4.15
 O001 -2.09
 Sr02 2.12
 Ti02 4.14
 O002 -2.08
 Sr02 2.10

A.2.4.9: Model 9

data_Model_9
 _cell_length_a 5.522461
 _cell_length_b 5.522461
 _cell_length_c 32.689829
 _cell_angle_alpha 90.0000
 _cell_angle_beta 90.0000
 _cell_angle_gamma 120.0000
 _cell_formula_units_Z 1
 _symmetry_space_group_name_H-M 'P-3'
 loop_
 _atom_site_label
 _atom_site_type_symbol
 _atom_site_fract_x
 _atom_site_fract_y
 _atom_site_fract_z
 _atom_site_occupancy
 _atom_site_B_iso_or_equiv

O1	O	0.000000	0.500000	0.000000	1.0000	0.800
Sr1	Sr	0.000000	0.000000	0.000000	1.0000	0.800
Ti1	Ti	0.666667	0.333333	0.033572	1.0000	0.800
Sr2	Sr	0.333333	0.666667	0.065732	1.0000	0.800
O2	O	0.333135	0.188317	0.068305	1.0000	0.800
Ti2	Ti	0.000000	0.000000	0.100027	1.0000	0.800
O3	O	0.130344	0.334145	0.136263	1.0000	0.800
Sr3	Sr	0.666667	0.333333	0.134113	1.0000	0.800

Ti3	Ti	0.333333	0.666667	0.165225	1.0000	0.800
O4	O	0.547313	0.985345	0.205852	1.0000	0.800
Sr4	Sr	0.000000	0.000000	0.203529	1.0000	0.800
Ti4	Ti	0.666667	0.333333	0.237507	1.0000	0.800
Ti5	Ti	0.333333	0.666667	0.252275	1.0000	0.800
O5	O	0.996648	0.335592	0.270971	1.0000	0.800
Ti6	Ti	0.000000	0.000000	0.316288	1.0000	0.800
Ti7	Ti	0.666667	0.333333	0.318949	1.0000	0.800
O6	O	0.326209	0.250361	0.338452	1.0000	0.800

loop_

_atom_site_label

_atom_bond_valence_sum

O1	-2.24
Sr1	2.15
Ti1	4.18
Sr2	2.24
O2	-2.23
Ti2	4.18
O3	-2.24
Sr3	2.24
Ti3	4.26
O4	-2.09
Sr4	2.37
Ti4	3.02
Ti5	3.06
O5	-1.62
Ti6	3.89
Ti7	3.63
O6	-2.08

A.2.4.10: Model 10

data_Model_10

_cell_length_a	5.522461
_cell_length_b	5.522461
_cell_length_c	31.699228
_cell_angle_alpha	90.0000
_cell_angle_beta	90.0000
_cell_angle_gamma	120.0000
_cell_formula_units_Z	1

```

_symmetry_space_group_name_H-M      'P-3'
loop_
_atom_site_label
_atom_site_type_symbol
_atom_site_fract_x
_atom_site_fract_y
_atom_site_fract_z
_atom_site_occupancy
_atom_site_B_iso_or_equiv
  O1      O      0.666667      0.333333      0.351011      1.0000      0.800
  O2      O      0.333333      0.666667      0.331259      1.0000      0.800
  O3      O      0.000000      0.000000      0.349187      1.0000      0.800
  Ti1     Ti      0.970672      0.663791      0.321755      1.0000      0.800
  O4      O      0.965340      0.297956      0.283633      1.0000      0.800
  Ti2     Ti      0.333333      0.666667      0.263900      1.0000      0.800
  Ti3     Ti      0.666667      0.333333      0.244429      1.0000      0.800
  Sr1     Sr      0.000000      0.000000      0.208305      1.0000      0.800
  O5      O      0.549878      0.988322      0.214513      1.0000      0.800
  Ti4     Ti      0.333333      0.666667      0.172004      1.0000      0.800
  Sr2     Sr      0.666667      0.333333      0.135517      1.0000      0.800
  O6      O      0.129439      0.333924      0.141708      1.0000      0.800
  Ti5     Ti      0.000000      0.000000      0.104073      1.0000      0.800
  O7      O      0.332558      0.189428      0.070837      1.0000      0.800
  Sr3     Sr      0.333333      0.666667      0.067387      1.0000      0.800
  Ti6     Ti      0.666667      0.333333      0.034661      1.0000      0.800
  Sr4     Sr      0.000000      0.000000      0.000000      1.0000      0.800
  O8      O      0.000000      0.500000      0.000000      1.0000      0.800

```

```

loop_
_atom_site_label
_atom_bond_valence_sum
  O1      -1.78
  O2      -2.02
  O3      -1.79
  Ti1     2.88
  O4      -2.03
  Ti2     2.55
  Ti3     3.22
  Sr1     2.42
  O5      -2.08
  Ti4     4.10
  Sr2     2.28

```

O6	-2.23
Ti5	4.11
O7	-2.24
Sr3	2.21
Ti6	4.13
Sr4	2.13
O8	-2.25